



Study of bioactivity, corrosion resistance and fatigue behavior of Ti-12Mo-6Zr-2Fe alloy after different surface treatments

Cesar Adolfo Escobar Claros

► To cite this version:

Cesar Adolfo Escobar Claros. Study of bioactivity, corrosion resistance and fatigue behavior of Ti-12Mo-6Zr-2Fe alloy after different surface treatments. Solid mechanics [physics.class-ph]. Université Grenoble Alpes [2020-..]; Universidade federal de São Carlos, 2020. English. NNT : 2020GRALI051 . tel-03098341

HAL Id: tel-03098341

<https://theses.hal.science/tel-03098341>

Submitted on 5 Jan 2021

HAL is a multi-disciplinary open access archive for the deposit and dissemination of scientific research documents, whether they are published or not. The documents may come from teaching and research institutions in France or abroad, or from public or private research centers.

L'archive ouverte pluridisciplinaire **HAL**, est destinée au dépôt et à la diffusion de documents scientifiques de niveau recherche, publiés ou non, émanant des établissements d'enseignement et de recherche français ou étrangers, des laboratoires publics ou privés.

THÈSE

Pour obtenir le grade de

DOCTEUR DE L'UNIVERSITÉ GRENOBLE ALPES et

**DOUTOR EM ENGENHARIA DE MATERIAIS,
UNIVERSIDADE FEDERAL DE SÃO CARLOS**
préparée dans le cadre d'une cotutelle *entre l'Université
Grenoble Alpes et Université Federal de São Carlos*

Spécialité : **Matériaux, Mécanique, Génie civil, Electrochimie**

Arrêté ministériel : le 6 janvier 2005 – 25 mai 2016

Présentée par

Cesar A. ESCOBAR CLAROS

Thèse dirigée par **Jean Claude LEPETRE (France) et Claudemiro Bolfarini (Brésil)** et codirigée par **Virginie ROCHE (France) et Leonardo Contri Campanelli (Brésil)**

préparée au sein des

- Laboratoire d'Electrochimie et de Physicochimie des Matériaux et des Interfaces (LEPMI), France
- Structural Characterization Laboratory (LCE), Brésil
- Centro de Caracterização e Desenvolvimento de Materiais (CCDM), Brésil

dans **l'École Doctorale Ingénierie - Matériaux, Mécanique, Environnement, Energétique, Procédés, Production (IMEP2)**

Etude de bioactivité, résistance à la corrosion et comportement en fatigue de l'alliage Ti-12Mo-6Zr-2Fe après différents traitements de surface

Thèse soutenue publiquement le **19 Novembre 2020**, devant le jury composé de :

M. Jean-Claude LEPRETRE

Professeur, Université Grenoble Alpes, Directeur de thèse

M. Claudemiro BOLFARINI

Professeur, Université Fédérale de São Carlos, Brésil, Directeur de thèse

Mme. Virginie ROCHE

Maître de conférences, Université Grenoble Alpes, Co-encadrante de thèse

M. Nicolas MARY

Maître de conférences, INSA Lyon, Rapporteur

M. Rubens CARAM

Professeur, Université d'État de Campinas, Examinateur

M. Alberto MOREIRA JORGE JUNIOR

Professeur, Université Fédérale de São Carlos, Brésil, Président et Examinateur

M. Dilermando NAGLE TRAVESSA

Professeur, Université Fédérale de São Paulo, Brésil, Rapporteur



**UNIVERSIDADE FEDERAL DE SÃO CARLOS
CENTRO DE CIÊNCIAS EXATAS E DE TECNOLOGIA
PROGRAMA DE PÓS-GRADUAÇÃO EM CIÊNCIA
E ENGENHARIA DE MATERIAIS**

**UNIVERSITE GRENOBLE ALPES - ÉCOLE DOCTORALE
DE INGENIERIE - MATERIAUX, MECANIQUE, ENVIRONNEMENT,
ENERGETIQUE, PROCEDES, PRODUCTION (IMEP2)**

**STUDY OF BIOACTIVITY, CORROSION RESISTANCE AND FATIGUE
BEHAVIOR OF Ti-12Mo-6Zr-2Fe ALLOY AFTER DIFFERENT SURFACE
TREATMENTS**

Cesar Adolfo Escobar Claros

Tese apresentada ao Programa de
Pós-Graduação em Ciência e Engenharia de
Materiais como requisito parcial à obtenção do
título de DOUTOR EM CIÊNCIA E
ENGENHARIA DE MATERIAIS

Orientador brasileiro: Prof. Dr. Claudemiro Bolfarini
Orientador francês: Prof. Dr. Jean-Claude Leprêtre
Coorientador brasileiro: Dr. Leonardo Contri Campanelli
Coorientador francês: Prof. Dr. Virginie Roche
Agência Financiadora: CNPq process:141952/2019-9;
CAPES-COFECUB: 88887.185801/2018-00

São Carlos

2020

ABSTRACT

Demand for new implants with improved bioactivity, corrosion resistance, and optimal mechanical properties has been increasing considerably. In this sense, different surface treatments are applied in titanium alloys to improve their osteointegration process. Nevertheless, the developments of new bioactive surfaces could cause a considerable reduction in fatigue and corrosion strength leading to catastrophic failures in clinical use. For these reasons, this work studied the biocompatibility, corrosion and fatigue performance of Ti-12Mo-6Zr-2Fe alloy treated with three different surface modifications, namely, chemical surface treatment (CST), nanotubes (Nt) and nanopores (NP). Samples were immersed in simulated body fluid (SBF) solution during different periods, 0, 1, 7, and 14 days. After 14 days immersed in SBF, samples with CST showed high hydroxyapatite (HAp) formation; Likewise, samples with Nt and NP exhibited lower and moderated HAP formation, respectively. In samples without surface treatment was not observed HAp formation. The electrochemical behavior was studied through polarization curves and electrochemical impedance spectroscopy (EIS). Samples with Nt and NP displayed higher corrosion resistance and lower passivation current (I_{pass}) compared with untreated samples, after 14 days of immersion in SBF; samples with CST showed the worst corrosion performance for all the surface conditions studied. Furthermore, within the framework of electrochemical investigations, EIS results of Nt and NP samples showed a characteristic behavior that could not be modeled by traditional equivalent circuits. Thus, it was proposed a two-channel transmission line model for analyzing this impedance results, leading to a successful fitting of the EIS data. Finally, was observed a reduction of the fatigue resistance in the samples treated with NP and CST, associated with hydrogen embrittlement processes, due to the pick-up of hydrogen during the respective surface treatments.

Keywords: Titanium alloy, Bioactivity, Corrosion resistance, Fatigue behavior, Hydrogen embrittlement.

RÉSUMÉ

La demande de nouveaux implants avec une meilleure bioactivité, résistance à la corrosion et des propriétés mécaniques optimisées a augmenté considérablement. Différents traitements de surface sont appliqués sur des alliages de titane pour améliorer leur processus d'ostéo-intégration. Néanmoins, le développement de nouvelles surfaces bioactives pourrait causer une réduction considérable de la résistance à la fatigue et à la corrosion, ce qui peut entraîner des défaillances catastrophiques dans leurs utilisations cliniques. Ainsi, dans ce travail, la performance en biocompatibilité, en fatigue et en corrosion de l'alliage de Ti-12Mo-6Zr-2Fe (TMZF) a été étudié. Cet alliage a été soumis à trois modifications de surface différentes, à savoir le traitement chimique de surface (CST, en anglais, pour *Chemical Surface Treatment*), les nanotubes (Nt) et les nanopores (NP). Les échantillons ont été immersés dans une solution physiologique appelée SBF (en anglais, pour *Simulated Body Fluid*) avec des durées d'immersion différentes : 0, 1, 7, et 14 jours. Après 14 jours d'immersion dans SBF, les échantillons qui ont subi un traitement chimique de surface ont montré une formation importante d'hydroxyapatite (HAp), nécessaire pour assurer une bonne osseo-intégration de l'implant. De même, les échantillons avec des nanotubes et nanopores montrent une formation, respectivement, faible et modérée de HAp. Dans les échantillons sans traitement de surface, la formation de HAp n'a pas été observée. Le comportement électrochimique a été étudié par des courbes de polarisation et par spectroscopie d'impédance électrochimique (SIE, ou EIS en anglais, pour *Electrochemical Impedance Spectroscopy*). Les échantillons avec Nt et NP manifestent une meilleure résistance à la corrosion et un domaine de passivité (I_{pass}) plus faible, en comparaison avec les échantillons non traités après 14 jours d'immersion dans SBF. Les échantillons qui ont subi un traitement chimique de surface (CST) ont démontré une résistance à la corrosion faible par rapport aux autres surfaces étudiées. Par ailleurs, dans le contexte des investigations électrochimiques, les résultats de SIE d'échantillons NT et NP ont montré un comportement caractéristique qui ne pouvait pas être modélisé par les circuits équivalents traditionnels. Ainsi, un modèle de ligne de transmission de deux canaux a été proposé pour analyser ces résultats d'impédance, permettant un ajustement réussi des données de SIE. Finalement, une réduction de la résistance à la fatigue a été observée dans les échantillons traités avec NP et CST, via une fragilisation par l'hydrogène, en raison du captage d'hydrogène pendant les traitements de surface.

Mots clés: Alliage de titane, bioactivité, résistance à la corrosion, comportement à la fatigue, fragilisation par l'hydrogène.

RESUMO

A demanda por novos implantes com melhor bioatividade, resistência à corrosão e ótimas propriedades mecânicas têm aumentado consideravelmente. Nesse sentido, diferentes tratamentos de superfície são aplicados em ligas de titânio para melhorar seu processo de osseointegração. No entanto, o desenvolvimento de novas superfícies bioativas pode causar uma redução considerável na fadiga e na resistência à corrosão, levando a falhas catastróficas no uso clínico. Por esses motivos, este trabalho estudou o desempenho em biocompatibilidade, corrosão e fadiga da liga Ti-12Mo-6Zr-2Fe tratada com três diferentes modificações de superfície, a saber: tratamento químico da superfície (CST), nanotubos (Nt) e nanoporos (NP). As amostras foram imersas em uma solução que simula o fluido corporal (SBF) durante diferentes períodos, 0, 1, 7 e 14 dias. Após 14 dias imersos em SBF, não foi observada formação de HAp nas amostras sem tratamento de superfície, porém amostras com CST mostraram alta formação de hidroxiapatita (HAp). Da mesma forma, amostras com Nt e NP exibiram baixa e moderada formação de HAp, respectivamente. O comportamento eletroquímico foi estudado através de curvas de polarização e espectroscopia de impedância eletroquímica (EIS). Amostras com Nt e NP apresentaram maior resistência à corrosão e menor corrente de passivação (I_{pass}) em comparação com amostras não tratadas, após 14 dias de imersão no SBF; amostras com CST apresentaram o pior desempenho à corrosão de todas as condições de superfície estudadas. Além disso, no âmbito de investigações eletroquímicas, os resultados de EIS das amostras de Nt e NP mostraram um comportamento característico que não foi possível modelar pelos circuitos equivalentes tradicionais. Assim, foi proposto um modelo de linha de transmissão de dois canais para analisar esses resultados de impedância, levando a um ajuste bem-sucedido dos dados de EIS. Por fim, observou-se uma redução da resistência à fadiga nas amostras tratadas com NP e CST, associadas aos processos de fragilização por hidrogênio, devido à captação de hidrogênio durante os respectivos tratamentos de superfície.

Palavras-chave: Liga de titânio, Bioatividade, Resistência à corrosão, Comportamento em fadiga, Fragilização por hidrogênio.

ACKNOWLEDGMENTS

I want to thank Professor Claudemiro Bolfarini for this opportunity, for all the trust he gave me and advice during all these years. I would also express my gratitude to my supervisors in France, Virginie Roche and Jean Claude Leprêtre for their valued help and productive discussions.

I want to express my special thanks to my co-advisor, Dr. Leonardo C. Campanelli, and professors Paulo Sérgio Pereira da Silva and Alberto Moreira Jorge Júnior, for guiding me, the technical discussions and everything taught.

I am grateful for the supports of the Brazilian National Council for Scientific and Technological Development (CNPq) (grant n° 141952/2019-9), French Committee for the Evaluation of Academic and Scientific Cooperation with Brazil (COFECUB) and CAPES (process n° 88887.137755/2017-00) for funding the bilateral cooperation, and to the CNPq universal project (n° 403955/2016-5).

This study was financed in part by the Coordenação de Aperfeiçoamento de Pessoal de Nível Superior - Brasil (CAPES) - Finance Code 001

To the Postgraduate Program in Materials Science and Engineering (PPGCEM) at the Federal University of São Carlos and the entire professor's Council, for the knowledge shared that contributed to my academic training.

Thanks to the Laboratory of Structural Characterization (LCE/DEMa/UFSCar), *Centro de Caracterização e Desenvolvimento de Materiais* (CCDM/UFSCar), and the *Consortium des Moyens Technologiques Communs* (CMTC/UGA) for allowing me to use their facilities.

I also want to thank all my colleagues from PPGCEM and LEPMI for their discussions, suggestions, and help during these doctoral years.

I would like to express my special thanks to my friends Kathe, Brenda, Tales, Rodriguinho, Vero, Chris, and many others for the coffee and tea sections, their motivation and support, and the time we shared together during these years.

Especialmente dedico esta conquista a mi familia, mi mamá, mi abuelo, mis hermanos y a Daniela, por estar siempre ahí apoyándome, por todo su amor, compresión, apoyo y motivarme día a día. Sin ustedes esto no sería posible.

A todos muchísimas gracias por contribuir en esta experiencia.

TABLE OF CONTENTS

INTRODUCTION	1
CHAPTER I	3
State of the Art	3
1.1 Metallic biomaterials.....	3
1.2 Titanium alloys	4
1.2.1 Ti-12Mo-6Zr-2Fe.....	5
1.3 Fixation method.....	6
1.3.1 Surface modification of medical implants	6
1.3.2 Chemical surface modification by acid etching and alkaline treatment ...	7
1.3.2.1 Acid etching	7
1.3.2.2 Alkaline treatment	8
1.3.3 Anodization process.....	9
1.3.3.1 Mechanisms of surface anodization.....	11
1.4 Corrosion of biomedical devices	13
1.4.1 Potentiodynamic polarization	14
1.4.2 Electrochemical Impedance Spectroscopy (EIS)	18
1.5 Fatigue in metallic biomaterials	21
CHAPTER II	25
Materials and Methods.....	25
2.1 Materials and samples	25
2.2 Surface modification processes	26
2.2.1 Surface preparation	26
2.2.2 Chemical surface treatment	26
2.2.3 Anodization process.....	27
2.3 Bioactivity assay.....	28
2.4 Electrochemical behavior	29
2.5 Fatigue resistance	30

2.6 Surface characterization.....	31
2.6.1 Roughness Measurements	31
2.6.2 Hydrogen absorption.....	31
CHAPTER III	33
Bioactivity and electrochemical behavior of TMZF samples treated with CST, nanopores and nanotubes	33
3.1 Hydroxyapatite formation test.....	37
3.2 Electrochemistry characterization	41
CHAPTER IV.....	47
Analysis and modeling of the impedance spectra for the different surface conditions obtained	47
4.1 EIS measurements over untreated TMZF samples	48
4.2 EIS measurements over TMZF samples treated with HCl and NaOH.....	55
4.3 EIS measurements over anodized TMZF samples	61
4.3.1 Analysis of the electrical models proposed in the literature.....	65
4.3.2 Porous electrode model and transmission line.....	67
4.3.3 Employment of the transmission line model to the case of anodized TMZF samples in SBF	71
CHAPTER V.....	83
Fatigue behavior of the different surface treatments	83
5.1 Fatigue resistance of TMZF samples untreated and treated with CST, and nanopores	83
5.2 Hydrogen embrittlement	93
GENERAL CONCLUSIONS	105
FURTHER RESEARCH	107
REFERENCES.....	109
RESUME DETAILLE EN FRANÇAIS	121
RESUMO DETALHADO EM PORTUGUÊS.....	167

LIST OF TABLES

Table 1.1 Anodization parameters and cell response of Ti-based metallic implants.	11
.....	
Table 2.1 nominal composition of the TMZF alloy [2].	25
.....	
Table 3.1 Quantitative chemical EDS analysis of untreated, nanotubes, nanopores, and CST samples. After 14 days of immersion in SBF solution.....	39
.....	
Table 4.1 Electrical parameters obtained by fitting the experimental results of impedance for untreated samples at 37 °C in SBF solution.....	53
Table 4.2 Electrical impedance parameters obtained by fitting the experimental results of CST samples immersed in SBF at 37 °C for the different periods 0, 1, 7 and 14 days.	60
Table 4.3 Electrical impedance parameters obtained by adjusting the experimental results of Nt samples.	75
Table 4.4 Electrical impedance parameters obtained by adjusting the experimental results of NP samples.	77
.....	
Table 5.1 Mechanical properties of the TMZF titanium alloy used in this study....	84
Table 5.2 Analysis of staircase method data for untreated TMZF alloy.....	85
Table 5.3 Topography measurements of Ra and Rz roughness of the untreated, CST and nanopores samples.....	87
Table 5.4 Hydrogen content results for: Untreated, CST, CST-polished and nanopores.....	89
Table 5.5 Analysis of staircase method data for CST-polished samples.....	90
Table 5.6 Tensile testing results of untreated, CST and nanopores samples.	100
Table 5.7 summary of the fatigue response for the different surface conditions studied in this work.	102

LIST OF FIGURES

Figure 1.1 Metallic biomaterials for orthopedic and dental applications (provided by Nakashima Medical Co. Ltd Japan and Japan Medical Materials (JMM) Co.) [11].....	4
Figure 1.2 Schematic illustration of the crystal structure of the major Titanium alloys for implants. a) Center-body cubed (α -Ti) and b) Compact hexagonal β -Ti.....	5
Figure 1.3 An artist's view of the titanium/tissue interface divided into five regions. The oxide of titanium is covered with a very thin layer of titanium peroxy compounds, which are in contact with the living bone (Adapted from [23]).	7
Figure 1.4 Schematic representation of the structural change in the surface of the metallic Titanium after the alkaline process and subsequent apatite formation on the treated surface (Adapted from ref. [21]).....	9
Figure 1.5 Human osteoblast cell attachment and proliferation on titanium pure and titanium pure with TiO_2 nanotubes [30].....	10
Figure 1.6 Schematic representations of the different stages of the anodization process: Stage I oxide layer formation; Stage II pores nucleation and dissolution of the TiO_2 layer; in Stage III the steady-state is established.....	13
Figure 1.7 Schematic illustration of the local anodes and cathodes and the local cell formed between them [44].....	14
Figure 1.8 Schematic illustration of potential vs current density curves of a metallic electrode. E_{corr} = corrosion potential; E_{eq} = equilibrium potential; I_{corr} = corrosion current density; i_0 = exchange current density [44].....	15
Figure 1.9 Schematic representation of the anodic part of the polarization curve (a) of a stainless steel in an acid medium (b) of a passive metal in a non-aggressive medium. Adapted from [31]	16
Figure 1.10 Anodic polarization curves of 316L stainless steel, cobalt-chromium alloy and pure Titanium immersed in Hanks solution [47].....	16
Figure 1.11 (a) Potentiodynamic polarization test results for CG and nanostructured titanium substrates, uncoated, PEO coated and RGD modified and PEO coating morphology for (b) coarse-grained and (c) nanostructured titanium substrates [48].	17
Figure 1.12 (a) Potentiodynamic polarization curves of the untreated and anodized titanium samples in NaCl (8 g/l); and (b) representative SEM images of the anodic treated titanium sample [49].....	18
Figure 1.13 Schematic representation of the principle of measurements by EIS. .	19

Figure 1.14 Schematic representation of the impedance results: a) Nyquist plot or complex plot; b) magnitude of the Bode plot and c) phase of the Bode plot... 20
Figure 1.15 representations of synthetic impedance data in standard units: a) Bode phase-angle; (b) Corrected Bode phase-angle. (adapted from [55]) 21
Figure 1.16 Axial loading S,N-curves in oxygen-saturated Ringer's solution: a) polished and grit blasted Ti-6Al-4V; b) polished, thermally and anodically oxidized Ti-6Al-7Nb (Adapted from [63]) 22
Figure 1.17 Plot of fatigue resistance (σ_f) in function of the Roughness (Rz) 23
Figure 1.18 Staircase fatigue diagrams for 5×10^6 endurance limits. "X" means failure and "O" means survival to the run-out [68]. 24
Figure 2. 1 Flowchart of the experimental procedure developed in this doctoral thesis. 25
Figure 2. 2 Dimensions of specimens for fatigue tests (in mm). 26
Figure 2. 3 electrochemical cells used in this work for anodization experiments: a) assembly for polished disks and b) assembly for fatigue specimens. 27
Figure 2. 4 Schematic representation of the experimental assembly used to bioactivity assays and the ion concentrations of the simulated body fluid (SBF) [72]. 28
Figure 2. 5 Schematic representation of the experimental assembly for the electrochemical characterization. (Adapted from [31]) 29
Figure 3. 1 (a) Microstructure and (b) XRD spectrum of the TMZF alloy. 34
Figure 3. 2 SEM image of the untreated samples after the grinded and polished processes. 34
Figure 3.3 SEM images of TMZF alloy, chemically treated by HCl 37% at 60 °C and NaOH 10 mol·L ⁻¹ at 60 °C for 24 h. 35
Figure 3.4 SEM images of anodized surfaces for different preliminary anodization parameter, varying the applied potential and the anodization time: a) 60V-1h, b) 40V-1h, c) 40V-2h, d) 20V-2h, e) 15V-2h and f) 10V-2h. 36
Figure 3.5 High-resolution SEM image of anodized samples: a) Nanotubes and b) Nanopores. 37
Figure 3.6 Quantitative evaluation by apatite mass gain of untreated, CST, nanotubes and nanopores samples after different immersion times in SBF. 38

Figure 3.7 SEM images for samples of TMZF alloy subjected to the bioactivity tests after 14 days immersed in SBF. a) Untreated; b) Nanotubes; c) Nanopores and d) CST samples	39
Figure 3.8 XRD patterns of untreated, CST, nanotubes and nanopores samples after 14 days of immersion in SBF.	40
Figure 3.9 Raman spectral mapping of nanotubes, nanopores and CST samples soaked during 7 and 14 days in SBF.	41
Figure 3.10 Anodic polarization curves, in SBF electrolyte at 37 °C for the TMZF alloy: a) Untreated; b) nanotubes; c) nanopores and d) CST.....	42
Figure 3.11 Electrochemical measurements of corrosion potential (E_{corr}) of TMZF alloy untreated and treated with nanotubes, nanopores, and CST for different immersion times in SBF at 37°C.	43
Figure 3.12 Electrochemical measurements of passivation current density (i_{pass}) of TMZF alloy untreated and treated with nanotubes, nanopores, and CST in different immersion times in SBF at 37°C.	44
Figure 4.1 a) SEM micrograph of untreated TMZF sample before the immersion period; impedance results for untreated samples immersed in SBF at 37 °C: b) Corrected-phase angle; c) Nyquist plot and d) Corrected-magnitude of the impedance for the different immersion time (0, 1, 7, and 14 days denoted as 0D, 1D, 7D and 14D respectively).	49
Figure 4.2 Schematic electrochemical impedance circuits: a) Randles circuit and b) porous passive layer circuit.....	50
Figure 4.3 Evolution of α_{eff} versus frequency, of the TMZF untreated samples for the different immersion periods (0, 1, 7, and 14 days denoted as 0D, 1D, 7D and 14D respectively).in SBF at 37 °C.	52
Figure 4.4 Electrical equivalent circuit for untreated samples and b) Nyquist plots of experimental and simulated results obtained through the Simad software, for the different immersion periods (0, 1, 7, and 14 days denoted as 0D, 1D, 7D and 14D respectively) in SBF at 37 °C. The error coefficient was lower than 1% for all the curves.....	53
Figure 4.5 Effective capacitances and thickness evolution of the passive inner layer for untreated TMZF samples during different immersion days in SBF solution at 37 °C.....	55
Figure 4.6 a) SEM micrographs of CST TMZF samples before the immersion periods; Schematic representation of the impedance results for CST samples	

immersed in SBF at 37 °C during the different periods (0, 1, 7, and 14 days denoted as 0D, 1D, 7D and 14D respectively): b) Corrected-phase angle; c) Nyquist plot and d) Magnitude of the impedance.....	56
Figure 4.7 Evolution of α_{eff} versus frequency, of the CST TMZF samples for the different immersion periods (0, 1, 7, and 14 days denoted as 0D, 1D, 7D and 14D respectively) in SBF solution at 37 °C.....	58
Figure 4.8 Equivalent circuit for CST TMZF samples (Adapted from [59]).	59
Figure 4.9 Nyquist plots of experimental and simulated results obtained through the Simad software, for the CST samples immersed in SBF at 37 °C during the different periods (0, 1, 7, and 14 days denoted as 0D, 1D, 7D and 14D respectively).....	60
Figure 4.10 Effective capacitance and thickness evolution of the passive inner layer for CST TMZF samples during different immersion days at 37 °C in SBF solution.	61
Figure 4.11 a) SEM micrographs of nanotubes TMZF sample before the immersion periods; impedance results for nanotubes samples immersed in SBF at 37 °C for the different periods (0, 1, 7, and 14 days denoted as 0D, 1D, 7D and 14D respectively): b) Corrected-phase angle; c) Nyquist plot and d) Corrected-magnitude of the impedance.....	62
Figure 4.12 a) SEM micrographs of nanopores TMZF sample before the immersion periods; Schematic representation of the impedance results for untreated samples immersed in SBF at 37 °C during the different periods (0, 1, 7, and 14 days denoted as 0D, 1D, 7D and 14D respectively): b) Corrected-phase angle; c) Nyquist plot and d) Magnitude of the impedance.....	64
Figure 4.13 Evolution of α_{eff} with the frequency of the anodized TMZF samples for the different immersion periods (0, 1, 7, and 14 days denoted as 0D, 1D, 7D and 14D respectively) in SBF at 37 °C: a) nanotubes and b) nanopores.....	65
Figure 4.14 Graphical representation of the EEC most frequently used for modeling the impedance results of anodized titanium samples.	66
Figure 4.15 Schematic representation of the telegraph cable considered by Thomson and Heaviside: a) representation showing a differential element with length dx and b) elementary components of a transmission line. For system shown in a, $Z_1 = R_0$ and $Z_2 = 1/j\omega C_{\text{wire}}$ [59].....	68
Figure 4.16 Schematic representations of a porous electrode: a) porous electrode with irregular channels between particles of electrode material and b) transmission line inside a cylindrical pore [59].	69

Figure 4.17 Schematic illustration of the inner region ($0 < x < L$) of a porous electrode divide by a porous film deposited on a conductive substrate. ζ represents the interfacial impedance disposed over the entire porous surface, Z_A is correlated with the impedance of the interface external solution solid and Z_B is used to describe the interface internal solution substrate. (adapted from [106]).....	70
Figure 4.18 Representative SEM images indicating the procedure to obtain the layer thickness of: a) Nanotubes and b) Nanopores.....	73
Figure 4.19 The transmission line model proposed to describe the impedance response of the anodized TMZF samples immersed in SBF at 37 °C during the different periods evaluated.....	74
Figure 4.20 Nyquist plots of experimental and simulated results acquired from Simad software for the anodized specimens immersed in SBF at 37 °C during different periods (0, 1, 7, and 14 days denoted as 0D, 1D, 7D and 14D respectively): a) Nanotubes and b) Nanopores.....	75
Figure 4.21 Endpoints parameters, R_A and Q_B , obtained from the transmission line model used in nanotubes samples after different immersion periods in SBF..	76
Figure 4.22 Apatite formation over nanotubes samples after different immersion periods in SBF (0, 1, 7 and 14 days).	77
Figure 4.23 Endpoints parameters, R_A and Q_B , obtained from the transmission line model used in nanopores samples after different immersion periods in SBF.	78
Figure 4.24 Apatite formation over nanopores samples after different immersion periods in SBF (0, 1, 7 and 14 days).	79
Figure 4.25 Corrosion response and bioactivity of untreated, CST, nanotubes, and nanopores samples after 14 days of immersion in SBF at 37 °C. Barrier resistance (R_B or R_A for the anodized samples) obtained from the impedance data, passivation current (I_{pass}) from the polarization curves, and bioactivity through the mass gain.	80
Figure 5.1 Staircase fatigue diagram for untreated samples. “●” Means failure and “◆” means survival to the run-out.....	84
Figure 5.2 Fractography of untreated sample, the dash line designates the approximate transition between the stable and unstable crack propagation regions and the square indicates the magnified region on the right side, pointing out the crack initiation site.....	86
Figure 5.3 . Representative 3D-images determined by confocal laser scanning microscopy of: a) untreated, b) CST and c) nanopores samples.	88

Figure 5.4 Staircase fatigue diagram for CST-polished samples. “●” Means failure, “◆” means survival to the run-out and “◊” specimens not considered in the analysis.....	90
Figure 5.5 Fractography of CST-polished sample, the square indicates the magnified region on the right side, pointing out the crack initiation site.	91
Figure 5.6 Staircase fatigue diagram for nanopores samples. “●” Means failure, “◆” means survival to the run-out and.....	92
Figure 5.7 a) Fractography of nanopores sample, which was tested at 500 MPa, b) magnified zone indicating a stable crack propagation region, c) magnified region of the nanopores sample indicating Wallner lines and d) magnified region of the CST-polished sample which was fatigue tested at 550 MPa indicating the Wallner lines pattern.	93
Figure 5.8 Images of the CST-polished sample and fatigue tested generated using the ASTAR system coupled to TEM: (a) virtual bright-field (VBF) image, (b) phase mapping (PM), (c) orientation image mapping (OIM) and (d) inverse pole figure (IPF) from where the colors were used to index orientations in the OIM.	95
Figure 5.9 Fractography of nanopores sample, which was fatigue tested at 650 MPa, the square indicates the magnified region on the right side.	96
Figure 5.10 Crack tip opening and striation formation mechanism in fatigue: (a) no hydrogen effect, (b) hydrogen effect. Extracted from [142].	97
Figure 5.11 a) Fractography of CST not-polished sample, which was fatigue tested at 300 MPa, b), c) and d) magnified zone indicating a stable crack propagation region at the hydrogenated zone indicate by black arrows.	98
Figure 5.12 a) Fractography of nanopores sample, which was fatigue tested at 300 MPa, b) magnified zone of the final failure, c) and d) zone indicating a stable crack propagation region at the hydrogenated area, indicated by black arrows.	99
Figure 5.13 Frontal and lateral fractography of: a) untreated, b) CST and c) nanopores samples.....	101
Figure 5.14 effect of the NDH-HT on crack growth rate of type 316L stainless steel (Extracted and edited from [142]).....	102

LIST OF ABBREVIATIONS

ASTM

American Standard for Testing of Materials

C_{dl}	Double layer capacitance
CPE	Constant-Phase-Element
CST	Chemical surface treatment with HCl etching and NaOH alkaline solution
E_{corr}	Corrosion potential
EDS	Energy dispersive spectroscopy
EEC	Electrical equivalent circuit
EIS	Electrochemical impedance spectroscopy
H_3PO_4	Phosphoric acid
Hap	Hydroxyapatite
HCl	Hydrochloric acid
HE	Hydrogen Embrittlement
I_{pass}	Passivation current density
NaOH	Sodium hydroxide
NP	Nanopores
Nt	Nanotubes
OCP	Open circuit potential
Q	Pseudocapacitance ($\Omega s^\alpha \cdot cm^2$)
R_{ct}	Charge transfer resistance
R_e	Electrolyte resistance or Ohmic resistance ($\Omega \cdot cm^{-2}$)
R_p	Polarization resistance
SBF	Solution body fluid
SCE	Saturated calomel electrode
SEM	Scanning electron microscopy
TEM	Transmission electron microscopy
TMZF	Ti-12Mo-6Zr-2Fe, titanium alloy
TL	Transmission line
W	Warburg element
X_1	Impedance distributed in the liquid phase of the transmission line ($\Omega \cdot cm^{-1}$)
X_2	Impedance distributed in the solid phase of the transmission line ($\Omega \cdot cm^{-1}$)
XRD	X-ray diffraction
ZA	Boundary impedance at the interface electrolyte top of the pores (Ω)
$Z_{A,B}$	Impedances of the boundary conditions of the transmission line
ZB	Boundary impedance at the interface electrolyte substrate (Ω)
$ Z $	Impedance modulus
α, n, d	CPE exponent

α_{eff}	Effective CPE exponent
β	body centered cubic phase of titanium
ξ	Interfacial impedance of the transmission line ($\Omega \cdot \text{cm}$)

INTRODUCTION

Metallic alloys for orthopedic implants have to show four essential characteristics: a) low stress-shielding effect, due to the elastic modulus incompatibility between bone and implant; b) biocompatibility avoiding toxic-elements; c) excellent fatigue performance for cyclically stressed implants, and d) high corrosion resistance [1].

Due to the presence of elements as Al and V, considered as cytotoxic and the high elastic modulus of the Ti–6Al–4V-ELI, (~110 GPa), new titanium alloys with no toxic elements and lower elastic modulus have been investigated. Metastable β -titanium alloys like Ti-12Mo-6Zr-2Fe alloy (TMZF) show high mechanical strength and lower elastic modulus than the Ti–6Al–4V-ELI [2].

Metallic materials as titanium and its alloys, stainless steel and cobalt-chromium alloys, are used under load-bearing conditions. However, the direct contact metal-bone does not imply the formation of a strong bond between them. Thus, it is necessary to develop more bioactive surfaces over these metals [3].

Some surface treatments are applied on titanium alloys to improve their osteointegration process. Previous studies have demonstrated that HCl etching plus NaOH treatment can be an effective way to develop nanometric features on the surface of Ti–6Al–4V-ELI (ELI for Extra Low Interstitial content) samples unchanging its static and cyclic mechanical properties [4].

An alternative to CST is the anodizing process; this procedure is widely used on pure titanium, creating TiO_2 nanotubes on the surface, maximizing the specific surface area of the material and obtaining better biocompatibility [5].

An indicator of the bone formation ability on metallic implants is the nucleation and growth of a hydroxyapatite (HAp) layer. This capacity can be measured through the specimen immersion in a simulated body fluid (SBF), whose ion concentrations nearly equal to those of human blood plasma [3, 6].

Thus, the main objective of this project is studying the biocompatibility and corrosion performance of Ti-12Mo-6Zr-2Fe samples with nanotubes, nanopores and chemical surface treatment (CST) immersed during various periods in SBF, as well as the fatigue resistance variation of these different surface conditions.

Chapter I

State of the Art

1.1 Metallic biomaterials

The first reports of titanium date from 1791 in England, when the amateur mineralogist William Gregor was able to remove iron from the "ilmenite" mineral consisting of iron, oxygen, and titanium (FeTiO_3), and the remaining titanium oxide was called "Mechanite", in reference to the place where it was found [7]. Then the chemist Martin Heinrich Klaproth isolated the metal from its oxide, naming it "Titanium" because of the difficulty of extracting it, associating it with the powerful titans of Greek mythology. And between 1937-1940, chemist Wilhelm Justin Kroll was able to optimize the industrial method of obtaining titanium, being the process hereinafter known as the "Kroll process"; this method is still the most used nowadays [8, 9].

The strong titanium affinity for oxygen makes it one of the most corrosion-resistant structural metals due to the thermodynamic stability of a protective oxide layer formed promptly in different harsh environments, especially in aqueous acid environments [9]. Due to its high resistance to density ratio, titanium is widely used in the aeronautical, chemical and biomaterials industries [10].

In the 1940s titanium and its alloys emerged commercially, developed for aerospace applications; However, in 1963 they began to be used as biomaterials due to the excellent combination of properties desired for this purpose. Branemark et al. (1964), were the first to successfully evaluate the phenomenon of human bone developing on the surface of titanium, a process they called osseointegration [11].

According to the World Health Organization, 30% of people aged 65-74 have no natural teeth, so titanium dental implants are a viable solution for replacing missing teeth [12]. Additionally, the number of total hip or knee arthroplasties has been increasing considerably, approximately 800,000 procedures are performed per year in the United States [13, 14]. It is estimated that by the year 2030 the increase in these procedures will be approximately 673% for total knee arthroplasty and 174% for total hip arthroplasty. Thus, the demand for new long-term implants is being required and the study of problems and defects arising from surface modifications may be effective to contribute to the knowledge and improvement of mechanical behavior of these materials which may favor the performance and reduce the risk of failure of these components [13, 14].

Orthopedic implants can be categorized into two main groups, temporary implants for fracture fixation and joint implants. The first group plays a structural role in a fractured bone segment until it consolidates, and can be surgically removed after the end of the process. The second group demands additional mechanical properties because the implant is subjected to cyclic stresses arising from human body movement and the transmission of loads, such as dental, hip, knee implants, etc. [15, 16], see examples in Figure 1.1. This work focus on this second group.

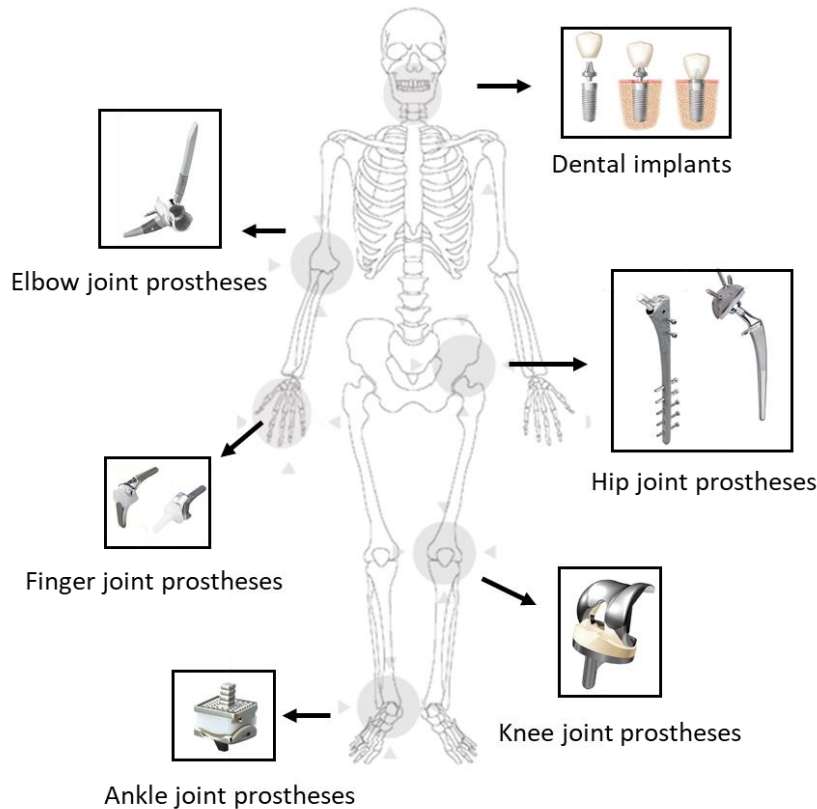


Figure 1.1 Metallic biomaterials for orthopedic and dental applications (provided by Nakashima Medical Co. Ltd Japan and Japan Medical Materials (JMM) Co.) [17].

1.2 Titanium alloys

Orthopedic implants require high mechanical properties, biocompatibility and osseointegration, high corrosion resistance, relatively low elastic modulus and high fatigue strength [14]. Titanium and its alloys have a high ability to become integrated with the bone. This property significantly improves the long-term behavior of implanted devices, reducing the risks of loosening and failure [18].

Titanium represents approximately 0.6% of the earth's crust, being the fourth most abundant structural metal, behind only aluminum, iron and magnesium [19].

Pure titanium exhibits allotropic phase transformation at 882 °C, moving from a high-temperature body centered cubic structure (β) to a compact hexagonal (α) at low temperatures (Figure 1.2). Conventionally commercial titanium alloys are classified into three categories, α , $\alpha + \beta$ and β alloys, according to the type and content of alloying elements. Substitutional elements such as Al, Sn, Ga, Zr and interstitial elements such as C, O and N dissolved in the titanium matrix are recognized as α stabilizers. Alloying elements, which decrease the phase transformation temperature, are known as β stabilizers. Generally stabilizing β elements are transition metals such as Mo, V, Ta, Fe, Mn, Cr, Ni and Nb. Additionally, some elements such as Zr, Hf and Sn behave neutrally, increasing or decreasing the transformation temperature α/β , depending on their concentrations [20–22].

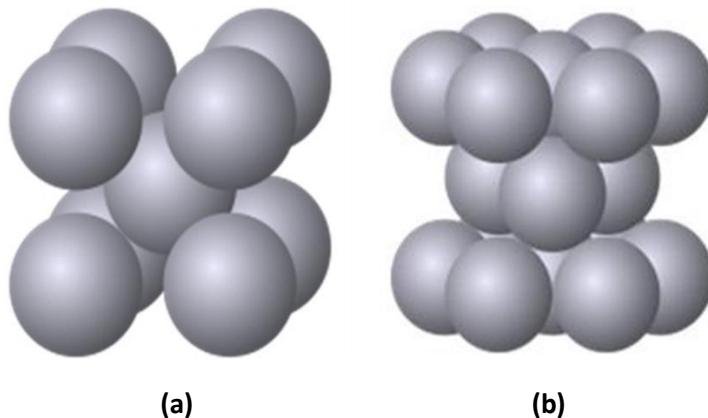


Figure 1.2 Schematic illustration of the crystal structure of the major Titanium alloys for implants. a) Center-body cubed (α -Ti) and b) Compact hexagonal β -Ti.

1.2.1 Ti-12Mo-6Zr-2Fe

Some studies have indicated that aluminum and vanadium present in the most widely used Ti-6Al-4V alloy may be harmful to human health. Thus, there was a need to develop titanium alloys free of these elements with a desirable lower modulus of elasticity. In the mid-1950s the Ti-15Mo alloy was developed, in 1969 *Crucible* developed the Ti-11.5Mo-6Zr-4.5Sn (Beta III) alloy, which has similar phase transformations as the Ti-15Mo alloy. Finally, in the nineties *Howmedica* added iron to increase resistance to beta III alloy, thereby resulting in the Ti-12Mo-6Zr-2Fe alloy [7, 23].

Ti-12Mo-6Zr-2Fe alloy, also known as TMZF, has excellent mechanical properties among metastable β alloys. According to ASTM F1813, the microstructure of this alloy, in order to be used as a biomaterial, must have a recrystallized β phase, and the appearance of phases α and α' is not allowed in a 100X magnification [24].

This provides an alloy with higher yield strength and better ductility than Ti-6Al-4V alloy, and a relatively low modulus of elasticity, lying in the range 74-85 GPa [25].

There are no surgical implant materials completely free of adverse reactions in the human body. However, the TMZF alloy has been tested “in vivo” in animals and has been used clinically for more than two decades. The results of these studies indicated a well-characterized level of local biological response that is equal to or less than that produced by the pure titanium used as reference material [24].

1.3 Fixation method

The fixation of the implant in the bone is very important and influences its useful life time. It can be of cemented or non-cemented type, in the first case there is cementation of the implant in the bone using a polymethyl methacrylate (PMMA) resin; in the second fixation method, a porous, bioactive surface is produced on the implant surface within which bone can grow [26].

Cemented implants are commonly used in elderly patients who do not have sufficient bone regeneration capacity to fix the implant through osseointegration. During use, small regions may lose adhesion without necessarily interfering with implant stability, in addition to the generation of PMMA and metallic debris that may result in adverse and inflammatory reactions [3].

The use of cementless prostheses increased in the 1980s due to its application in younger patients with a higher bone regeneration capacity. Currently, younger and more active patients requiring replacement surgery are treated with cementless prostheses [26]. This is because they have an adequate structure and surface composition to produce a durable mechanical anchor with the bone.

1.3.1 Surface modification of medical implants

Surface modifications are employed in metallic biomaterials to improve biological and mechanical compatibility to receive hard/soft tissues, resulting in the promotion of osseointegration; however, this should happen without impairing wear, corrosion, and fatigue resistance [26].

A schematic illustration of the regions formed at the titanium/bone interface is shown in Figure 1.3. From the left side of the figure, towards the right side, five distinct regions are highlighted. The first refers to the metallic titanium (region 1) covered by a layer of oxide (TiO_2) forming region 2. This, in turn, after interaction with hydroxyl groups of water, forms a material with a gel consistency (region 3). At this stage, proteins present in body fluids adhere to the Ti-Gel layer (region 4) and

the process continues by the adhesion of osteoblastic cells (region 5) towards the bone formation and osseointegration [27].

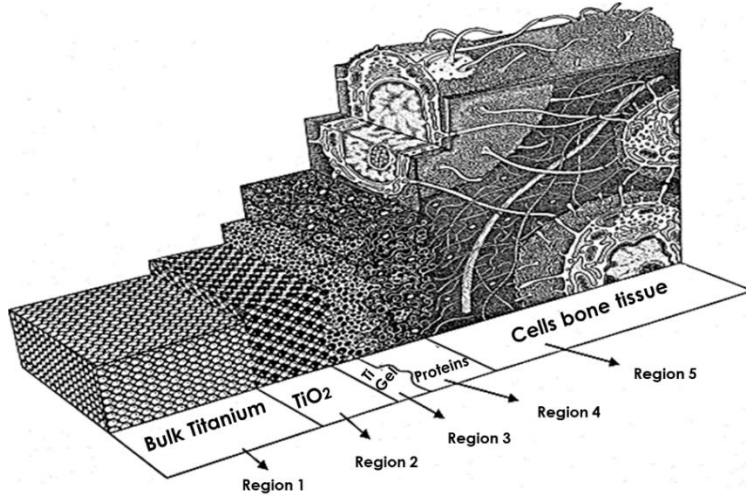


Figure 1.3 An artist's view of the titanium/tissue interface divided into five regions. The oxide of titanium is covered with a very thin layer of titanium peroxy compounds, which are in contact with the living bone (Adapted from [28]).

1.3.2 Chemical surface modification by acid etching and alkaline treatment

Several chemical modification methods make the implant surface more favorable for cell growth and adhesion. An example of chemical modification follows the principle of obtaining roughness through an acid attack with a subsequent alkaline treatment that generates a chemically biocompatible layer.

1.3.2.1 Acid etching

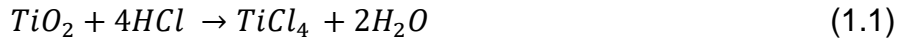
Acid attacks on titanium-based alloys are employed to remove oxidation and surface contaminants as a result of previously performed processing steps. Due to the reoxidation process that occurs, the acid attack also alters the roughness, surface composition and wettability [29].

The dual acid etching procedure, commonly described in the literature, consists of immersing the metal in a mixture of concentrated HCl and H₂SO₄ for a certain time at a temperature of 100°C [30]. These studies suggest that there is greater apposition of osteogenic cells, when increasing the surface roughness of the material, also increasing the bone/implant contact. This type of surface promotes rapid osseointegration by improving osteoconductivity processes, resulting in bone formation directly on the implant surface favored by the topography generated on the titanium surface [3].

1.3.2.2 Alkaline treatment

Alkaline treatment imprints changes in chemical composition, roughness and topography on the treated surface by forming a layer of sodium titanate (in the case of titanium); this procedure makes materials bioactive , favoring, stimulating or catalyzing hydroxyapatite precipitation (Figure 1.4) [31, 32].

The passive oxide film spontaneously formed on the titanium metal initially suffers a degradation reaction during the acid etching, as follows:



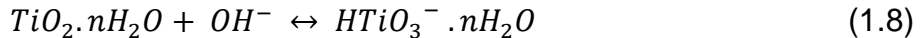
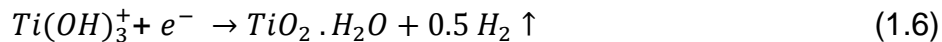
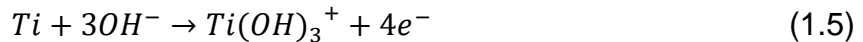
Simultaneously, titanium reacts with HCl:



On the TiH_2 intermediate layer, a new passive oxide layer is formed and subsequently reacts with the NaOH solution. At first, the passive layer is partially dissolved to form $HTiO_3^-$:



At the same time, the metallic titanium is hydrated forming $HTiO_3^- \cdot nH_2O$:



Finally, positively charged alkali ions (Na^+) react with negatively charged groups, to produce an alkali titanate hydrogel layer. Then, the samples treated in the alkaline medium can be immersed in a solution known as simulated body fluid (SBF), where apatite precipitation is stimulated (Figure 1.4) [3, 33].

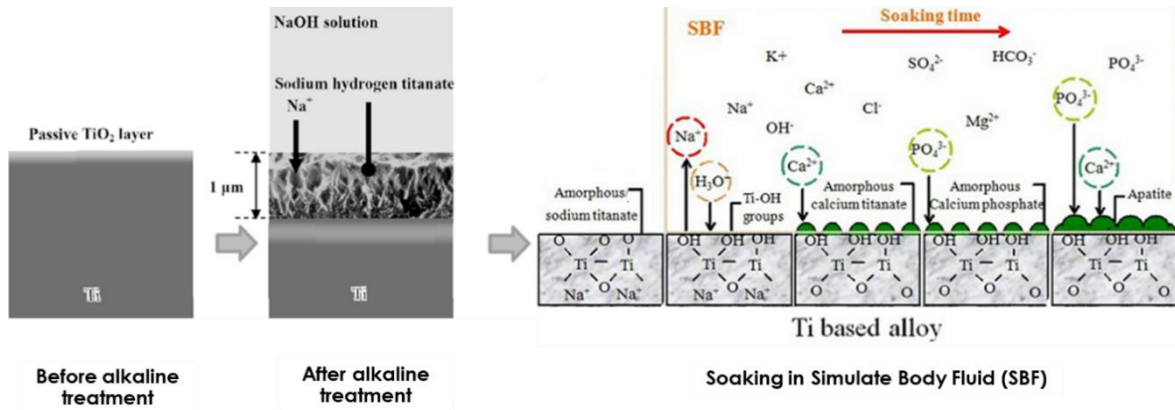


Figure 1.4 Schematic representation of the structural change in the surface of the metallic Titanium after the alkaline process and subsequent apatite formation on the treated surface (Adapted from ref. [3]).

In some cases, these attacks (acid etching and alkaline treatment) may cause a decrease in mechanical properties, especially its ductility and resistance to fatigue. Probably, due to surface irregularities that tend to be crack nucleation sites, besides the possible embrittlement caused by the absorption of hydrogen [34]. Therefore, another interesting surface modification could be the electrochemical anodization, in order to improve the biological, electrochemical and mechanical properties of the TMZF alloy avoiding hydrogen embrittlement.

1.3.3 Anodization process

Special attention has been paid over the last decades to the formation of TiO_2 nanotubes or nanopores, in particular by anodizing pure titanium. This method is a promising alternative to the deposition of hydroxyapatite, in particular because it allows to grow, simply, quickly, and at low cost, a layer of TiO_2 bioactive, directly connected to the titanium substrate, and therefore very adherent [14,15].

The presence of nanotubes on titanium surfaces changes the structural properties of the bulk titanium substrate, becoming a more attractive material for tissue engineering applications because of the higher porosity and increased surface area, improved cell attachment and tissue ingrowth, and therefore osseointegration. Figure 1.5 shows human osteoblast cell attachment on blank titanium and TiO_2 nanotubes after seven days of culture [35].

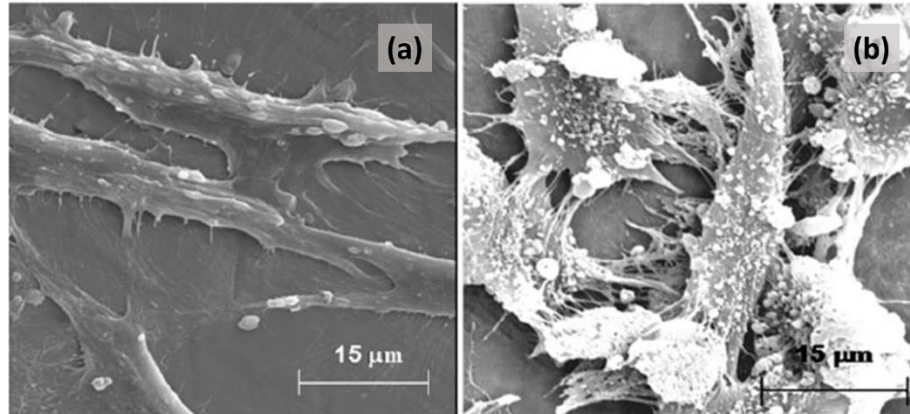


Figure 1.5 Human osteoblast cell attachment and proliferation on a) titanium and b) titanium with TiO_2 nanotubes [30].

Table 1.1 summarizes the anodization conditions, characteristics and cell response of TiO_2 nanotubes on titanium investigated by different research groups to date. It is possible to observe the diverse anodization processes and the different nanotubes characteristics obtained; the morphologic characteristics as diameter and lengths of the nanotubes could influence the cell response and therefore their osseointegration.

Nanotube diameter had a critical impact on cell response. Some studies claimed that 15 nm is the maximum permissible diameter prior to cell apoptosis for mesenchymal stem cells [31,32]. Nevertheless, reports also indicated nanotubes with diameters exceeding 100 nm favoring cell proliferation in case of osteoblast cells [36]. Thus, these contradictory results suggest that the interaction mechanism between cells and anodized surfaces is not yet clearly understood.

Table 1.1 Anodization parameters and cell response of Ti-based metallic implants

Material	Synthesis conditions of NTs			NTs dimensions		Cell response	Ref.
	Electrolyte	Applied Voltage (V)	Anodization Time (min)	Diameter (nm)	Length (nm)		
Ti	HF	20	60	70	250	Osteoblasts showed adhesion on TiO_2 Nt.	[37]
Ti	H_3PO_4 +HF	1 - 20		10 - 15	600	Excellent biocompatibility for mesenchymal stem cells on 15 nm TiO_2 Nt, compared to cell apoptosis on 100 nm Nt.	[38]
Ti	H_3PO_4 +HF	1 - 20	60	15 - 100		Osteoblast and osteoclast apoptosis when cultured on TiO_2 Nt of diameter 15 nm.	[39]
Ti	Acetic acid/HF	5 - 20	30	30 - 100		Human mesenchymal stem cell adhesion on Nt of both 30 and 100 nm diameter, with more cell proliferation, and migration, but also osteogenic differentiation on 30 nm Nt.	[40]
Ti	NH_4F + Ethylene glycol	30	180	100	4000	Osteoblast-like cells demonstrated high viability on Nt.	[41]
Ti	NH_4F + Ethylene Glycol/Glycerol	10-20	120	45 -130	360-4500	Crystallized and higher diameter NTs lead to better cellular activity than amorphous and/or smaller Nt.	[36]

1.3.3.1 Mechanisms of surface anodization

In the initial phase of the anodization process, when the titanium surface is exposed to sufficiently anodic voltage in an electrochemical configuration, an oxidation reaction occurs forming a compact oxide layer (Equations 1.9 – 1.12). These reactions are known as a field-assisted oxidation process and are the first step of the anodization process. At the anode oxidation of the metal takes place, which releases Ti^{4+} ions and electrons [42]:

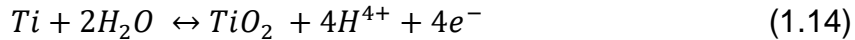


Simultaneously, hydrogen evolution will take place at the cathode:

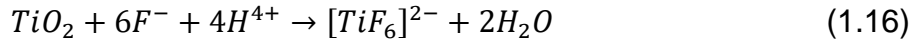


In the overall process the oxidized metal can be dissolved in the electrolyte or else

form an oxide, according to equation [43]:



In the case of titanium anodization, the predominant phenomenon is the formation of an oxide on the surface. The presence of fluoride ions in the electrolytes will form fluoride water-soluble $[TiF_6]^{2-}$ species. The fluoride ions that are present in the electrolytes can react with Ti^{4+} or can chemically attack the formed TiO_2 :



These fluoride ions will lead to the field-assisted chemical dissolution of TiO_2 (Equation 1.16) Small pits are formed due to the localized dissolution of the oxide, these pits acting as pore-forming centers.

Anodization processes with electrolyte containing species capable of dissolving the anodized oxide layer (F^-), show three characteristic stages. In the first stage, a barrier oxide layer is formed (a few tens of nm). Then, during stage two, the surface begins to be locally dissolved and the pores grow randomly. The initiation of these pores leads to an increase in the active area and therefore an increase in the current [44]. Consequently, the pores share the available current equitably, which leads to the formation of a network of vertically ordered nanotubes (stage three). In this phase the current becomes constant. More precisely, the steady-state is established when the growth rate of the oxide is equal to its rate of dissolution (Figure 1.6) [44].

During the anodization process it is possible to obtain nanotubes and nanopores surfaces according to the anodization parameters. Both nanotubes and nanopores are interesting and will be investigated in this project.

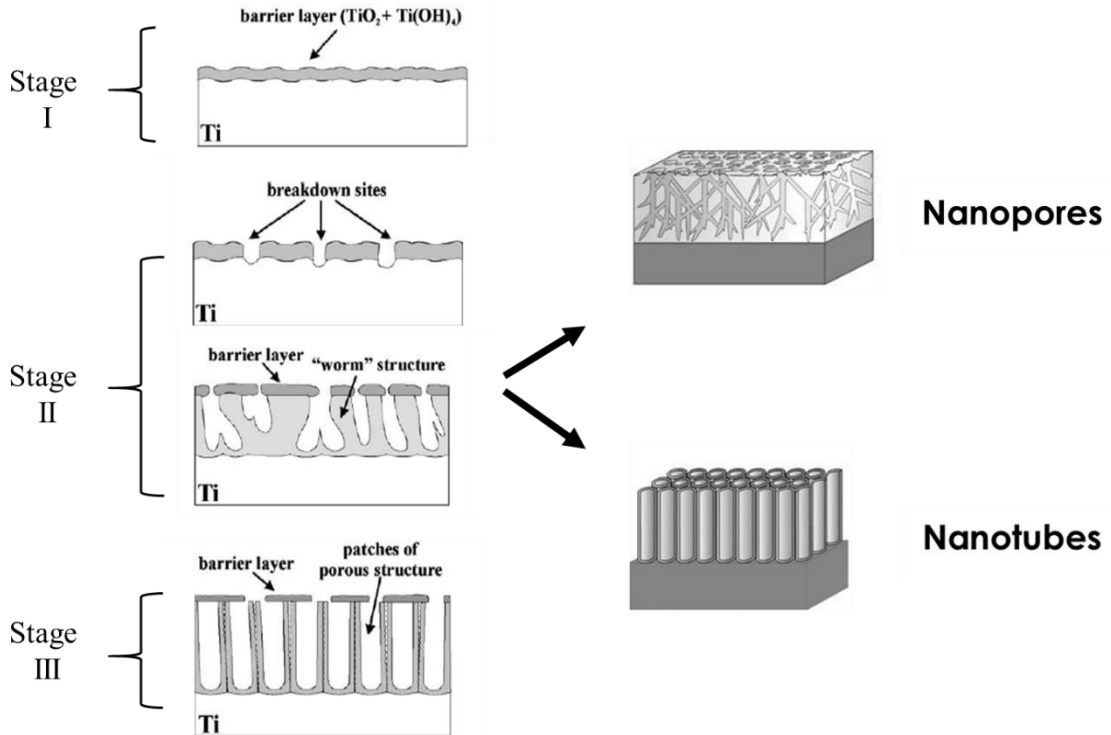


Figure 1.6 Schematic representations of the different stages of the anodization process: Stage I oxide layer formation; Stage II pores nucleation and dissolution of the TiO₂ layer; in Stage III the steady-state is established.

After the anodization process, the samples are often subjected to an annealing treatment at high temperatures (400 to 600 °C) to transform the TiO₂ from an amorphous phase to a crystalline one [45]. Crystalline nanotubes possess a stronger adhesion to the titanium substrate and increased hydrophilicity [46]. Additionally, this thermal treatment decreases the amount of fluoride remaining in the anodized surface, which might be toxic to the cells, favoring the biological response [36, 47].

1.4 Corrosion of biomedical devices

Surface degradation on biomedical devices occurs due to the interfacial reaction between the passive film and the surrounding environment. Generally, surface modifications to improve the biological response, modify the surface area and the chemical characteristics of the surface, causing a decrease in the corrosion performance. High corrosion resistance is required to reduce the release of metallic ions to the body, which can be harmful to the organism. A very small amount of released metal ions may cause an allergic response and carcinogenesis in the human body [48, 49].

Corrosion of metallic biomaterials causes the loss of their structural integrity

and surface function. It accelerates their fatigue, fretting fatigue and wear and, conversely, such damages accelerate the corrosion [49]. Due to these problems, electrochemical characterization is one of the most important mediators to evaluate new surface treatments for metallic biomaterials [48].

Generally, when a metallic material is immersed in an electrolyte, an infinite number of atomic-size anodes and cathodes are formed as shown in Figure 1.7. At this moment short-circuit current flows between local anodes and cathodes. The place of local anodes and cathodes changes every moment in the case of general corrosion. Moreover, the total anodic current is equivalent to the total cathodic current. As a result, the whole surface is uniformly attacked [49].

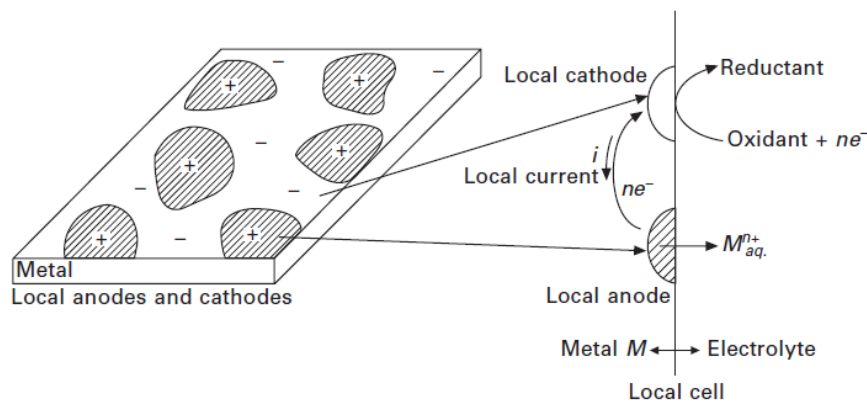


Figure 1.7 Schematic illustration of the local anodes and cathodes and the local cell formed between them [49].

1.4.1 Potentiodynamic polarization

Polarization is an electrochemical process induced by deviation of the electrochemical equilibrium potential (E_{corr}), the potential at which anodic and cathodic reactions have an equal rate (net current is zero). The rate of the anodic partial reaction at the corrosion potential in Figure 1.8 is called corrosion current density (I_{corr}), which is proportional to the corrosion rate [49, 50].

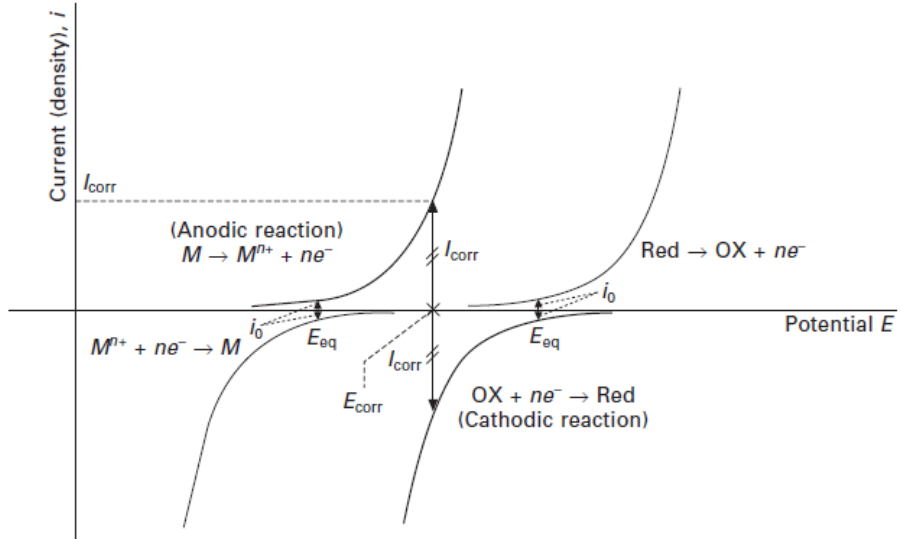


Figure 1.8 Schematic illustration of potential vs current density curves of a metallic electrode. E_{corr} = corrosion potential; E_{eq} = equilibrium potential; I_{corr} = corrosion current density; i_0 = exchange current density [49].

Some metallic materials, such as stainless steel, aluminum, titanium and their alloys, can passivate as they spontaneously form a protective oxide layer on the surface. The anodic currents measured for these systems are then often very low and the shape of the current-voltage curve is modified as is possible to see in Figure 1.9 [51].

Figure 1.9a illustrates, for example, the characteristic shape of the anodic polarization curve of stainless steel in an acid electrolyte. In such an aggressive medium, this stainless steel loses its passive layer, and undergoes generalized corrosion, see "Active region", left part of the graph. With an increase in potential, the passive layer can reform, causing a decrease in the current density. For still slightly higher potentials, the current density stabilizes and we see a passive plateau appearing (i_{pass}). In this area, the metal is protected by the spontaneous formation of the passive layer. Finally, for very high potentials, the passive layer can be destroyed; it is the domain of transpassivity, see right part of the graph [51].

Figure 1.9b illustrates the shape of the anodic polarization curve of a passivable metal in a non-aggressive medium. This is the case of titanium in a neutral medium, for which the passive layer is very stable over a wide range of potential; and this even in the presence of chlorides. Here, only the domain of passivity (i_{pass}) is observed [36].

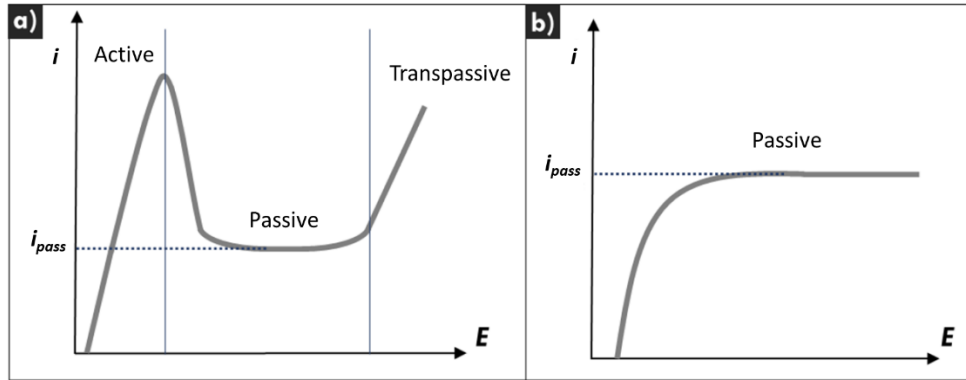


Figure 1.9 Schematic representation of the anodic part of the polarization curve (a) of a stainless steel in an acid medium (b) of a passive metal in a non-aggressive medium. Adapted from [36].

In Figure 1.10 is possible to observe the different characteristic polarization behavior for three different common metallic biomaterials, these anodic polarization curves were measured after one-week immersion in Hanks' solution. As examples, the curve of 316L stainless steel shows an abrupt increase in current density due to stable pitting corrosion that finishes the passive region, the cobalt-chromium alloy shows an increase in current density due to transpassive dissolution following the passive region whereas pure titanium shows a constant passive current density in the potential region of this study [52].

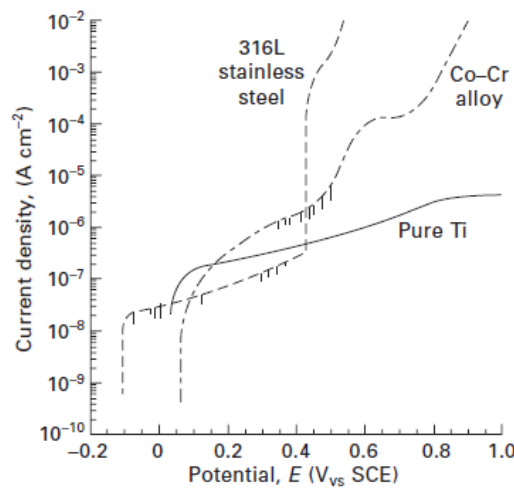


Figure 1.10 Anodic polarization curves of 316L stainless steel, cobalt-chromium alloy and pure Titanium immersed in Hanks solution [52].

Recently proposed works suggest the use of biomimetic materials in order to imitate the mechanical, physical, chemical and biological properties of the bones. An example consists in modifying titanium surface with a composite coating obtained by plasma electrolytic oxidation (PEO) with organic pore filler of integrin-active RGD.

This surface modification improved its biological properties. On the other hand, it reduced the corrosion resistance, showing higher corrosion current density values when compared with uncoated samples, CG-Ti and nano-Ti, see Figure 1.11. This behavior was attributed to the electrochemically active Ca and Na species contained in the coating layer and more defects in the layer [53].

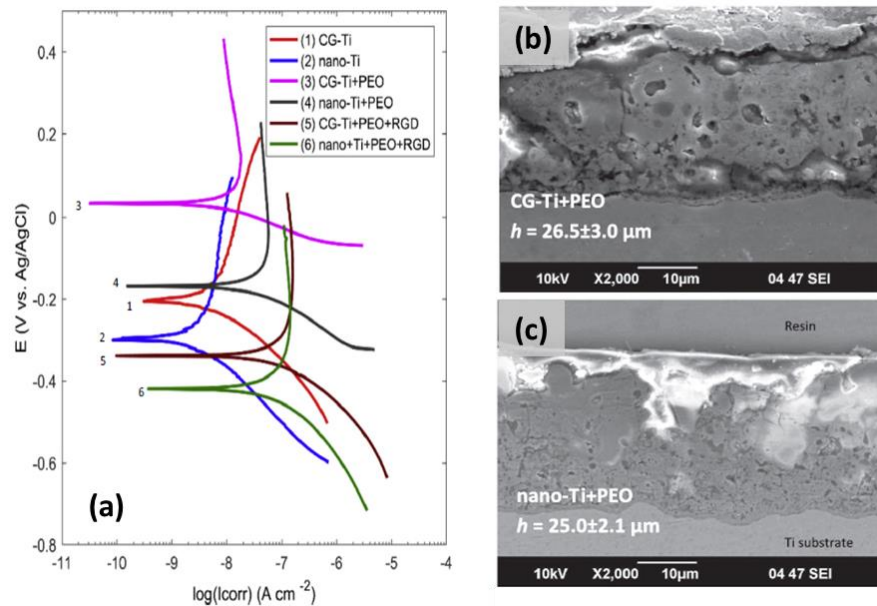


Figure 1.11 (a) Potentiodynamic polarization test results for CG and nanostructured titanium substrates, uncoated, PEO coated and RGD modified and PEO coating morphology for (b) coarse-grained and (c) nanostructured titanium substrates [53].

On the other hand, some surface modification processes as anodization of the commercial pure titanium have proven to be very interesting, forming a surface highly bioactive, and maintaining a high corrosion resistance compared with the untreated titanium, see Figure 1.12. The anodized surfaces showed a clear increase in the corrosion potential and lower values of the corrosion current density compared with untreated titanium. The authors attributed these results to an increase in the thickness of the oxide layer [54].

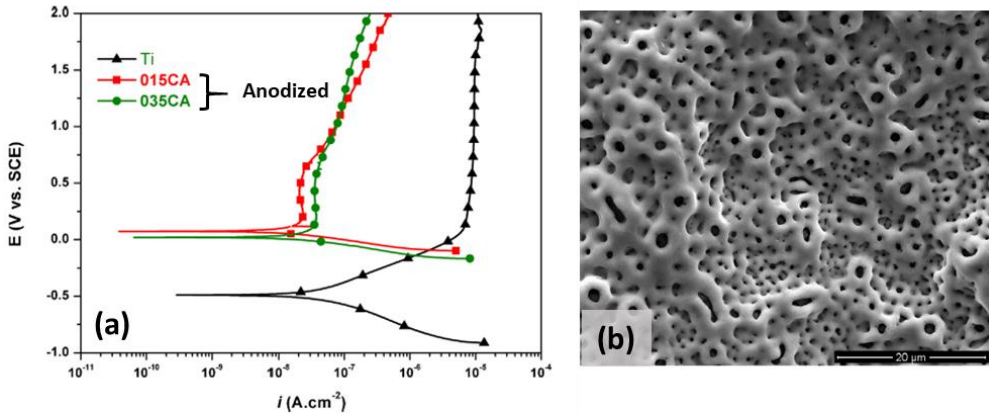


Figure 1.12 (a) Potentiodynamic polarization curves of the untreated and anodized titanium samples in NaCl (8 g/l); and (b) representative SEM image of the anodic treated titanium sample [54].

1.4.2 Electrochemical Impedance Spectroscopy (EIS)

Although rich in information the potentiodynamic polarization test is a destructive method and provides information about the slowest phenomena taking place on the surface of a material exposed to a corrosive environment [55]. On the other hand, the EIS is a non-destructive test and a very sensitive detection method of the coated metal condition. Hence, the EIS technique has been used to evaluate the corrosion state of different metallic biomaterials [53]. Contrary to the potentiodynamic polarization methods, which use direct current (DC), the EIS is based on the excitation of the interface by a low amplitude alternating current (AC). A small-amplitude sinusoidal potential perturbation is typically applied to the working electrode (5-10 mV) at a number of discrete frequencies. During the EIS test, a potential waveform of a few millivolts is applied across the circuit, and the current response to the frequency signal generates impedance data. Thus, the impedance data is related to a phase shift angle and a variation in potential and current amplitudes. (See Figure 1.13) [54].

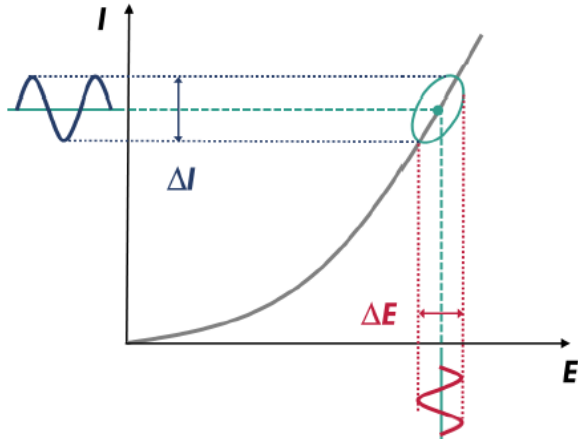


Figure 1.13 Schematic representation of the principle of measurements by EIS.

The impedance measurements are valid when the system is stationary or quasi-stationary, linear and time-invariant. The linearity is verified by the use of an input signal of low amplitude (typically 10 mV), the stationarity and the invariance are ensured by the measurement of the potential in open circuit (OCP) preceding the measurement of impedance [56]. Thus, the impedance of the system is defined by the ratio between the input signal and the output signal. This relationship can be written as:

$$Z(\omega) = \frac{E_0}{I_0} \exp(j\Phi) = |Z| (\cos\Phi + j\sin\Phi) = Z_r(\omega) + jZ_i(\omega) \quad (1.17)$$

Where E_0 is the amplitude of the excitation signal, I_0 is the amplitude of the output signal, ω is the angular frequency ($\omega = 2\pi f$ where f is the frequency in Hz) and Φ is the phase shift (in °) between the input signal and the output signal, Z_r is the real part of the impedance (in Ω or $\Omega \text{ cm}^2$), Z_i the imaginary part (in Ω or $\Omega \text{ cm}^2$) and $|Z|$ the module or magnitude of the impedance vector (in Ω or $\Omega \text{ cm}^2$) [57].

The magnitude of the impedance can be expressed in terms of the real and imaginary components as:

$$|Z(\omega)| = \sqrt{Z_r(\omega)^2 + Z_i(\omega)^2} \quad (1.18)$$

The phase angle can be obtained from:

$$\Phi(\omega) = \tan^{-1}\left(\frac{Z_i(\omega)}{Z_r(\omega)}\right) \quad (1.19)$$

Two types of complementary graphic representations are used to analyze the impedance measurements. One of them is a complex plane plot called the Nyquist plot or complex plot. It is a curve of the imaginary part of the impedance (Z_i or Z'') versus the real part of the impedance (Z_r or Z') (Figure 1.14 (a)). In this plot, the imaginary impedance of the electrochemical systems is usually negative [58].

The second type is the Bode plots, divided in the impedance modulus ($|Z|$) or the phase angle (ϕ), versus the frequency (ω). This representation generally makes easier to count the interfacial phenomena involved in the impedance response. It also allows quick visualization of the value of the low-frequency module, which provides information on the corrosion resistance of the system [36].

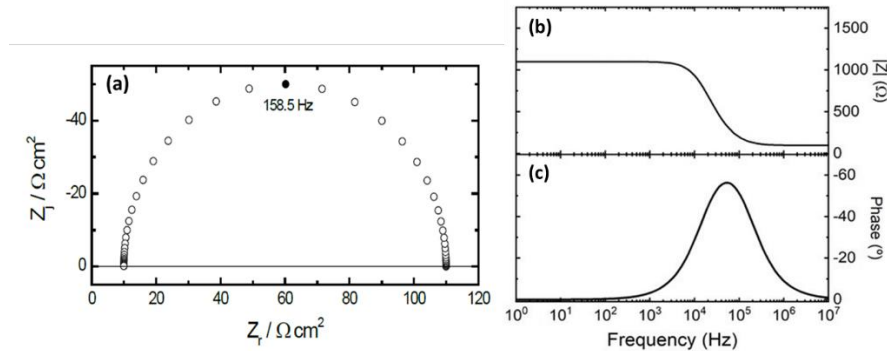


Figure 1.14 Schematic representation of the impedance results: a) Nyquist plot or complex plot; b) magnitude of the Bode plot and c) phase of the Bode plot.

The Bode representation shows some disadvantages in electrochemical systems due to the influence of electrolyte resistance (R_e). For instance, in the traditional phase angle plots shows the current and potential in phase at high frequencies; however, in this region, the current and surface potential are exactly out of phase. This alteration is associated with the fact that at high frequencies, the impedance of the surface tends toward zero, and the R_e dominates the impedance response. Thus, R_e obscures the behavior of the electrode surface in the phase angle plots [59].

It is possible to correct the influence of electrolyte resistance, according to:

$$|Z|_{corrected} = \sqrt{(Z_r - R_e)^2 + Z_i^2} \quad (1.20)$$

The phase angle can be obtained from:

$$\Phi_{corrected} = \tan^{-1}\left(\frac{Z_i}{Z_r - R_e}\right) \quad (1.21)$$

Cordoba-Torres et al [60]. showed that in some systems the number of distributed processes involved in the impedance response can be determined using the corrected bode phase angle plots. This knowledge is a crucial point in the choice of the equivalent circuit if reliable results are desirable. The corrected Bode phase angle plot (Figure 1.15 b) shows three distributed processes involved, which are, however, hardly recognized in the Bode phase angle plot (Figure 1.15 a), using the same impedance data.

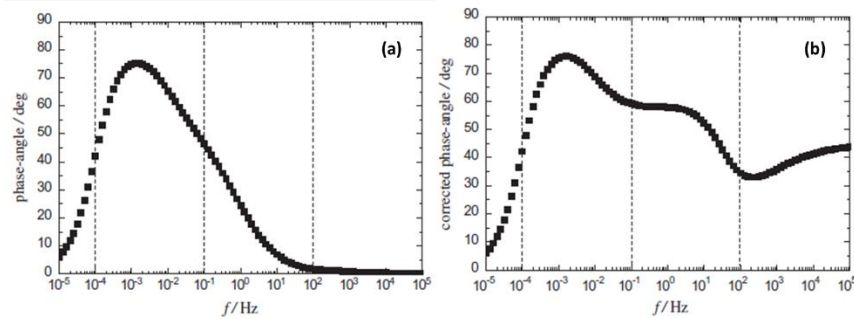


Figure 1.15 representations of synthetic impedance data in standard units: a) Bode phase-angle; (b) Corrected Bode phase-angle. (adapted from [60])

1.5 Fatigue in metallic biomaterials

Fatigue strength is one of the most important mechanical properties in implants exposed to cyclic loading conditions. When a specimen or component is subjected to repeated or fluctuating reproductions, it may break under a maximal acting stress lower than the strength limit of the material [61]. Final fatigue failure usually occurs suddenly (macroscopically) and catastrophically, after the generated fatigue crack grows over time to a critical value unsupported by the structure [62].

Crack nucleation in fatigue occurs due to localized submicroscopic damage, and the presence of any localized stress amplifier may favor the onset of premature damage, and, subsequently, the formation of a crack [63]. This stress amplifier is usually caused by a notch or a discontinuity present in the component. These defects can be introduced on purpose and are known as structural notches; examples are gear teeth, screw threads, or any general holes [63].

Surface topography in titanium alloys is very important due to the fact that it will determine the level of cell adhesion and growth on the implants [64, 65]. Thus, those processes that modify surfaces for better osseointegration may also cause changes in fatigue life behavior [66].

Leinembach et al [67] studied the fatigue performance of Ti-6Al-4V alloy after an Al_2O_3 particle blasting process, generating a $\text{Ra} \approx 4.6 \mu\text{m}$ roughness. In this $\alpha + \beta$ alloy, a 31% decrease in fatigue strength was observed when compared to polished surface, a result which was attributed to the concentration of surface stresses generated by the presence of the remaining blasting particles, as well as to the roughness generated. A different behavior was observed in the work of Pazos et al [66] when pure titanium was blasted with Al_2O_3 particles, resulting in fatigue strength similar to the condition of polished specimens.

Ti-6Al-7Nb specimens ($\alpha + \beta$ alloy) were treated by thermal and anodic oxidation, showing a roughness of $0.121 \mu\text{m}$ and $0.065 \mu\text{m}$, respectively. The

anodically oxidized samples showed a slight decrease in fatigue performance when compared to the polished ones, but showed a more positive response when compared to the thermally oxidized samples (Figure 1.16). This behavior was attributed to a more fragile characteristic of the oxide layer formed by heat treatment [68].

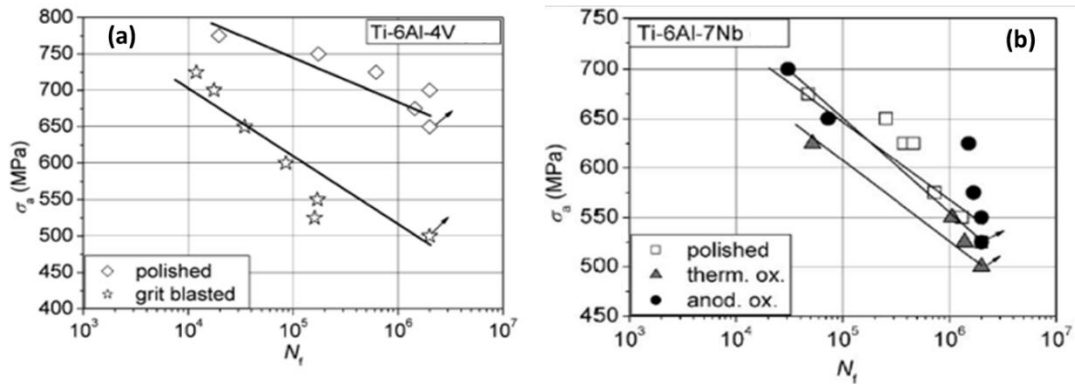


Figure 1.16 Axial loading S,N-curves in oxygen-saturated Ringer's solution: a) polished and grit blasted Ti-6Al-4V; b) polished, thermally and anodically oxidized Ti-6Al-7Nb (Adapted from [68])

Plasma electrolytic oxidation process was employed in order to produce porous oxide layers on the surface of Ti-6Al-7Nb and Ti-6Al-4V alloys, it was observed that this treatment markedly decreased the fatigue strength of these alloys, being between 17- 61%. This decrease can be attributed to two factors, the first being the formation of fragile TiO_2 layers that favor surface cracking, and the second to the propagation of pre-existing cracks and the accumulation of internal stresses during the oxidation process [69].

Due to the great variability in fatigue results for these titanium alloys used as biomaterials, P. S de Carvalho et al. [70] determined the notch sensitivity of Ti-6Al-4V-ELI alloy by calculating the critical value of roughness $R_{z,cri} = 2.8 \mu\text{m}$ (Figure 1.17), which indicates that variations of the surface roughness above the critical value may result in a large reduction of the fatigue resistance of this alloy [70].

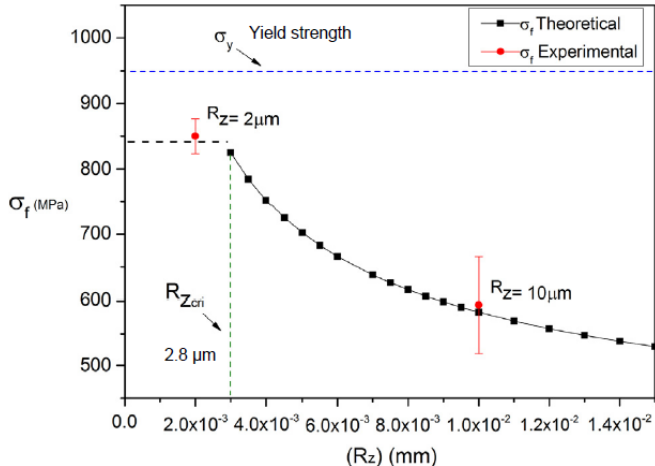


Figure 1.17 Plot of fatigue resistance (σ_f) in function of the Roughness (R_z)

Ordered arrays of TiO_2 nanotubes are considered as very promising to improve the osseointegration of titanium-based implants to living tissues. However, this improvement could be accompanied by an alteration in mechanical properties. An array of self-organized TiO_2 nanotubes with an amorphous structure was produced on the biomedical Ti-6Al-4V and Ti-6Al-7Nb alloys. This surface modification was not deleterious to the fatigue response of both $\alpha+\beta$ alloys mainly due to the nano-scale dimension of the nanotubes layer [71].

Some studies show a decrease in mechanical properties due to the incorporation of hydrogen inside titanium alloys after they are chemically treated in acidic solutions. During these processes, hydrogen ions are dissolved in the titanium matrix causing brittleness and degrading the mechanical properties. Just a small addition of hydrogen (40 ppm) can cause great harm in this TA15 titanium alloy (34% reduction of the number of cycles to failure) [72].

Other interesting studies appoint that increasing the volume fraction of β phase in $\alpha+\beta$ alloy could reduce the sensitivity of the hydrogen embrittlement due to higher solubility of this element in β phase, approximately 5 times higher than in α phase [66]. Nevertheless, some β titanium alloys as the Ti-5Al-5Mo-5V-3Cr with a microstructure consisting of a large volume fraction of fine secondary α in the β matrix, shows that a slight increase in hydrogen content produces a reduction in fracture toughness (38%) and fatigue resistance (Figure 1.18) [73]. These results show that the role of the β phase in the hydrogen embrittlement process of titanium alloys is still unclear.

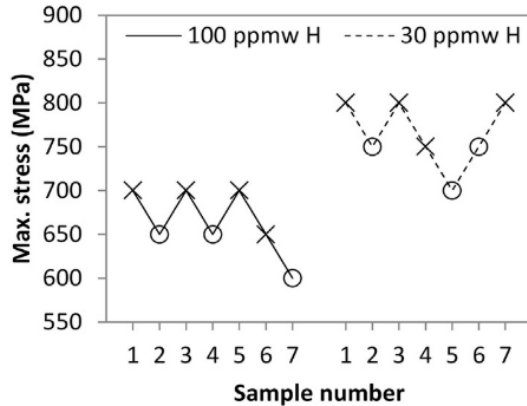


Figure 1.18 Staircase fatigue diagrams for 5×10^6 endurance limits. “X” means failure and “O” means survival to the run-out [73].

Summarizing, surface topography is very important in orthopedic and dental implants since it will determine the level of cell adhesion and osseointegration. Modifying the surface of the implant for better osseointegration may decrease its corrosion and fatigue performance. Therefore, finding a balance between biological, electrochemical and mechanical properties is a challenge in designing an implant device subjected to cyclic loadings. Thus, in this thesis the surface of the commercial β titanium alloy was modified by anodizing processes and acid etching together with an alkaline attack, to improve their bioactivity response. Then, the electrochemical and fatigue behavior of these samples were studied as will be detailed further in the manuscript.

Chapter II

Materials and Methods

The main experimental procedures developed during this doctoral project are contained in the flowchart in Figure 2.1

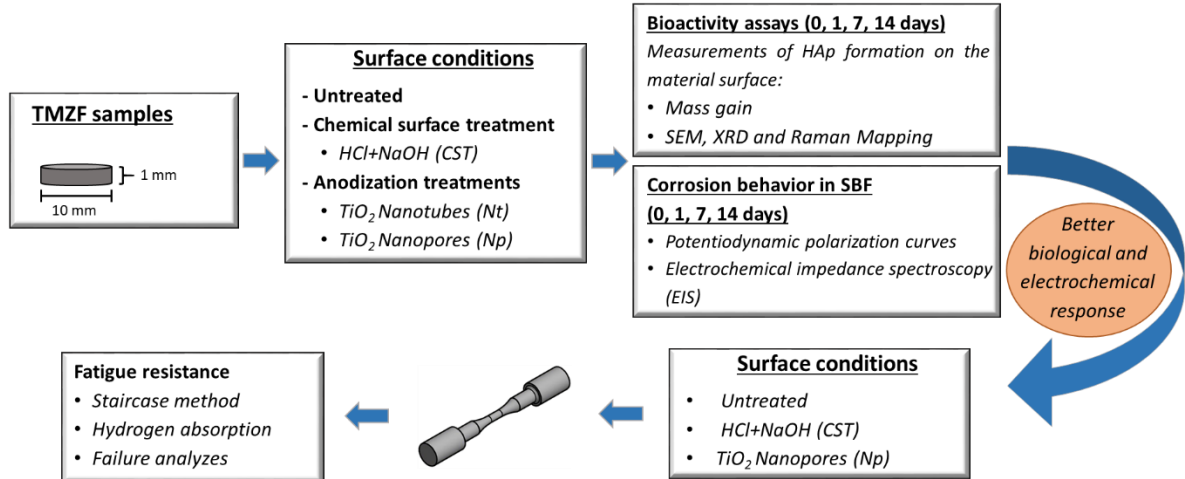


Figure 2.1 Flowchart of the experimental procedure developed in this doctoral thesis.

2.1 Materials and samples

The material used for this study was the β TMZF alloy. It is a commercial titanium alloy, purchased in the form of an ingot, and supplied by *Ercata GmbH*. The nominal composition of the alloy is shown in Table 2.1. Later, the material was submitted to the rotary swaging process in an open matrix, with repeated heating cycles in a muffle furnace to a temperature of 1000 °C, providing bars with a diameter of 11 mm.

Table 2.1 nominal composition of the TMZF alloy [2].

Material	Ti	Al	Mo	V	Cr	Zr	Fe	O
TMZF	Balance	-	10,0-13,0	-	-	5,0-7,0	1,5-2,5	0,008-0,28

For biomedical and corrosion tests the TMZF bars were cut into disks of 10 mm of diameter and 1 mm of thickness. For fatigue tests, the specimens were machined from the same TMZF bars, according to the dimensions illustrated in

Figure 2. 2, assuring the relationship between the dimensions according to the ASTM E466-07 standard [74]. All samples were heat-treated at 800 °C for two hours and then fast cooled in water to obtain a fully recrystallized beta phase structure [2]. Then, the elastic modulus was obtained employing the pulse excitation technique (ASTM E1876).

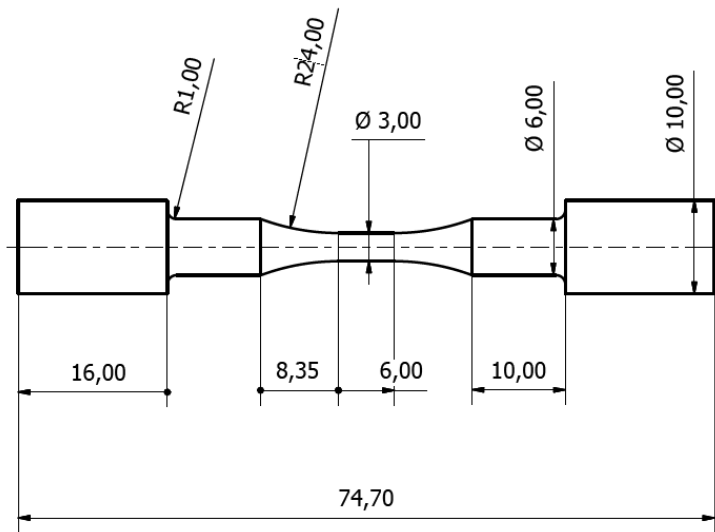


Figure 2. 2 Dimensions of specimens for fatigue tests (in mm).

2.2 Surface modification processes

Four different surface conditions were investigated on TMZF samples: untreated surface, surface treated with HCl etching and alkaline NaOH solution (CST), and two anodized condition – nanotubes (Nt) and nanopores (NP).

2.2.1 Surface preparation

In order to eliminate the machining marks, all specimens were successively grounded with 120, 240, 360, 400, 600 and 1200 grade silicon carbide papers and then polished with alumina of 3 and 1 µm. Then, they were cleaned ultrasonically into deionized water (Milli-Q®), acetone, and ethanol for 10 minutes in each case. Finally, the samples were rinsed with distilled water and dried with compressed air.

2.2.2 Chemical surface treatment

The surface modification of the specimens was carried out in two steps: initially with HCl, and subsequently with NaOH. The acid etching was carried out as a pre-treatment to remove surface oxidation and contaminants, and to generate a micro-rough and uniform surface. After the acid etching the specimens were treated with NaOH to generate submicron and nanometric changes, forming a bioactive sodium titanate layer on the treated surface.

For acid etching, samples were immersed into an HCl solution (37 wt.%) heated at 60 °C for 30 min. The alkali treatments were performed using polyethylene containers with 45 ml of NaOH 10 mol·L⁻¹ for each sample, and a furnace with a digital controller was used to keep the alkaline medium at 60 °C for 24 h. The pH of the acid and alkaline solutions was <2 and >13, respectively. After the chemical modification, the samples were immersed into deionized water and sonicated for 10 min, followed by 10 min in acetone.

2.2.3 Anodization process

The TiO₂ nanostructures were obtained by anodization of the polished samples. The anodization processes were carried out in an electrochemical cell with a conventional two-electrode arrangement. The counter electrode (cathode) was a cylindrical platinum grid placed ~3 cm away from the polished disks, which were used as the working electrode (anode) in the case of bioactivity and corrosion test samples (Figure 2.3a). For the fatigue specimens (anodes), the counter electrode was a 304 stainless steel tube (Figure 2.3b).

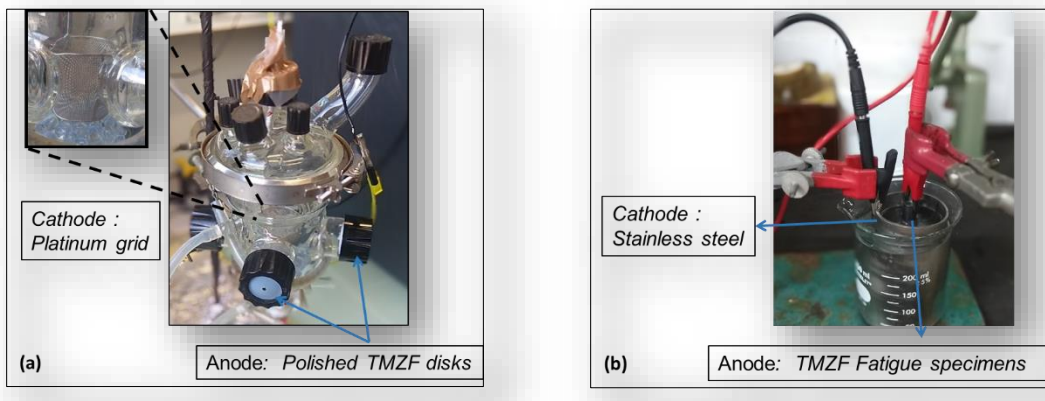


Figure 2.3 electrochemical cells used in this work for anodization experiments: a) assembly for polished disks and b) assembly for fatigue specimens.

The anodization experiments were performed at 25 °C, in an organic electrolyte consisting of glycerol, containing 25 vol% of water and 0.25M of NH₄F [75]. The DC constant potential applied to obtain nanotubes was 10V during 2h and 20V during 1h was employed to obtain nanopores.

After the anodization processes, the samples were rinsed with distilled water, then with acetone, and finally dried with compressed air.

Finally, the samples were annealed in air at 550 °C for 2 h to crystallize the TiO₂ surface layer into a mix of anatase and rutile phases.

2.3 Bioactivity assay

Some bioactive materials bond to living bone through a layer of apatite. It has been shown that this apatite layer can be reproduced on the materials surfaces in an acellular and protein-free simulated body fluid (SBF) with ion concentrations nearly equal to those of human blood plasma (Figure 2.4.), and that apatite thus formed is similar to the bone mineral in its composition and structure [6].

In order to characterize the bioactivity of the four different surface modified conditions, it was measured the amount of apatite (Ap) spontaneously deposited on the different samples immersed into SBF. The bone-like apatite can biologically bond with living tissue, which can estimate the *in vivo* bone bioactivity of the surface.

The protocol followed in this study for carrying out bioactivity tests was proposed by Kokubo and Takadama [76] and in ISO 23317: 2014 [6]. In this protocol, the samples are placed in hermetically closed plastic containers with 50 ml of SBF solution at 37 °C and pH 7.4. It is important to place the active surface to be tested perpendicularly to the bottom part of the container, as shown in Figure 2.4. Indeed, the SBF solution being unstable, Ca / P compounds could precipitate and deposit on the surface of the sample, which would distort the evaluation of bioactivity [6, 76].

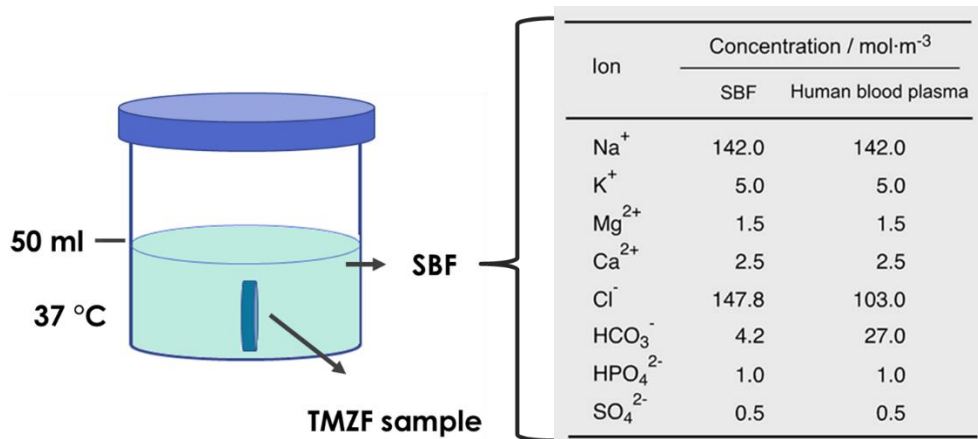


Figure 2.4 Schematic representation of the experimental assembly used to bioactivity assays and the ion concentrations of the simulated body fluid (SBF) [6].

After 1, 7 and 14 days of immersion, the samples were removed from the solution, gently rinsed and dried in a desiccator. Three samples per condition and soaking time were evaluated. Apatite formation was then evaluated by weighing the samples before and after immersion, and the morphology of each surface treatment was examined by Scanning Electron Microscopy (SEM), chemical analysis by energy dispersive spectroscopy (EDS), X-Ray diffraction (XRD) and Raman Mapping.

2.4 Electrochemical behavior

After the surface treatments, all specimens were air-aged at room temperature for 24 hours and then electrochemically tested. The electrochemical characterization was performed with a potentiostat (Gamry Instruments, Reference 600+), using SBF at 37°C and pH 7.40. A conventional three-electrode cell was used, where the TMZF samples were the working electrode with an exposed area of 0.283 cm², flat platinum mesh as the counter electrode, and a Saturated Calomel Electrode (SCE, 0.242 V vs. SHE at 25 °C) as the reference electrode. The counter and the working electrodes were always kept at almost the same distance (~3 cm). In order to avoid any exchange of solutes between the reference electrode and the electrolyte, the SCE electrode was immersed into an extension tube containing a 1 mol·L⁻¹ KNO₃ solution, positioned close to the work surface. In addition, the reference electrode was connected in parallel to a platinum wire connected to a capacitor of 1 μF. This device is used to avoid capacitive and inductive artifacts that can happen when recording the high-frequency impedance measurements [77]. A schematic representation of the experimental setup is provided in Figure 2.5.

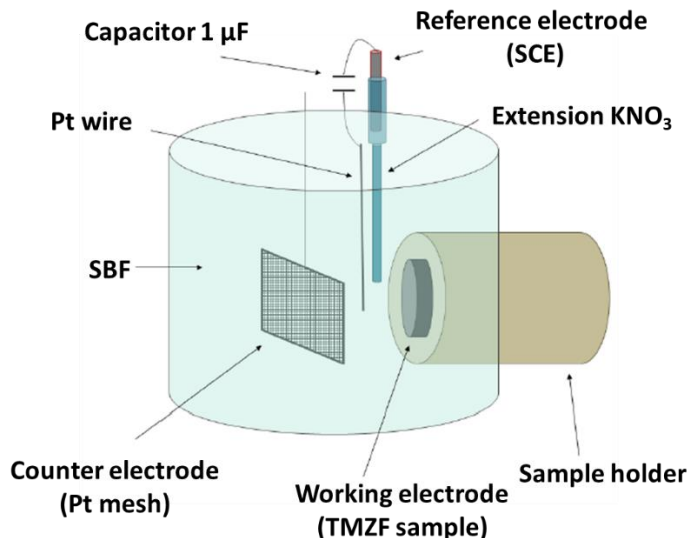


Figure 2.5 Schematic representation of the experimental assembly for the electrochemical characterization. (Adapted from [36])

The experimental assembly was placed inside a Faraday cage (steel box) connected to an Earth ground. It reduces current noise picked up by the working electrode and voltage noise picked up by the reference electrode. Additionally, the electrochemical characterizations were performed in dark environment, thus reproducing physiological conditions [36].

For the corrosion studies, three electrochemical techniques were employed. The characterization sequence firstly consisted of recording the evolution of the Open Circuit Potential (OCP) during 1 hour of immersion in the electrolyte to allow steady-state conditions to be reached. Subsequently, electrochemical impedance spectroscopy measurements (EIS) were recorded at the OCP with a frequency range of 10^{-2} - 10^4 Hz with a sinusoidal perturbation signal of $10 \text{ mV}_{\text{rms}}$ amplitude relative to the OCP (amplitude large enough for the output signal to be easily measured but which also allows the linearity criterion to be satisfied). Finally, the corrosion resistance was assessed through potentiodynamic polarization curves recorded over the potential range of -0.03 V/SCE to +1.2 V/SCE relative to the OCP, with a scan rate of 0.3 mVs^{-1} . These corrosion tests were performed over untreated samples, CST, Nt, and NP in four different immersion periods inside the SBF solution 0, 1, 7, and 14 days. Three samples were evaluated per condition and soaking time (different samples each time, but with the same surface treatment).

After performing the bioactivity and the electrochemical characterizations, the surface conditions that showed better results were evaluated to determine if these modifications affect the fatigue behavior.

2.5 Fatigue resistance

To accurately determine the effect of surface treatments on the fatigue response of the titanium alloy, a high cycle fatigue test called staircase (or *up and down*) was employed. This method was carried out according to ISO 12107 [78]. This is an incremental method in the sense that each test is established based on the result of the previous one. The method starts by subjecting the first specimen to a level close to the maximum stress value for a given number of cycles (typically $N=5 \times 10^6$ cycles for implants). Sequentially, new specimens are then tested according to the following criteria: if the immediately previous test resisted to the established life, the next one is subjected to a higher stress level in a d value (step or fixed value of stress increase or decrease), while, if it didn't resist, it is tested at a lower level in d . In this way, seven specimens from each of the surface conditions (untreated, CST and NP specimens) were tested, promoting a confidence level of 50% and a probability of failure of 10%, being suitable for exploratory research. To determine the fatigue strength and standard deviation values, the Dixon and Mood statistical method was used [78].

The fracture surfaces of the different specimens were observed in the Scanning Electron Microscope in order to analyze the fracture mechanisms present.

2.6 Surface characterization

The specimens with the modified surfaces were analyzed morphologically and chemically via Scanning Electron Microscopy (SEM), chemical analysis by energy dispersive spectroscopy (EDS), crystalline apatite formation by X-Ray diffraction (XRD) and Raman Mapping.

Raman characterization was performed using a Renishaw InVia Raman spectrometer equipped with dielectric filters (InVia) to remove the Rayleigh line. Raman photons were collected with a cooled CCD. In all cases, the excitation light was the green line of an Ar laser (514.53 nm). The scanning area was 4 x 4 cm 2D map with a step size of 100 µm. Spectra were recorded at the wavelength range between 900-1000 cm⁻¹, following the characteristic peak of Hydroxiapatite at 962cm⁻¹.

2.6.1 Roughness Measurements

The roughness measurements were performed with the help of an Olympus LEXT OLS4100 LASER confocal microscope with 50X and 100X objective lenses. The Olympus Stream image analysis software was employed to perform a qualitative and quantitative analysis of the generated surfaces. Additionally, it was possible to produce a 3D image of the surface of the samples.

2.6.2 Hydrogen absorption

A LECO ONH836 element analyser was used to determine the amount of hydrogen present in the material before and after chemical treatments. Initially, the sample to be analysed was weighed (~ 20 mg) and deposited in a graphite container, after which the material was heated until it released the hydrogen as a gas, which is detected using non-dispersive infrared cells. The hydrogen concentration was determined relatively using calibration standards. Additionally, to determine the possibility of hydrides formation was employed a Transmission Electron Microscopy (TEM) equipped with an orientation-phase mapping precession unit NanoMEGAS (model ASTAR) and with a DigiSTAR P1000 unit.

Chapter III

Bioactivity and electrochemical behavior of TMZF samples treated with CST, nanopores and nanotubes

The biological and electrochemical response of the commercially pure titanium and the Ti-6Al-4V ELI alloy treated with chemical and electrochemical processes has been extensively studied. However, the need for the use of β titanium alloys with low elastic modulus makes interesting the study of these treatments on commercial β -Ti alloys such as Ti-12Mo-6Zr-2Fe (TMZF).

In the present chapter, Hydroxyapatite (HAp) mass gain test was carried out as an indicator of the osseointegration behavior of the different surface treatments obtained over the TMZF samples surface. Additionally, the HAp growth resulting from soaked specimens in SBF solution was confirmed by SEM, EDS, XRD and Raman mapping.

Corrosion of metallic prosthesis modify their structural integrity and can cause alterations of the surrounding environment, such as changes in pH, and decrease of dissolved oxygen. Furthermore, the metal ions released may cause an allergic response and can be harmful to the patient. For these reasons, the study of the corrosion process is critical and necessary for metallic biomaterials. In this way, was studied the electrochemical behavior of the surface treated with CST, nanopores, and nanotubes through potentiodynamic polarization curves.

The microstructure of swaged and heat-treated materials consisted of equiaxed grains with grain size of 80-100 μm , as presented in Figure 3.1 (a). The evaluation of the microstructure through XRD suggested the existence of recrystallized β phase (Figure 3.1 b), which met the requirements of the standard ASTM F1813. This microstructure provides an alloy with an intermediate modulus of elasticity $\sim 90 \pm 6$ GPa, measured by the impulse excitation technique.

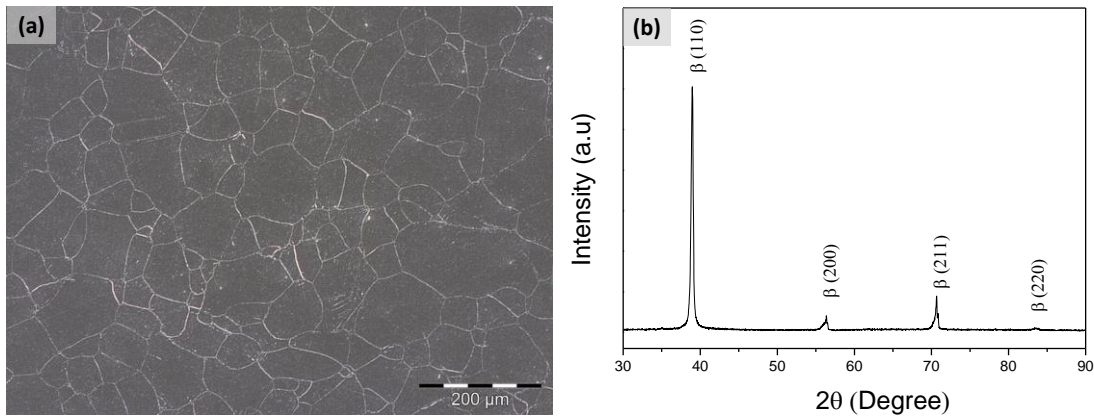


Figure 3.1 (a) Microstructure and (b) XRD spectrum of the TMZF alloy.

Figure 3.2 shows the surface of the untreated TMZF sample after the polishing process. Here, a soft topography is noted with the presence of small marks or scratches, due to the abrasion during grinding and subsequent polishing processes. This surface will be used as the reference one for the different bioactivity, electrochemical, and fatigue tests.

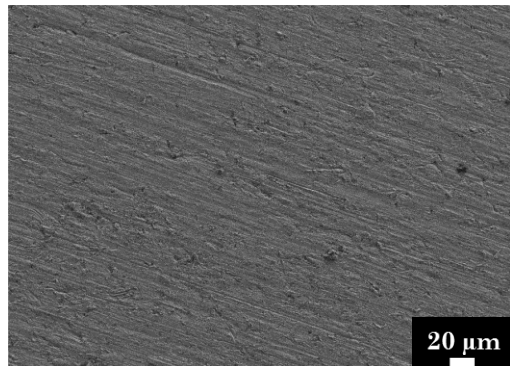


Figure 3.2 SEM image of the untreated samples after the grinded and polished processes.

The images in Figure 3.3 refer to the sample treated with hydrochloric (HCl) acid and sodium hydroxide (NaOH); it is possible to observe the effect of the attack on the entire polished surface, changing the initial, smooth morphology, by a surface with micropores uniformly distributed and revealing the grain boundaries. A higher

magnification (Figure 3.3 b), was used to evaluate the presence of nanometric characteristics on the sample surface, confirming the effect of the NaOH. Here, it is possible to observe coral-like structures in the submicrometric and nanometric scale formed during the alkaline treatment.

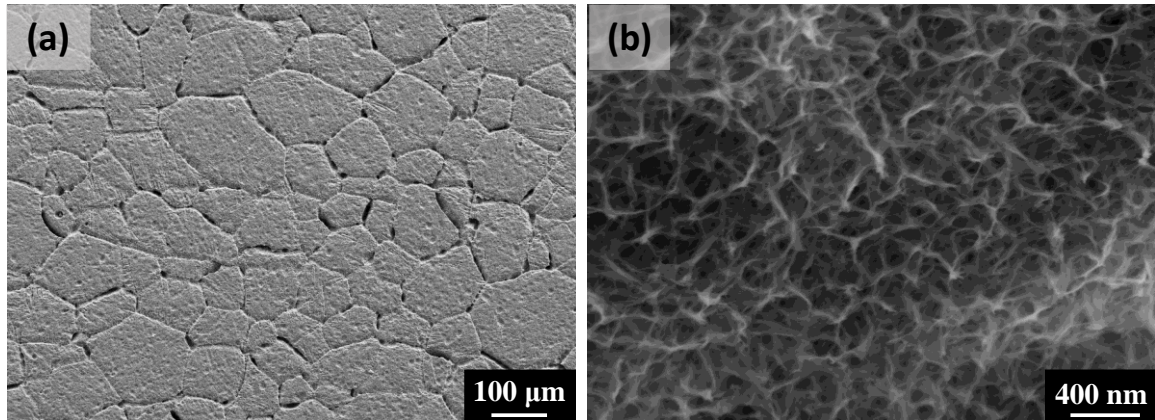


Figure 3.3 SEM images of TMZF alloy, chemically treated by HCl 37% at 60 °C and NaOH 10 mol·L⁻¹ at 60 °C for 24 h.

To find the synthesis parameter for nanotubes was a little more time-demanding than expected, because the traditional parameters used for pure titanium, does not produce nanotubes in this β titanium alloy. After several try-outs varying time and voltage, it was possible to see that reducing the potential to values close or lower than 15V favors the formation of nanotubes homogeneously distributed on the TMZF surface (see Figure 3.4). Additionally, during these try-outs were found the anodization parameters for another attractive surface referred as nanopores surface.

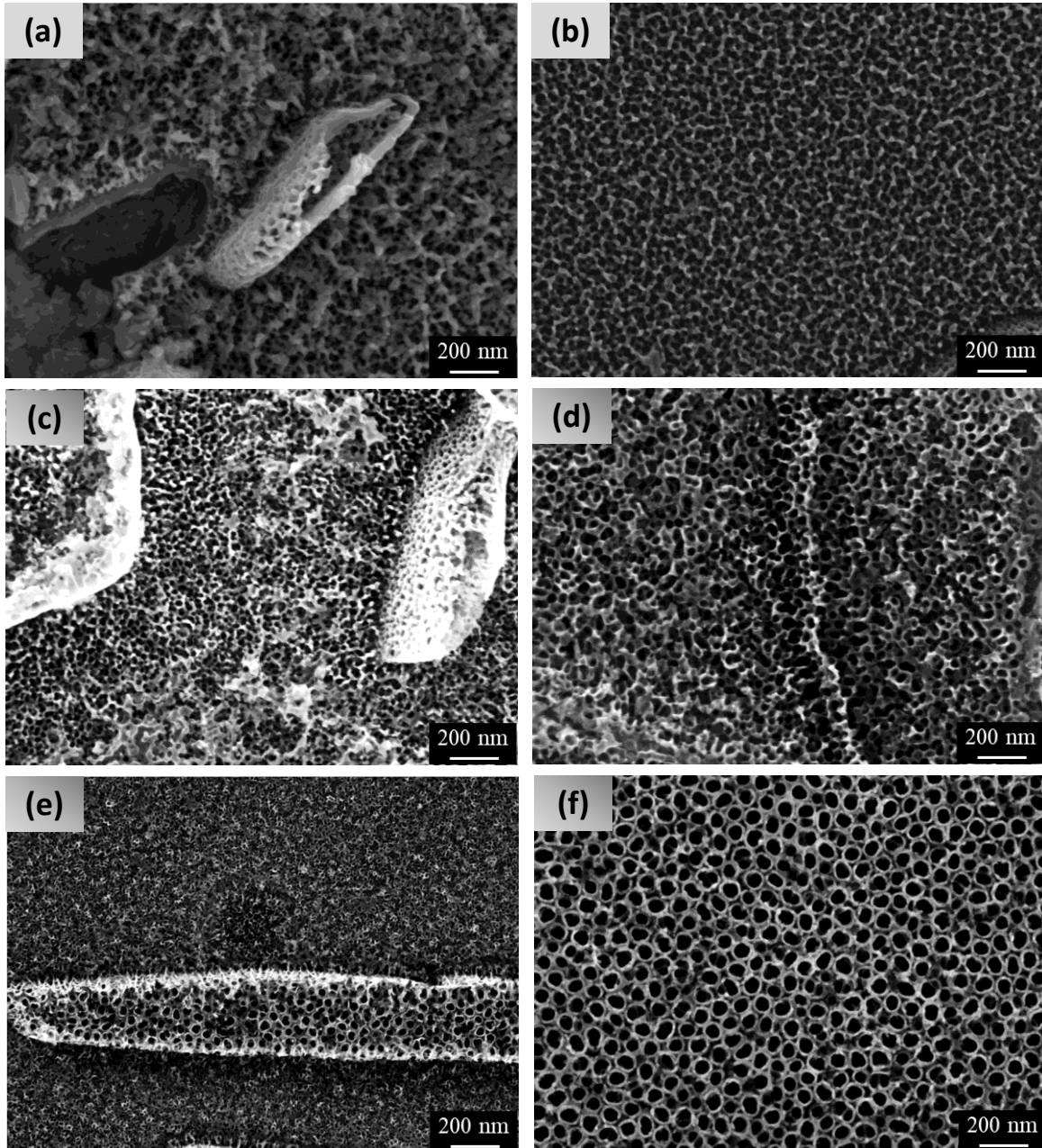


Figure 3.4 SEM images of anodized surfaces for different preliminary anodization parameter, varying the applied potential and the anodization time: a) 60V-1h, b) 40V-1h, c) 40V-2h, d) 20V-2h, e) 15V-2h and f) 10V-2h.

High-resolution SEM image in Figure 3.5 shows the final surface condition of the two different anodized systems studied in this work. Figure 3.5 (a) shows the formation of a network of vertically self-organized tubes uniformly distributed over the entire surface, while Figure 3.5 (b) shows a nanometric and disordered worm-like structure; this later mesopores surface was named as nanopores.

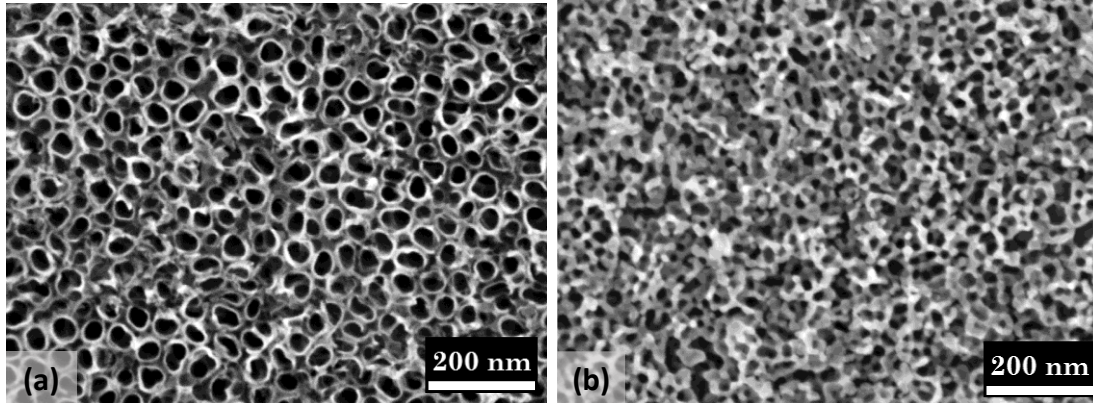


Figure 3.5 High-resolution SEM image of anodized samples: a) Nanotubes and b) Nanopores.

3.1 Hydroxyapatite formation test

The bioactivity assays were performed on TMZF disks untreated, with CST, nanotubes and nanopores conditions. Three samples for each condition were immersed in 50 ml of classic SBF solution at 37 °C for different periods (1, 7 and 14 days) and it was measured the amount of hydroxyapatite (HAp) spontaneously deposited on the sample surface [6].

Figure 3.6 summarizes the average value of the mass gain for three samples of each surface condition during the different periods. It is possible to see that there is no apatite deposit on the untreated TMZF alloy and nanotubes. In contrast, nanopores samples showed a moderate HAp formation after 14 days of immersion (mass gain higher than 0.5 mg).

On the other hand, CST samples show a better bone-bonding ability compared to the anodized and untreated samples. After 7 days soaking, this surface evidenced a significant apatite formation with a mass gain higher than 0.8 mg; this nucleation and growth process is maintained, showing the highest mass gain value around 1.8 mg after 14 days.

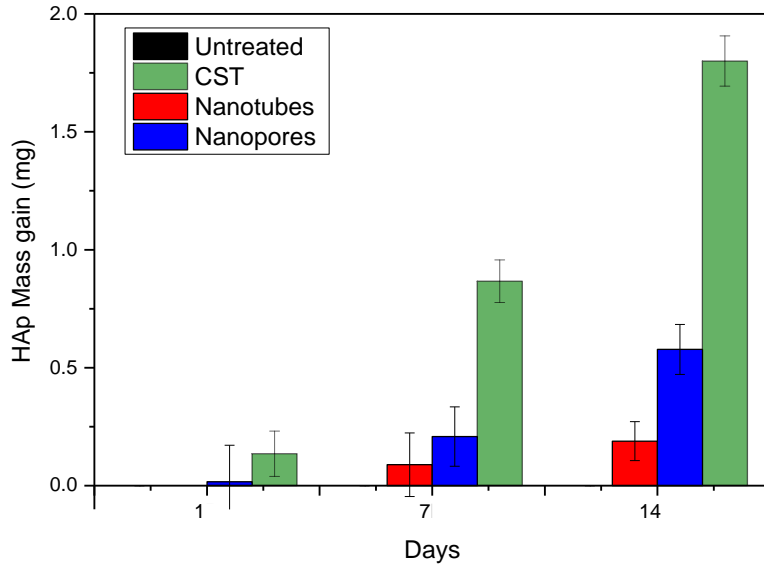


Figure 3.6 Quantitative evaluation by apatite mass gain of untreated, CST, nanotubes and nanopores samples after different immersion times in SBF.

SEM images in Figure 3.7 reveal that even after 14 days of immersion in the physiological solution, none or slight traces of HAp are detected on untreated, nanotubes and nanopores surfaces. Nevertheless, it was possible to observe HAp spheres on the CST sample after the same 14 days in SBF (Figure 3.7 d). This visual information corroborates the mass gain values obtained for the different surface treatments after soaking times.

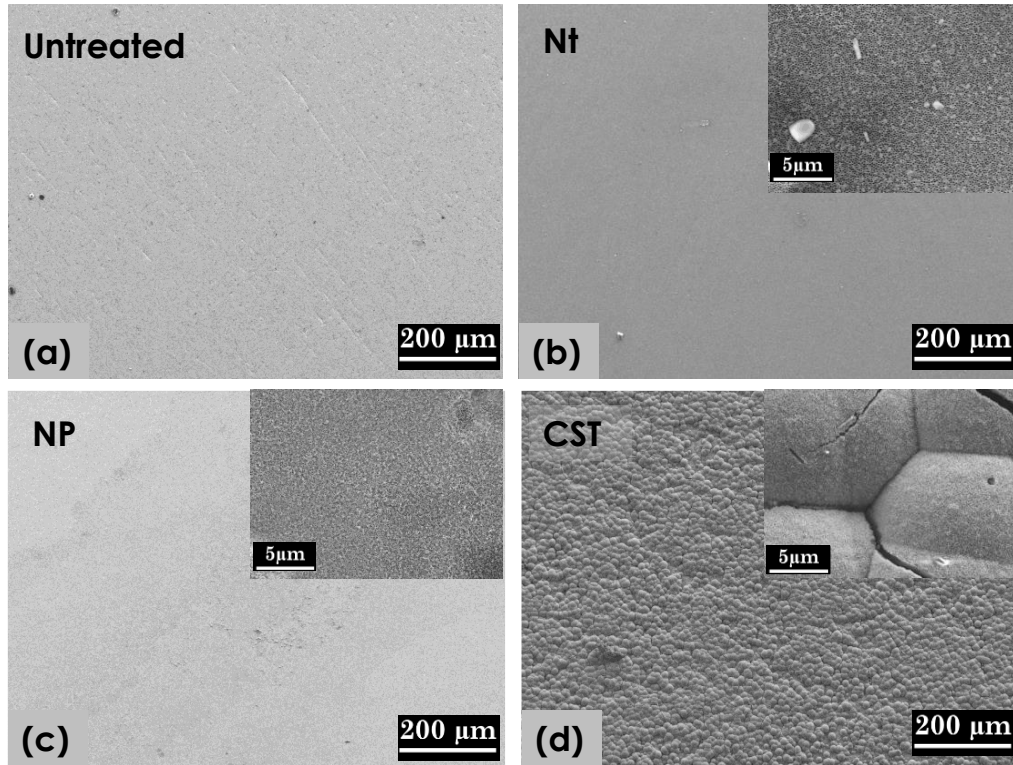


Figure 3.7 SEM images for samples of TMZF alloy subjected to the bioactivity tests after 14 days immersed in SBF. a) Untreated; b) Nanotubes; c) Nanopores and d) CST samples.

Table 3.1 shows the EDS results performed on untreated, CST, nanotubes and nanopores samples after 14 days of immersion. Only on CST and nanopores surfaces were detected the presence of calcium, phosphorus and oxygen elements that are characteristic of the hydroxyapatite present in the human body [79]. This result is corroborated by XRD patterns in Figure 3.8, where is possible to see the diffraction peaks of the crystalline HAp phase solely in the samples with CST after 14 days of immersion.

Table 3.1 Quantitative chemical EDS analysis of untreated, nanotubes, nanopores, and CST samples. After 14 days of immersion in SBF solution.

Condition	Chemical element (% at.)						
	Ti	Mo	Zr	Fe	O	Ca	P
Untreated	67.32	3.79	2.15	1.94	22.75	-	-
Nanotubes	57.65	3.64	1.97	-	35.36	-	-
Nanopores	46.28	3.10	1.60	-	48.89	0.60	0.40
CST	11.88	0.54	0.24	-	59.06	16.97	9.34

In a physiological fluid, for instance SBF solution, OH⁻ groups are adsorbed to the surface of TiO₂ to form Ti-OH bonds. Since these hydroxyl groups are slightly negatively charged, the result is an electrostatic attraction of the calcium cations, thus forming amorphous calcium titanate [75]. With the immersion time, this calcium titanate interacts with the PO₄³⁻ phosphate ions of the SBF solution to form an amorphous calcium phosphate compound [26, 79, 80]. Then, since hydroxyapatite is the most stable calcium phosphate compound in aqueous medium at pH 7.4, the surface deposit crystallizes in this form. Once formed, the crystalline apatite layer consumes the calcium and phosphate ions from the SBF solution [79].

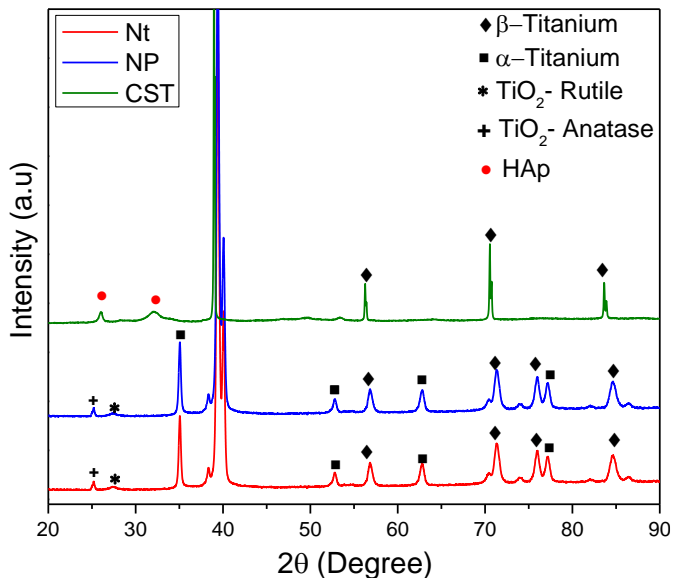


Figure 3.8 XRD patterns of untreated, CST, nanotubes and nanopores samples after 14 days of immersion in SBF.

Another complementary test to know if we have the crystalline form of the calcium phosphate (HAp) deposited on the surfaces treated, is the Raman spectral mapping. For this test was employed the wavenumber characteristic of HAp, 961cm⁻¹. In this qualitative result, the HAp formation is determined through the red color intensity; higher intensity zones mean more precipitation of this compound.

Figure 3.9 shows the difference between the different treated samples after 7 and 14 days of immersion in SBF. Independent of the immersion time, nanotubes samples showed maps with low Raman intensity, indicating low HAp formation even after 14 of immersion. In the case of nanopores samples the results are slightly better, showing different zone with precipitates of HAp after 14 days of immersion in SBF.

On the other hand, CST samples showed the best bioactivity behavior. As a result, was observed a greater amount of crystalline calcium phosphate precipitated

along the entire surface of the material, even just after 7 days of immersion, indicating more favorable surface conditions for osseointegration.

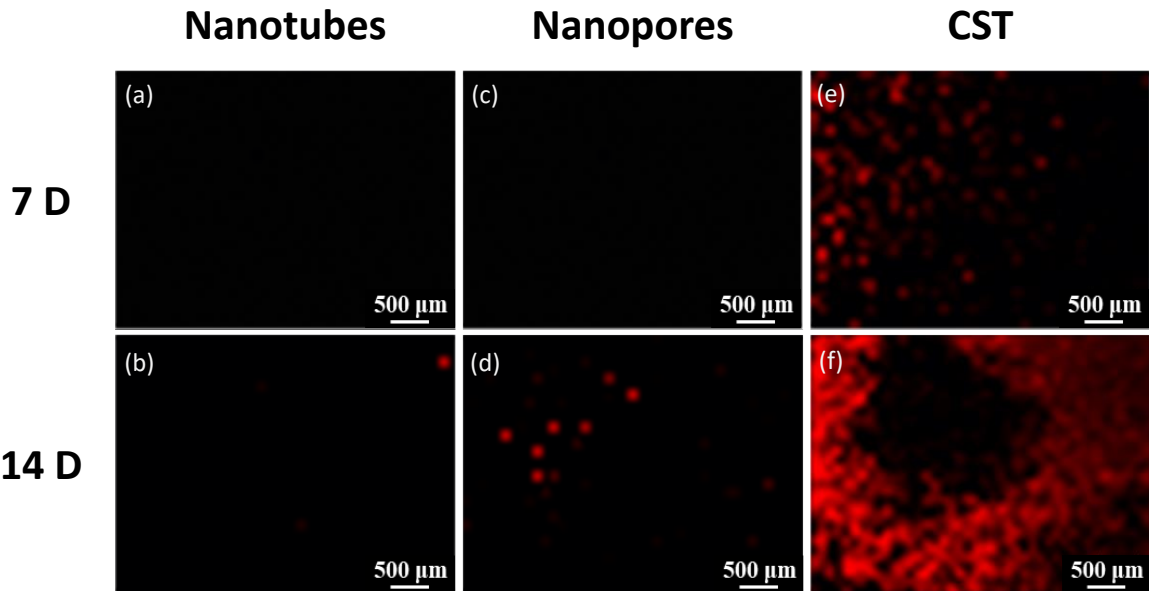


Figure 3.9 Raman spectral mapping of nanotubes, nanopores and CST samples soaked during 7 and 14 days in SBF.

The large area developed by the nanotubes and nanopores allows the formation of a significant number of -OH bonds and thus increase the number of nucleation zones responsible for the initiation of the apatite layer [81]. However, surface contamination by other oxides of metallic elements present in the alloy as Mo, Zr, and Fe, could decrease this surface potential, decelerating the apatite nucleation [82].

3.2 Electrochemistry characterization

Figure 3.10 compare typical potentiodynamic polarization curves of a representative sample for each surface condition and immersion time. From these curves, was calculated the corrosion potential (E_{corr}) corresponding to the position where the net current is zero and is indicated as the "peak" directed downwards on the polarization curves.

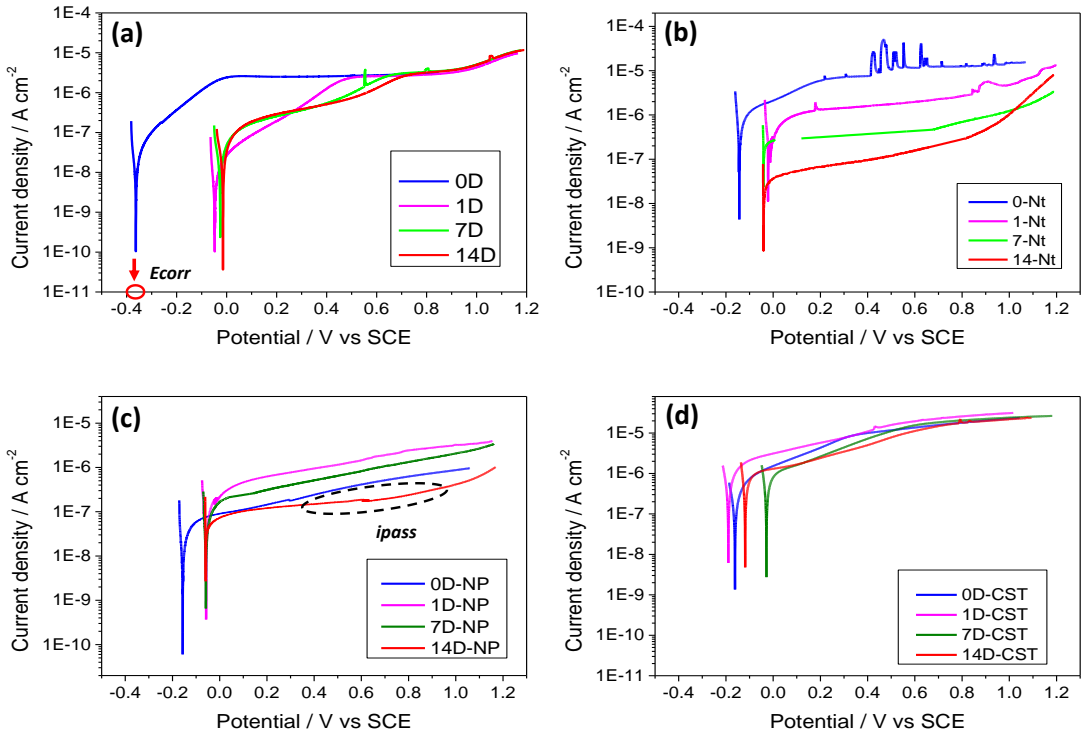


Figure 3.10 Anodic polarization curves, for the TMZF alloy in SBF electrolyte at 37 °C: a) Untreated; b) nanotubes; c) nanopores and d) CST.

The nature of the polarization curves indicated stable passive behavior for all the surface conditions and immersion periods. However, in the nanotubes sample at 0 days is observed fluctuations in the passivity domain due to the creation of a localized aggressive environment that breaks down the passivation layer [83]. These kinds of oscillations can be attributed to the competition between the formation and dissolution of the passive film. Remain fluoride ions trapped into the tubes from the anodization process could favor this phenomenon [84].

The values of E_{corr} for the four different surface treatments are summarized in Figure 3.11. These values are comparable with the potential obtained for each condition after one hour of OCP. Untreated samples show, initially, a low corrosion potential close to -0.370 V_{SCE}, but this value increases considerably after 1 day of immersion and remains almost constant at -0.050 V_{SCE} until 14 days in SBF solution.

Furthermore, nanotubes, nanopores and CST samples showed a nobler behavior (-0.072, -0.115 and -0.190 V_{SCE}, respectively) compared to untreated samples at 0 day. After 1 day of immersion in SBF solution, all of them exhibited a tendency to higher potential values close to -0.050 V_{SCE}, this behavior was less pronounced for the samples treated with HCl etching plus alkaline treatment, indicating a lower corrosion protection than the anodized samples (Figure 3.11).

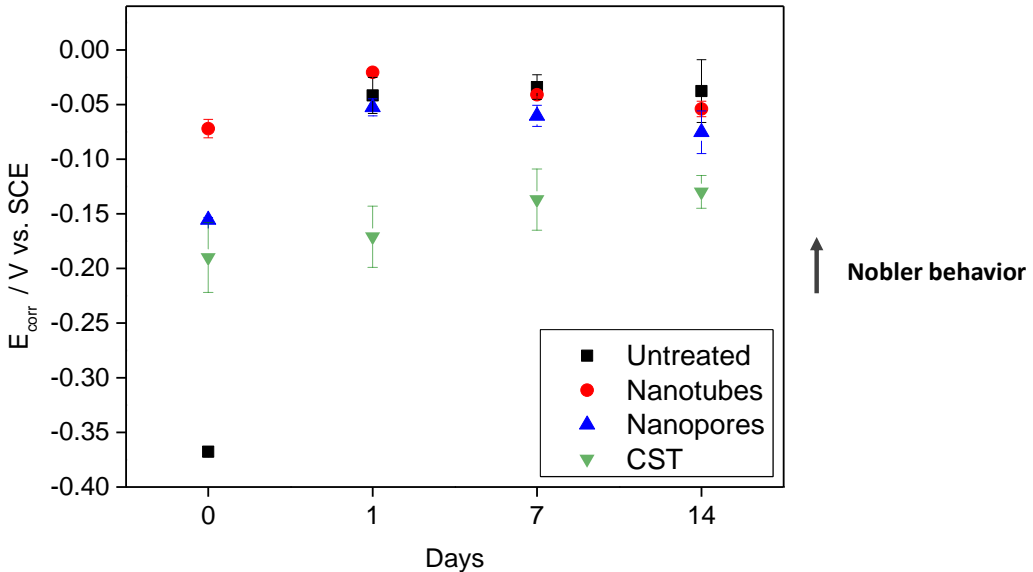


Figure 3.11 Electrochemical measurements of corrosion potential (E_{corr}) of TMZF alloy untreated and treated with nanotubes, nanopores, and CST for different immersion times in SBF at 37°C.

As part of this study, the current density of the passivation plate (i_{pass}) was chosen instead of the current density of corrosion (i_{corr}) in order to establish a better comparison between the different surfaces obtained, which are prone to passivation. However, in some passivating materials exposed to physiological environments, the current density is not independent of the potential in the passive state. One reason is the dynamic nature of the test; the changes of the film with the potential are very slow to remain stable with the scan. Another possibility is that the changes in the passive layer are uncompensated for the increased oxidative driving force during the test [83].

In practice, the shapes of the anodic branches are not identical for all the samples, and the determination of i_{pass} can be non-trivial (Figure 3.10), for these reasons the method for the determination of i_{pass} , consisted of calculating, for each sample, the average of the current densities measured in the range of potentials between +0.4 V_{SCE} and +1 V_{SCE} relative to the OCP [5].

Metallic implants are deemed to be corrosion resistant, and the rate of ion transfer establishes the effectiveness of their passive layer. In this way, TMZF alloys in a physiological environment with i_{pass} lower than 12.5 $\mu\text{A.cm}^{-2}$ or corrosion rate lower than 10⁻¹ mm/year are considered belonging to the “Stable” corrosion resistance category and lower than 1.25 $\mu\text{A.cm}^{-2}$ or 10⁻² mm/year are placed in the “Very stable” resistance class [85].

Figure 3.12 shows the i_{pass} values and the corrosion resistance category for the different surface treatments in different immersion time. Untreated specimens show

moderate-low and stable results with i_{pass} closer to $2.0 \mu\text{A.cm}^{-2}$, during the different periods analyzed, due to the presence of a homogenous and thin passive layer on the alloy's surface.

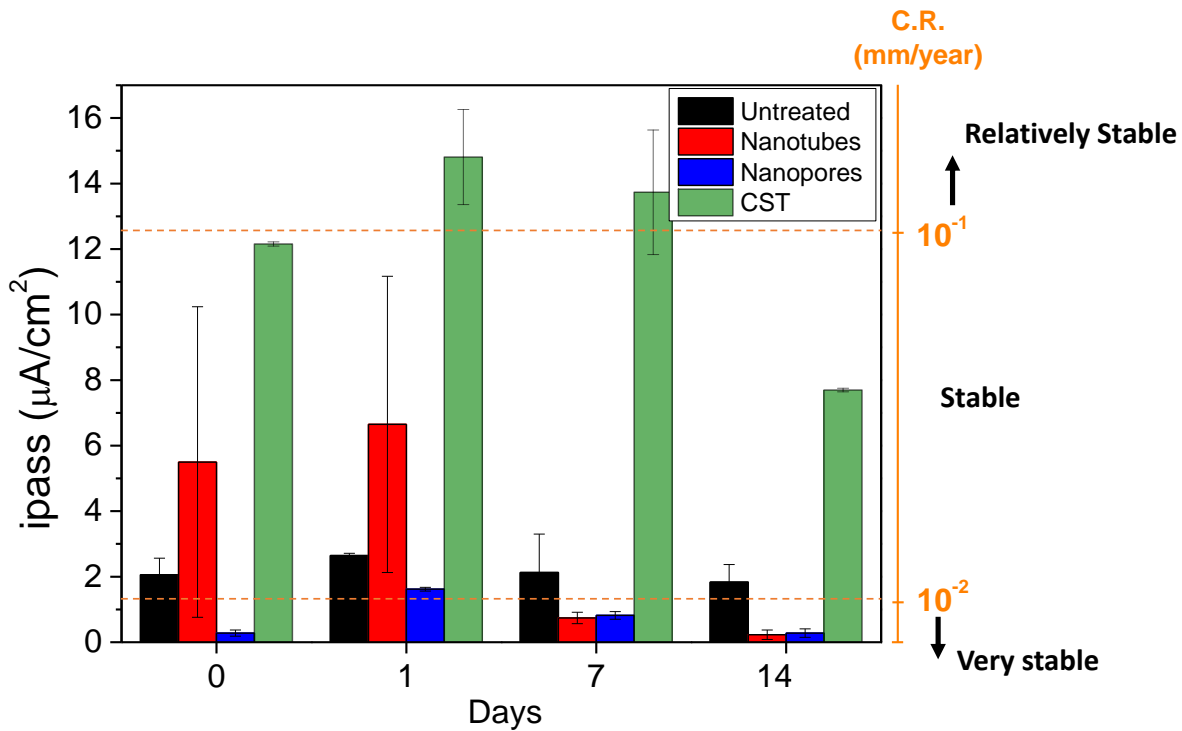


Figure 3.12 Electrochemical measurements of passivation current density (i_{pass}) and corrosion rate (C.R.) of TMZF alloy untreated and treated with nanotubes, nanopores, and CST in different immersion time in SBF at 37°C .

Initially, for 0 and 1 day of immersion, nanotubes samples showed high i_{pass} values, around $5.0 \mu\text{A.cm}^{-2}$. This behavior could be attributed to surface heterogeneities created during the anodization process. Nonetheless, after 7 and 14 days, the i_{pass} values were lower than $0.8 \mu\text{A.cm}^{-2}$. Initially, ordered nanotubes offered a free path for ion diffusion between the bulk electrolyte and the electrode, after a few days of immersion these channels begin to close by the deposition of calcium phosphate on the outer and bottom part of the nanotubes, with additional growth of the inner passive film [86], which could have hindered the transfer of ions through these channels. This discussion will be taken again in section 4.3.3.

Nanopores samples exhibited good electrochemical behavior with low and stable i_{pass} values during all immersion periods, with i_{pass} values lower than $0.3 \mu\text{A.cm}^{-2}$ after 14 days soaked in SBF. This performance is due to its homogeneous passive layer; this layer is thicker than the passive layer for the untreated samples.

From an electrochemical point of view, samples with CST showed the least corrosion resistance among the four systems studied for the different immersion times, showing i_{pass} values higher than $12 \mu\text{A.cm}^{-2}$ for 0, 1 and 7 days of immersion in SBF. However, after 14 days, it was possible to see a reduction in its i_{pass} value ($\sim 8.0 \mu\text{A.cm}^{-2}$) positioning it in the “Stable” resistance category. This chemical treatment produces micro, submicron and nanometer features on the titanium sample. These fine network structures are favorable for accelerating apatite nucleation due to the formation of a sponge-like structure, but consequently, this structure facilitates the diffusion and charge transfer between the electrolyte and the TMZF substrate [87].

The hydroxyapatite formation and electrochemical behavior investigated through potentiodynamic polarization curves of TMZF samples untreated and treated with CST, nanopores and nanotubes, has been studied and the conclusions are summarized in the following paragraphs:

- Surface treatments as nanotubes, nanopores and chemical surface treatment on β -TMZF alloy were successfully obtained.
- Nanotubes and nanopores show a lower and moderate apatite formation (respectively) when compared with CST samples. This behavior could be associated with the reduction of the surface potential due to the formation of oxides of metallic elements present in the alloy as Mo, Zr, and Fe. Thus, decelerating the apatite nucleation.
- On the other hand, CST samples showed the best bioactivity behavior attributed to the high electrostatic interaction between the functional groups on the surface and the ions in the fluid.
- E_{corr} values reveal that nanotubes and nanopores show a nobler behavior than untreated and CST samples, indicating a more stable and protective surface.
- Although nanotubes and nanopores surfaces showed moderate passivation currents values in the early stages of immersion (0 and 1 day), densification processes of the oxide film and deposition of calcium phosphates improve their corrosion resistance, reducing the i_{pass} values, close to $0.2 \mu\text{A.cm}^{-2}$ after 14 days immersed in SBF.

Chapter IV

Analysis and modeling of the impedance spectra for the different surface conditions obtained

In recent years, Electrochemical Impedance Spectroscopy (EIS) has been successfully applied to corrosion systems. EIS has been used effectively to measure the polarization resistance and determinate the corrosion mechanisms in different systems. Passive, oxide and porous layers show complex impedance responses and the interpretation of their impedance behavior is not trivial.

Traditionally, the impedance test results are modeled by electrical circuits, through the combination of electrical components such as resistors, capacitors, and inductors; however, it is essential to remark that the way to use these elements must have a physical and electrochemical meaning [88].

More specifically, the objective in this chapter is to study the impedance spectra response for the different surface treatments studied in this thesis, via Electrical Equivalent Circuit (EEC), in order to go further in understanding their electrochemical behavior in physiological medium.

Initially, throughout this chapter, some generalities on the principle of modeling the impedance measurements will be presented. Then, different equivalent circuits proposed in the literature will be reviewed and applied for the EIS data of the untreated and CST samples. Finally, a new model will be developed for the anodized samples and its applicability will be evaluated.

The program used in this study to perform the simulations and adjustments of the impedance parameters is the *Simad* software. It was developed at the Laboratoire Interfaces et Systèmes Electrochimiques (LISE) at Pierre et Marie Curie University (UPMC).

4.1 EIS measurements over untreated TMZF samples

In order to complete the electrochemical characterization discussed in Chapter III of the surfaces selected for this study, additional information is obtained from EIS measurements and the interpretation of their data. Figure 4.1 shows the evolution of the Nyquist plots and the Bode diagrams with immersion time in SBF solution of untreated TMZF samples (polished samples); replicate specimens show similar results but are not plotted for better visualization of the diagrams (reproducibility was checked).

Nyquist and Bode representations of impedance measurements of samples without surface treatments are shown in Figure 4.1 (b-d). The data plotted in the figures of this chapter have been corrected by the geometric area (0.283 cm^2) exposed to the electrolyte. Graphics of Figure 4.1b and 4.1.d have been corrected for the ohmic resistance or electrolyte resistance (R_e), estimated between $20\text{-}30\text{ }\Omega\cdot\text{cm}^2$, which was deduced from the high-frequency limit ($f = 10^4\text{ Hz}$).

Nyquist diagram for untreated samples in Figure 4.1c reflected the typical response of a capacitive-resistive or pseudocapacitive system independent of the immersion time. It means that the charge transfer, and therefore the reactions are limited due to the protective behavior of the passive oxide layer [36, 89].

The continuous increase of the impedance modulus $|Z|$ throughout the immersion time suggests that the first two weeks in SBF enhances the corrosion resistance of the untreated samples (Figure 4.1d). This observation is consistent with the E_{corr} measurements (Figure 3.11), which shows a significant increase from the first day of immersion and remains almost constant until 14 days.

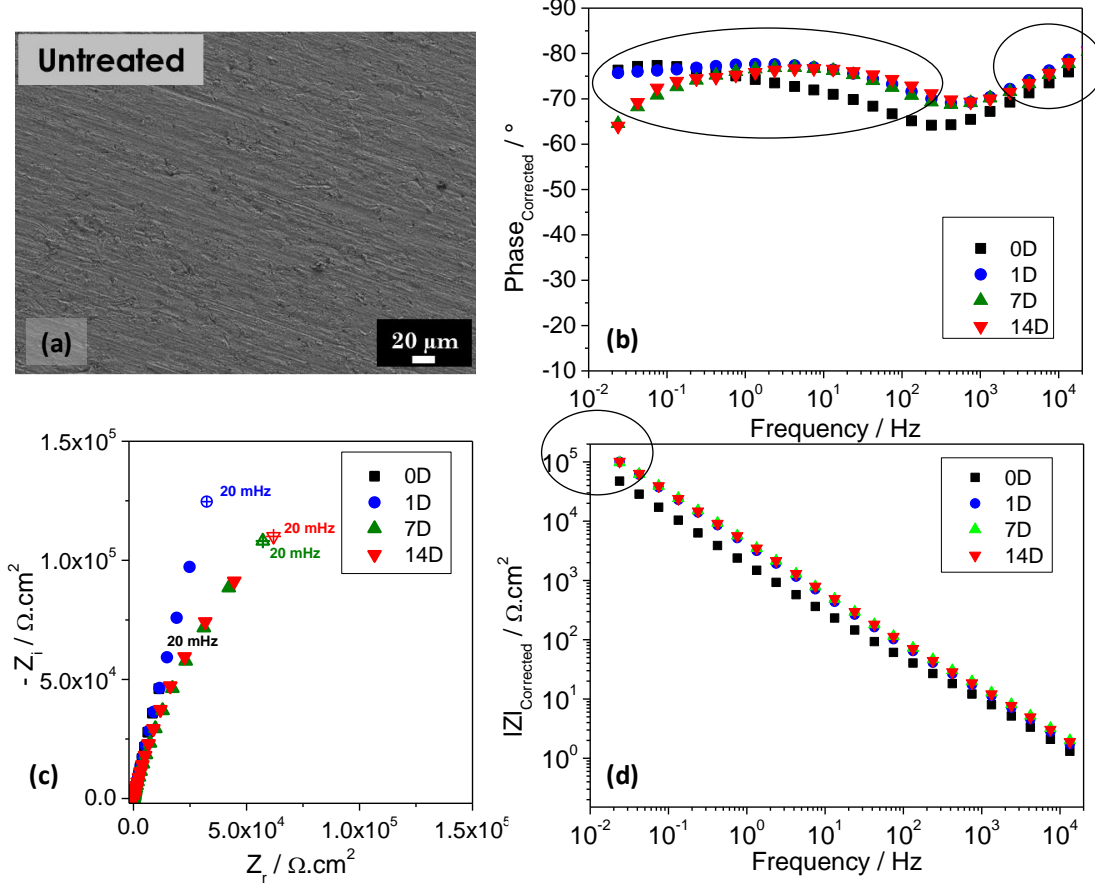


Figure 4.1 a) SEM micrograph of untreated TMZF sample before the immersion period; b) Impedance results for untreated samples immersed in SBF at 37 °C; c) Corrected-phase angle; d) Nyquist plot and e) Corrected-magnitude of the impedance for the different immersion time (0, 1, 7, and 14 days denoted as 0D, 1D, 7D and 14D respectively).

The impedance responses of electrochemical systems can be modeled by analytical expressions and also by EEC. The construction of these circuits consists of combining in series and/or in parallel electrical elements such as resistor (R), capacitors (C) or inductors (L). Note that the element L is indicated here but will not be mentioned again because this phenomenon was not encountered in this study. When the electrochemical responses are not ideal and cannot be represented by a connection of simple R-C-L elements, a Constant Phase Element (CPE) is used. This CPE element indicated the non-ideal capacitive behavior and model the presence of distributed processes [90–92]. The combination and use of these elements depend strictly on the physical aspects of the interface, considering what could happen at this interface.

The most common EEC for the metal /solution interface is the Randles circuit in Figure 4.2a, which consists of three elements: a resistor representing the electrolyte resistance, R_e , in series with the parallel combination of a capacitor representing the double layer capacitance, C_{dl} , and a resistor indicating the charge transfer resistance R_{ct} or the polarization resistance R_p in metals that form protective passive layers [50]

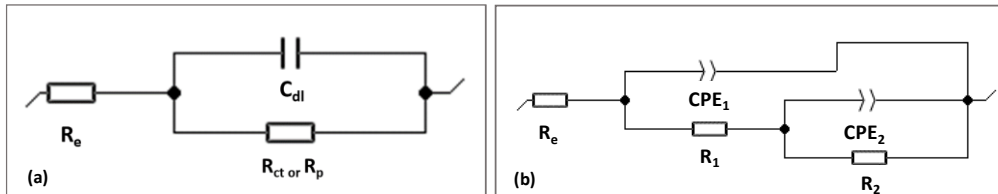


Figure 4.2 Schematic electrochemical impedance circuits: a) Randles circuit and b) porous passive layer circuit.

Another interesting model is shown in Figure 4.2b, for an electrode with a protective porous layer [93]. This circuit uses two times constant, one for the high frequency that characterizes the electrode/coating system and another at low frequencies that characterizes the electrode/aqueous medium system. It is a consequence of the coating having pores or defects through which the electrolyte accesses the electrode base.

To determine suitable results from the impedance analysis is necessary to understand how many processes are happening on the studied surface during the test and then define the adequate model. In this way, using alternative graphical representations of the impedance results as the corrected Bode plots help to define the appropriate EEC [94].

Traditionally, the Bode plot has been particularly useful in recognizing the number of time constants of the system to check the validity of an EEC. These curves are more sensitive to modelling parameters than other traditional impedance plots. Nevertheless, the presence of the electrolyte resistance or ohmic resistance covers the real behavior at high frequencies. For this reason, modified Bode curves corrected from ohmic resistance is used as a reliable option when the solution resistance is not negligible [94]. Therefore, all Bode diagrams in this work were corrected from the electrolyte resistance using Equations 1.20 and 1.21 (Chapter I).

Over the untreated TMZF surface is expected the formation of a passive bi-layer which has been observed in similar titanium alloys containing zirconium and molybdenum [95]. This passive bi-layer would be composed by an external porous layer and inner barrier layer; thus, it is expected to found two relaxation processes or time constants in the impedance results.

The corrected Bode representations for the untreated TMZF sample are shown in Figure 4.1b and d. Using the corrected-phase plot (Figure 4.1b), it is possible to observe two time constants present during the impedance test. One of them is in the range of 10^{-2} Hz to 10^2 Hz and the second one in high frequency around 10^4 Hz, confirming the theory of the porous passive layer formation indicated above. Thus, the most appropriate EEC for modeling the impedance results obtained for the samples without treatments is the model shows in Figure 4.2b.

The principal disadvantage of the corrected Bode phase plot is the need for a precise estimation of the electrolyte resistance. Inaccurate estimations could provide the wrong idea of an additional time constant at high frequencies. Besides that, the corrected curves are very sensitive to the data noise at high frequencies [60]. For these reasons, a complementary curve for the corrected Bode plots is the graphical representation of the effective CPE exponent (α_{eff}), extracted from the imaginary part of the impedance (Z_i) according to [60]:

$$\alpha_{\text{eff}}(f) = \left| \frac{d \log |Z_i(f)|}{d \log f} \right| \quad (4.1)$$

Traditionally, in the curve of α_{eff} , the CPE elements are associated with plateaus extended during various levels of frequencies. However, these regions can decrease to form bumps or smooth peaks due to the interaction of events with close relaxation processes [60]. In this sense, Figure 4.3 clearly shows two time constants for all samples, and thus modeled by two CPE, one of them in the range of 10^{-2} Hz to 10^2 Hz and the second one in high frequency around to 10^4 Hz.

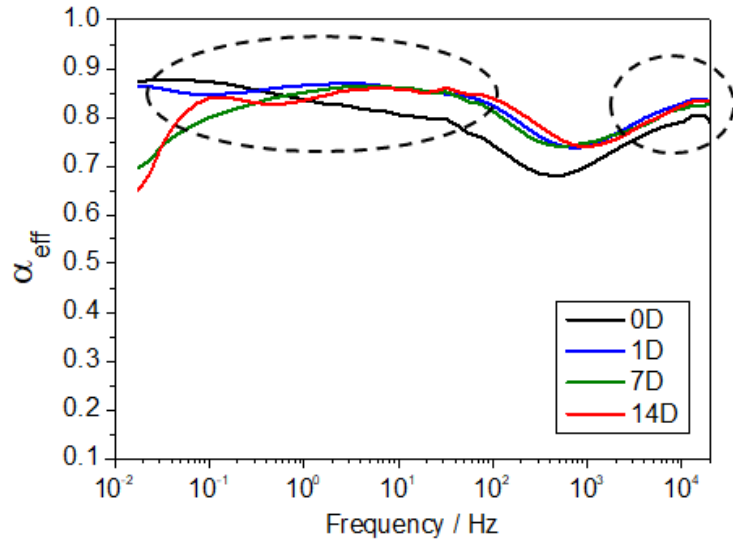


Figure 4.3 Evolution of α_{eff} versus frequency, of the TMZF untreated samples for the different immersion periods (0, 1, 7, and 14 days denoted as 0D, 1D, 7D and 14D respectively).in SBF at 37 °C.

According to the information obtained through the Bode phase and the α_{eff} plots (Figure 4.2b and Figure 4.3), the EEC for the untreated sample will be composed of two relaxation processes, a similar configuration as the EEC shown in Figure 4.2b. Such characteristic phase pattern may be related to a bi-layered microstructure of the passive films formed on the titanium alloys surface [93, 95].

In this electrical circuit (Figure 4.4), R_e denotes the resistance of the SBF solution, between the working electrode and the reference electrode. The suffix B and OP are associated with the elements that represent the inner barrier layer and the outer porous oxide layer, respectively. The use of a CPE, instead of a pure capacitor was considered due to the assumption of a heterogeneous distribution of charge on the sample surface [59, 95].

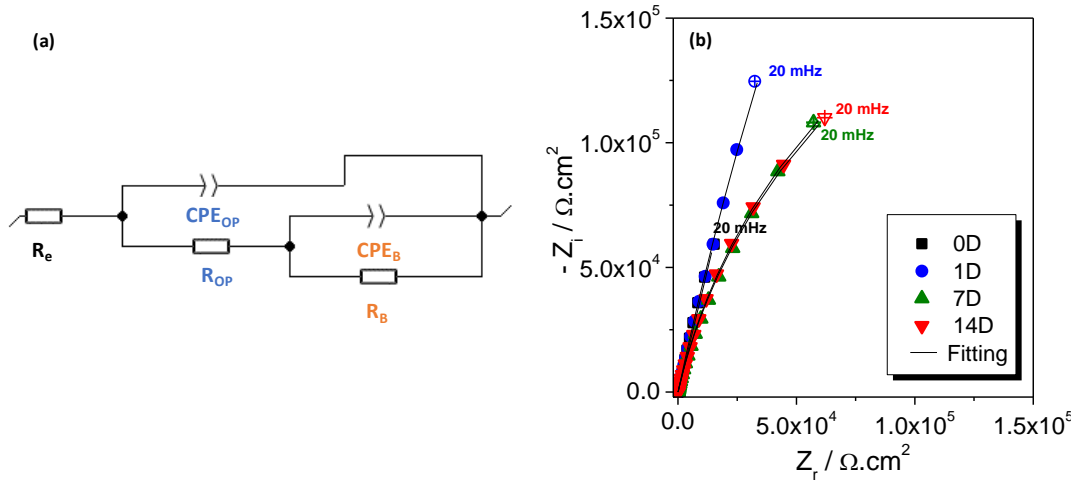


Figure 4.4 Electrical equivalent circuit for untreated samples and b) Nyquist plots of experimental and simulated results obtained through the Simad software, for the different immersion periods (0, 1, 7, and 14 days denoted as 0D, 1D, 7D and 14D respectively) in SBF at 37 °C. The error coefficient was lower than 1% for all the curves.

The impedance of a phase element is defined as $Z_{CPE} = [Q(j\omega)^\alpha]^{-1}$. The value of α is related to the heterogeneous distribution of current as a result of the non-uniform surface. The capacitance is Q , while j and ω are the current and frequency, respectively. The resistance, capacitance and α values of the porous and barrier layers, obtained by adjusting the experimental data using the EEC are given in Table 4.1 Electrical parameters obtained by fitting the experimental results of impedance for untreated samples at 37 °C in SBF solution.. The α values of around 0.9 suggest that the behavior of such passive layer approached that of an ideal capacitor, independent of the immersion time [59].

Table 4.1 Electrical parameters obtained by fitting the experimental results of impedance for untreated samples at 37 °C in SBF solution.

Immersion Days	R_e ($\Omega \cdot \text{cm}^2$)	Q_{OP} ($\Omega s^{-\alpha} \cdot \text{cm}^2$)	α_{OP}	R_{OP} ($\Omega \cdot \text{cm}^2$)	Q_B ($\Omega s^{-\alpha} \cdot \text{cm}^2$)	α_B	R_B ($10^5 \Omega \cdot \text{cm}^2$)	X (%)
0	23	1.74E-05	0.85	94	1.37E-05	0.83	2.83	0.45
1	20	8.35E-06	0.88	63	6.02E-06	0.84	2.90	0.23
7	21	4.80E-06	0.92	49	8.55E-06	0.81	4.64	0.22
14	20	1.04E-05	0.84	77	2.95E-06	0.88	4.60	0.77

The resistance values, R_B , associated with the inner barrier layer, increases with the immersion days and are significantly larger than the values associated with the outer porous layer, R_{OP} , which remains nearly constant, as Table 4.1 shows. These results indicate that the protection provided by the passive layer is predominantly due to the inner barrier layer, as also observed in other titanium alloys [93, 95, 96].

The Ohmic resistance (R_e), estimated from the proposed model, varies between 20-23 $\Omega \cdot \text{cm}^2$ during the immersion days, and is in a good agreement with the one deduced from the high-frequency limit (20-30 $\Omega \cdot \text{cm}^2$) from the Bode diagrams (Figure 4.1).

From the values of CPE (Q and α), R_e , and R_{OP} , R_B and using the Brug equation (Equation 4.2), it is possible to obtain the values of the effective capacitance of the passive layer, considering the titanium surface composed by an outer porous layer and an inner compact layer.

$$C_{eff} = Q^{1/\alpha} (R_e^{-1} + R_{OP,B}^{-1})^{(\alpha-1)/\alpha} \quad (4.2)$$

The C_{eff} calculated from the values listed in Table 4.1 for the different immersion periods are ranged from 18 to 9 $\mu\text{F} \cdot \text{cm}^{-2}$ for the porous layer and from 12 to 3 $\mu\text{F} \cdot \text{cm}^{-2}$ for the inner compact layer, values similar to the observed in the AISI 316L stainless steel immersed in physiological solutions [97, 98]. This capacitance reduction is associated with an increase in the passive layer thickness [75, 99]. Traditionally, low capacitance values are associated with nobler electrochemical behavior [75, 93, 99].

The passive film thickness of the inner compact layer can be calculated from Equation 4.3, which is valid for the parallel-plate capacitor model of a homogeneous oxide layer, associating the overall effective capacitance to the protective oxide layer:

$$d_{ox} = \frac{\varepsilon_r \varepsilon_0}{C_{ox}} \quad (4.3)$$

Where ε_0 is the vacuum permittivity ($8.85 \times 10^{-14} \text{ F} \cdot \text{cm}^{-1}$) and ε_r is the relative dielectric constant of the material (taken as $\varepsilon_r = 100$, the dielectric constant of TiO_2 [75]). Using this information, it was possible to obtain an approximation of the passive layer thickness for the different immersion days. The passive layer grew with the increase of the immersion days, initially, from 7 nm for non-immersed samples, to 27 nm after 14 days (Figure 4.5).

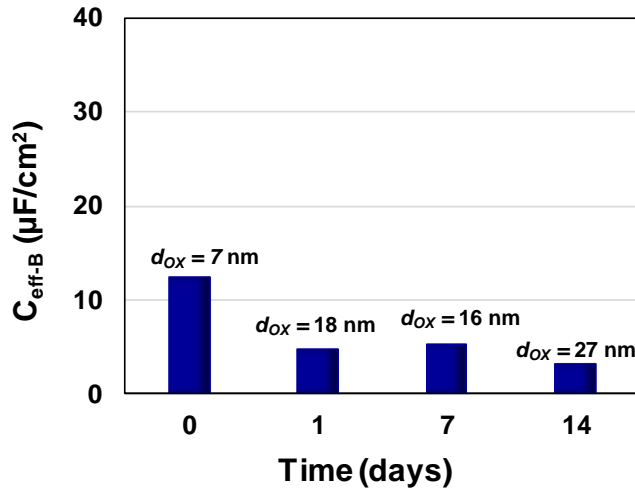


Figure 4.5 Effective capacitances and thickness evolution of the passive inner layer for untreated TMZF samples during different immersion days in SBF solution at 37 °C.

The agreement between experimental and simulated results indicates that the experimental results are well fitted by the proposed equivalent circuit. Error values (X) lower than 1% were found during these EIS data treatments, indicating a satisfactory fitting level (Table 4.1) [75].

4.2 EIS measurements over TMZF samples treated with HCl and NaOH

A similar study to that conducted in section 4.1 was carried out on the CST samples. Electrochemical impedance spectroscopic measurements were employed to investigate the changes on the chemically treated surface after different immersion time in SBF solution (0, 1, 7 and 14 days).

The effect of the immersion periods through impedance curves for the acid and alkali treated samples is presented in Figure 4.6. The evolution of the overall impedance in the Nyquist plots displays semicircles arc flattened at low frequencies. The radius of these arcs decreases with the increase of immersion time (Figure 4.6 c).

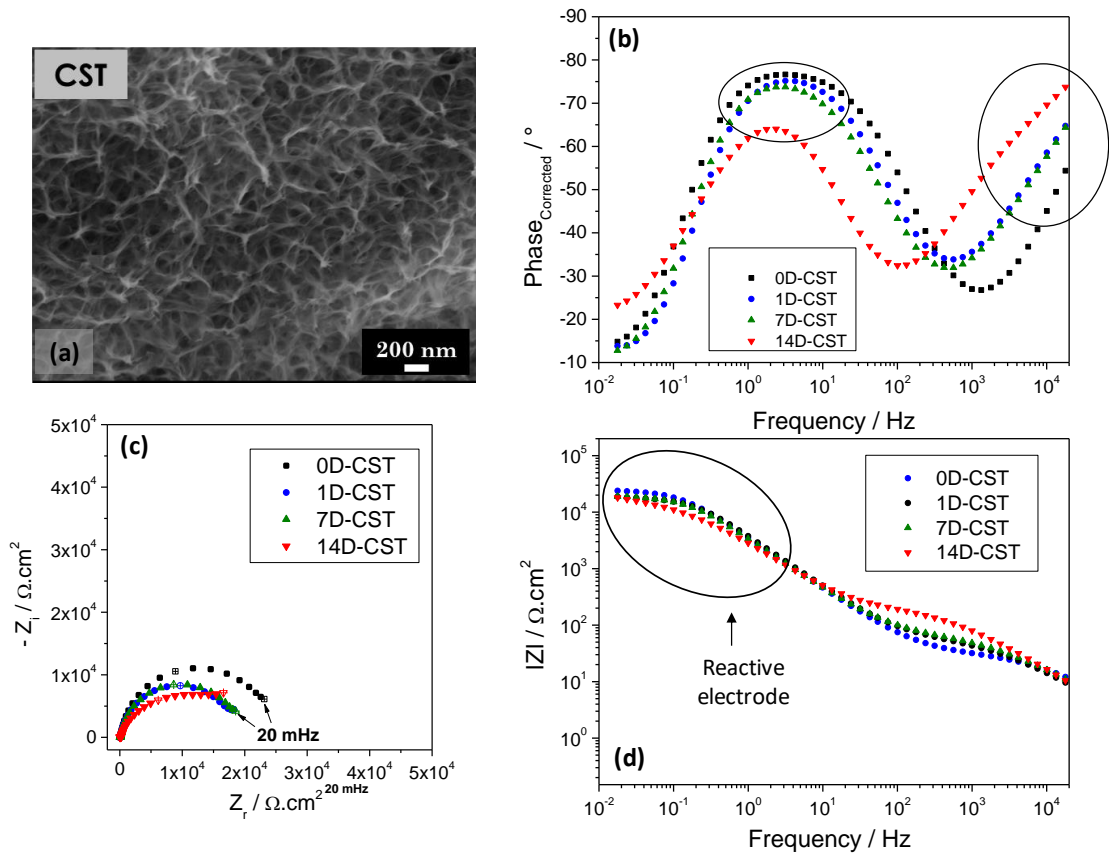


Figure 4.6 a) SEM micrographs of CST TMZF samples before the immersion periods; Schematic representation of the impedance results for CST samples immersed in SBF at 37 °C during the different periods (0, 1, 7, and 14 days denoted as 0D, 1D, 7D and 14D respectively): b) Corrected-phase angle; c) Nyquist plot and d) Corrected-magnitude of the impedance.

Figure 4.6 (b and d) shows the Bode curves of treated TMZF samples soaked in SBF for different immersion times. Samples without previous immersion or on zero days (0D), exhibit a progressive increase of the phase angle from high to middle frequencies, with a variation of the phase angle from -54° to -27°. After that, the phase achieved a minimum value of -74° in the frequencies between 10⁰ Hz – 10¹ Hz and remained approximately constant. The behavior mentioned above can be associated with the sodium titanate layer formed on the substrate during the CST; this layer is considered low capacitive owing to its porous constitution. Then, reducing ever more the frequencies is possible to observe a new increment of the phase angle until reaching a value of approximately -15°.

A uniform variation in the phase angle curves is observed with the increase of immersion periods. At intermediate frequencies, it was observed a slightly reduction in the phase angle in samples 1 and 7 days of immersion, compared with samples

without previous immersion. This behavior was associated with the precipitation and growth of the first nucleus of calcium phosphate on the sample surface. In the same region, after 14 days of immersion, the plateau appeared in a higher phase angle around -62°. After 1 and 7 days of immersion, the phase angle increase with the reduction in frequency attaining a value around -12° at the lowest frequency. Similar to the behavior observed in 0 days. However, after 14 days the angle achieved a lower value, -23°, at the same frequency.

Similar behavior to the above mentioned has been attributed to the presence of a porous layer accompanied by the formation of a new layer. The porous layer can be associated with the gel sodium titanate layer, and the formation of the new layer, to the hydroxyapatite layer grown [84].

Hodgson et al. [100] associated the interaction between the ions present in the physiological solution and the electrode surface with a change in the phase angle at the frequencies region in the Bode curves. Relating these variations to a physical change in the sodium titanate layer present on the CST samples.

As shown in Figure 4.1d, untreated TMZF samples exhibited a performance similar to a blocking electrode, characterized by a slope value of -1 at all frequency. However, independent of the immersion period, the CST samples behave differently and show plots with magnitude smaller than unity at the lower frequency region (Figure 4.6d). Indicating a behavior typical of a more reactive electrode [59].

The modified Bode representations for the CST sample are shown in Figure 4.6b and d, Using the corrected-phase plot (Figure 4.6b), two relaxation processes or time constants present during the impedance test are possible to be determined. It can be observed that the two constant phase angle regions for the chemically treated samples are smaller compared to the constant region of the untreated titanium alloy. This short distribution of the time constants indicates a less protective and homogeneous surface.

Effective CPE exponent (α_{eff}) plot is used for a better characterization of the relaxation process occurring over the surface of chemically treated samples. Figure 4.7 shows a similar behavior at high and intermediated frequencies on the corrected-phase plot. Nevertheless, this plot shows an additional bump at low frequencies (10^{-2} Hz to 10^{-1} Hz), This interesting behavior was associated with an extra relaxation process.

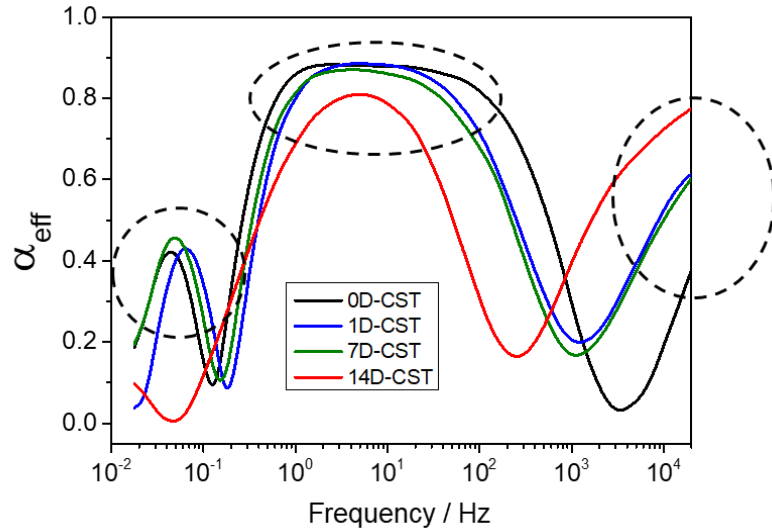


Figure 4.7 Evolution of α_{eff} versus frequency, of the CST TMZF samples for the different immersion periods (0, 1, 7, and 14 days denoted as 0D, 1D, 7D and 14D respectively) in SBF solution at 37 °C.

According to the information obtained from the α_{eff} plot, this third relaxation process is attributed to a diffusion phenomenon, which is typically revealed during low-frequency disturbances during the impedance measurements [101]. Initially, it was thought to use a Warburg element to model this phenomenon, due to values of the effective alpha close to 0.5. However, the values of the obtained parameters were outliers and the results were not satisfactory due to high fitting errors. Therefore, an extra CPE element was indicated, related to a general diffusion element.

Over the CST is expected to find three relaxation processes acting during the impedance test, one more than the two found in the untreated samples, and it is associated with the external sodium titanate layer created during the chemical treatment with HCl and NaOH.

As mentioned above and confirmed by the information obtained from the Bode phase and the α_{eff} plots, the EEC for the CST TMZF samples shall be composed of three relaxation processes. The circuit is shown in Figure 4.8 and provides a good representation for systems with a compact inner layer, an intermediate porous oxide layer and an outer gel sodium titanate layer.

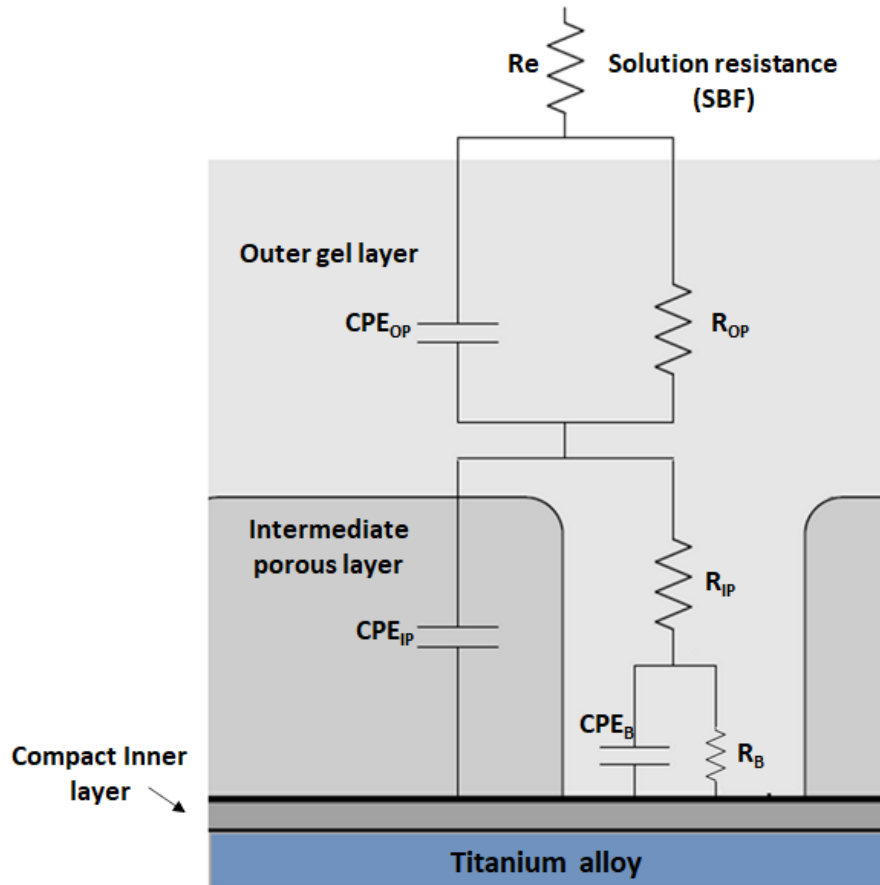


Figure 4.8 Equivalent circuit for CST TMZF samples (Adapted from [59]).

In the electrical circuit of Figure 4.8, R_e represents the electrolyte resistance (SBF solution), R_{OP} and CPE_{OP} represent the resistances and the capacitances of the outer porous layer, associated with the gel sodium titanate layer dissolution and the HAp growth. R_{IP} and R_B are the resistances of the intermediate porous oxide layer and the inner barrier layers, and the CPE_{IP} and CPE_B are used to designate the capacitances of the outer porous layer and the compact inner layer, respectively.

The Nyquist representation of the fitting EIS data for CST samples is shown in Figure 4.9, and the simulated curves were modeled through of the EEC presented in Figure 4.8. The errors measured (χ) for the experimental and simulated data were lower than 1% independently of the immersion period, indicating a satisfactory fitting level.

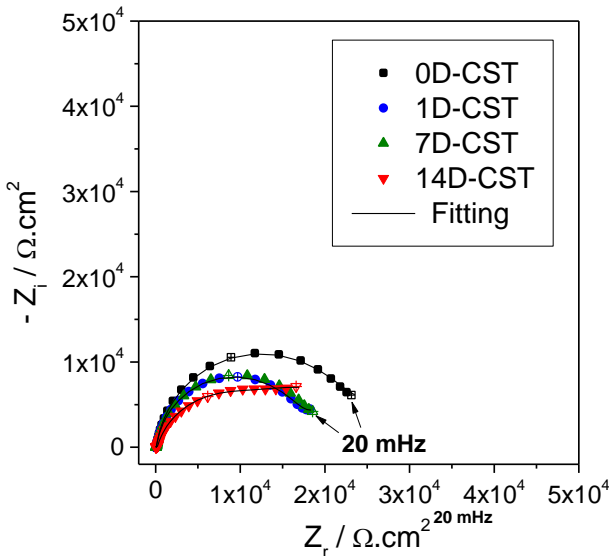


Figure 4.9 Nyquist plots of experimental and simulated results obtained through the Simad software, for the CST samples immersed in SBF at 37 °C during the different periods (0, 1, 7, and 14 days denoted as 0D, 1D, 7D and 14D respectively).

The electrochemical impedance parameters as resistance, capacitance and α values of the porous and barrier layers obtained from the equivalent circuit are displayed in Table 4.2.

Table 4.2 Electrical impedance parameters obtained by fitting the experimental results of CST samples immersed in SBF at 37 °C for the different periods 0, 1, 7 and 14 days.

Immersion Days	R_e ($\Omega \cdot \text{cm}^2$)	Q_{OP} ($\Omega s^{-\alpha} \cdot \text{cm}^2$)	α_{OP}	R_{OP} ($\Omega \cdot \text{cm}^2$)	Q_{IP} ($\Omega s^{-\alpha} \cdot \text{cm}^2$)	α_{IP}	R_{IP} ($\Omega \cdot \text{cm}^2$)	Q_B ($\Omega s^{-\alpha} \cdot \text{cm}^2$)	α_B	R_B ($\Omega \cdot \text{cm}^2$)	C_{effB} ($\mu\text{F}/\text{cm}^2$)	X (%)
0	25	8.61 E-04	0.57	35.05	3.31 E-06	0.71	819	1.69 E-05	0.91	48562	32	0.39
1	21	2.79 E-04	0.55	50.14	6.66 E-06	0.72	283	1.39 E-05	0.95	16366	29	0.26
7	24	3.30 E-04	0.53	112.33	9.28 E-06	0.60	283	2.46 E-05	0.84	11916	22	0.71
14	23	1.45 E-04	0.80	178.97	4.08 E-06	0.76	155	1.81 E-05	0.85	11513	18	0.82

With the increase of the immersion days from 0 to 7 days, the Q_{OP} values decreased showing a dissolution process of the gel sodium titanate layer. This might be associated with the interaction between the ions present in the physiological solution and the ions in the titanate layer [86].

Between 7 and 14 days in the SBF a mature HAp layer arises from the complete dissolution of the sodium titanate layer, which acts as a diffusion barrier corroborate by the higher α_{OP} value at 14 days. This behavior is confirmed in the

Nyquist spectrum at 14 days of immersion (Figure 4.9), where it is possible to see a semicircle arc smoothed at low frequencies [86].

The resistance R_B decreased continuously, and at the same time, the R_{OP} increased with the immersion days, attaining a constant value between 7 and 14 days. This behavior can be associated with the continuous dissolution and formation processes of the barrier layer and the HAp layer, respectively [86].

Previous investigations employing Auger emission spectroscopy confirmed the presence of an oxide film between the sodium titanate layer and the titanium surface [102, 103]. Through the impedance results and employing the equation 4.2 and the fitting results C_{effB} from Table 4.2, it is possible to calculate an approximation value of the titanium oxide inner layer thickness, whose values are summarized in Figure 4.10.

CST samples without immersion in SBF showed a thinner compact layer compared with the untreated samples in the same condition. During acid etching with HCl, the thin passive titanium oxide layer dissolves to form TiH_2 ; immediately after, in contact with air moisture, a new titanium oxide layer is formed. However, this layer is thinner than the initial one [31, 104, 105]. Similar to the untreated samples, the passive layer on the CST samples grew with the increase of the immersion days (Figure 4.10).

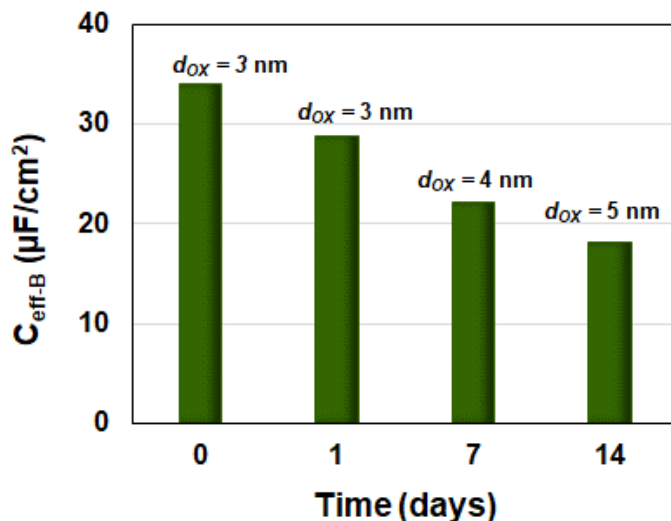


Figure 4.10 Effective capacitance and thickness evolution of the passive inner layer for CST TMZF samples during different immersion days at 37 °C in SBF solution.

4.3 EIS measurements over anodized TMZF samples

Electrochemical impedance spectroscopic results were employed to investigate the changes in two different anodized systems (nanotubes and

nanostructures (surfaces) after different immersion periods in SBF solution (0, 1, 7 and 14 days).

High-resolution SEM image in Figure 4.11 shows the surface condition of the TMZF samples with nanotubes before the immersion periods. Initially, it was analyzed the electrochemical evolution of the nanotube samples through the Nyquist plots and the Bode diagrams shown in Figure 4.11 (b-d).

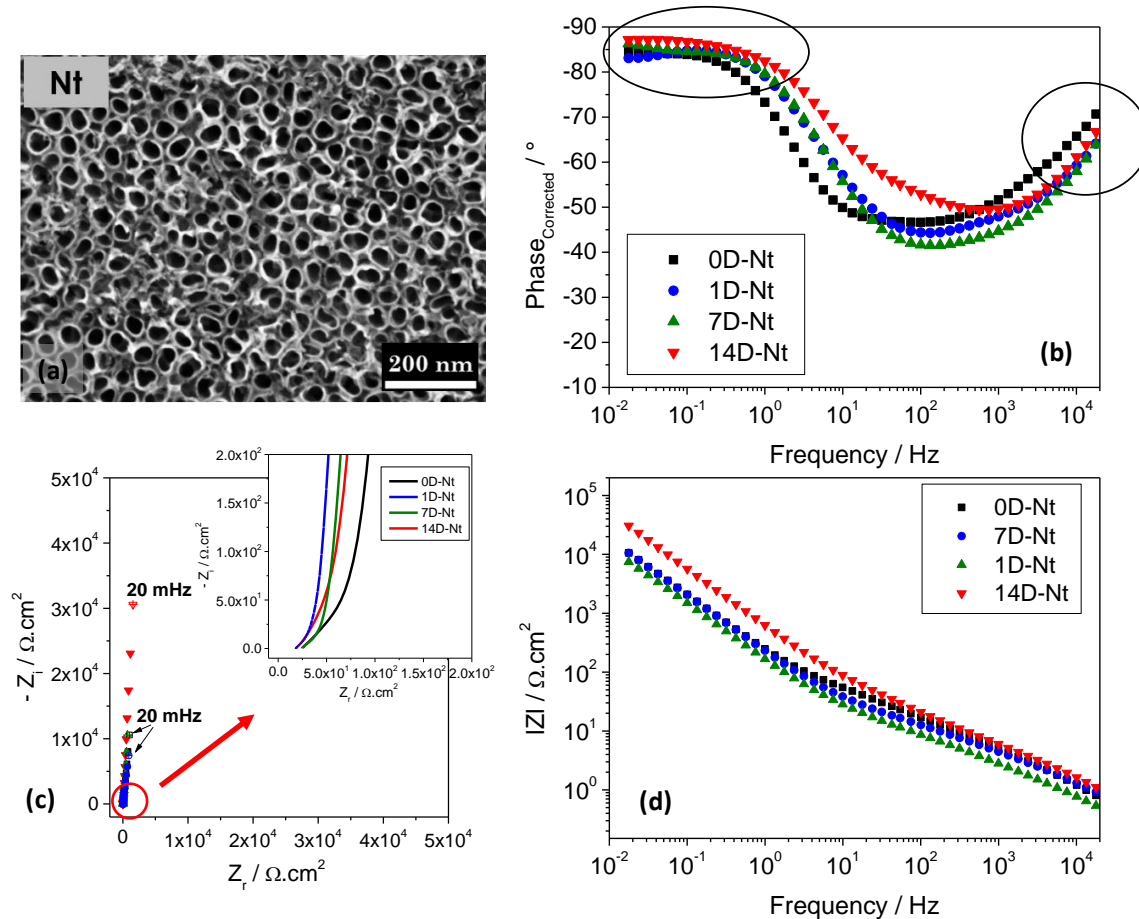


Figure 4.11 a) SEM micrographs of nanotubes TMZF sample before the immersion periods; impedance results for nanotubes samples immersed in SBF at 37 °C for the different periods (0, 1, 7, and 14 days denoted as 0D, 1D, 7D and 14D respectively): b) Corrected-phase angle; c) Nyquist plot and d) Corrected-magnitude of the impedance.

Observation of the Nyquist diagrams reveals that regardless of the immersion time studied, the shape of the CST impedance spectra (arc) is typical of a reactive system (section 4.2), whereas in Figure 4.11(c) the samples with nanotubes are apparently rather purely capacitive (straight line), or at least pseudocapacitive (inclined straight line). This means that the faradaic reactions are very limited [59].

These anodized samples showed a particular behavior in the Nyquist diagram, observing an inclined straight line or an arc at high frequencies range (Enlarged region Figure 4.11c) and a capacitive or pseudocapacitive branch at low frequencies. This is a typical characteristic of a porous electrode, as will be demonstrated in section 4.4.

The corrected Bode phase angle plots of TMZF samples with nanotubes immersed in SBF are shown in Figure 4.11(b). At low and middle frequencies (10^{-2} Hz to 10^1 Hz), the phase angle remains almost constant, presented with values approaching -90° which is the typical capacitive behavior of a compact oxide film. The protective character of this film seemed to be enhanced with increased immersion, indicating a more protective behavior after 14 days.

With the further increase in frequency, the phase angle progressively increased to the highest value close to -45° and decreased again at the higher frequencies zone. Thus, two relaxation processes or time constants were identified from the Bode phase angle plot. One of them is in the range of 10^{-2} Hz to 10^1 Hz and the second one at a high frequency around to 10^4 Hz Figure 4.11(b).

Figure 4.11(d), shows the modulus of impedance for nanotubes samples, showing a similar behavior for all the immersion days, separated by two distinct zones. Between low and middle-frequency (10^{-2} Hz – 10^1 Hz), the curves exhibited a constant linear slope close -1, less inclined than the slope at high-frequency, around to -0.5. This behavior is characteristic of capacitive surfaces [84].

Figure 4.12 shows the evolution of the Nyquist plots and the Bode diagrams with immersion time in the SBF solution, for the TMZF samples with nanopores. Additionally, in Figure 4.12 (a) is possible to see the surface condition of the nanopores TMZF samples before the immersion periods.

Similar to the nanotubes, nanopores specimens show a capacitive or pseudocapacitive behavior, which was observed in the Nyquist diagram independently of the immersion time studied (Figure 4.12 (c)). These curves are typically observed in low reactive porous systems.

Observing the enlarged region in Figure 4.12 (c), the nanopores samples showed the same behavior of a porous film over a conductive substrate [106], with a straight line at $\sim 45^\circ$ at high frequencies, with a capacitive straight line corresponding to the capacitance of the pore wall [107].

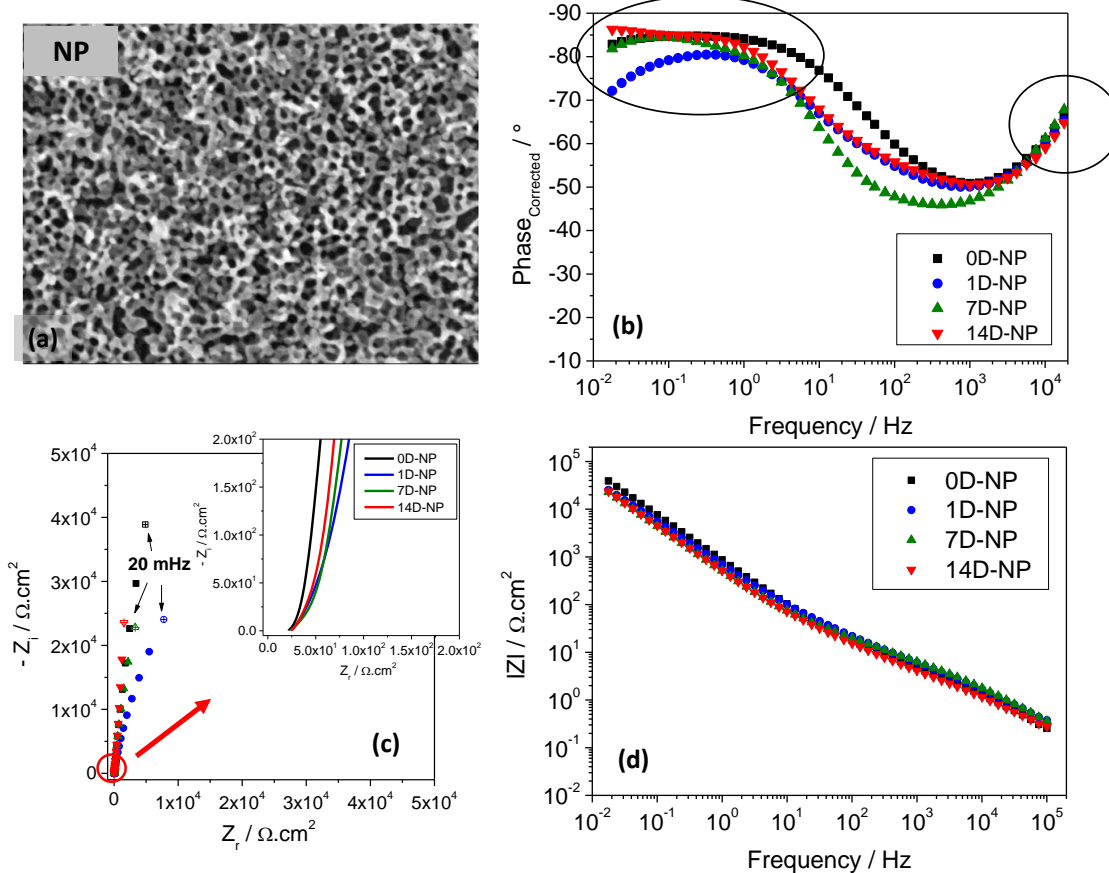


Figure 4.12 a) SEM micrographs of nanopores TMZF sample before the immersion periods; Schematic representation of the impedance results for untreated samples immersed in SBF at 37 °C during the different periods (0, 1, 7, and 14 days denoted as 0D, 1D, 7D and 14D respectively): b) Corrected-phase angle; c) Nyquist plot and d) Corrected-magnitude of the impedance.

The corrected Bode phase representations of nanopores TMZF samples immersed in SBF are shown in Figure 4.12 (b). Here, two relaxation processes are present during the impedance test. One of them in the range of 10⁻² Hz to 10¹ Hz in values approaching -90° and the second one in high frequency around to 10⁴ Hz.

Figure 4.12 (d) shows the Bode impedance plot of TMZF samples anodized with nanopores and after immersion periods in the SBF solution. Independent of the soaking time, all samples showed a stable behavior, characterized by two slopes with a slight tilt between them. One of them, is at the low-intermediary frequency region (10⁻² Hz to 10¹ Hz) and the second one, between the intermediary and high frequency (10¹ Hz – 10⁴ Hz). This behavior is similar to the one observed by nanotubes.

Graphical representations of the α_{eff} (Figure 4.13) were built to determine the number of time constants present during the impedance tests to help us choose the

more appropriate EEC system to fit the result of the anodized samples (Nt and NP). Figure 4.13 shows two-time constants for the Nt and NP samples whatever the immersion time.

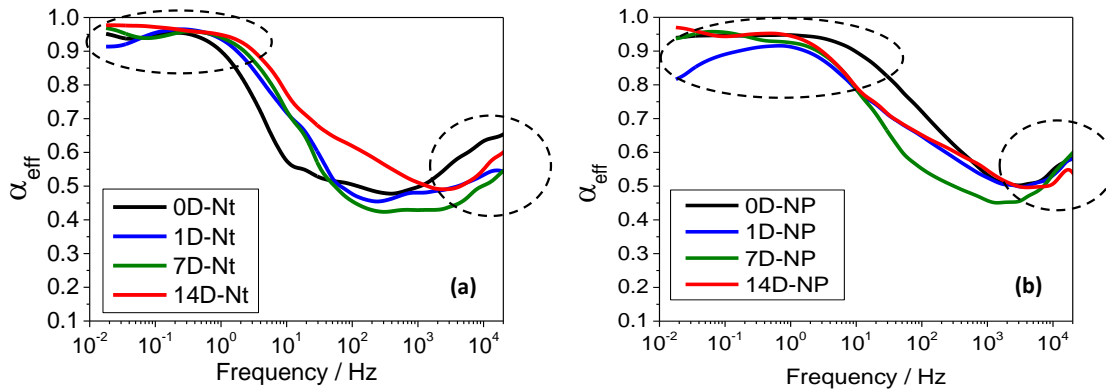


Figure 4.13 Evolution of α_{eff} with the frequency of the anodized TMZF samples for the different immersion periods (0, 1, 7, and 14 days denoted as 0D, 1D, 7D and 14D respectively) in SBF at 37 °C: a) nanotubes and b) nanopores.

According to the information obtained through the Bode phase and the α_{eff} plots, initially, the anodized samples were fitted considering a similar electrical circuit as the one used for untreated samples, Figure 4.2b, which is related to passive film with bi-layered microstructure. However the fitting results for both anodized conditions were not satisfactory as already mentioned in different works [75, 108]; the adjustment errors are large and the values of the parameters obtained are outliers.

4.3.1 Analysis of the electrical models proposed in the literature

Various equivalent electrical circuits have been suggested to model the impedance response of anodized titanium surfaces [60, 109–113]. The first explanation for this may lie in the diversity of experimental conditions, for example, the temperature, the position of the electrodes, the nature of the electrolyte, etc. In the case of anodized samples, the measurement can also be very sensitive to the topography and the crystal structure of the surface, and also to the ambient luminosity. Indeed, TiO_2 being a photosensitive semiconductor, its electrical response depends greatly on light [114]. As mentioned in Chapter II, in this thesis, the impedance measurements were conducted in a dark environment to reproduce the conditions of the human body.

Figure 4.14 presents the electrical circuits with two relaxation processes most frequently found in the literature to model the impedance response of the anodized titanium surfaces. Model (a) shows a circuit with two time constants in series widely used. In this model, R_o and Q_o are respectively attributed to the resistance and the

pseudo-capacity of the external porous layer while the elements R_b and Q_b model the internal barrier layer [110, 111].

On the other hand, a model with three time constants combining cascade and parallel sequences is introduced [60, 109], where Q_o represents the capacitive contribution of the nanotubes walls, R_{ep} is the resistance of the electrolyte in the pore, R_i and Q_i are associated with the interface at the bottom of the pore and finally Q_b and R_b model the barrier layer (Figure 4.14 b).

Finally, some authors have also proposed to introduce an element of Warburg (W) into their electrical circuits associating it with a diffusion impedance as reported in the models (c) and (d) [112, 113]; however, the experimental impedance results for nanotubes and nanopores samples analyzed in the present thesis did not show characteristics of a Warburg element.

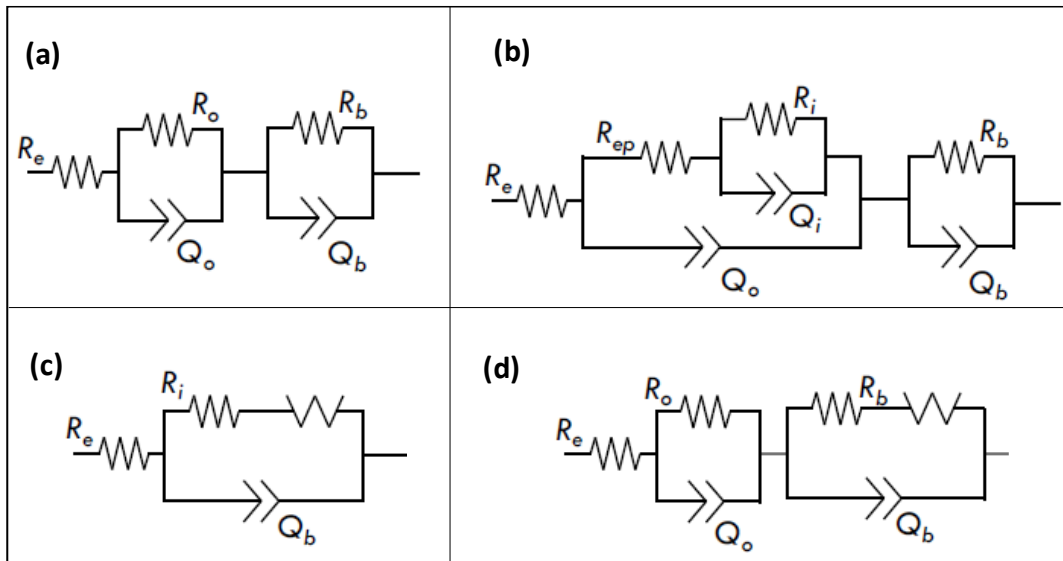


Figure 4.14 Graphical representation of the EEC most frequently used for modeling the impedance results of anodized titanium samples.

In most of the publications cited above, the Nyquist representation presents spectrum in the form of a semicircle (or flattened semicircle, or portion of a semicircle), which is the typical signature of EEC based on R/Q or R/C arrangements. Therefore, this observation justifies the use of EEC like those presented in Figure 4.14 to model the experimental results of the anodized samples.

However, in this thesis work, the Nyquist representations of nanotubes and nanopores are not characterized by semicircles but rather by a line inclined at low frequencies which tends towards infinity and a portion distorted to high frequencies inclined by almost 45° (as presented in Figure 4.11 and Figure 4.12).

Therefore, modeling the impedance results of this work with classical equivalent circuits as those mentioned above does not seem relevant. Moreover, the preliminary adjustment tests carried out with the circuits presented in Figure 4.14 were unsatisfactory; the adjustment errors were large (higher than 10% in some cases) and the values of the parameters obtained were atypical.

Thereby, a new model based on a non-classical theory is employed to model the impedance response of anodized TMZF samples in SBF. As mentioned in the Nyquist representations for nanotubes and nanopores samples, these surfaces show similar behavior as the porous electrodes. Similar behavior was described by De Levie [115, 116]. This author modeled the impedance results of a porous electrode through an alternative model describe as the Transmission Line (TL) model.

After the theory described by De Levie, some authors as Bisquert et al. have already shown the TL applicability for the modeling of porous TiO₂ deposits made for solar applications [117, 118]. The model has also been used by other groups to analyze porous film impedance measurements of TiO₂ for photosensitive pigment solar cells [119, 120].

Recently anodized titanium surfaces have been studied through impedance using transmission line models [36, 108]. These studies have shown excellent compatibility between experimental and modeling results, as well as, consistency in the values of the parameters obtained. In this way, the rest of this chapter will be dedicated to the study of the porous electrodes using the TL model, applied to nanotubes and nanopores in a physiological environment.

4.3.2 Porous electrode model and transmission line

TL models owe their origin and name to the development of mathematical theory for the performance of submarine telegraph lines. William Thompson showed that an impulse would broaden by the time it reached the other end of the cable, requiring a significant reduction in transmission speed to resolve the pulses. He considered that, because the capacitive coupling would be to the seawater adjacent to the cable, the advent of submarine cables required a more careful analysis of the problem [59].

Thomson modeled a submerged telegraph line as a conducting wire of radius r_1 separated from a conductive ocean by an insulating concentric cylinder of radius r_2 (Figure 4.15), and expressed the capacitance per unit length of the coated wire by:

$$C_{wire} = \frac{2\pi\epsilon\epsilon_0}{\ln(r_2/r_1)} \quad (4.4)$$

Where ϵ is the dielectric constant, and ϵ_0 is the permittivity of vacuum with a value of $\epsilon_0 = 8.8542 \times 10^{-14}$ F/cm.

Heaviside extended the theory for telegraphy expressing the problem in frequency rather than time domain and including the effect of inductance per unit length of the cable. He later generalized this analysis in terms of transmission lines [59].

An equivalent circuit of a transmission line is given in Figure 4.15 (b), where Z_1 represents the resistance of the wire with units $\Omega \cdot \text{cm}$ and Z_2 represents the capacitive coupling through the insulating material and the seawater. It is an impedance by a unit length, with unit Ω/cm .

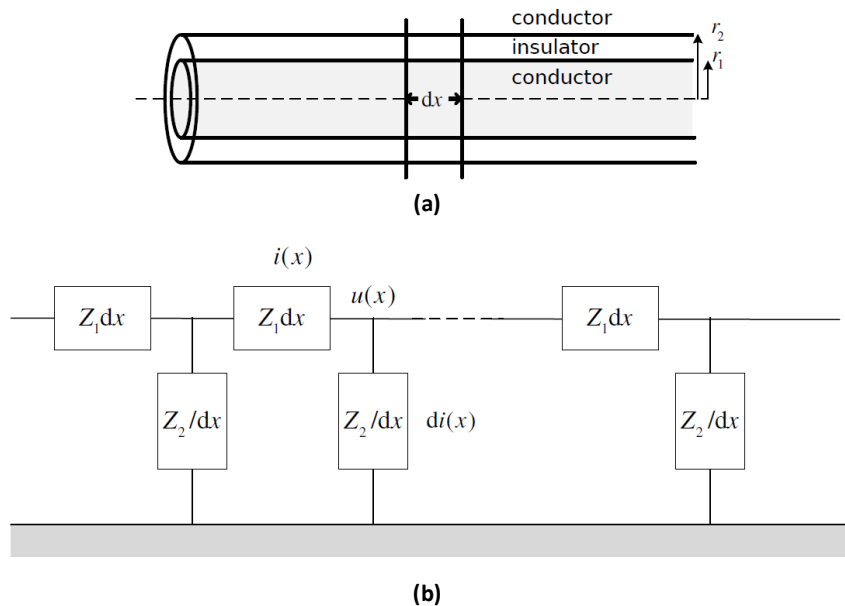


Figure 4.15 Schematic representation of the telegraph cable considered by Thomson and Heaviside: a) representation showing a differential element with length dx and b) elementary components of a transmission line. For system shown in a, $Z_1 = R_0$ and $Z_2 = 1/j\omega C_{\text{wire}}$ [59].

Porous electrodes are used in numerous industrial applications because they have the advantage of an increased effective active area. Figure 4.16 (a) illustrates the random structure of the porous electrode. However, the porous electrode is usually represented by the simplified single-pore model shown in Figure 4.16 (b), in which pores are assumed to have a cylindrical shape with a length ℓ and a radius r .

Figure 4.16 (b) displays a graphical representation of the transmission line model, where R_0 is the solution resistance for the pore length, with units of $\Omega \cdot \text{cm}^{-1}$,

Z_0 is the interfacial impedance along of the pore length, with units of $\Omega \cdot \text{cm}$, expressed in function of the pore radius as:

$$R_0 = \frac{\rho}{\pi r^2} \quad (4.5)$$

And

$$Z_0 = \frac{Z_{eq}}{2\pi r} \quad (4.6)$$

Z_{eq} is the interfacial impedance, and ρ is the electrolyte resistivity. With the restrictive assumption that Z_0 and R_0 are independent of the distance x , de Levie calculated analytically the impedance of one pore to be [121]:

$$Z_{pore} = (R_0 Z_0)^{1/2} \coth(\ell \sqrt{\frac{R_0}{Z_0}}) \quad (4.7)$$

Finally, The impedance of the overall electrode is obtained by accounting for the ensemble of n pores and for the electrolyte resistance outside the pore, i.e.,

$$Z = R_e + \frac{Z_{pore}}{n} \quad (4.8)$$

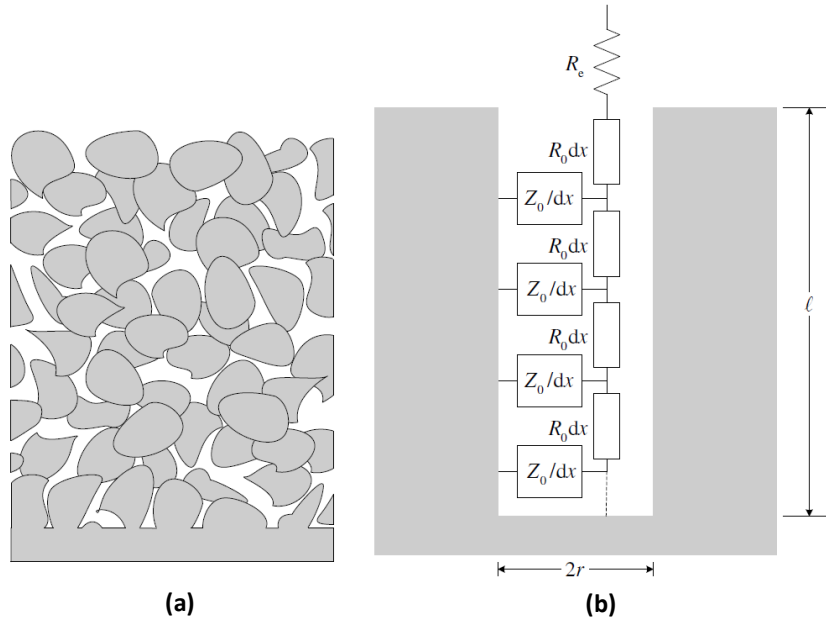


Figure 4.16 Schematic representations of a porous electrode: a) porous electrode with irregular channels between particles of electrode material and b) transmission line inside a cylindrical pore [59].

Subsequently, to explain the impedance behavior of non-ideal porous electrodes Bisquert [106] studied and developed a generalized model involving the concept of the transmission line, using as an important reference point, the work developed by De Levie [121]. Bisquert assumed a configuration that consists of a

porous electroactive film deposited on a conducting substrate and dipped in an electrolyte, as is represented in Figure 4.17.

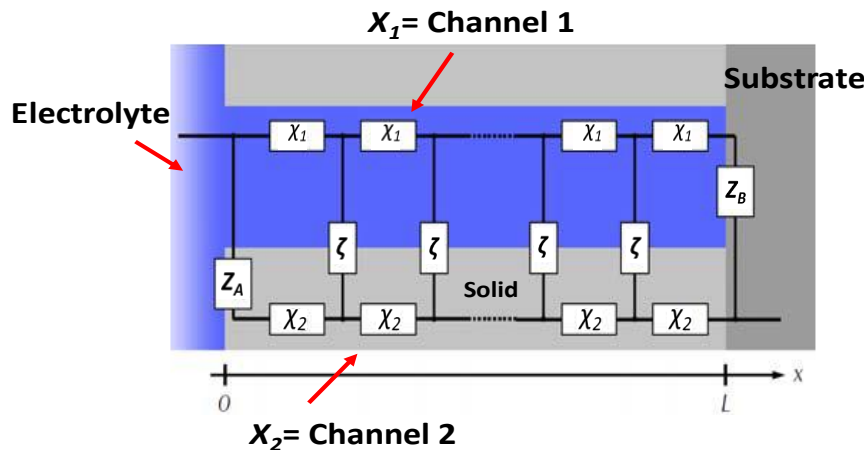


Figure 4.17 Schematic illustration of the inner region ($0 < x < L$) of a porous electrode divide by a porous film deposited on a conductive substrate. ζ represents the interfacial impedance disposed over the entire porous surface, Z_A is correlated with the impedance of the interface external solution | solid and Z_B is used to describe the interface internal solution | substrate. (adapted from [106]).

Thus, the electrode region is viewed as a mixture of two phases that conduct different species, electronic and ionic, and where the macroscopic boundaries are impermeable to different species. As the porous structure implies a distribution of the current in different directions of space [117], it cannot be modeled by a classic arrangement in series or in parallel of R-L-C elements. The equivalent type of circuit that may apply in this case is a transmission line, as shown in Figure 4.17.

This TL model is described in Figure 4.17, with the equivalent circuit modeling the ac behavior of the film. It is considered that exists a freely ionic exchanged between the species into the pores and the bulk solution at the top of the pores ($X = 0$). Besides, the electronic charge carrier in the nanotubes walls can be interchanged freely at the interface with the titanium substrate ($X = L$).

In this model, faradaic currents and polarization may occur at the inner surface separating the two phases. Additionally, it is assumed that the elements in the distributed equivalent circuit are homogeneous, independent of the position normal to the plane of the electrode.

Elements X_1 and X_2 describe the local ohmic drop at each point of the transport channels, depending on media conductivity and more generally on transport properties. The element ζ represents the interfacial impedance (internal solution | porous solid). Z_A and Z_B are associated with boundary conditions, more

precisely, Z_A is the impedance coming from the interface, external solution | porous solid, while Z_B describes the interface, internal solution | substrate at the bottom of the pores.

The quantities X_1 and X_2 are impedances per unit length ($\Omega \cdot \text{cm}^{-1}$) corresponding to the whole electrode area, and ζ is an impedance-length ($\Omega \cdot \text{cm}$) also for the whole electrode area. The full analytical expression for such a transmission line is [106]:

$$\begin{aligned} Z = & \frac{1}{X_1 + X_2} \left[\lambda(X_1 + X_2)S_\lambda + (Z_A + Z_B)C_\lambda + \frac{1}{\lambda(X_1 + X_2)} Z_A Z_B \lambda \right]^{-1} \cdot \left(L\lambda X_1 X_2 (X_1 + \right. \\ & X_2) S_\lambda + X_1 [\lambda X_1 S_\lambda + L X_2 C_\lambda] Z_A + X_2 [\lambda X_2 S_\lambda + L X_1 C_\lambda] Z_B + \frac{1}{X_1 + X_2} \left[2 X_1 X_2 + \right. \\ & \left. \left. (X_1^2 + X_2^2) C_\lambda + \frac{L}{\lambda} X_1 X_2 S_\lambda \right] Z_A Z_B \right] \end{aligned} \quad (4.9)$$

Where the notations $C_\lambda = \cosh(L/\lambda)$, $S_\lambda = \sinh(L/\lambda)$, and $\lambda = [\zeta/(X_1 + X_2)]^{1/2}$ have been used.

This model is very versatile and, depending on the particular case, can be adapted to attend and simulated the different surface conditions. In this way, the TL model for anodized TMZF samples will be described below.

4.3.3 Employment of the transmission line model to the case of anodized TMZF samples in SBF

The TL model suggested in this study to describe the impedance behavior of anodized titanium samples in SBF was applied to two different surface topographies, nanotubes and nanopores.

The TL model illustrated in Figure 4.17 can be useful for modeling different microstructures and geometries regarding different types of hypotheses. For instance, the geometry indicated above of long cylinders over the substrate or permeable film with irregular geometries or even fine semiconducting particles embedded in a matrix [117]. Additionally, it is necessary to remark that this model involves the volume processes distributed over the whole electrode surface.

Hereafter, it is assumed that quantities X_1 , X_2 , and ζ are independent of position, meaning that these quantities are only functions of frequency. Additionally, a limit condition for the charge carriers was established, for example, when the electrons reach the external edge of the solid part at $x = 0$, and when the ions find a wall at $x = L$. Typically, those hypotheses are defined by the premise that the electric current disappears at the outer part of the porous layer and the ionic current at the

end of the liquid channel. This restriction provides a considerable simplification of analysis.

The analysis of the Nyquist diagrams in Figure 4.11 (c) and Figure 4.12 (c) reveals that the two morphologies, nanotubes and nanopores, present a distorted branch at high frequencies and an inclined line at low frequencies. The high-frequency distortion could come from the presence of an influent Z_B pore bottom impedance at the end of a shorted channel or an anomalous transport phenomenon in the resistive channel, e.g., the semiconductor behavior of the TiO₂ layer [117].

In order to build a model in agreement with these observations three hypotheses were defined. The first, consists of admitting that the electrolyte contained in the pores is represented by the resistive channel, X_1 , which is modeled by a distributed resistance:

$$X_1 = R_1 \quad (4.10)$$

And thus, the total resistance ($\Omega \cdot \text{cm}$) distributed in the resistive channel and normalized by the area is given by:

$$R_1 = L \cdot r_1 \quad (4.11)$$

In the second hypothesis was adopted the anomalous transport formalism to model the channel 2 (solid phase of TiO₂). Thus, X_2 is represented by a parallel arrangement of r_2 and q_2 . Indeed, TiO₂ in the anatase form can be assimilated to a moderately doped semiconductor [122]. It is then expected that its crossover frequency be lower than the range of frequencies investigated by impedance in this work. The expression of impedance that describes this behavior is:

$$X_2 = \frac{1}{1 + r_2 q_2 (iw)^\beta} \quad (4.12)$$

It is pointed out that Equation (4.12) represents an unique transport mechanism taking place in the channel 2 and not the association of a charge transfer phenomenon in parallel with a capacitive phenomenon, as it is normally the case during analysis of impedance results [75, 123].

In the transition region between the internal solution and the pore wall, a potential difference is maintained and is modeled by an interfacial capacitance. Therefore, the third hypothesis proposed that the capacitance of the polarizable interface depends on the frequency and is modeled by a constant phase element or CPE [124, 125].

$$\zeta = \frac{1}{q_3} (iw)^{-n} \quad (4.13)$$

Where q_3 is a constant with dimension $F \cdot s^{n-1}$ and the exponent n can be any number in the range $0 < n < 1$. The impedance of Equation 4.13 consists on a tilted

straight line in the complex plot, and the total pseudocapacitance (Q_3) describing the interface is defined by:

$$Q_3 = L \cdot q_3 \quad (4.14)$$

Where L is the length of the pores (in cm), associated with the thickness of the nanotubes and nanopores layers.

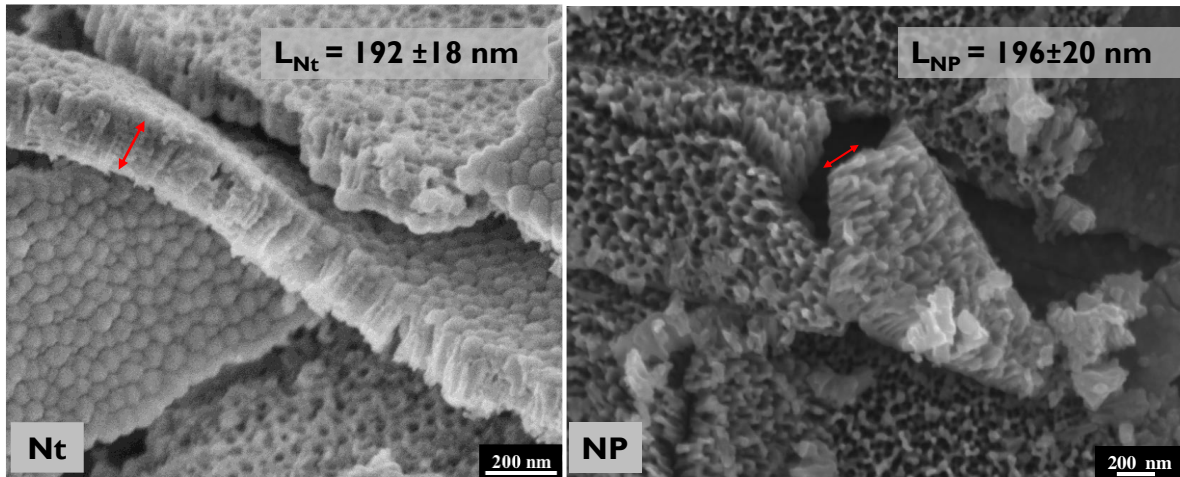


Figure 4. 18 Representative SEM images indicating the procedure to obtain the layer thickness of: a) Nanotubes and b) Nanopores.

When the slope at high frequencies is not equal to 1 and 0.5 at low frequencies, the impedance of the boundary condition Z_B (Interface electrolyte/substrate) has to be consider and modeled by a CPE (Q_B). Similar to the capacitive contribution of the ζ .

$$Z_B = \frac{1}{Q_B} (iw)^{-\beta} \quad (4.15)$$

Finally, the last hypothesis assumes that the boundary impedance Z_A (Electrolyte / top of the pores) is modeled by an impedance consisting of a resistance (R_A).

According to the hypothesis established, it was proposed a transmission line model to describe the impedance response of the anodized TMZF samples immersed in SBF at 37 °C during different periods. Figure 4.19 shows a schematic representation of the model. Channel 1 is represented as a distributed resistance, transport in channel 2 is considered anomalous, that is to say, the impedance X_2 is equivalent to a parallel arrangement of a CPE (Q_2) and a resistance (R_2). The interfacial impedance ζ is considered pseudocapacitive (Q_3) and in the limits an impedance Z_B (Q_B) and a resistance Z_A (R_A).

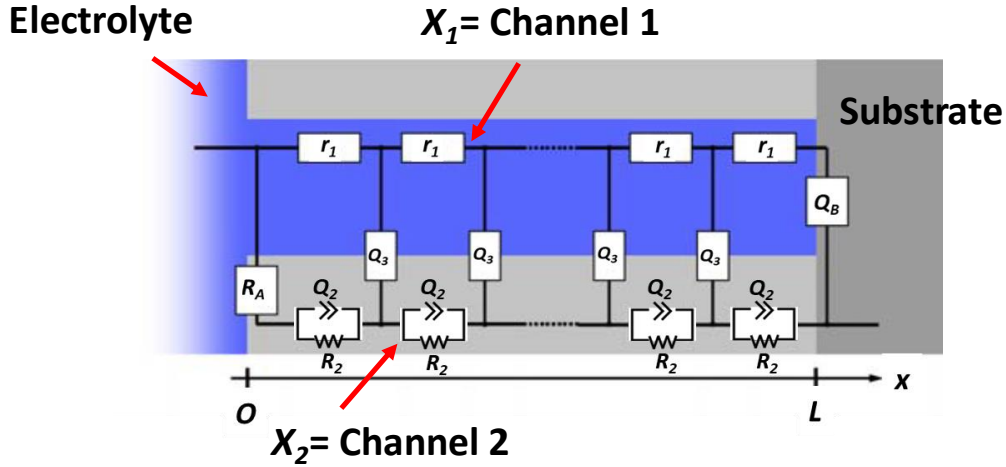


Figure 4.19 The transmission line model proposed to describe the impedance response of the anodized TMZF samples immersed in SBF at 37 °C during the different periods evaluated.

Equation 4.16 shows the solution of the TL employed in this work to model the impedance results:

$$\begin{aligned}
 Z = \frac{1}{X_1 + X_2} & \left[\lambda(X_1 + X_2)S_\lambda + (Z_A + Z_B)C_\lambda + \frac{1}{\lambda(X_1 + X_2)}Z_AZ_B\lambda \right]^{-1} \cdot \left(L\lambda X_1 X_2 (X_1 + \right. \\
 & \left. X_2)S_\lambda + X_1[\lambda X_1 S_\lambda + LX_2 C_\lambda]Z_A + X_2[\lambda X_2 S_\lambda + LX_1 C_\lambda]Z_B + \frac{1}{X_1 + X_2} \right. \\
 & \left. \left(X_1^2 + X_2^2 \right)C_\lambda + \frac{L}{\lambda}X_1 X_2 S_\lambda \right] Z_A Z_B \quad (4.16)
 \end{aligned}$$

Where $X_1 = r_1$; $X_2 = \frac{1}{1 + r_2 q_2 (iw)^\beta}$; $\zeta = \frac{1}{q_3} (iw)^{-\beta}$; $Z_A = R_A$; $Z_B = \frac{1}{Q_B} (iw)^{-\beta}$

$C_\lambda = \cosh(L/\lambda)$, $S_\lambda = \sinh(L/\lambda)$, and $\lambda = [\zeta/(X_1 + X_2)]^{1/2}$.

Figure 4.20 shows the adjustment results (indicated by a solid line) of the experimental measurements of anodized samples with nanotubes and nanopores using the model proposed in Equation 4.16 and illustrated in Figure 4.19. The TL model is composed of 10 parameters that satisfactorily describes the behavior of the interface. The error between the experimental points and the simulation was lower than 1.0 % independently of anodized morphology and immersion time. Only the nanotube condition after 14 days showed a higher value (1.7%), which is quite reasonable.

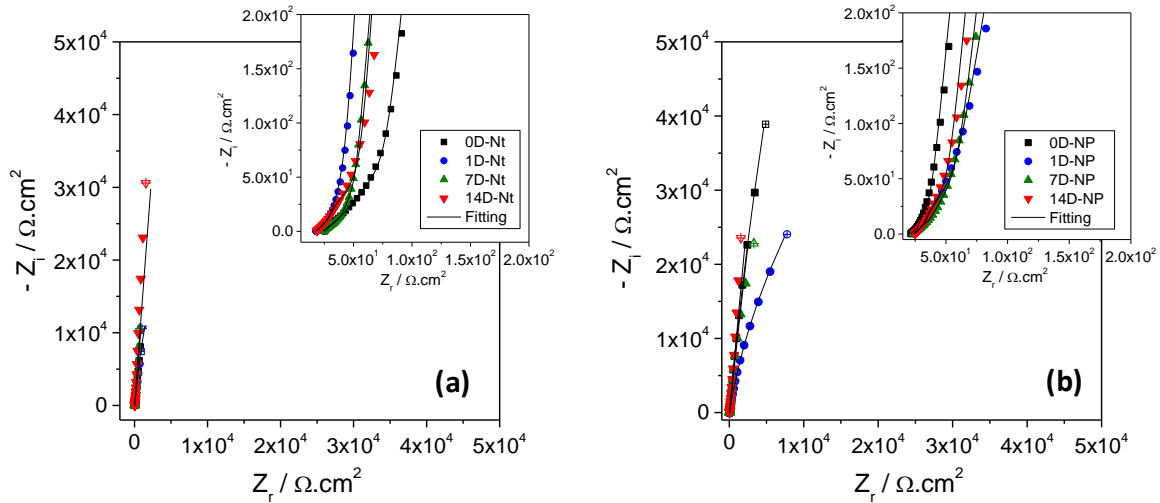


Figure 4.20 Nyquist plots of experimental and simulated results acquired from *Simad* software for the anodized specimens immersed in SBF at 37 °C during different periods (0, 1, 7, and 14 days denoted as 0D, 1D, 7D and 14D respectively): a) Nanotubes and b) Nanopores.

Table 4.3 shows the electrochemical impedance parameters obtained by adjusting the experimental results of nanotubes samples for the different immersion days. Additionally, the values of the crossover frequency (ω_c) that represent the transport mechanism through the channel 2 (X_2) were calculated using 4.17 and showed in Table 4.3.

$$\omega_c = \frac{1}{r_2 q_2 (iw)^{1/\beta}} \quad (4.17)$$

Table 4.3 Electrical impedance parameters obtained by adjusting the experimental results of Nt samples.

Days	X1		X2		ζ	ZA	ZB		L (cm)	ω_c (Hz)	X (%)
	R ₁ ($\Omega \cdot \text{cm}$)	R ₂ ($\Omega \cdot \text{cm}^2$)	Q ₂ ($\Omega \cdot \text{s}^{-e} \cdot \text{cm}^2$)	e	Q ₃ ($\Omega \cdot \text{s}^{-b} \cdot \text{cm}$)		R _A ($\Omega \cdot \text{cm}^2$)	Q _B ($\Omega \cdot \text{s}^{-n} \cdot \text{cm}^2$)			
0	827	217	6.53 E-07	0.96	1.63 E-04	0.96	7.22 E+06	3.69 E-05	0.91	2.0 E-05	0.035
1	956	222	4.55 E-07	0.76	2.96 E-04	0.96	2.99 E+05	1.69 E-05	0.84	2.0 E-05	0.023
7	938	209	6.06 E-07	0.78	3.91 E-04	0.95	4.90 E+08	5.58 E-06	0.92	2.0 E-05	0.019
14	860	145	2.81 E-06	0.72	9.96 E-05	0.96	5.25 E+09	7.80 E-06	0.89	2.0 E-05	0.003

The pseudocapacitance values Q_3 varies as the immersion time increases; this could indicate the processes of formation and dissolution of small nuclei of calcium phosphates on the nanotubes walls. Between days 7 and 14, the nucleation process is favored, showing an evident decrease in the interface impedance. Besides, the coefficient b is close to 1, showing homogeneity and stability of the pore walls, independently of the immersion time.

Figure 4.21 was graphed to understand the behavior of the endpoints of the line (Z_A and Z_B) during the immersion days, represented by resistance and capacitance of R_A and Q_B , respectively. The values of R_A and Q_B were obtained from Table 4.3.

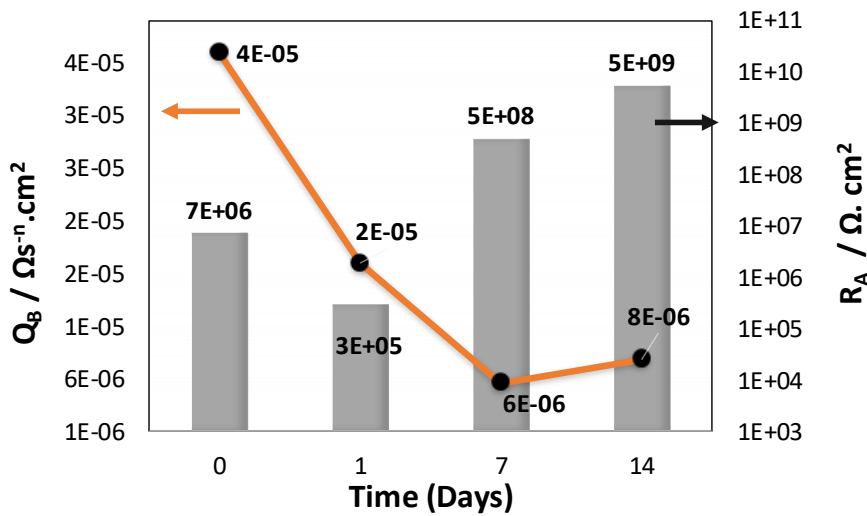


Figure 4.21 Endpoints parameters, R_A and Q_B , obtained from the transmission line model used in nanotubes samples after different immersion periods in SBF.

During the immersion time in SBF, the resistance R_A gradually increases and the Q_B decrease. This behavior could be associated with the formation and growth of calcium phosphate nuclei (Initial step to the apatite formation) on the outer part of the nanotube and the bottom part of the channel. This behavior is observed in Figure 4.22 (red circles). Additionally, the Q_B decrease could be associated with the growth of the inner passive film [86].

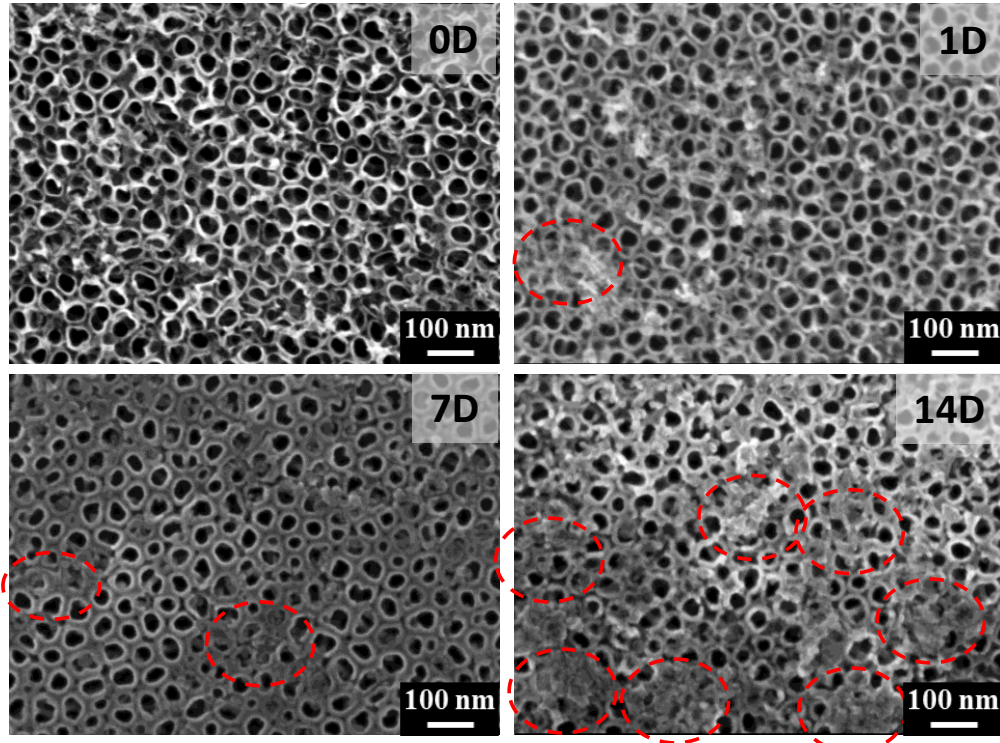


Figure 4.22 Apatite formation over nanotubes samples after different immersion periods in SBF (0, 1, 7 and 14 days).

Table 4.4 shows the electrochemical impedance parameters obtained by adjusting the experimental results of nanopores samples for the different immersion days. Similar to the adjustment for the nanotubes samples, an average value was chosen of L (2×10^{-5} cm) for the nanopores samples. This value was used in the fitting model.

Table 4.4 Electrical impedance parameters obtained by adjusting the experimental results of NP samples.

Days	X1		X2		ζ	ZA	ZB		L (cm)	ω_C (Hz)	X (%)
	R_1 ($\Omega \cdot \text{cm}$)	R_2 ($\Omega \cdot \text{cm}^2$)	Q_2 ($\Omega s^{-e} \cdot \text{cm}^2$)	e	Q_3 ($\Omega s^{-b} \cdot \text{cm}$)	b	R_A ($\Omega \cdot \text{cm}^2$)	Q_B ($\Omega s^{-n} \cdot \text{cm}^2$)	n		
0	559	203	8.52 E-07	0.60	7.73 E-05	0.96	1.40 E+06	5.32 E-06	0.90	2.0E-05	0.003
1	826	207	9.24 E-07	0.64	7.52 E-05	0.97	2.00 E+05	1.15.E-05	0.82	2.0E-05	0.004
7	787	209	6.06 E-07	0.96	8.68 E-05	0.97	8.83 E+07	9.18 E-06	0.92	2.0E-05	0.004
14	936	218	6.88 E-07	0.60	7.60 E-05	0.97	4.90 E+08	5.59 E-06	0.89	2.0E-05	0.003

For nanopore samples, the pseudocapacitance Q_3 values are lower compared to nanotubes and remain almost constant regardless of the immersion time, due to the stable behavior of the interfacial impedance (ζ), even in the first immersion days. Besides, the coefficient b is close to one showing homogeneity and stability of the pore walls.

Figure 4.23 shows the endpoints parameters represented by resistance and capacitance of R_A and Q_B , respectively. These values were graphed to understand the behavior of the transmission line endpoints (Z_A and Z_B) during the immersion days. The values of R_A and Q_B were obtained from Table 4.4.

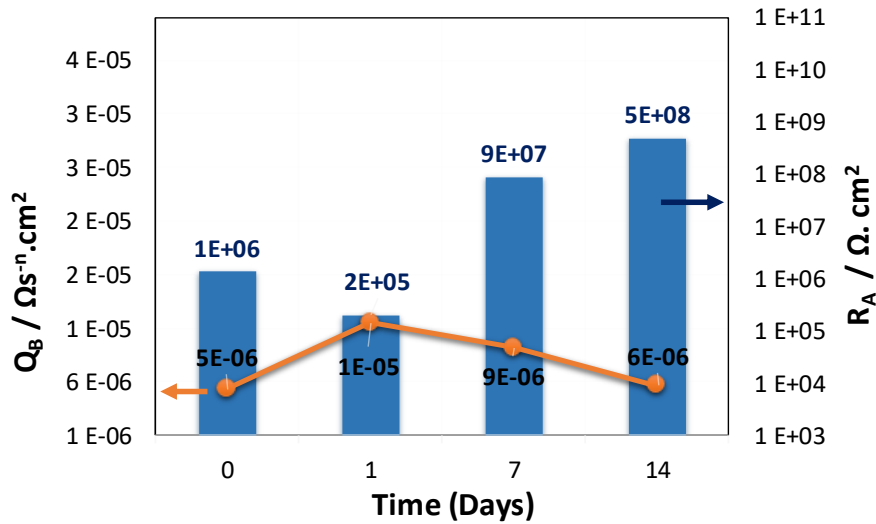


Figure 4.23 Endpoints parameters, R_A and Q_B , obtained from the transmission line model used in nanopores samples after different immersion periods in SBF.

During the immersion time in SBF, the resistance R_A gradually increases. This behavior could be associated with the possible nucleation and growth of hydrated silica gel and amorphous calcium phosphate on the outer and inner parts of the nanopores, both predecessors for the apatite formation [126]. This behavior could be observed in Figure 4.24 (red circles). Moreover, the Q_B values were low and constant indicating a stable and protective behavior of the inner passive film during the entire time analyzed.

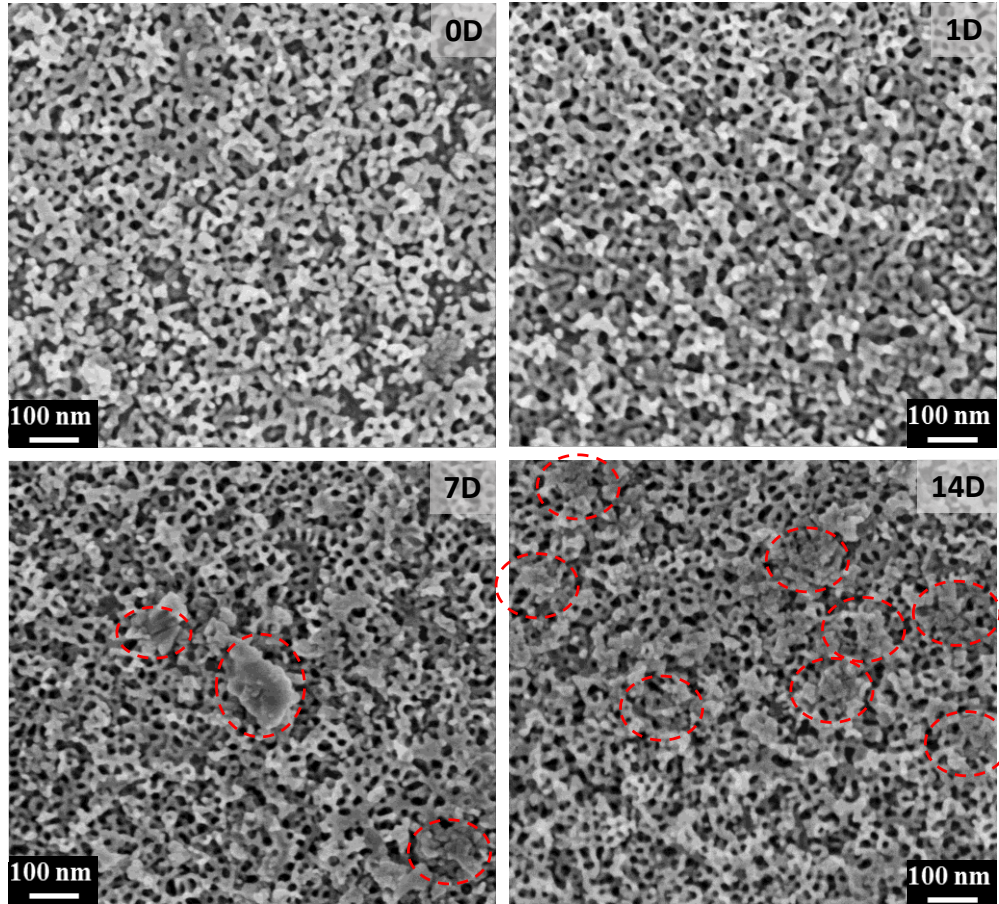


Figure 4.24 Apatite formation over nanopores samples after different immersion periods in SBF (0, 1, 7 and 14 days).

As it was indicated in the transport process in channel 2 (X_2), it is represented by a different model termed as “anomalous transport model” (parallel connection of a Constant-Phase-Element, Q_2 , and a resistance, R_2), since the charge carrier transport mechanism depends on the frequency (Equation 4.12). For both anodizing conditions, nanotubes and nanopores, ω_c was between 0.003 to 0.035 Hz. These low values indicated a low charge transfer through the channel 2 in the frequency regime studied in this work (10^{-2} - 10^4 Hz).

Figure 4.25, summarize the corrosion response and the bioactivity after 14 days of immersion in SBF of the different surface conditions studied in this work; the barrier resistance values (R_B or R_A for the anodized samples) associated with the corrosion resistance obtained from the impedance data, the I_{pass} obtained from the polarization curves and the bioactivity through the mass gain.

Untreated samples showed a good corrosion response indicated by a high resistance value and acceptable I_{pass} , lower than $2 \mu\text{A} \cdot \text{cm}^{-2}$; however, in this surface condition was not detected HAp formation.

Samples treated with HCl and NaOH contrary to untreated samples, showed excellent bioactivity with the highest mass gain value, around 1.8 mg after 14 days of immersion in SBF. Still, their corrosion resistance was deficient, proved by the lowest R_B and the highest i_{pass} values.

Finally, the anodized samples showed the best corrosion resistance corroborated by the highest and lowest values of R_A and i_{pass} , respectively. On the other hand, specimens with nanotubes and nanopores exhibited low and moderated values of HAp formation after 14 days in SBF.

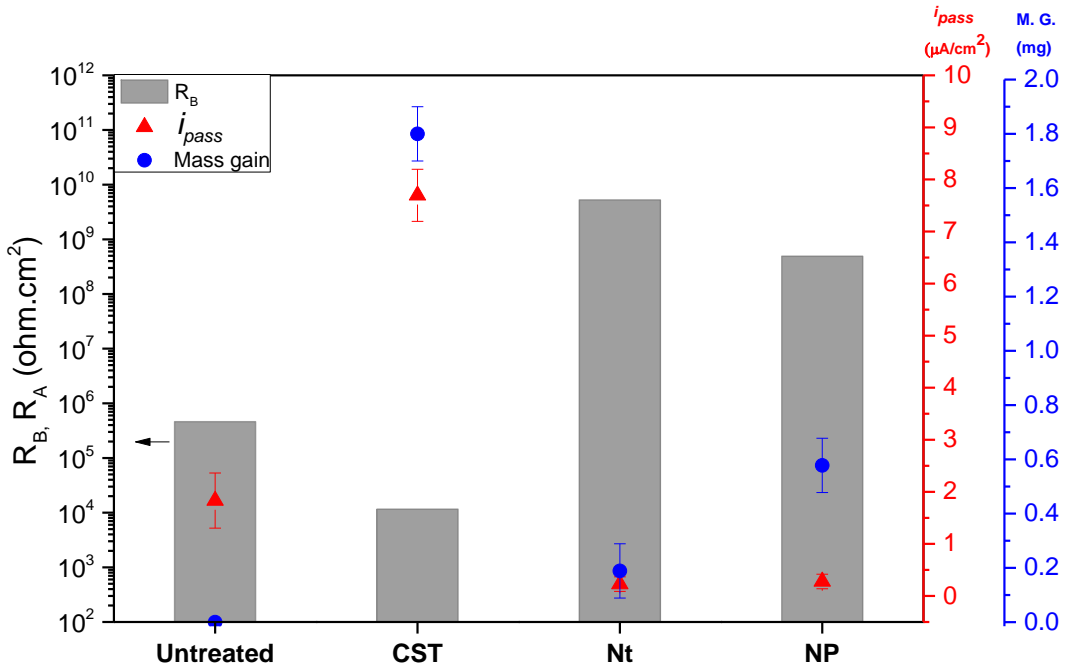


Figure 4.25 Corrosion response and bioactivity of untreated, CST, nanotubes, and nanopores samples after 14 days of immersion in SBF at 37 °C. Barrier resistance (R_B or R_A for the anodized samples) obtained from the impedance data, passivation current (i_{pass}) from the polarization curves, and bioactivity through the mass gain.

Impedance behavior of the four different treated surface samples has been successfully studied and the conclusions are summarized in the following paragraphs:

- Nyquist and Bode plots for untreated TMZF samples showed a pseudocapacitive behavior due to their very protective passive layer.
- The continuous increase of the impedance modulus $|Z|$ in the untreated samples suggests that the corrosion resistance enhances with the immersion time.
- Bode representation corrected for ohmic resistance as a primary approach, and followed by the graphical representation of α_{eff} were successfully employed to determine the more accurate EEC.
- The EEC for the untreated sample was composed of a bi-layered microstructure, an outer porous oxide layer, and an inner barrier layer.
- The inner barrier layer grew through the immersion periods, indicating that the corrosion protection increase was mainly due to the effect of this barrier.
- Through the Nyquist and Bode plots, the CST samples showed a more reactive behavior compared with the untreated samples, independently of the immersion time in SBF.
- The impedance results for the CST samples after 14 days of immersion, corroborated the presence of the apatite layer over the surface.
- Alpha effective plots for CST samples indicated an extra relaxation process at low frequency, associated with diffusion phenomena occurring through the outer porous layers.
- TMZF samples after CST showed a thinner passive layer compare with untreated samples. It was associated with the dissolution of the oxide layer during the HCl attack.
- Impedance measurements of anodized samples in SBF showed a peculiar behavior that could not be modeled by the traditional equivalent circuits. It resembled the behavior of a porous electrode. Thus, it was proposed a two-channel transmission line model for analyzing the impedance results.
- Nyquist diagrams for nanotubes and nanopores samples reveal a capacitive or at least pseudocapacitive behavior. This means that the electrochemical reactions on the surface were very limited.
- Bode representations for the anodized samples independent of the soaking time showed a characteristic response of capacitive surface films.
- The impedance ζ , between the solution and the porous walls was purely pseudo-capacitive. This interface is almost not reactive, and the CPE behavior results from surface heterogeneities.

- During the immersion time in SBF, the resistance R_A gradually increased and the capacitance Q_B decreased. It could be associated with the initial steps to the apatite formation on the outer and inner parts of the anodized layers.
- The described models led to the successful fitting of EIS data measurements of the four different surface morphologies on TMZF samples, with meaningful fitting parameter values and low error between the experimental points and the simulation.

A final observation concerns the fact that these results illustrate the difficulty of extracting reliable parameters from the fitting of EIS through traditional EEC and TL models. This is a widely used procedure that must be carried out very carefully.

Chapter V

Fatigue behavior of the different surface treatments

Surface topography in titanium alloys applied in orthopedic and dental implants is essential because it will determine the level of cell adhesion and growth on them. Thus, those processes as anodizing and chemical surface treatments with HCl and NaOH that modify surfaces for better osseointegration may also cause changes in fatigue life behavior.

The fatigue performance analysis of metallic materials is mainly based on two phenomena, the first is the crack nucleation process, and the second is the process of propagation of these cracks, both due to cyclic solicitations.

Surface alteration processes, such as those used in this project, could lead to the formation of notches of considerable sizes, becoming cracks nucleation sites and therefore reducing the fatigue resistance of the material.

Additionally, during some stages of these modification processes, hydrogen gas is produced, and due to the affinity of the titanium β phase for the hydrogen, it could be absorbed in sufficient quantity causing embrittlement problems of the material, which could directly affect the propagation process of fatigue cracks.

In this way, the fatigue response of untreated samples (polished surface), treated with HCl and NaOH (CST) and anodized samples (nanopores) was evaluated. The fatigue resistance was determined through the staircase tests, and then the fracture surfaces were analyzed to assess the evidence of embrittlement mechanisms.

5.1 Fatigue resistance of TMZF samples untreated and treated with CST, and nanopores

Microstructure, chemical composition and tensile mechanical properties of the employed material followed the requirements of ASTM F1813-13. Table 5.1 shows the mechanical properties of the TMZF alloy used in this work compared to the standard minimal requirements.

Table 5.1 Mechanical properties of the TMZF titanium alloy used in this study.

Material	Yield strength 0.2% (MPa)	Tensile strength (MPa)	Elongation (%)
TMZF used	1060 ±19	1071±14	17±2
ASTM F1813-13	931	897	12

Orthopedic implants are subjected to cyclical loads due to the mechanical demands of the human body, submitting these components to high cycle fatigue conditions (HCF). High cycle fatigue tests ($N = 5 \times 10^6$ cycles) were performed using the staircase method to evaluate the fatigue performance of the different surfaces studied in this work.

As it was mentioned in section 2.2.1, untreated samples were grinded and polished, aiming to minimize the influence of surface defects induced by machining on the fatigue properties. Figure 5.1 displays the results of the staircase method for untreated samples. A maximum stress of 750 MPa was selected as the initial value based on the tensile test results (~70% of the yield strength) shown in Table 5.1

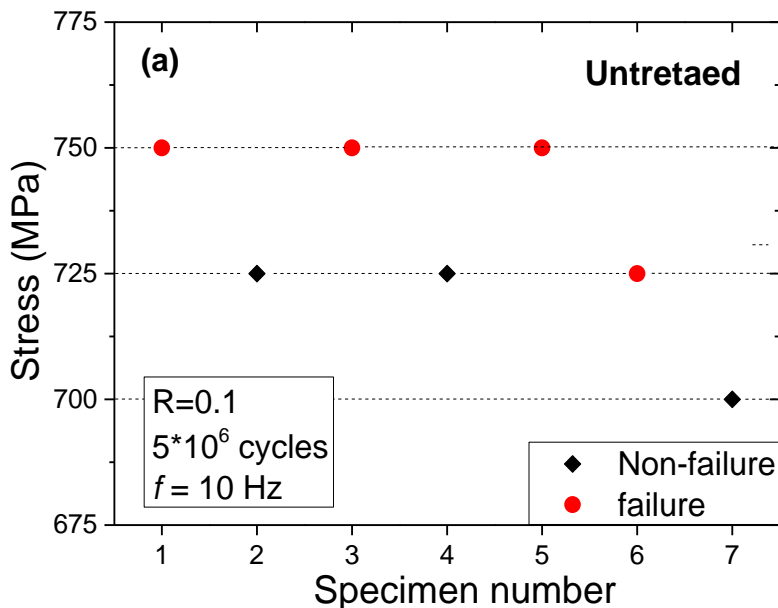


Figure 5.1 Staircase fatigue diagram for untreated samples. “●” Means failure and “◆” means survival to the run-out.

The data plotted in Figure 5.1 were rearranged and put in Table 5.2 to count the frequencies of failures and non-failures of the specimens tested at different stress levels. This procedure serves as a guide for the statistical calculation using

the method of Dixon and Mood [4]. This statistical analysis has to be used for the events with the least number of observations between “failure” and “non-failure.”

Table 5.2 Analysis of staircase method data for untreated TMZF alloy.

Non-failure				
Stress (MPa)	Level i	n_i	$i * n_i$	$i^2 * n_i$
750	2	0	0	0
725	1	2	2	4
700	0	1	0	0
Sum	-	3	1	1
		N	A	B

The following expressions allow the calculation of the fatigue strength (σ_F):

$$\sigma_F = \sigma_0 + d \cdot \left(\frac{A}{N} \pm 0,5 \right) \quad (5.1)$$

Were $N = \sum n_i$

$$A = \sum (i \cdot n_i)$$

$$B = \sum (i^2 \cdot n_i)$$

i = is the number of stress levels used ($i = 0, 1, 2, 3, \dots i_{\max}$)

n_i = Number of occurrences of the selected event (failure, non-failure) at the level i

σ_0 = Minimum tension reached in the test, where no specimen broke.

The sign (+) is used when the selected event is, non-failure and (-) when the event is, failure.

The standard deviation assessment is given as follows:

$$\mu = 1.62 \cdot d \cdot \left(\frac{N \cdot B - A^2}{N^2} + 0.029 \right) \quad (5.2)$$

When the ratio is:

$$\left(\frac{N \cdot B - A^2}{N^2} \right) \geq 0.3 \quad (5.3)$$

Or equal to:

$$\mu = 0.53 \cdot d \quad (5.4)$$

When the ratio is:

$$\left(\frac{N \cdot B - A^2}{N^2} \right) < 0.3 \quad (5.5)$$

The fatigue limit in terms of maximum stress and the standard deviation calculated with the Dixon-Mood statistical approach are respectively 730 and 13 MPa.

Figure 5.2. shows the fracture surface of the untreated specimens to examine and determine the fracture characteristic after the fatigue tests. Crack nucleation on the surface (region 1) has been the leading initiation site for untreated samples. The zone of stable crack propagation or region 2 occupies around 50% of the entire surface and is characterized by well-defined fatigue striations and river patterns. The remaining area comprises a transition zone of unstable crack propagation.

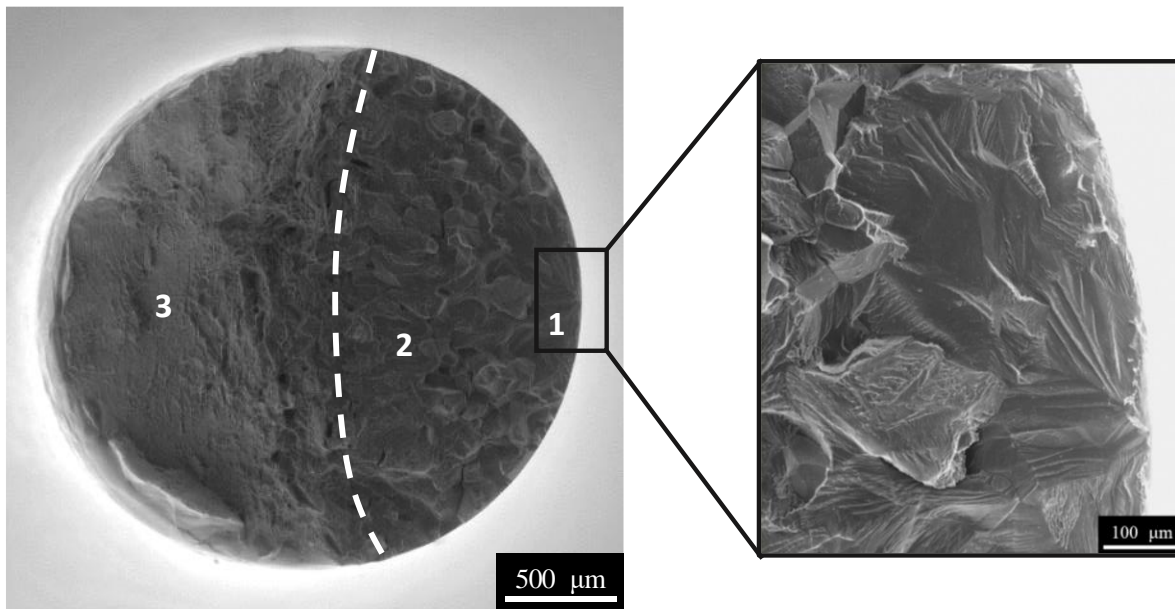


Figure 5.2 Fractography of untreated sample, the dash line designates the approximate transition between the stable and unstable crack propagation regions and the square indicates the magnified region on the right side, pointing out the crack initiation site.

With the aid of a laser scanning confocal microscope, topographic characteristics were obtained, such as roughness and morphology of the different treatments studied.

Table 5.3 reports the average roughness values (R_a) and peak-to-valley roughness (R_z) with the standard deviation values for each of the treatments.

Untreated samples were polished to obtain a homogeneous and smooth surface, as it can be seen in Figure 5.3 (a). The polishing process eliminates the risks arising from the machining process, which is corroborated by the low values of R_a and R_z roughness. This flat surface prevents or delays the nucleation of superficial fatigue cracks and is used as a suitable surface condition to determine the fatigue strength of a metallic material, in an attempt to minimize the effect of previous machining and heat treatment upon fatigue behavior variability [127].

Table 5.3 Topography measurements of R_a and R_z roughness of the untreated, CST and nanopores samples.

	R_a (μm)	R_z (μm)
Untreated	<0.100	<0.100
CST	0.443 ± 0.082	3.390 ± 0.841
Nanopores	<0.100	0.313 ± 0.044

Figure 5.3 (b) shows the topography of a representative sample treated with HCl and NaOH. This combined attack produces a surface with formation of generalized micro-pits in an approximate size of $3.40 \mu\text{m}$. Higher than the value observed in the polished samples (<0.100 μm).

As it was indicated in section 1.5, roughness scattering (i.e., notches) can lead to considerable differences in the fatigue response of the component. For instance, grooves of approximately $3.50 \mu\text{m}$ on the Ti-6Al-4V alloy could reduce the fatigue resistance by around 12% [70].

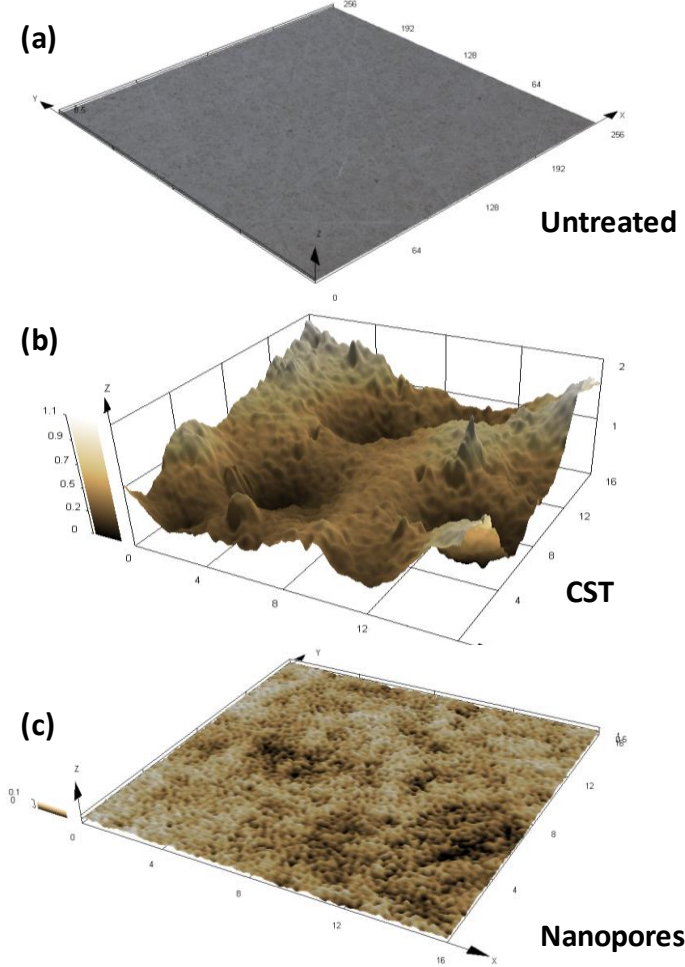


Figure 5.3 . Representative 3D-images determined by confocal laser scanning microscopy of: a) untreated, b) CST and c) nanopores samples.

Preliminary fatigue results of CST samples showed a drastic decrease of the fatigue resistance to a value lower than 370 MPa (maximum principal tensile stress for a hip stem geometry [128]). This high reduction of the fatigue strength (~ 50% compared with the untreated samples) indicates the existence of an additional phenomenon to the notch sensitivity that is affecting the fatigue response of the material.

Previous studies employing HCl etching and NaOH treatment over an $\alpha+\beta$ titanium alloy showed a significant increase in the hydrogen content [129]. Even a slight increase in hydrogen content could cause embrittlement in titanium alloys, producing a reduction in fracture toughness and fatigue resistance [130, 131].

In this way, it was calculated the hydrogen content of the different surface conditions (Table 5.4), showing an increase after the surface treatments compared with the untreated samples. CST samples show the highest values, close to 310

ppm. This high hydrogen content could explain the drastic decrease in fatigue resistance of the CST specimens.

Table 5.4 Hydrogen content results for: Untreated, CST, CST-polished and nanopores.

	H (ppm)
Untreated	99 ± 22
CST not -polished	310 ± 23
CST-polished	261 ± 4
Nanopores	127 ± 23

To determine if there is an alteration of the fatigue performance by the hydrogen absorbed after the chemical treatment, TMZF specimens treated chemically were grinded and polished (using the same protocol employed in untreated samples) to eliminate the micro-pits formed, and thus avoid the notch effect. Then, the specimens were tested through the staircase fatigue method.

Figure 5.4. shows the results of the staircase method for CST-polished samples. Using the previous information of untreated conditions, the stress value of 725 MPa was selected as the initial one. This stress level was very high, and the initial specimens failed prematurely (empty rhombus in Figure 5.4); thus, they were not considered in the analysis of the fatigue resistance. On the other hand, the first specimen employed for the determination of the fatigue resistance failed at 550 MPa.

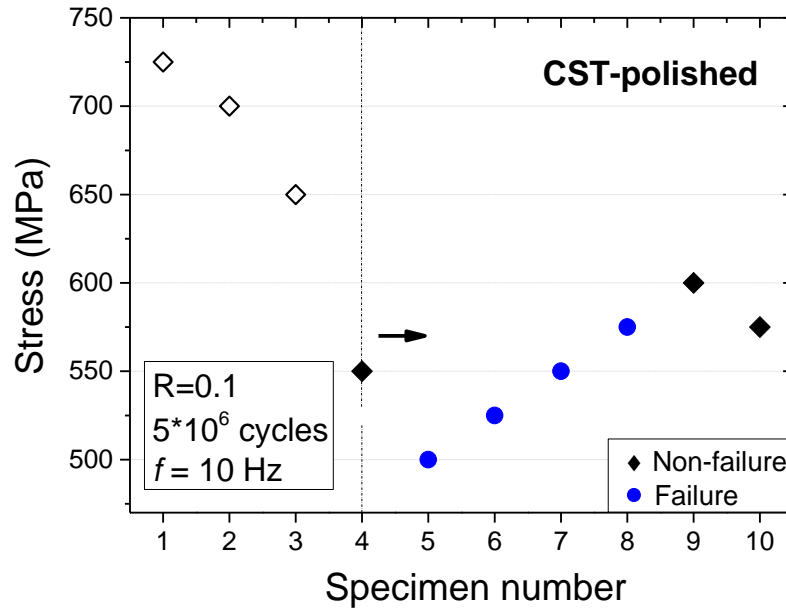


Figure 5.4 Staircase fatigue diagram for CST-polished samples. “●” Means failure, “◆” means survival to the run-out and “◊” specimens not considered in the analysis.

The data obtained from Figure 5.4 were organized and placed in Table 5.5. This information was employed in the Dixon and Mood statistical approach to determine the fatigue strength of the CST-polished samples. Here, the event with the least number of observations was “failure.”

Table 5.5 Analysis of staircase method data for CST-polished samples.

Failure					
Stress (MPa)	Level i	n_i	$i * n_i$	$i^2 * n_i$	
600	2	1	2	4	
575	1	1	1	1	
550	0	1	0	0	
Sum	-	3	3	5	
		N	A	B	

The fatigue limit in terms of maximum stress and the standard deviation calculated are respectively 563 and 28 MPa for the samples chemically treated and

polished. The reduction of 25% of the fatigue resistance compared with the untreated samples could be associated with the significant increase in the hydrogen content detected in the material even after grinding and polishing the surface of the specimens (Table 5.4).

Figure 5.5 shows the fracture surface of the CST-polished specimens. Here the propagation region is characterized by cleavage steps or river patterns. The branches of these river patterns join in the direction of crack propagation and can be used to establish the local fracture direction and the crack nucleation point, indicated by the black square.

The magnified region in Figure 5.5 shows evidence of secondary cracks formed through the grain boundaries. Generally, this fracture type is associated with hydrogen embrittlement phenomena, such as grain boundary embrittlement or even the repeated formation and rupture of brittle hydride phases close to the grain boundary [63, 132].

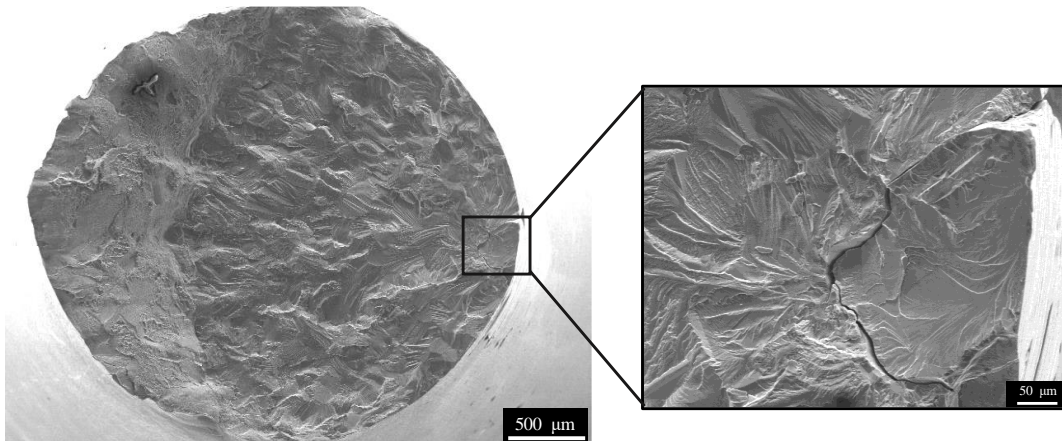


Figure 5.5 Fractography of CST-polished sample, the square indicates the magnified region on the right side, pointing out the crack initiation site.

As observed in Table 5.4, the samples anodized with nanopores presented a slight increase in the hydrogen content, close to 130 ppm. This value is lower than the observed in samples treated with CST. Moreover, from confocal measurements (Table 5.3), nanopores samples displayed a refined surface with low roughness values ($R_z = 0.3 \mu\text{m}$), avoiding a possible notch effect. These two conditions could indicate better fatigue behavior than the CST specimens.

In this way, fatigue specimens anodized with nanopores were tested. Initially, the maximum axial stress was 725 MPa, similar to the protocol established for CST samples. Contrary to the expected behavior, the specimen failed after few cycles (3258 cycles). Subsequently, new specimens tested at lower stress levels showed a similar behavior, as indicated in Figure 5.6. All of them failed, even the specimen

tested at 300 MPa, at stress values lower than the maximum principal tensile stress for a hip stem geometry (370 MPa) [128]. Only the specimen tested at 200 MPa survived to the run-out. Indicating that even avoiding the possibility of notch effect, the anodization process reduced the fatigue resistance, and it could be associated with the hydrogen content in the samples.

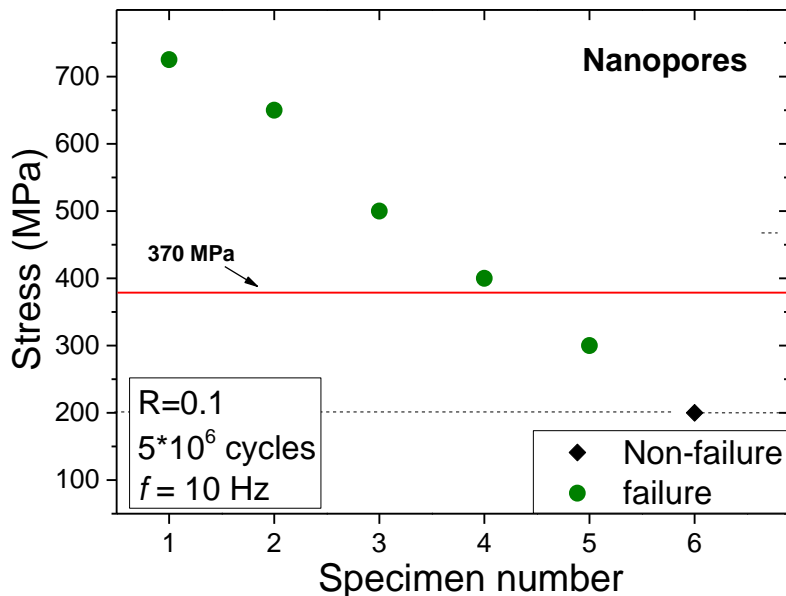


Figure 5.6 Staircase fatigue diagram for nanopores samples. “●” Means failure, “◆” means survival to the run-out and.

The fatigue fracture surface corresponding to the nanopores sample tested at 500 MPa is illustrated in Figure 5.7(a). As it is observed in the region (b), typical features of cyclic fatigue crack growth such as river patterns and cleavage steps appear and become the primary propagation mechanism in this region. This stable propagation zone of the fatigue crack is restricted to a small elliptical region.

The fractographies in Figure 5.7 (c-d) of the samples treated with nanopores and CST show more evidence of brittle fracture. Here an interesting and distinct cleavage pattern called Wallner lines is observed (indicated by black arrows). This arrangement is observed in fracture surfaces of brittle materials, brittle inclusions, or intermetallic compounds. It consists of two sets of parallel cleavage steps that often intersect to produce a crisscross pattern. Wallner lines result from the simultaneous propagation of a crack front and an elastic shock wave in the material [133].

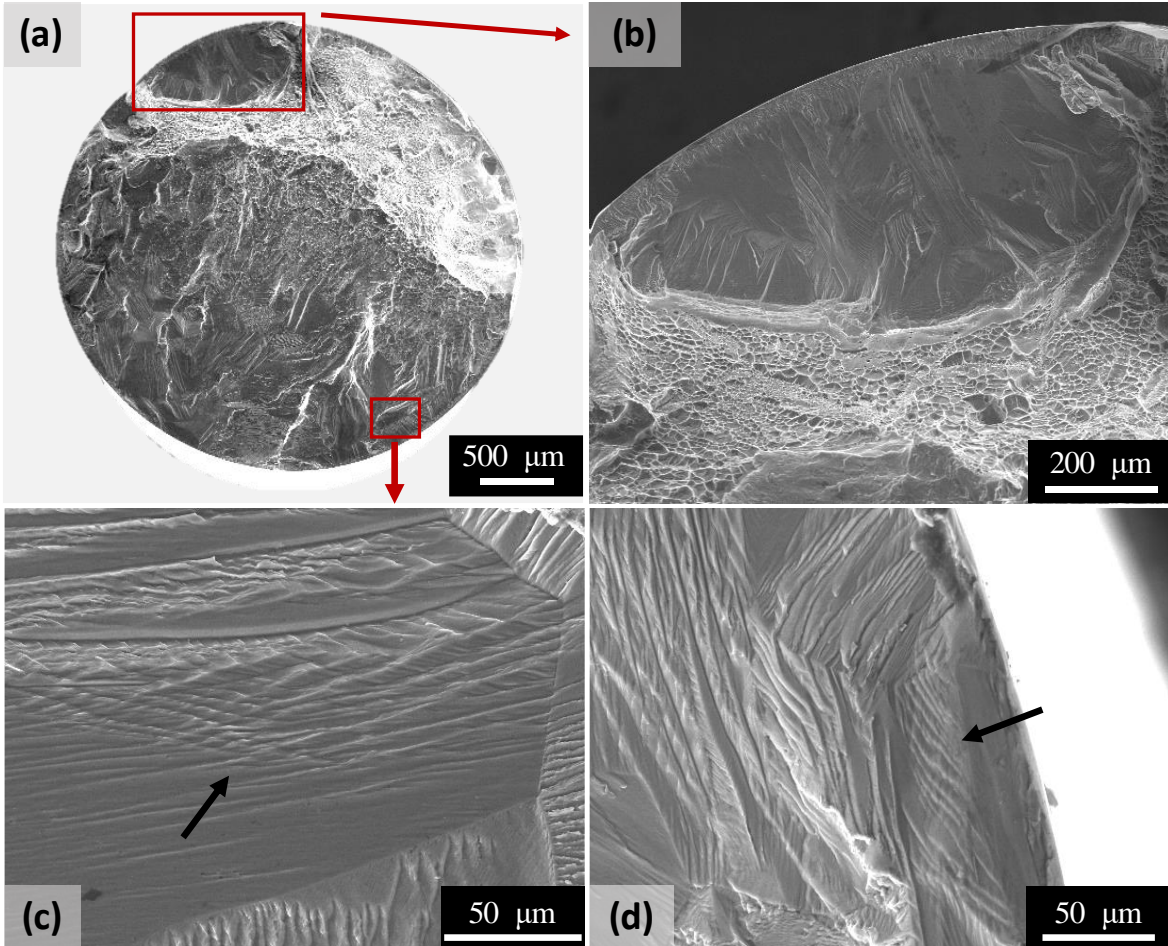


Figure 5.7 a) Fractography of nanopores sample, which was tested at 500 MPa, b) magnified zone indicating a stable crack propagation region, c) magnified region of the nanopores sample indicating Wallner lines and d) magnified region of the CST-polished sample which was fatigue tested at 550 MPa indicating the Wallner lines pattern.

5.2 Hydrogen embrittlement

Hydrogen embrittlement (HE) is an interesting but harmful phenomenon, and it could be presented in a wide variety of metals and alloys. HE involves a group of mechanisms associated with reducing the mechanical properties attributed to the hydrogen as the principal actor [63].

It is usually challenging to determine directly how hydrogen influences the behavior of metallic materials due to the difficulty in measuring and observing this element accurately. Therefore, its effects are indirectly deduced from variations in mechanical properties. Moreover, its effect depends on the way it is in the material, either trapped at crystal defects, in solution, or forming hydrides [134, 135].

Atomic hydrogen can be transported easily in titanium alloys by a combination of interstitial and intergranular diffusion, which in turn reduces the ductility and strength of the metal [63, 131, 132]. Different theories have been studied to explain how hydrogen causes embrittlement. However, the fracture mechanism behind this embrittlement in the titanium alloys is not fully understood.

This difficulty is especially true for metastable β titanium alloys where the effect of hydrogen on the mechanical behavior has been explained in terms of: (i) failure due to stress-induced hydride formation [130, 136], (ii) hydrogen-induced decohesion [63, 137, 138] and (iii) hydrogen-enhanced localized plasticity (HELP) [139, 140]. Even in single phase systems, as is the case of the TMZF alloy, the identification of the embrittlement mechanism is complex, and multiple hydrogen-related fracture mechanisms can operate simultaneously [137, 138, 140]. While a number of mechanisms have been proposed to explain hydrogen embrittlement, the aforementioned are considered to be the most applicable to this study.

Embrittlement attributed to hydride-forming is normally associated to the brittle characteristic of the hydride phase and the failure along the fragile hydride/metal interface. The degree of embrittlement should exhibit an inverse strain rate dependence, since hydride formation kinetics is diffusion-controlled, and low strain rates provide more time for the hydrides to form. Moreover, the hydrogen concentration at which this mechanism causes fracture depends on thermodynamic factors, as the local stress intensity, the volume change associated with hydride formation from solid solution, and the attractive H-H interaction [130, 136].

Since β titanium alloys exhibit very high hydrogen solubility, they do not readily form hydrides [141]. However, J. Von Pezold et al. [142] employed simulations combining density functional theory (DFT) and the semi-empirical embedded atom method (EAM), and showed that it is possible to obtain stress-induced hydride seeds even in samples with hydrogen content lower than 160 ppm, due to an increase in the hydrogen local concentration in the tensile strain field of crystallographic defects [142].

Figure 5.8 shows the analysis by the automated crystal orientation mapping (ACOM-TEM) of the samples treated with CST and then fatigue tested. In addition to the β phase of the matrix, it is observed on the phase map the presence of very fine TiH_2 particles or seeds with a tetragonal lattice. The presence of those brittle hydrides is strong evidence of the effect of hydrogen in reducing the fatigue strength of the material.

These hydrides may result from the increase of the local hydrogen concentration in the tensile strain field of extended lattice defects, such as dislocations. Therefore, it is suggested that, as hydrogen exhibits a considerable

solubility in the β phase, and according to the phenomenon known as stress-induced hydride, the localized deformation during the fatigue test induced the segregation of hydrogen [142, 143]. Consequently, TiH_2 precipitation occurred at high-energy grain boundaries, as observed in Figure 5.8b and 5.8c.

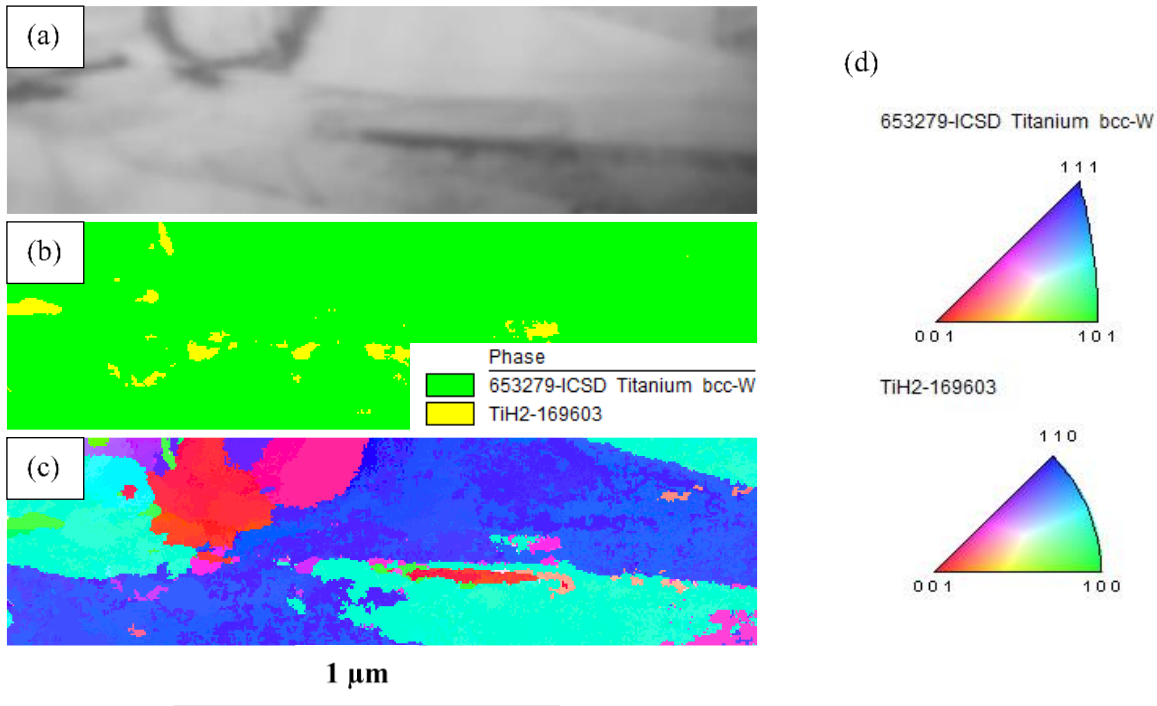


Figure 5.8 Images of the CST-polished sample and fatigue tested generated using the ASTAR system coupled to TEM: (a) virtual bright-field (VBF) image, (b) phase mapping (PM), (c) orientation image mapping (OIM) and (d) inverse pole figure (IPF) from where the colors were used to index orientations in the OIM.

The second HE mechanism inferred from the TMZF specimens studied in this work is the hydrogen-induced decohesion, which associates the fracture stress reduction of the lattice with the decrease of its cohesive energy by the presence of the solute hydrogen into the matrix [137, 139]. Usually, in alloys with low hydrogen content, the supporting evidence is the fracture surface characteristics, define by intergranular failures by decohesion of the grain boundaries [137, 138].

During the crack propagation, the work required to separate the grain boundary into two free surfaces decreases with increasing the hydrogen content [139]. Figure 5.9 shows evidence of this phenomenon on nanopores samples fractured after fatigue tests at 650 MPa. Here, the hydrogen weakens the bonding to allow the decohesion mechanism with little plasticity. Thus, the high stress intensity (high crack velocities) causes failure of the grain boundaries by intergranular decohesion.

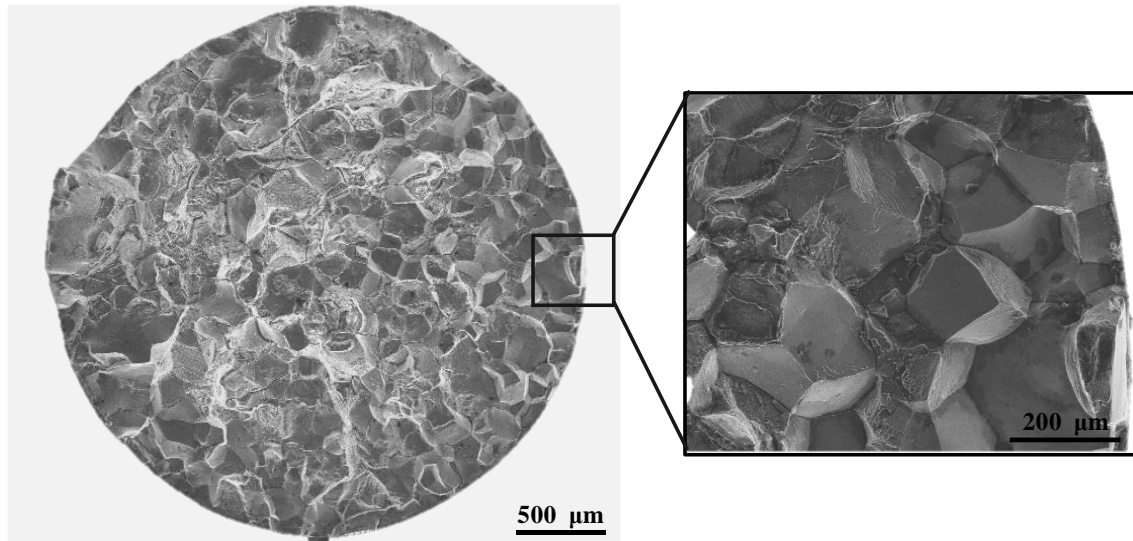


Figure 5.9 Fractography of nanopores sample, which was fatigue tested at 650 MPa, the square indicates the magnified region on the right side.

The third HE mechanism studied in this work is the hydrogen-enhanced localized plasticity (HELP). In this theory, the nucleation and motion of dislocations are favored by the hydrogen content [137, 144]. In this sense, it is expected an increase of deformation and plasticity at the zone with high hydrogen concentration. Thus, evidence justifying the HELP mechanism is observed in fractography with localized ductile crack propagation, contrary to a brittle characteristic ahead of the crack tip [139, 140].

Traditionally, the fatigue crack growth mechanism in metals depend on striations formed by slip at a crack tip [133]. During the crack growth, the crack tip blunt until the saturation level, at the maximum load (Figure 5.10 a). Nevertheless, when the hydrogen is present, it diffuses toward crack tips and concentrates in this zone (Figure 5.10 b-2). Thus, the hydrogenated crack continues growing even after the maximum load. Thereby, the fatigue crack growth rates of hydrogen-charged zones are more favorable than those of non-charged [140].

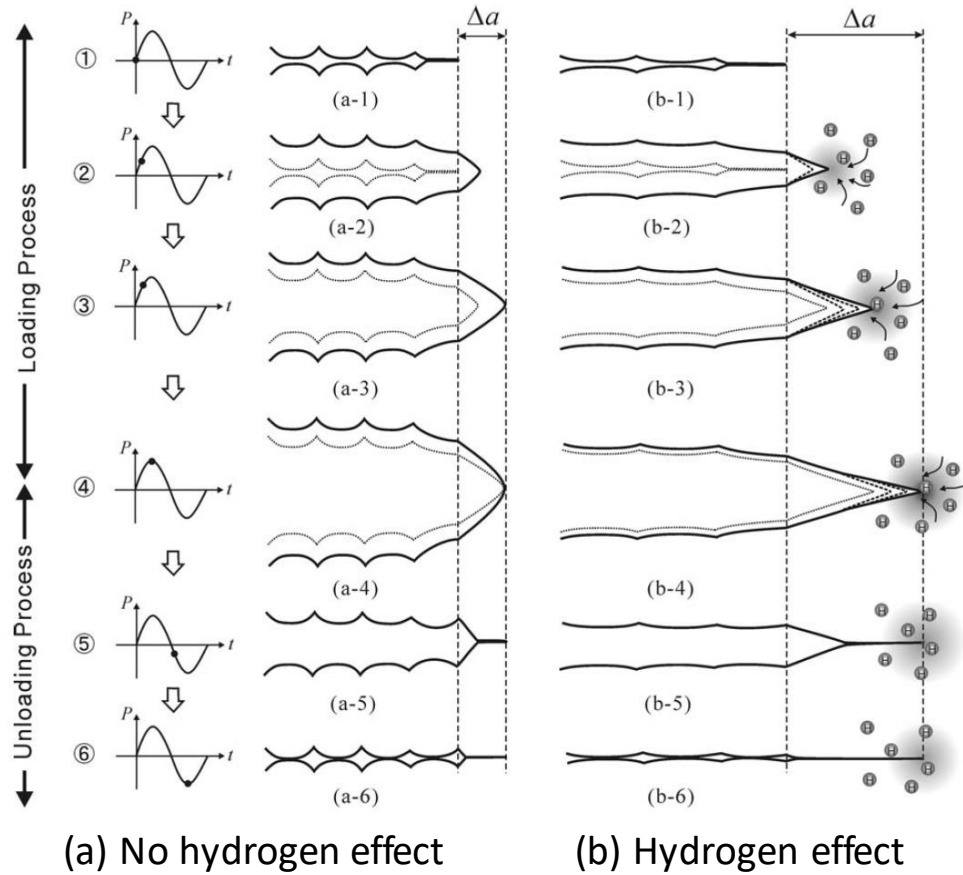


Figure 5.10 Crack tip opening and striation formation mechanism in fatigue: (a) no hydrogen effect, (b) hydrogen effect. Extracted from [144].

As mentioned in Chapter 1, hydrogen is produced during these two treatments (CST and anodized) at the metal/electrolyte interface. Simultaneously, a quantity of this element is absorbed and diffused into the titanium alloy; however, a high quantity is accumulated adjacent to the specimen surface. This condition facilitated the observation of the HELP mechanism acting on the nanopores and CST not-polished samples during the fatigue tests.

Figure 5.11 shows evidence of the HELP mechanism acting on the CST not-polished samples during the fatigue test at 300 MPa. Through the magnified images it is possible to observe a circumferential crack propagating in the round specimen. The propagation of this localized ductile crack is confined within a region of approximately $26 \pm 5 \mu\text{m}$ from the sample surface (Figure 5.11 b-d), favored by an increase in dislocation nucleation and mobility, due to the higher concentration of hydrogen in this subsurface region.

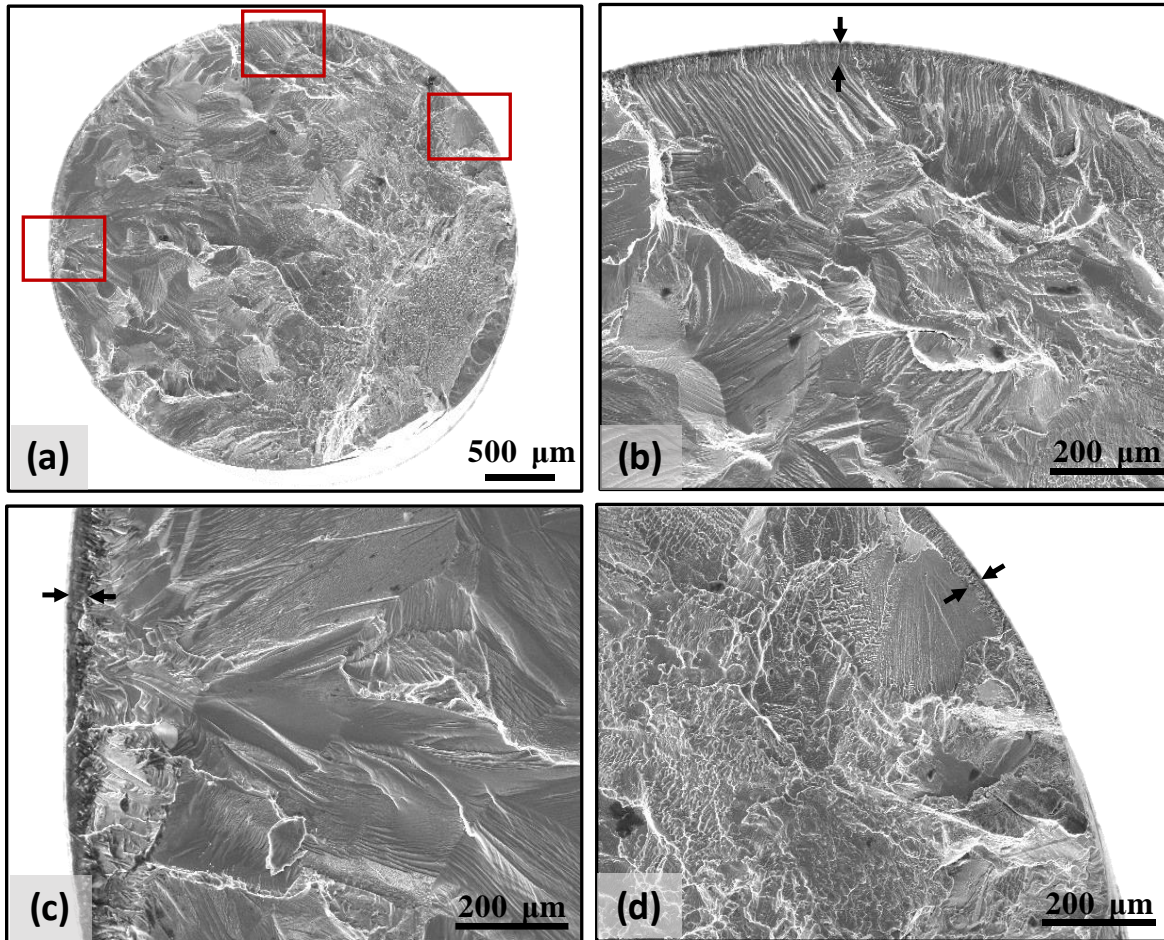


Figure 5.11 a) Fractography of CST not-polished sample, which was fatigue tested at 300 MPa, b), c) and d) magnified zone indicating a stable crack propagation region at the hydrogenated zone indicated by black arrows.

Similar behavior was observed in the nanopores samples fractured after the fatigue tests. Figure 5.12 shows the evidence of a circumferential crack propagating around the specimen. These observations suggest that the values displayed in Table 5.4, for the samples with nanopores and CST could be higher than indicated, due to the high hydrogen concentration at the sample surface and the experimental difficulties to obtain the accurate concentration in this region.

Here, the confined region of the circumferential crack is a little bit more diffuse due to a lower quantity of hydrogen absorbed during the anodizing treatment compared with the quantity absorbed by the samples during the CST as it was indicated in Table 5.4.

Figure 5.12 shows that the circumferential surface crack is generated and propagated during the initial cycles. From this, new crack nucleates and then spread radially into the sample on a plane normal to the external load (Figure 5.12 c). Finally,

failure happens under overload displaying shallow dimples. As observed in Figure 5.12, this final failure connects directly with the pre-existence circumferential crack, which corroborates the fracture sequence mentioned.

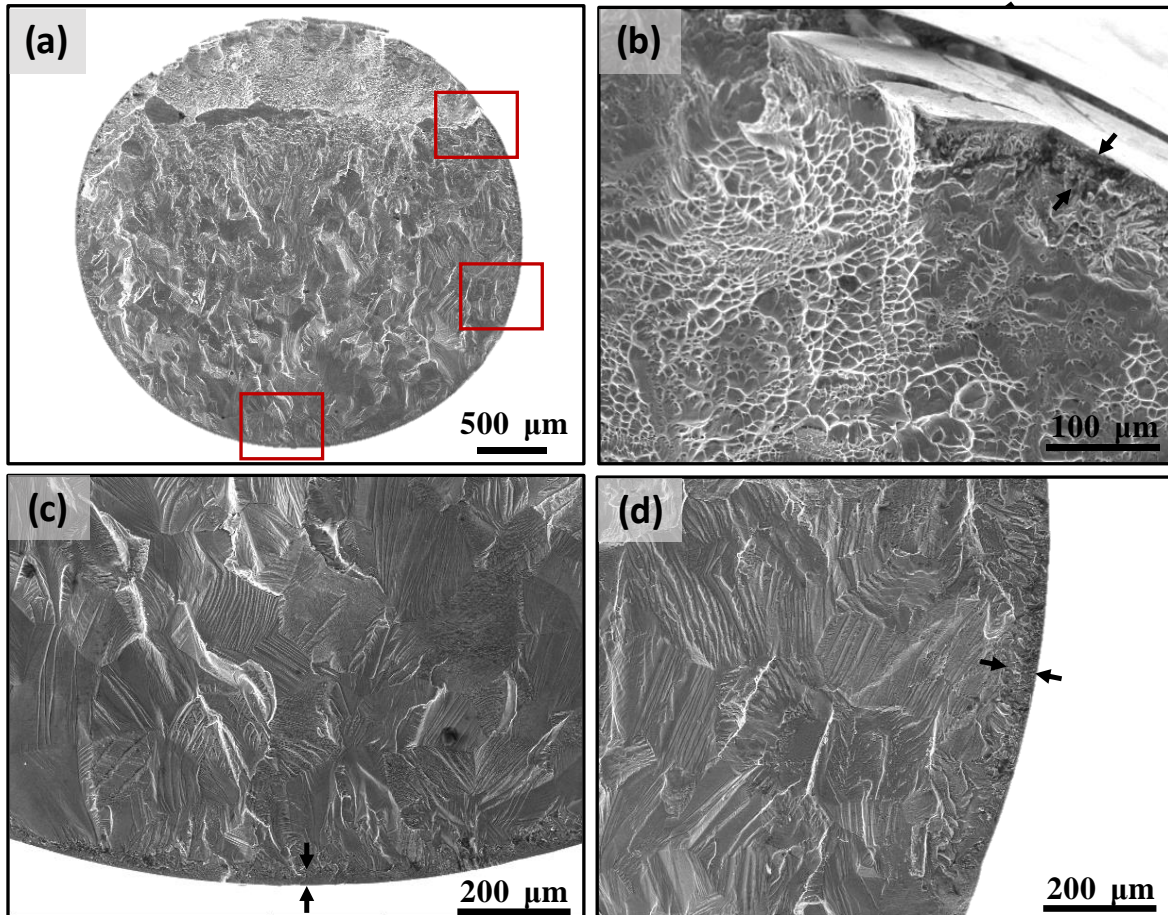


Figure 5.12 a) Fractography of nanopores sample, which was fatigue tested at 300 MPa, b) magnified zone of the final failure, c) and d) zone indicating a stable crack propagation region at the hydrogenated area, indicated by black arrows.

Table 5.6 shows the results of exploratory tensile testing of CST and nanopores specimens, together with the results of the untreated samples to determine if the hydrogen content produces significant changes in the tensile properties. A negligible difference in the yield strength and ultimate tensile strength was observed for the different treatments. Nevertheless, the elongation decreased in both treatments, but it was more evident in the nanopores samples.

Table 5.6 Tensile testing results of untreated, CST and nanopores samples.

	Yield strength 0.2% (MPa)	Tensile strength (MPa)	Elongation (%)
Untreated	1060 ±19	1071±14	17±2
CST	1059±18	1077±8	14±2
Nanopores	1020±20	1030±10	5±2

Additional to the elongation reduction, the untreated and treated samples showed different fracture characteristics, as observed in Figure 5.13. Untreated samples show a ductile fracture with evidence of plastic deformation and formation of a necking region. The magnified zone of the untreated sample in Figure 5.13 (a) displays deep dimples with conical shape. Unlike the CST and nanopores samples, the dimples become shallower due to the mode of fracture changed to intergranular decohesion in these hydrogen-embrittled samples (Figure 5.13 b and c).

The lateral view of the fractured samples displays more evidence of the hydrogen embrittlement mechanism. In Figure 5.13 b and c it is observed the presence of multiple secondary cracks that propagated in a direction perpendicular to the tensile axis. This peculiar crack grow is favored by the HELP mechanism.

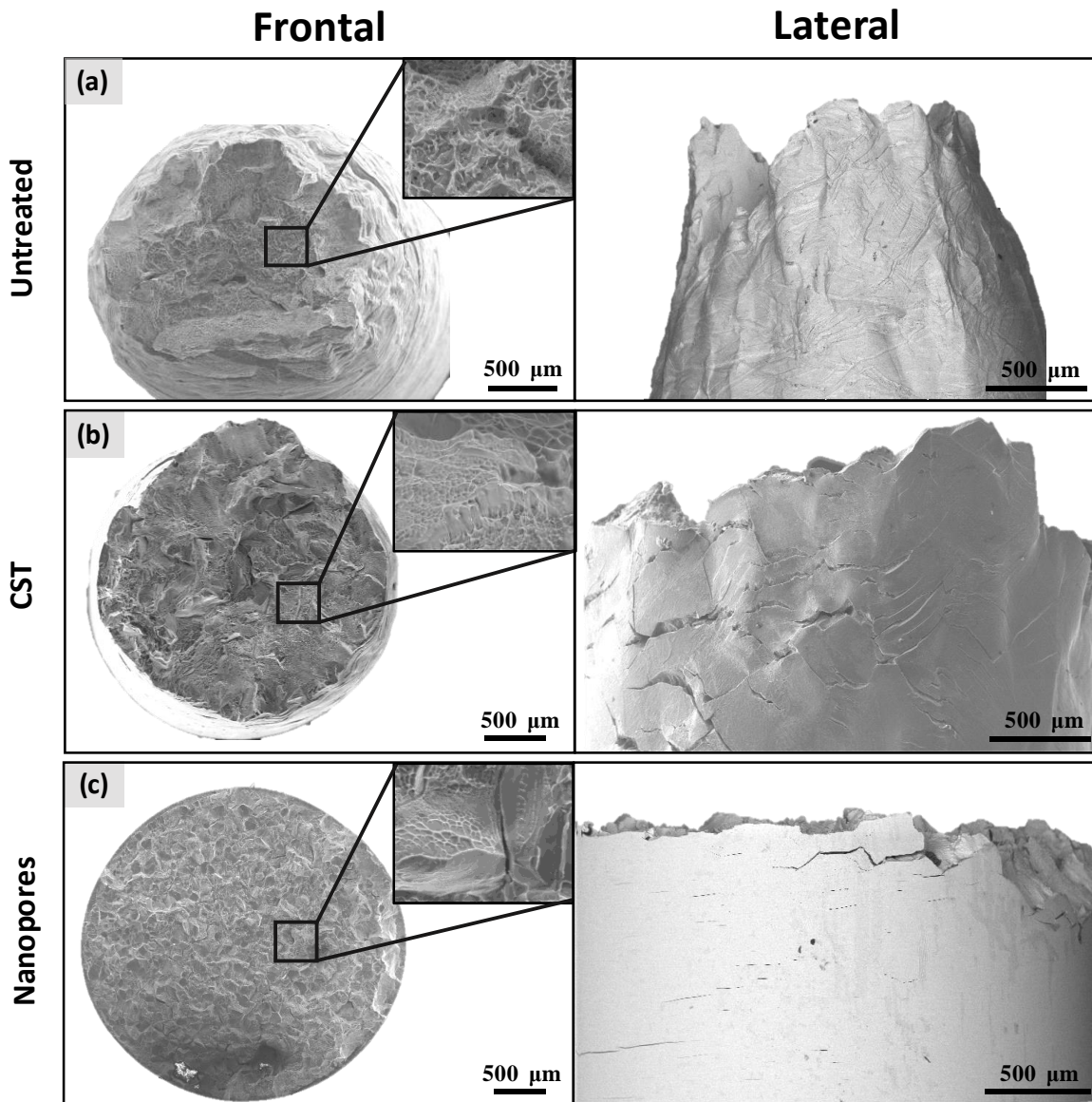


Figure 5.13 Frontal and lateral fractography of: a) untreated, b) CST and c) nanopores samples.

All of this fractographic information evidence the embrittlement processes produced by the hydrogen pick-up during the different surface treatments. Moreover, the drastic fatigue reduction observed in the NP specimens could indicate a higher hydrogen content that was not accurately detected during the measurement.

Table 5.7 summary of the fatigue response for the different surface conditions studied in this work.

	Roughness condition	Fatigue stress (MPa)	Fractographic Observations
Untreated	Polished surface	730	<ul style="list-style-type: none"> Well define fatigue striation and river patterns.
CST not -polished	Roughness	< 300	<ul style="list-style-type: none"> Circumferential crack propagation associated with HELP mechanism. High roughness, possibility of notch effect.
CST-polished	Polished surface	563	<ul style="list-style-type: none"> Secondary cracks at the grain boundaries. Evidence of hydride formation.
Nanopores	Soft	< 300	<ul style="list-style-type: none"> Intergranular fracture in samples tested at high stress level and correlated with the hydrogen-induced decohesion mechanism. Circumferential crack propagation associated with HELP mechanism.

As it was demonstrated in this chapter, hydrogen levels of 150 to 350 ppm could drastically reduce the fatigue strength of the TMZF titanium alloy (Table 5.7). However, some studies as the one developed by Y. Murakami et al. [140, 144] indicate that it is possible to revert this phenomenon through a hydrogen desorption process. They employed a special heat treatment called non diffusible hydrogen desorption-heat treatment (NDH-HT), to remove the hydrogen trapped at the interstitial sites. This process decreases substantially the hydrogen content whereby reduce the fatigue crack growth (Figure 5.14).

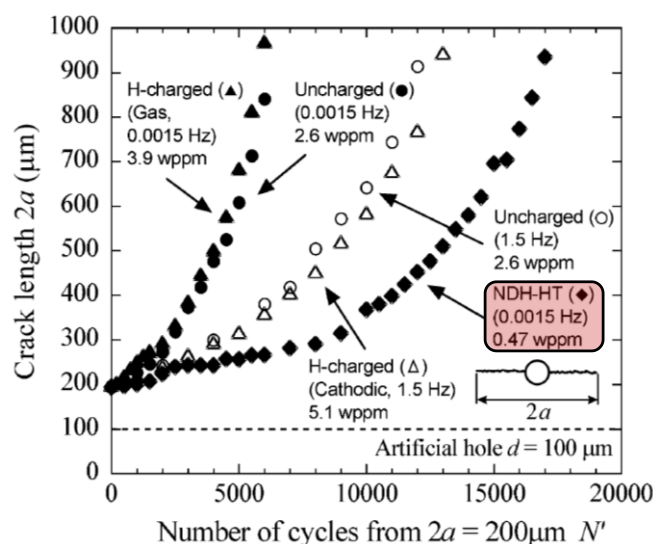


Figure 5.14 effect of the NDH-HT on crack growth rate of type 316L stainless steel (Extracted and edited from [144]).

In this chapter the fatigue response of untreated samples, treated with HCl and NaOH and nanopores samples was studied, and the conclusions are summarized in the following paragraphs:

- Untreated TMZF samples showed a high fatigue limit in terms of maximum stress of 730 MPa.
- Fatigue results of CST samples without subsequent polishing showed a drastic decrease in the fatigue resistance, greater than 50%, compared with the fatigue resistance of the untreated samples.
- CST-polished samples showed better fatigue behavior than the CST not-polished. However, they showed a decrease of 25% of the fatigue resistance compared with the untreated samples.
- Elemental analyses showed a significant increase in the hydrogen content in the samples treated with CST even after grinding and polishing the surface.
- Even with a slight increase in the hydrogen content, nanopores samples showed a dramatic reduction of the fatigue resistance, similar to the fatigue resistance of the CST not-polished.
- Clear evidence of brittle fracture was observed in the fractographies of the CST and nanopores samples called Wallner lines; these patterns are observed on fracture surfaces of brittle materials.
- In this study three principal hydrogen embrittlement mechanisms possibly acted over the treated samples: stress-induced hydride formation, hydrogen-induced decohesion and hydrogen-enhanced localized plasticity.
- Analysis by the automated crystal orientation mapping showed the presence of small TiH₂ particles or seeds. These hydrides increase the local dislocation density, favoring the micro-cracks nucleation.
- Evidence of the hydrogen-induced decohesion and HELP mechanisms were observed in the fractography of the nanopores and CST samples fatigue tested; however, more studies are necessary to certify these mechanisms.
- Equally, it was found evidence of the hydrogen embrittlement acting over the treated samples during the tensile testing, reducing the elongation and providing brittle fracture characteristics.
- The fatigue results and the hydrogen embrittlement mechanisms observed in this study point out the risk of well-known methods as cited in this chapter to design the titanium surface for osseointegration improvements.

General Conclusions

In this thesis it was studied the biocompatibility and corrosion performance of Ti-12Mo-6Zr-2Fe samples with nanotubes, nanopores and CST immersed during 0, 1, 7 and 14 days in SBF, as well as the fatigue resistance variation of untreated samples, treated with CST and nanopores. The conclusions from these analyses are summarized in the following paragraphs:

- Surface treatments as nanotubes, nanopores and CST on β -TMZF alloy were successfully obtained.
- After 14 days of immersion in SBF, nanotubes and nanopores samples showed a lower and moderate HAp formation (respectively). Meanwhile, the CST samples showed the best bioactivity behavior.
- Potentiodynamic polarization curves of nanotubes and nanopores surfaces revealed a more protective behavior against corrosion, placed them in the “Very stable” resistance class.
- Through the electrochemical tests, the CST samples showed a more reactive behavior independently of the immersion time in SBF.
- Impedance curves of the anodized samples revealed a pseudocapacitive behavior, corroborating the protective response of these surface conditions. Additionally, it was observed a particular behavior that could be modeled successfully by a transmission line model.
- Untreated TMZF samples showed a high fatigue limit in terms of maximum stress of 730 MPa.
- Fatigue results of CST samples showed a drastic decrease of the fatigue resistance around to 50% compared with the untreated samples, due to the notch effect and the additional high hydrogen content.
- In order to avoid the notch effect, new CST samples were polished and then fatigue tested. However, they showed a decrease of 25% of the fatigue resistance compared with the untreated samples, which was associated with the hydrogen absorbed during the CST.
- Even with a slight increase in the hydrogen measured, nanopore samples with low surface roughness showed a dramatic reduction in fatigue resistance, similar to the CST not-polished samples. This behavior was associated with the possibility of a high hydrogen concentration at the sample surface.
- In this study was observed evidence of three hydrogen embrittlement

mechanisms possibly acting over the treated samples. However, more studies are necessary to corroborate it.

- These results motivate us to conduct systematic evaluations of mechanical and electrochemical properties when metallic surfaces are modified to improve their osseointegration.

Further research

- Study alternative anodizing parameters and also complementary treatments above the two anodization processes to improve their HAp formation process.
- Study in more detail the hydrogen embrittlement mechanisms acting in the TMZF alloy.
- Investigate the hydrogen effect on another commercial β titanium alloys treated with CST, nanotubes, and nanopores.
- Investigate the possibility of reverting the hydrogen embrittlement phenomenon through hydrogen desorption processes.

References

- [1] S. Minagar, C. C. Berndt, J. Wang, E. Ivanova, and C. Wen, A review of the application of anodization for the fabrication of nanotubes on metal implant surfaces, *Acta Biomater.*, vol. 8, no. 8, pp. 2875–2888, 2012.
- [2] ASTM, F1813 Standard Specification for Wrought Titanium-12Molybdenum-6Zirconium-2Iron Alloy for Surgical Implant (UNS R58120), ASTM Int. Conshohocken, PA, www.astm.org, pp. 1–5, 2013.
- [3] T. Kokubo and S. Yamaguchi, Bioactive Metals Prepared by Surface Modification: Preparation and Properties Tadashi, vol. 52. Springer New York, 2011.
- [4] C. A. E. Claros and D. P. de Oliveira, Fatigue behavior of Ti–6Al–4V alloy in saline solution with the surface modified at a micro- and nanoscale by chemical treatment, *Mater. Sci. Eng. C*, vol. 67, pp. 425–432, 2016.
- [5] F. Hilario, V. Roche, R. P. Nogueira, and A. M. J. Junior, Influence of morphology and crystalline structure of TiO₂ nanotubes on their electrochemical properties and apatite-forming ability, *Electrochim. Acta*, vol. 245, pp. 337–349, 2017.
- [6] Technical Committee ISO/TC 150, International Standard ISO 23317: Implants for surgery — In vitro evaluation for apatite-forming ability of implant materials, 2014.
- [7] C. Leyens and M. Peters, *Titanium and Titanium Alloys*. 2003.
- [8] Y. Zheng, Nucleation Mechanisms of Refined Alpha Microstructure in Beta Titanium Alloys, no. May 2013, p. 211, 2013.
- [9] G. Lütjering and J. C. Williams, *Titanium*. Berlin, Heidelberg: Springer Berlin Heidelberg, 2007.
- [10] C. Leyens and M. Peters, Edited by *Handbook of Cellular Metals Phase Transformations in Materials*. 2003.
- [11] P. I. Branemark, U. Breine, B. Johansson, P. J. Roylance, H. Röckert, and J. M. Yoffey, REGENERATION OF BONE MARROW, Cells Tissues Organs, vol. 59. pp. 1–46, 1964.
- [12] International Titanium Association, *Titanium today, medical edition*. 2017.
- [13] R. Del Pozo, Jose, Patel, Infection Associated with Prosthetic Joints, *N. Engl. J. Med.*, vol. 361, no. 8, pp. 787–794, 2009.

- [14] Y. Li, C. Yang, H. Zhao, S. Qu, X. Li, and Y. Li, New Developments of Ti-Based Alloys for Biomedical Applications, *Materials (Basel)*., vol. 7, no. 3, pp. 1709–1800, 2014.
- [15] C. R. Schwartsmann, L. C. Boschin, R. Z. Gonçalves, A. K. Yépez, and L. De Freitas Spinelli, New bearing surfaces in total hip replacement, *Rev. Bras. Ortop.*, vol. 47, no. 2, pp. 154–159, 2012.
- [16] A. dos Santos, Comportamento mecânico da liga Ti-6Al-4V com superfície modificada por laser de femtosegundo para uso biomédico, Universidade Federal de São Carlos, 2012.
- [17] T. Narushima, New-generation metallic biomaterials, in *Metals for Biomedical Devices*, Elsevier, 2010, pp. 355–378.
- [18] M. Navarro, a Michiardi, O. Castaño, and J. a Planell, Biomaterials in orthopaedics., *J. R. Soc. Interface*, vol. 5, no. July, pp. 1137–1158, 2008.
- [19] Lütjering G. and W. J. C., *Titanium*. 2007.
- [20] Y. Oshida, *Bioscience and Bioengineering of Titanium Materials*, 1st ed. 2007.
- [21] M. Niinomi, Fatigue characteristics of metallic biomaterials, *Int. J. Fatigue*, vol. 29, pp. 992–1000, 2007.
- [22] D. Banerjee and J. C. Williams, Perspectives on titanium science and technology, *Acta Mater.*, vol. 61, no. 3, pp. 844–879, 2013.
- [23] L. D. Zardiackas, M. J. Kraay, and H. L. Freese, *Titanium, Niobium, Zirconium, and Tantalum for Medical and Surgical*. 2005.
- [24] F. Technique, R. Metals, R. Metals, T. Alloys, A. Bar, and T. Alloys, Standard Specification for Wrought Titanium-12Molybdenum-6Zirconium-2Iron Alloy for Surgical Implant (UNS R58120) 1, pp. 1–5, 2017.
- [25] K. K. Wang, Larry J Gustavson, and J. H. Dumbleton, Microstructure and properties of a new beta titanium alloy, Ti-12Mo- 6Zr-2Fe, developed for surgical implants, pp. 76–87, 1996.
- [26] X. Liu, P. K. Chu, and C. Ding, Surface modification of titanium, titanium alloys, and related materials for biomedical applications, *Mater. Sci. Eng. R Reports*, vol. 47, no. 2004, pp. 49–121, 2004.
- [27] D. P. De Oliveira, Tratamentos de superfície em Ti-CP , Ti-6Al-4V e Ti-6Al-7Nb visando a osseointegração de implantes : propriedades das superfícies e respostas osteoblásticas Tratamentos de superfície em Ti-CP , Ti-6Al-4V e Ti-6Al-7Nb visando a osseointegração de implantes, Universidade Federal de

- Sao Carlos, 2013.
- [28] R. Bränemark, P. I. Bränemark, B. Rydevik, and R. R. Myers, Osseointegration in skeletal reconstruction and rehabilitation: a review., *J. Rehabil. Res. Dev.*, vol. 38, no. 2, pp. 175–181, 2001.
 - [29] L. Le Guéhennec, a. Soueidan, P. Layrolle, and Y. Amouriq, Surface treatments of titanium dental implants for rapid osseointegration, *Dent. Mater.*, vol. 23, pp. 844–854, 2007.
 - [30] L. Jon, Biomimetic apatite formation on chemically treated titanium, vol. 25, pp. 1187–1194, 2004.
 - [31] L. Jonásová, F. a Müller, A. Helebrant, J. Strnad, and P. Greil, Hydroxyapatite formation on alkali-treated titanium with different content of Na⁺ in the surface layer., *Biomaterials*, vol. 23, no. 15, pp. 3095–101, 2002.
 - [32] H. Takadama, H. Kim, T. Kokubo, and T. Nakamura, An X-ray photoelectron spectroscopy study of the process of apatite formation on bioactive titanium metal, *J Biomed Mater Res.*, vol. 55, pp. 185–193, 2001.
 - [33] M. Wei, H. M. Kim, T. Kokubo, and J. H. Evans, Optimising the bioactivity of alkaline-treated titanium alloy, *Mater. Sci. Eng. C*, vol. 20, no. 1–2, pp. 125–134, 2002.
 - [34] A. Nagaoka, K. Yokoyama, and J. Sakai, Evaluation of hydrogen absorption behaviour during acid etching for surface modification of commercial pure Ti, Ti-6Al-4V and Ni-Ti superelastic alloys, *Corros. Sci.*, vol. 52, no. 4, pp. 1130–1138, 2010.
 - [35] K. Das, S. Bose, and A. Bandyopadhyay, TiO₂ nanotubes on Ti: Influence of nanoscale morphology on bone cell-materials interaction, *J. Biomed. Mater. Res. - Part A*, vol. 90, no. 1, pp. 225–237, 2009.
 - [36] F. Hilario, Synthèse et caractérisations de nanotubes de TiO₂ pour applications biomédicales : propriétés électrochimiques et bioactivité, Université Grenoble Alpes, 2018.
 - [37] M. Li, M. J. Mondrinos, X. Chen, M. R. Gandhi, F. K. Ko, and P. I. Lelkes, Elastin Blends for Tissue Engineering Scaffolds, *J. Biomed. Mater. Res. Part A*, vol. 79, no. 4, pp. 963–73, 2006.
 - [38] J. Park, S. Bauer, K. Von Der Mark, and P. Schmuki, Nanosize and vitality: TiO₂ nanotube diameter directs cell fate, *Nano Lett.*, vol. 7, no. 6, pp. 1686–1691, 2007.
 - [39] J. Park, S. Bauer, K. A. Schlegel, F. W. Neukam, K. Der Von Mark, and P.

- Schmuki, TiO₂ nanotube surfaces: 15 nm - an optimal length scale of surface topography for cell adhesion and differentiation, *Small*, vol. 5, no. 6, pp. 666–671, 2009.
- [40] K. Von Der Mark, S. Bauer, J. Park, and P. Schmuki, Another look at “Stem cell fate dictated solely by altered nanotube dimension,” *Proc. Natl. Acad. Sci. U. S. A.*, vol. 106, no. 24, p. 2009, 2009.
 - [41] Y. Wang, C. Wen, P. Hodgson, and Y. Li, Biocompatibility of TiO₂ nanotubes with different topographies, *J. Biomed. Mater. Res. - Part A*, vol. 102, no. 3, pp. 743–751, 2014.
 - [42] A. Jaroenworaluck, D. Regonini, C. R. Bowen, R. Stevens, and D. Allsopp, Macro, micro and nanostructure of TiO₂ anodised films prepared in a fluorine-containing electrolyte, *J. Mater. Sci.*, vol. 42, no. 16, pp. 6729–6734, 2007.
 - [43] K. Lee, A. Mazare, and P. Schmuki, One-Dimensional Titanium Dioxide Nanomaterials : Nanotubes, 2014.
 - [44] J. M. Macak, H. Tsuchiya, A. Ghicov, K. Yasuda, R. Hahn, S. Bauer, and P. Schmuki, TiO₂ nanotubes: Self-organized electrochemical formation, properties and applications, *Curr. Opin. Solid State Mater. Sci.*, vol. 11, no. 1–2, pp. 3–18, 2007.
 - [45] A. Roguska, M. Pisarek, M. Andrzejczuk, M. Dolata, M. Lewandowska, and M. Janik-Czachor, Characterization of a calcium phosphate- TiO₂ nanotube composite layer for biomedical applications, *Mater. Sci. Eng. C*, vol. 31, no. 5, pp. 906–914, 2011.
 - [46] N. K. Awad, S. L. Edwards, and Y. S. Morsi, A review of TiO₂ NTs on Ti metal: Electrochemical synthesis, functionalization and potential use as bone implants, *Mater. Sci. Eng. C*, vol. 76, pp. 1401–1412, 2017.
 - [47] W. Q. Yu, Y. L. Zhang, X. Q. Jiang, and F. Q. Zhang, In vitro behavior of MC3T3-E1 preosteoblast with different annealing temperature titania nanotubes, *Oral Dis.*, vol. 16, no. 7, pp. 624–630, 2010.
 - [48] J. Lario, M. Viera, Á. Vicente, A. Igual, and V. Amigó, Corrosion behaviour of Ti6Al4V ELI nanotubes for biomedical applications, *J. Mater. Res. Technol.*, vol. 8, no. 6, pp. 5548–5556, 2019.
 - [49] M. Niinomi, Metals for biomedical devices. 2010.
 - [50] Nestor Perez, Electrochemistry and Corrosion Science. 2016.
 - [51] B. N. Popov, Corrosion Engineering: Principles and Solved Problems. 2015.

- [52] S. Hiromoto and T. Hanawa, Corrosion of Implant Metals in the Presence of Cells, *Corros. Rev.*, vol. 24, no. 5–6, pp. 323–352, 2011.
- [53] E. V. Parfenov, L. V. Parfenova, G. S. Dyakonov, K. V. Danilko, V. R. Mukaeva, R. G. Farrakhov, E. S. Lukina, and R. Z. Valiev, Surface functionalization via PEO coating and RGD peptide for nanostructured titanium implants and their in vitro assessment, *Surf. Coatings Technol.*, vol. 357, no. October 2018, pp. 669–683, 2019.
- [54] A. C. Alves, F. Wenger, P. Ponthiaux, J. P. Celis, A. M. Pinto, L. A. Rocha, and J. C. S. Fernandes, Corrosion mechanisms in titanium oxide-based films produced by anodic treatment, *Electrochim. Acta*, vol. 234, pp. 16–27, 2017.
- [55] G. Denuault, *Electrochimie Physique et Analytique*, *J. Electroanal. Chem.*, 2002.
- [56] C. Boissy, *Transport de matière au sein du film passif - Développement d'une méthodologie sélective corrélant le Point Defect Model et les modèles descriptifs*, 2014.
- [57] M. E. Orazem and B. Tribollett, *Electrochemical Impedance Spectroscopy*. 2008.
- [58] A. Lasia, *Electrochemical impedance spectroscopy and its applications*, vol. 9781461489. 2014.
- [59] Mark E. Orazem and B. Tribollett, *Electrochemical Impedance Spectroscopy*, in *Agricultural and Food Electroanalysis*, Second edi., 2015, pp. 381–419.
- [60] P. Córdoba-Torres, N. T. C. Oliveira, C. Bolfarini, V. Roche, and R. P. Nogueira, Electrochemical impedance analysis of TiO₂ nanotube porous layers based on an alternative representation of impedance data, *J. Electroanal. Chem.*, vol. 737, pp. 54–64, 2015.
- [61] A. Garcia, J. A. Spim, and C. A. dos Santos, *Ensaio dos materiais*. 2000.
- [62] A. F. Padilha, *Materiais de engenharia*, p. 349, 1997.
- [63] P. P. Milella, *Fatigue and Corrosion in Metals*. 2013.
- [64] M. Long and H. J. Rack, Titanium alloys in total joint replacement--a materials science perspective., *Biomaterials*, vol. 19, pp. 1621–1639, 1998.
- [65] A. Heiskanen and J. Emnéus, Applications of Electrochemistry and Nanotechnology in Biology and Medicine I, vol. 52. 2011.
- [66] L. Pazos, P. Corengia, and H. Svoboda, Effect of surface treatments on the fatigue life of titanium for biomedical applications, *J. Mech. Behav. Biomed.*

- Mater., vol. 3, no. 6, pp. 416–424, 2010.
- [67] C. Leinenbach, B. Schwilling, and D. Eifler, Cyclic deformation behaviour and fatigue induced surface damage of titanium alloys in simulated physiological media, *Mater. Sci. Eng. C*, vol. 25, no. 3, pp. 321–329, 2005.
 - [68] C. Leinenbach and D. Eifler, Fatigue and cyclic deformation behaviour of surface-modified titanium alloys in simulated physiological media, *Biomaterials*, vol. 27, no. 8, pp. 1200–1208, 2006.
 - [69] I. Apachitei, B. Lonyuk, L. E. Fratila-Apachitei, J. Zhou, and J. Duszczyk, Fatigue response of porous coated titanium biomedical alloys, *Scr. Mater.*, vol. 61, no. 2, pp. 113–116, 2009.
 - [70] P. S. C. P. da Silva, L. C. Campanelli, C. A. Escobar Claros, T. Ferreira, D. P. Oliveira, and C. Bolfarini, Prediction of the surface finishing roughness effect on the fatigue resistance of Ti-6Al-4V ELI for implants applications, *Int. J. Fatigue*, vol. 103, pp. 258–263, 2017.
 - [71] L. C. Campanelli, C. C. Bortolan, P. S. C. P. da Silva, C. Bolfarini, and N. T. C. Oliveira, Effect of an amorphous titania nanotubes coating on the fatigue and corrosion behaviors of the biomedical Ti-6Al-4V and Ti-6Al-7Nb alloys, *J. Mech. Behav. Biomed. Mater.*, vol. 65, pp. 542–551, 2017.
 - [72] C. Fu, W. Tian, K. Yang, M. Yu, and J. Liu, Effects of sodium tartrate anodizing on fatigue life of TA15 titanium alloy, *Chinese J. Aeronaut.*, vol. 28, no. 4, pp. 1281–1286, 2015.
 - [73] L. C. Campanelli, P. S. C. P. da Silva, A. M. Jorge, and C. Bolfarini, Effect of hydrogen on the fatigue behavior of the near- β Ti-5Al-5Mo-5V-3Cr alloy, *Scr. Mater.*, vol. 132, pp. 39–43, 2017.
 - [74] ASTM, Standard Practice for Conducting Force Controlled Constant Amplitude Axial Fatigue Tests of Metallic Materials, *Test*, vol. 03, pp. 4–8, 2002.
 - [75] F. Hilario, V. Roche, A. M. Jorge, and R. P. Nogueira, Application of the transmission line model for porous electrodes to analyse the impedance response of TiO_2 nanotubes in physiological environment, *Electrochim. Acta*, vol. 253, pp. 599–608, 2017.
 - [76] T. Kokubo and H. Takadama, How useful is SBF in predicting in vivo bone bioactivity?, *Biomaterials*, vol. 27, no. 15, pp. 2907–2915, 2006.
 - [77] S. Fletcher*, The two-terminal equivalent network of a three-terminal electrochemical cell, *Electrochim. Acta*, vol. 55, no. 6, pp. 1907–1911, 2010.

- [78] International Organization for Standardization, Metallic materials — Fatigue testing — Statistical planning and analysis of data 12107:2003, 2003.
- [79] H. Takadama, H. M. Kim, T. Kokubo, and T. Nakamura, TEM-EDX study of mechanism of bonelike apatite formation on bioactive titanium metal in simulated body fluid, *J. Biomed. Mater. Res.*, vol. 57, no. 3, pp. 441–448, 2001.
- [80] Zahid Amjad, Calcium phosphates in biological and industrial systems, p. 368, 1998.
- [81] H. Tsuchiya, J. M. Macak, L. Mu, J. Kunze, F. Mu, and P. Greil, Hydroxyapatite growth on anodic TiO₂ nanotubes, pp. 23–25, 2006.
- [82] S. Yamaguchi, H. Hashimoto, R. Nakai, and H. Takadama, Impact of surface potential on apatite formation in Ti alloys subjected to acid and heat treatments, *Materials (Basel.)*, vol. 10, no. 10, 2017.
- [83] R. J. Narayan, ASM Handbook, Volume 23 Materials for Medical Devices, 1 st., vol. 23. 2012.
- [84] A. K. Shukla, R. Balasubramaniam, and S. Bhargava, Properties of passive film formed on CP titanium, Ti-6Al-4V and Ti-13.4Al-29Nb alloys in simulated human body conditions, *Intermetallics*, vol. 13, no. 6, pp. 631–637, 2005.
- [85] E. Vasilescu, P. Drob, D. Raducanu, I. Cinca, D. Mareci, J. M. Calderon Moreno, M. Popa, C. Vasilescu, and J. C. Mirza Rosca, Effect of thermo-mechanical processing on the corrosion resistance of Ti6Al4V alloys in biofluids, *Corros. Sci.*, vol. 51, no. 12, pp. 2885–2896, 2009.
- [86] S. Tamilselvi, V. Raman, and N. Rajendran, Surface modification of titanium by chemical and thermal methods - Electrochemical impedance spectroscopic studies, *Corros. Eng. Sci. Technol.*, vol. 46, no. 4, pp. 585–591, 2011.
- [87] S. Y. Kim, Y. K. Kim, Y. S. Jang, I. S. Park, S. J. Lee, J. G. Jeon, and M. H. Lee, Bioactive effect of alkali-heat treated TiO₂ nanotubes by water or acid treatment, *Surf. Coatings Technol.*, vol. 303, pp. 256–267, 2016.
- [88] M. L. D. C. R. D. A. Carvalho, Corrosion of copper alloys in natural seawater – Effects of hydrodynamics and pH, UNIVERSITÉ PIERRE ET MARIE CURIE, 2014.
- [89] V. Augustyn, P. Simon, and B. Dunn, Pseudocapacitive oxide materials for high-rate electrochemical energy storage, *Energy Environ. Sci.*, vol. 7, no. 5, pp. 1597–1614, 2014.
- [90] M. A. Macdonald and H. A. Andreas, Method for equivalent circuit determination for electrochemical impedance spectroscopy data of protein

- adsorption on solid surfaces, *Electrochim. Acta*, vol. 129, pp. 290–299, 2014.
- [91] H. Luo, C. F. Dong, X. G. Li, and K. Xiao, The electrochemical behaviour of 2205 duplex stainless steel in alkaline solutions with different pH in the presence of chloride, *Electrochim. Acta*, vol. 64, pp. 211–220, 2012.
 - [92] N. Ebrahimi, M. Momeni, A. Kosari, M. Zakeri, and M. H. Moayed, A comparative study of critical pitting temperature (CPT) of stainless steels by electrochemical impedance spectroscopy (EIS), potentiodynamic and potentiostatic techniques, *Corros. Sci.*, vol. 59, pp. 96–102, 2012.
 - [93] D. Q. Martins, W. R. Osório, M. E. P. Souza, R. Caram, and A. Garcia, Effects of Zr content on microstructure and corrosion resistance of Ti-30Nb-Zr casting alloys for biomedical applications, *Electrochim. Acta*, vol. 53, no. 6, pp. 2809–2817, 2008.
 - [94] M. E. Orazem, N. Pábre, and B. Tribollet, Enhanced graphical representation of electrochemical impedance data, *J. Electrochem. Soc.*, vol. 153, no. 4, pp. 129–136, 2006.
 - [95] H. Liu, J. Yang, X. Zhao, Y. Sheng, W. Li, C. L. Chang, Q. Zhang, Z. Yu, and X. Wang, Microstructure, mechanical properties and corrosion behaviors of biomedical Ti-Zr-Mo-xMn alloys for dental application, *Corros. Sci.*, vol. 161, no. May, pp. 2–15, 2019.
 - [96] S. L. De Assis, S. Wolynec, and I. Costa, Corrosion characterization of titanium alloys by electrochemical techniques, *Electrochim. Acta*, vol. 51, no. 8–9, pp. 1815–1819, 2006.
 - [97] A. Kocijan, D. K. Merl, and M. Jenko, The corrosion behaviour of austenitic and duplex stainless steels in artificial saliva with the addition of fluoride, *Corros. Sci.*, vol. 53, no. 2, pp. 776–783, 2011.
 - [98] K. B. Devi, K. Singh, and N. Rajendran, Synthesis and characterization of nanoporous sodium-substituted hydrophilic titania ceramics coated on 316L SS for biomedical applications, *J. Coatings Technol. Res.*, vol. 8, no. 5, pp. 595–604, 2011.
 - [99] S. Gudi, J. Radoševi, and M. Kliški, Study of passivation of Al and Al-Sn alloys in borate buffer solutions using electrochemical impedance spectroscopy, *Electrochim. Acta*, vol. 47, no. 18, pp. 3009–3016, 2002.
 - [100] A. W. E. Hodgson, Y. Mueller, D. Forster, and S. Virtanen, Electrochemical characterisation of passive films on Ti alloys under simulated biological conditions, *Electrochim. Acta*, vol. 47, no. 12, pp. 1913–1923, 2002.

- [101] M. Cai and S. M. Park, Oxidation of zinc in alkaline solutions studied by electrochemical impedance spectroscopy, *J. Electrochem. Soc.*, vol. 143, no. 12, pp. 3895–3902, 1996.
- [102] T. Kokubo, F. Miyaji, H.-M. Kim, and T. Nakamura, Spontaneous Formation of Bonelike Apatite Layer on Chemically Treated Titanium Metals, *J. Am. Ceram. Soc.*, vol. 79, pp. 1127–1129, 1996.
- [103] H. M. Kim, F. Miyaji, T. Kokubo, and T. Nakamura, Preparation of bioactive Ti and its alloys via simple chemical surface treatment., *J. Biomed. Mater. Res.*, vol. 32, pp. 409–417, 1996.
- [104] L. Jonášová, F. a. Müller, A. Helebrant, J. Strnad, and P. Greil, Biomimetic apatite formation on chemically treated titanium, *Biomaterials*, vol. 25, pp. 1187–1194, 2004.
- [105] S. Ban, Y. Iwaya, H. Kono, and H. Sato, Surface modification of titanium by etching in concentrated sulfuric acid, *Dent. Mater.*, vol. 22, pp. 1115–1120, 2006.
- [106] J. Bisquert, Influence of the boundaries in the impedance of porous film electrodes, 2000.
- [107] M. Schlesinger, Modelling and Numerical Simulations II, vol. 44, no. 4. 2009.
- [108] Diego Alfonso Godoy Pérez, Influence Of Surface Treatments on Corrosion Resistance Properties Of Ultrafine Grained Titanium Alloys For Biomedical applications, Universite Grenoble Alpes And Universidade Federal De São Carlos, 2019.
- [109] L. Mohan, C. Anandan, and N. Rajendran, Electrochemical behavior and effect of heat treatment on morphology, crystalline structure of self-organized TiO_2 nanotube arrays on Ti–6Al–7Nb for biomedical applications, *Mater. Sci. Eng. C*, vol. 50, pp. 394–401, 2015.
- [110] A. Mazare, M. Dilea, D. Ionita, and I. Demetrescu, Electrochemical behavior in simulated body fluid of TiO_2 nanotubes on TiAlNb alloy elaborated in various anodizing electrolyte, *Surf. Interface Anal.*, vol. 46, no. 3, pp. 186–192, 2014.
- [111] C. Liu, Y. Wang, M. Wang, W. Huang, and P. K. Chu, Electrochemical stability of TiO_2 nanotubes with different diameters in artificial saliva, *Surf. Coatings Technol.*, vol. 206, no. 1, pp. 63–67, 2011.
- [112] B. Munirathinam and L. Neelakantan, Titania nanotubes from weak organic acid electrolyte: Fabrication, characterization and oxide film properties, *Mater. Sci. Eng. C*, vol. 49, pp. 567–578, 2015.

- [113] B. Munirathinam, H. Pydimukkala, N. Ramaswamy, and L. Neelakantan, Influence of crystallite size and surface morphology on electrochemical properties of annealed TiO₂ nanotubes, *Appl. Surf. Sci.*, vol. 355, pp. 1245–1253, 2015.
- [114] L. V. Taveira, J. M. Macák, H. Tsuchiya, L. F. P. Dick, and P. Schmuki, Initiation and growth of self-organized TiO₂ nanotubes anodically formed in NH₄F/(NH₄)₂SO₄ electrolytes, *J. Electrochem. Soc.*, vol. 152, no. 10, pp. 2–8, 2005.
- [115] R. de Levie, On porous electrodes in electrolyte solutions*, *Electrochim. Acta*, vol. 9, no. 9, pp. 1231–1245, 1964.
- [116] R. de Levie, On porous electrodes in electrolyte solutions-IV, *Electrochim. Acta*, vol. 9, no. 9, pp. 1231–1245, 1964.
- [117] J. Bisquert, G. Garcia-Belmonte, F. Fabregat-Santiago, N. S. Ferriols, P. Bogdanoff, and E. C. Pereira, Doubling Exponent Models for the Analysis of Porous Film Electrodes by Impedance. Relaxation of TiO₂ Nanoporous in Aqueous Solution, *J. Phys. Chem. B*, vol. 104, no. 10, pp. 2287–2298, 2000.
- [118] S. Gimenez, H. K. Dunn, P. Rodenas, F. Fabregat-Santiago, S. G. Miralles, E. M. Barea, R. Trevisan, A. Guerrero, and J. Bisquert, Carrier density and interfacial kinetics of mesoporous TiO₂ in aqueous electrolyte determined by impedance spectroscopy, *J. Electroanal. Chem.*, vol. 668, pp. 119–125, 2012.
- [119] H. L. Yao, G. J. Yang, C. X. Li, and C. J. Li, Influence of TiO₂ film/substrate contact on photovoltaic performance and improved efficiency in dye-sensitized solar cells, *J. Nanosci. Nanotechnol.*, vol. 16, no. 7, pp. 7395–7403, 2016.
- [120] M. Mahbuburrahman, N. Chandraebnath, and J. J. Lee, Electrochemical Impedance Spectroscopic Analysis of Sensitization-Based Solar Cells, *Isr. J. Chem.*, vol. 55, no. 9, pp. 990–1001, 2015.
- [121] R. de Levie, Electrochemical Responses of Porous and Rough Electrodes,” in *Advances in Electrochemistry and Electrochemical Engineering*, vol. 6, pp. 329–397, 1967.
- [122] P. Roy, S. Berger, and P. Schmuki, TiO₂ nanotubes: Synthesis and applications, *Angew. Chemie - Int. Ed.*, vol. 50, no. 13, pp. 2904–2939, 2011.
- [123] G. Garcia-Belmonte, J. Bisquert, E. C. Pereira, and F. Fabregat-Santiago, Switching behaviour in lightly doped polymeric porous film electrodes. Improving distributed impedance models for mixed conduction conditions, *J. Electroanal. Chem.*, vol. 508, no. 1–2, pp. 48–58, 2001.

- [124] G. Láng and K. E. Heusler, Remarks on the energetics of interfaces exhibiting constant phase element behaviour, *J. Electroanal. Chem.*, vol. 457, no. 1–2, pp. 257–260, 1998.
- [125] T. Pajkossy, Impedance of rough capacitive electrodes, *J. Electroanal. Chem.*, vol. 364, no. 1–2, pp. 111–125, 1994.
- [126] C. Shuai, H. Sun, P. Wu, C. Gao, Y. Yang, W. Guo, D. Yang, F. Xu, P. Feng, and S. Peng, Biosilicate scaffolds for bone regeneration: Influence of introducing SrO, *RSC Adv.*, vol. 7, no. 35, pp. 21749–21757, 2017.
- [127] ASTM, Standard Practice for Conducting Force Controlled Constant Amplitude Axial Fatigue Tests of Metallic Materials - E466-15, Test, vol. 03, pp. 4–8, 2015.
- [128] B. J. S. de Oliveira, L. C. Campanelli, D. P. Oliveira, A. P. de Bribean Guerra, and C. Bolfarini, Surface characterization and fatigue performance of a chemical-etched Ti-6Al-4V femoral stem for cementless hip arthroplasty, *Surf. Coatings Technol.*, vol. 309, pp. 1126–1134, 2017.
- [129] C. A. Escobar Claros, Estudo da resistência à fadiga da liga Ti-6Al-4V com superfície modificada por tratamento químico, Universidad de Sao carlos, 2016.
- [130] V. Madina and I. Azkarate, Compatibility of materials with hydrogen. Particular case: Hydrogen embrittlement of titanium alloys, *Int. J. Hydrogen Energy*, vol. 34, no. 14, pp. 5976–5980, 2009.
- [131] L. C. Campanelli, P. S. C. P. da Silva, A. M. Jorge, and C. Bolfarini, Effect of hydrogen on the fatigue behavior of the near- β Ti-5Al-5Mo-5V-3Cr alloy, *Scr. Mater.*, vol. 132, pp. 39–43, 2017.
- [132] ASM International. Handbook, *ASM Handbook: Volume 12: Fractography*, Met. Handb., vol. 2, p. 857, 1998.
- [133] ASM, *ASM Handbook Volume 12: Fractography*, vol. 2. 1987.
- [134] L. C. Campanelli, P. S. C. P. da Silva, and C. Bolfarini, High cycle fatigue and fracture behavior of Ti-5Al-5Mo-5V-3Cr alloy with BASCA and double aging treatments, *Mater. Sci. Eng. A*, vol. 658, pp. 203–209, 2016.
- [135] Y. Chang, A. J. Breen, Z. Tarzimoghadam, P. Kürnsteiner, H. Gardner, A. Ackerman, A. Radecka, P. A. J. Bagot, W. Lu, T. Li, E. A. Jägle, M. Herbig, L. T. Stephenson, M. P. Moody, D. Rugg, D. Dye, D. Ponge, D. Raabe, and B. Gault, Characterizing solute hydrogen and hydrides in pure and alloyed titanium at the atomic scale, *Acta Mater.*, vol. 150, pp. 273–280, 2018.

- [136] P. D. Nezhadfar, A. S. Johnson, and N. Shamsaei, Fatigue Behavior and Microstructural Evolution of Additively Manufactured Inconel 718 under Cyclic Loading at Elevated Temperature, *Int. J. Fatigue*, p. 105598, 2020.
- [137] D. F. Teter, I. M. Robertson, and H. K. Birnbaum, The effects of hydrogen on the deformation and fracture of β -titanium, *Acta Mater.*, vol. 49, no. 20, pp. 4313–4323, 2001.
- [138] A. M. Alvarez, I. M. Robertson, and H. K. Birnbaum, Hydrogen embrittlement of a metastable β -titanium alloy, *Acta Mater.*, vol. 52, no. 14, pp. 4161–4175, 2004.
- [139] W. Barrows, R. Dingreville, and D. Spearot, Traction-separation relationships for hydrogen induced grain boundary embrittlement in nickel via molecular dynamics simulations, *Mater. Sci. Eng. A*, vol. 650, pp. 354–364, 2016.
- [140] Y. Murakami, J. Yamabe, and H. Matsunaga, Microscopic mechanism of hydrogen embrittlement in fatigue and fracture, *Key Eng. Mater.*, vol. 592–593, pp. 3–13, 2014.
- [141] E. Tal-Gutelmacher and D. Eliezer, Hydrogen-assisted degradation of titanium based alloys, *Mater. Trans.*, vol. 45, no. 5, pp. 1594–1600, 2004.
- [142] J. Von Pezold, L. Lymerakis, and J. Neugebeauer, Hydrogen-enhanced local plasticity at dilute bulk H concentrations: The role of H-H interactions and the formation of local hydrides, *Acta Mater.*, vol. 59, no. 8, pp. 2969–2980, 2011.
- [143] P. J. Ferreira, I. M. Robertson, and H. K. Birnbaum, Hydrogen effects on the character of dislocations in high-purity aluminum, *Acta Mater.*, vol. 47, no. 10, pp. 2991–2998, 1999.
- [144] Y. Murakami, T. Kanezaki, Y. Mine, and S. Matsuoka, Hydrogen embrittlement mechanism in fatigue of austenitic stainless steels, *Metall. Mater. Trans. A Phys. Metall. Mater. Sci.*, vol. 39 A, no. 6, pp. 1327–1339, 2008.

Résumé Détailé en Français

ÉTUDE DE BIOACTIVITÉ, RÉSISTANCE A LA CORROSION ET COMPORTEMENT EN FATIGUE DE L'ALLIAGE Ti-12Mo-6Zr-2Fe APRÈS DIFFÉRENTS TRAITEMENTS DE SURFACE

1 Introduction

Les alliages métalliques pour implants orthopédiques doivent présenter quatre caractéristiques essentielles : a) phénomène de *stress-shielding* (lié à la différence de module d'élasticité entre l'os et l'implant) faible ; b) biocompatibilité (pas d'éléments toxiques) ; c) excellente résistance à la fatigue pour des implants soumis à des contraintes cycliques et d) résistance à la corrosion élevée [1].

En raison de la présence d'éléments comme Al et V, considérés cytotoxiques, et en raison du haut module d'élasticité du Ti–6Al–4V-ELI (~110 GPa), de nouveaux alliages de titane sans éléments toxiques et avec un module d'élasticité inférieur ont été étudiés. Les alliages β -titane métastables, comme l'alliage Ti-12Mo-6Zr-2Fe, présentent une résistance mécanique élevée et un module d'élasticité inférieur à celui du Ti–6Al–4V-ELI [2].

Les matériaux métalliques comme le titane et ses alliages, l'acier inoxydable et les alliages à base de cobalt-chrome sont utilisés comme biomatériaux pour leurs propriétés mécaniques. Néanmoins, le contact direct métal-os ne suppose pas la formation d'une liaison forte entre eux. Ainsi, il est nécessaire de développer des surfaces plus bioactives sur de tels matériaux [3].

Quelques traitements de surface sont appliqués sur les alliages de titane pour améliorer leur processus d'ostéo-intégration. Des études antérieures ont démontré que le traitement d'attaque chimique avec HCl et NaOH peut être une manière efficace de développer des caractéristiques nanométriques sur la surface d'échantillons de Ti–6Al–4V-ELI (ELI, en anglais, pour *Extra Low Interstitial content*), sans changer ses propriétés mécaniques [4].

Une alternative au traitement chimique de surface (CST) est le procédé d'anodisation. Il est largement utilisé sur titane pur et permet de créer des nanotubes de TiO_2 sur la surface, en maximisant l'aire spécifique de la surface du matériel et d'obtenir une meilleure biocompatibilité [5].

Un indicateur de capacité de formation osseuse dans les implants métalliques est la nucléation et croissance d'une couche d'hydroxyapatite (HAp). Cette capacité peut être mesurée par l'immersion de l'échantillon dans SBF solution (en anglais, pour *Simulated Body Fluid*), dont les concentrations d'ions sont presque les mêmes que celles du plasma sanguin humain [3, 6].

Ainsi, l'objectif principal de ce projet est d'étudier la performance en biocompatibilité et en corrosion d'échantillons de Ti-12Mo-6Zr-2Fe avec nanotubes, nanopores et CST immersés pendant des durées différentes dans SBF, et la résistance à la fatigue de ces différentes conditions de surface.

2 Matériaux et Méthodes

Quatre conditions différentes de surface ont été étudiées avec des substrats de TMZF : surface sans traitement, surface traitée avec HCl et solution alcaline de NaOH (CST) et deux conditions anodisées – NT et NP.

La modification avec CST des échantillons a été réalisée en deux étapes : d'abord avec HCl et ensuite avec NaOH. Pour l'attaque acide, une plaque chauffée à 60 °C pendant 30 min a été utilisée. Les traitements alcalins ont été préparés dans un récipient en polyéthylène contenant 45 ml de NaOH 10 mol·L⁻¹ pour chaque échantillon, et un four avec un contrôleur numérique a été utilisé pour maintenir le milieu alcalin à 60 °C pendant 24h.

Les nanostructures de TiO₂ ont été, quant à elles, obtenues par anodisation des échantillons polis dans une cellule électrochimique selon un montage classique à deux électrodes. Les essais d'anodisation ont été réalisés à 25 °C, dans un électrolyte organique à base de glycérol contenant 25 vol% d'eau et 0.25M de NH₄F. Le potentiel appliqué pour l'obtention des nanotubes était de 10V pendant 2h et 20V pendant 2h pour les nanopores. Après l'étape d'anodisation, les échantillons ont été recuits à 550°C pendant 2h sous air, pour cristalliser les nanotubes TiO₂ et obtenir un mélange de phases anatase et rutile.

Pour les études en corrosion, trois techniques électrochimiques ont été employées en utilisant une solution électrolytique de SBF à 37°C et pH 7.4, dans l'obscurité, afin de reproduire les conditions corporelles. Une cellule conventionnelle à trois électrodes a été utilisée : les échantillons de TMZF étaient l'électrode de travail, avec une aire exposée de 0.283 cm²; une grille en platine, la contre-électrode ; et une Électrode au Calomel Saturé (ECS, ou SCE en anglais, pour *Saturated Calomel Electrode*), l'électrode de référence. La distance entre l'électrode de travail et la contre-électrode était de ~3 cm. Initialement, le potentiel en circuit ouvert (OCP, pour *open circuit potential*) a été enregistré pendant une heure d'immersion dans l'électrolyte. Ensuite, les mesures de la spectroscopie SIE ont été enregistrés avec une gamme de fréquence allant de 100 MHz à 20 mHz avec un signal de perturbation sinusoïdale d'amplitude 10 mV par rapport à l'OCP (amplitude suffisamment grande pour que le signal de sortie soit facilement mesurable mais qui permet également de satisfaire au critère de linéarité) et, finalement, les courbes de polarisation potentiodynamique, sur la gamme -0.03 V/ECS à +1.2 V/ECS par rapport à l'OCP avec une vitesse de balayage de 0.3 mVs⁻¹. Ces mesures

électrochimiques ont été réalisées avec les échantillons non traités, Nt, NP et CST pour quatre temps différents d'immersion : 0, 1, 7 et 14 jours, dans la solution SBF. Trois échantillons ont été étudiés pour chaque condition et durée.

Après avoir réalisé les caractérisations électrochimiques et de bioactivité, les conditions des surfaces qui présentaient les meilleurs résultats ont été évaluées pour déterminer si ces modifications affectent la résistance à la fatigue, à l'aide d'un essai de fatigue à grand nombre de cycles, protocole de type *Staircase* (ou méthode de l'escalier).

3 Bioactivité et comportement électrochimique d'échantillons de TMZF traités avec CST, nanopores et nanotubes

La réponse biologique et électrochimique du titane commercialement pur et de l'alliage Ti-6Al-4V ELI, traité avec des procédures chimiques et électrochimiques, a été largement étudiée. Néanmoins, le besoin d'utiliser des alliages de β -titane avec un faible module d'élasticité rend intéressant l'étude de ces traitements dans des alliages commerciaux de β -Ti, comme Ti-12Mo-6Zr-2Fe (TMZF).

Dans ce chapitre, la mesure de gain de masse d'hydroxyapatite (HAp) a été réalisé en tant qu'indicateur du comportement de l'ostéo-intégration des différents traitements de surface de TMZF. En outre, le résultat de croissance de HAp d'échantillons immergés dans la solution SBF a été confirmé par les techniques de Microscope Electronique à Balayage (MEB, ou SEM en anglais, pour *Scanning Electron Microscope*), EDS (pour *Energy Dispersive Spectroscopy*), de Diffraction des Rayons X (DRX, ou XRD en anglais, pour *X-Ray Diffraction*) et cartographie Raman.

Les images sur la Figure 3.1 font référence à l'échantillon traité avec l'acide chlorhydrique (HCl) et Hydroxyde de Sodium (NaOH) ; il est possible d'observer l'effet de l'attaque sur toute la surface polie, qui modifie la morphologie souple initiale pour une surface en micropores uniformément distribués et qui révèle aussi la limite des grains. Un grossissement supérieur (Figure 3.1 b) a été utilisé pour évaluer la présence de caractéristiques nanométriques sur la surface des échantillons, ce qui confirme l'effet du NaOH. Il a été possible d'y observer des structures du type corail à l'échelle submicrométrique et nanométrique formées pendant le traitement alcalin.

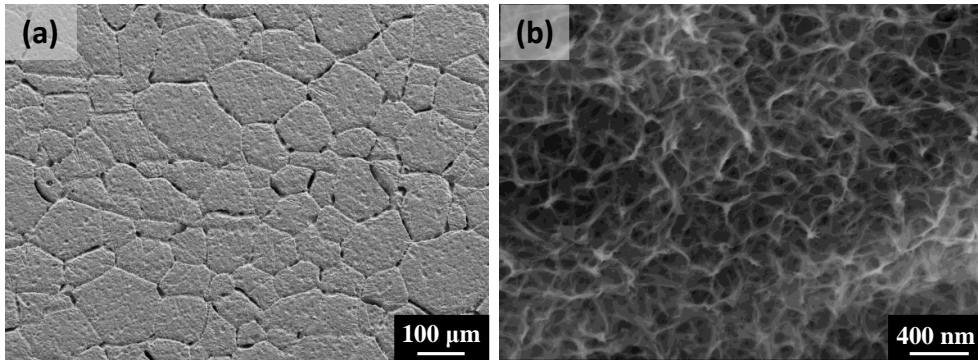


Figure 3.1 Images MEB de l'alliage de TMZF, chimiquement traité par HCl 37% à 60 °C et NaOH 10 mol·L⁻¹ à 60 °C pendant 24h.

L'image MEB à haute résolution sur la Figure 3.2 montre l'état de surface finale de deux échantillons différents anodisés étudiés dans ce travail. La Figure 3.2 (a) montre la formation d'un réseau de tubes auto organisés verticalement et distribués uniformément sur toute la surface, alors que la Figure 3.2 (b) montre une structure nanométrique désordonnée ; cette dernière surface de mésopores a été identifiée comme nanopores.

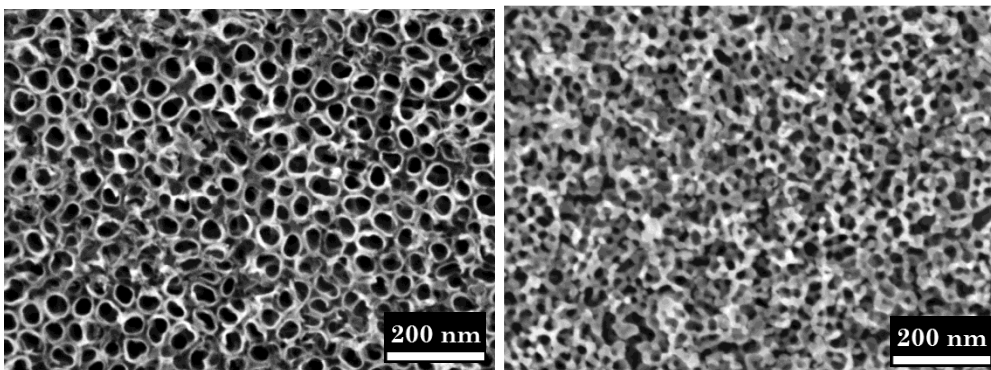


Figure 3.2 MEB à haute résolution d'échantillons anodisés : a) Nanotubes et b) Nanopores.

3.1 Essai de formation de l'Hydroxyapatite

La Figure 3.3 résume la valeur moyenne de gain de masse pour trois échantillons de chaque condition de surface pendant les différentes périodes. Il est possible de voir qu'il n'y a pas de dépôt d'apatite sur l'alliage de TMZF non traité. Pour la surface recouverte de NT, le gain de masse est nul à 1 jour et augmente jusqu'à 14j mais reste toujours assez faible. En revanche, les échantillons avec les nanopores montrent une formation de HAp dès le jour 1 et après 14 jours d'immersion, le gain de masse est supérieur à 0,5 mg.

D'autre part, les échantillons de CST montrent une meilleure capacité d'intégration osseuse en comparaison avec les échantillons anodisés et non traités.

Après 7 jours d'immersion, cette surface a mis en évidence une formation significative d'apatite avec gain de masse supérieur à 0,8 mg ; cette procédure de nucléation et croissance est maintenue, d'où la plus grande valeur de gain de masse, d'environ 1,8 mg après 14 jours.

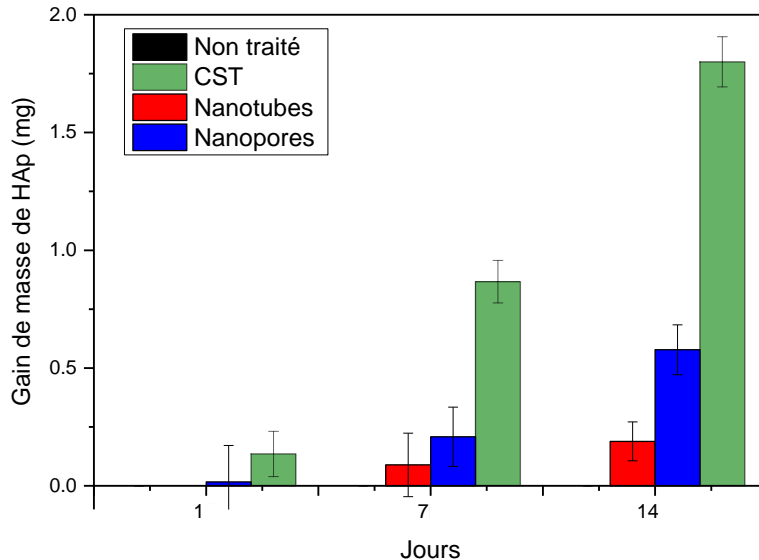


Figure 3.3 Évaluation quantitative pour gain de masse de HAp dans les échantillons non traités, CST, nanotubes et nanopores après différents temps d'immersion dans SBF.

Les images MEB sur la Figure 3.4 indiquent que, même après 14 jours d'immersion dans la solution physiologique, aucune ou peu de traces de HAp n'a été détecté sur les surfaces non traitées, nanotubes et nanopores. Par contre, il a été possible d'observer des sphères de HAp dans l'échantillon de CST après les mêmes 14 jours dans SBF (Figure 3.4 d). Cette information visuelle corrobore les valeurs de gain de masse obtenues pour les différents traitements de surface après le temps d'immersion.

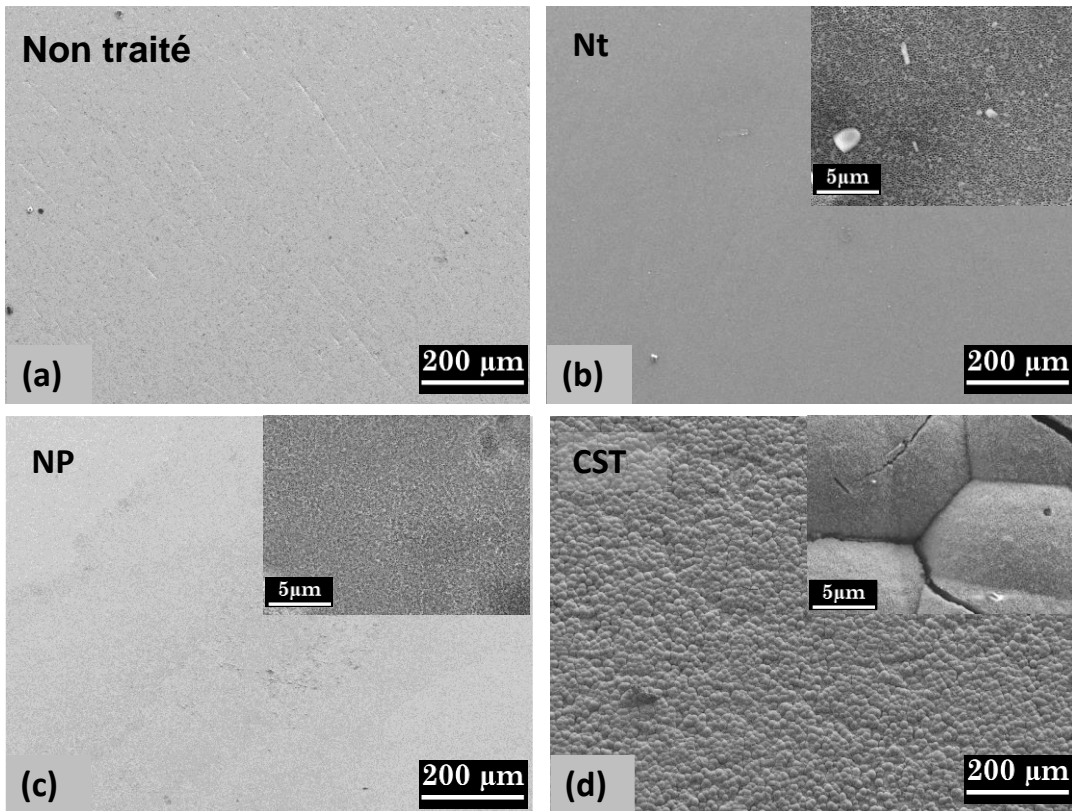


Figure 3.4 Images MEB pour les échantillons d'alliage de TMZF soumis aux essais de bioactivité après 14 jours d'immersion dans SBF. a) Non traité ; b) Nanotubes ; c) Nanopores et d) Échantillons de CST.

Le Tableau 3.1 montre les résultats des analyses de EDS réalisés dans les échantillons non traités, traités avec CST, nanotubes et nanopores après 14 jours d'immersion. Seulement dans les surfaces de CST et nanopores il a été détecté la présence de calcium, phosphore et oxygène, caractéristiques de l'hydroxyapatite présente dans le corps humain [1]. Ce résultat est corroboré par les mesures DRX sur la Figure 3.5, où il est possible de voir les pics de diffraction de la phase HAp cristalline seulement dans les échantillons avec CST après 14 jours d'immersion.

Tableau 3.1 Analyse chimique quantitative de EDS des échantillons non traités, nanotubes, nanopores et SCT. Après 14 jours d'immersion en solution SBF.

Condition	Élément chimique (% at.)						
	Ti	Mo	Zr	Fe	O	Ca	P
Non traité	67.32	3.79	2.15	1.94	22.75	-	-
Nanotubes	57.65	3.64	1.97	-	35.36	-	-
Nanopores	46.28	3.10	1.60	-	48.89	0.60	0.40
CST	11.88	0.54	0.24	-	59.06	16.97	9.34

Une autre étude complémentaire pour savoir si le phosphate de calcium (HAp) déposée sur les surfaces traitées était cristallisé, a été menée via la cartographie spectrale Raman. Pour cet essai le nombre d'onde typique du HAp, 961cm^{-1} a été utilisé. Dans ce résultat qualitatif, la formation de HAp est représentée par la couleur rouge ; les zones avec plus d'intensité signifient plus de précipitation de cette solution.

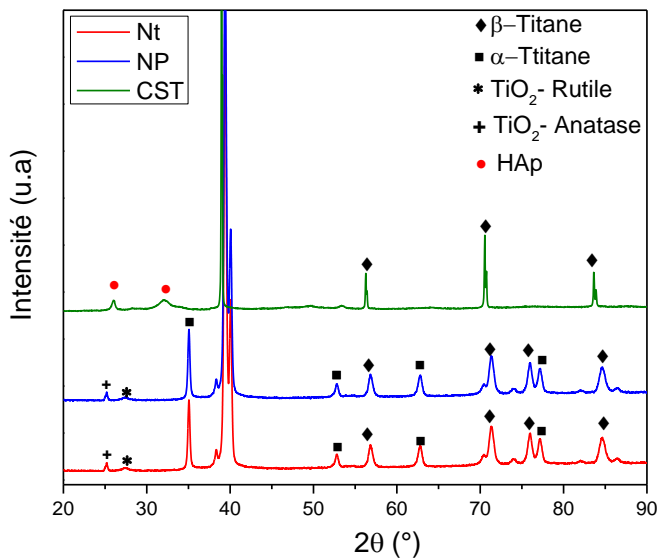


Figure 3.5 Mesures DRX d'échantillons non traités, CST, nanotubes et nanopores après 14 jours d'immersion dans SBF.

La Figure 3.6 montre la différence entre les différents échantillons traités après 7 et 14 jours d'immersion dans SBF. Sans tenir compte du temps d'immersion, les échantillons de nanotubes ont montré des plans à faible intensité Raman, ce qui indique une faible formation de HAp même après 14 jours d'immersion. Dans le cas des échantillons nanoporeux, les résultats sont légèrement meilleurs, et montrent plusieurs zones avec précipitation de HAp après 14 jours d'immersion dans SBF. Les échantillons de CST montrent le meilleur comportement en bioactivité avec une quantité plus grande de phosphate de calcium cristallin précipité sur toute la surface du matériau.

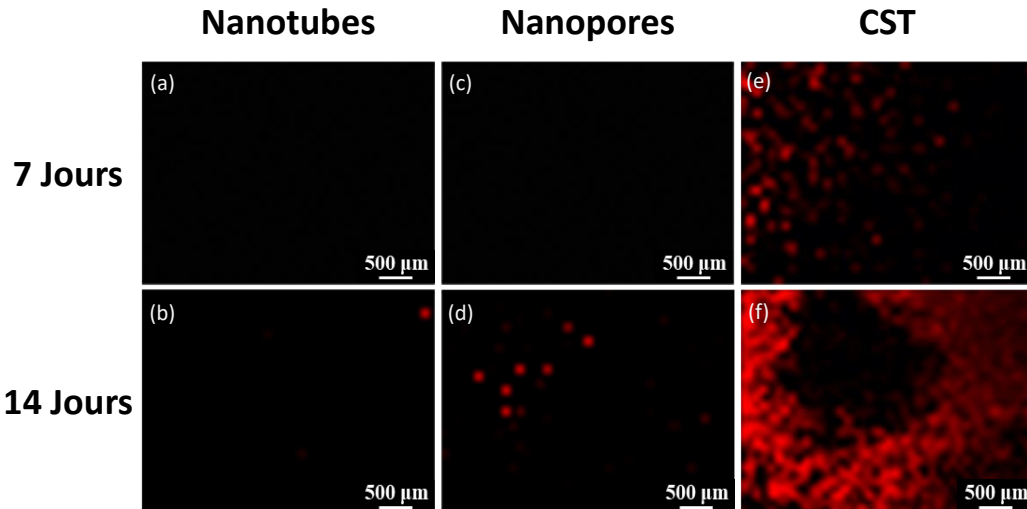


Figure 3.6 Cartographie spectrale Raman des échantillons de nanotubes (a et b), nanopores (c et d), et CST (e et f) immersés pendant 7 et 14 jours dans SBF.

3.2 Caractérisation électrochimique

La Figure 3.7 compare les courbes de polarisation potentiodynamique d'un échantillon représentatif de chaque condition de surface et temps d'immersion. À partir de ces courbes, le potentiel de corrosion (E_{corr}) a été déterminé. Il correspond à la valeur de potentiel à courant total nul et il est indiqué par le «pic» dirigé vers le bas dans les courbes de polarisation.

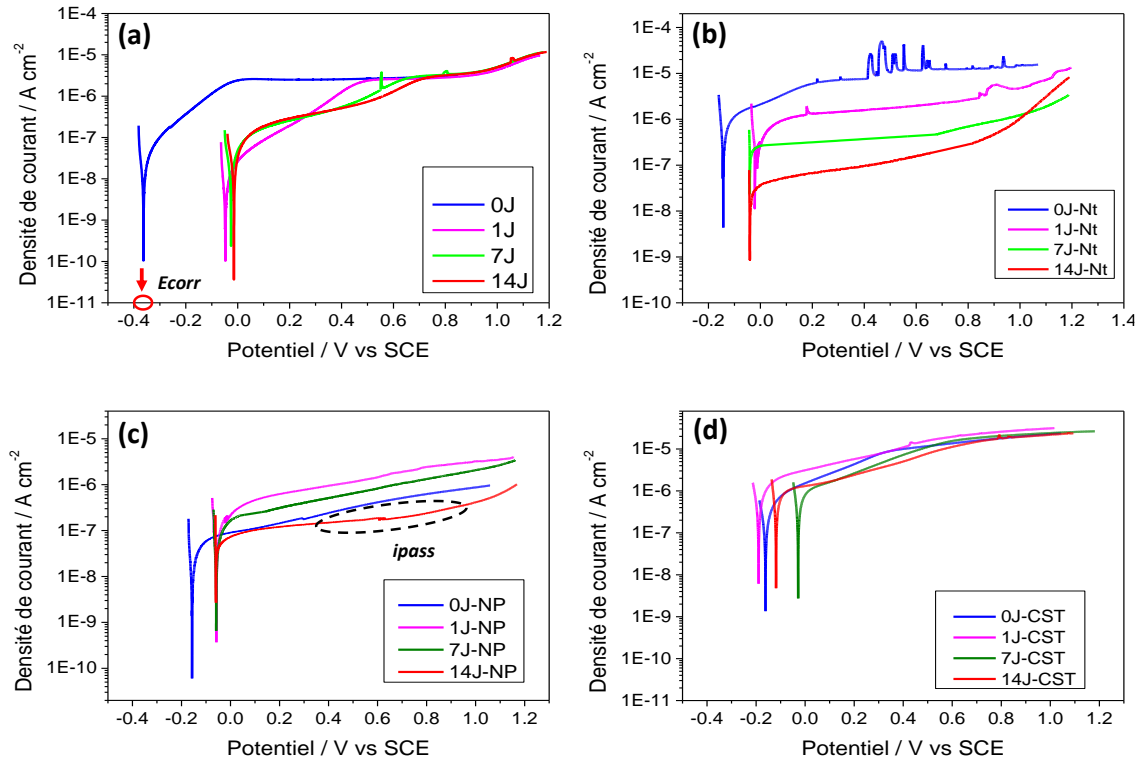


Figure 3.7 Courbes de polarisation anodique, dans électrolyte SBF pour les différentes périodes d'immersion (0, 1, 7, et 14 jours, indiqués comme 0J, 1J, 7J et 14J respectivement) à 37 °C pour l'alliage de TMZF: a) non traité ; b) nanotubes ; c) nanopores et d) CST.

Le genre des courbes de polarisation a indiqué un comportement passif stable associée à la présence d'un plateau pour toutes les conditions de surface et périodes d'immersion. Néanmoins, dans l'échantillon de nanotubes à 0 jour, des fluctuations sont observées dans le domaine de passivité en raison de la création d'un environnement agressif local qui décompose la couche de passivation [2]. Ces types d'oscillations peuvent être attribuées à la compétition entre la formation et la dissolution du film, des ions fluorures résiduels bloqués dans les tubes après le processus d'anodisation favorisent ce phénomène. Ce phénomène est facilité par une procédure de nettoyage insuffisante de ces échantillons [3].

Les valeurs de E_{corr} pour les quatre différents traitements de surface sont résumées sur la Figure 3.8. Ces valeurs sont comparables au potentiel obtenu pour chaque condition après une heure de OCP. Les échantillons non traités montrent, d'abord, un faible potentiel de corrosion d'environ -0.370 V vs SCE, mais cette valeur augmente considérablement après 1 jour d'immersion et reste presque constante à -0.050 V vs SCE jusqu'à 14 jours d'immersion.

En outre, les échantillons de nanotubes, nanopores et CST montrent un comportement plus noble (-0.072, -0.115 et -0.190 V vs SCE, respectivement) en

comparaison avec les échantillons non traités au jour 0. Après 1 jour d'immersion dans solution de SBF, tous ont montré une tendance à une augmentation de E_{corr} , ce comportement a été moins marqué pour des échantillons traités avec HCl et NaOH, ce qui indique une plus faible résistance contre la corrosion que celle des échantillons anodisés (Figure 3.8).

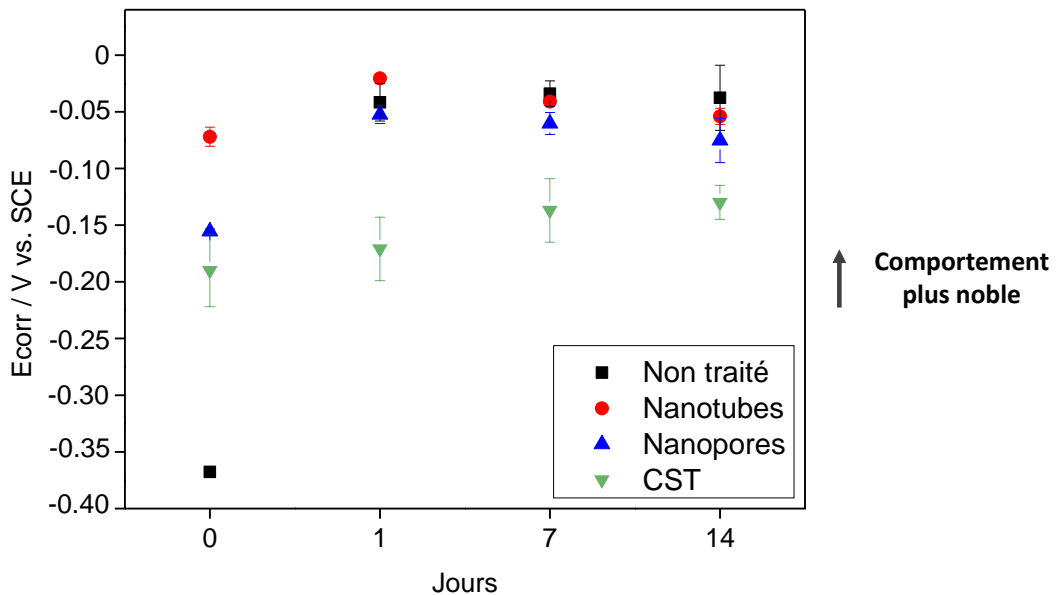


Figure 3.8 Mesures électrochimiques de potentiel de corrosion (E_{corr}) de l'alliage de TMZF non traité et traité avec nanotubes, nanopores et CST pour différents temps d'immersion dans SBF à 37°C.

Dans cette étude, a été choisi la densité de courant du plateau de passivation (i_{pass}) au lieu de la densité de courant de corrosion (i_{corr}) afin d'établir une meilleure comparaison entre les différentes surfaces passives obtenuesy. Dans la pratique, les formes des branches anodiques ne sont pas identiques pour tous les échantillons et la détermination de i_{pass} peut être non triviale (Figure 3.7). Pour ces raisons, la méthode de détermination de i_{pass} consistait en calculer, pour chaque échantillon, la moyenne des densités de courant mesurées dans la gamme des potentiels entre +0.4 V / ECS et +1 V / SCE par rapport à l'OCP [4].

Les implants métalliques sont considérés résistants à la corrosion et la corrosion se passera en présence de la couche passive. Ainsi, les valeurs de i_{pass} sont utilisées pour déterminer la résistance à la corrosion [2]. De cette façon, les alliages de TMZF dans un environnement physiologique avec i_{pass} inférieur à 12.5 $\mu\text{A.cm}^{-2}$ ou une vitesse de corrosion inférieure à 10^{-1} mm/an, sont considérés comme résistant à la corrosion ie stable et ceux, inférieurs à 1.25 $\mu\text{A.cm}^{-2}$ ou 10^{-2} mm/an, sont placés dans le groupe très résistant ie « très stable » [5] (Figure 3.9).

Les spécimens non traités présentent des résultats modérés-faibles et stables, avec i_{pass} d'environ $2.0 \mu\text{A.cm}^{-2}$, pendant les différentes périodes analysées, en raison de la présence d'une couche passive homogène et fine sur la surface de l'alliage.

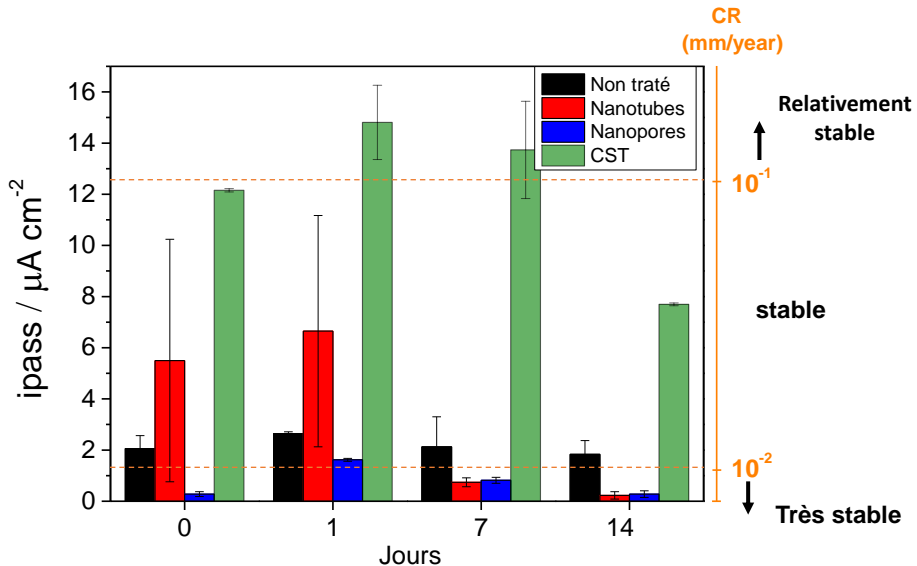


Figure 3.9 Mesures électrochimiques de densité de courant de passivation (i_{pass}) et de la vitesse de corrosion (ou CR, pour *corrosion rate*) de l'alliage de TMZF non traité, traité avec nanotubes, nanopores et CST pendant différents temps d'immersion dans SBF à 37°C.

D'abord, pour les jours 0 et 1 d'immersion, les échantillons de nanotubes présentent des valeurs de i_{pass} élevées, $5.0 \mu\text{A.cm}^{-2}$ environ. Ce comportement peut être justifié par les hétérogénéités de surface créées pendant le processus d'anodisation. Cependant, après 7 et 14 jours, les valeurs de i_{pass} sont inférieures à $0.8 \mu\text{A.cm}^{-2}$. Au début les nanotubes ordonnés fournissent un chemin libre pour le transfert de charge entre l'électrolyte et l'électrode. Après quelques jours d'immersion, ces canaux commencent à se fermer en raison du dépôt de phosphate de calcium dans la partie externe du nanotube et dans la partie inférieure du canal, avec une croissance additionnelle du film passif interne [6], ce qui rend difficile le transfert d'ions. Cette discussion sera reprise dans la section 4.3.3.

Les échantillons nanoporeux présentent un bon comportement électrochimique avec des valeurs faibles et stables pendant toutes les périodes d'immersion, avec des valeurs de i_{pass} inférieures à $0.8 \mu\text{A.cm}^{-2}$ après 14 jours immergé dans SBF. Cette performance est liée à la présence d'une couche passive homogène sur la surface du TMZF, cette couche est plus épaisse que la couche passive des échantillons non traités et plus compacte que la couche des échantillons de nanotubes.

Du point de vue électrochimique, les échantillons avec CST ont montré la plus faible résistance à la corrosion pour les différents temps d'immersion, en présentant des valeurs de i_{pass} supérieures à $12 \mu\text{A.cm}^{-2}$ pour les jours 0, 1 et 7 d'immersion dans SBF. Cependant, après 14 jours, il a été possible d'observer une réduction dans sa valeur de i_{pass} ($\sim 8.0 \mu\text{A.cm}^{-2}$).

4 Analyse et modélisation du spectre d'impédance des différents traitements de surface

4.1 Mesures par SIE des échantillons de TMZF non traités

Pour conclure la caractérisation électrochimique des surfaces sélectionnées pour cette étude, les informations additionnelles ont été obtenues par SIE. La Figure 4.1 montre l'évolution des courbes de Nyquist et des diagrammes de Bode avec le temps d'immersion dans la solution de SBF des échantillons de TMZF non traités ; la reproductibilité a été vérifiée : des échantillons répliqués montrent des résultats similaires, mais ils ne sont pas tracés pour une meilleure visualisation des diagrammes.

Les représentations de Nyquist et Bode des mesures d'impédance des échantillons sans traitement de surface sont représentées sur la Figure 4.1 (b-d). Toutes les données tracées dans ce travail ont été corrigées par l'aire géométrique (0.283 cm^2) exposée à l'électrolyte. Les graphiques des Figures 4.1b et 4.1.d ont été corrigés de la résistance ohmique ou résistance de l'électrolyte (R_e), estimée entre $20-30 \Omega.\text{cm}^2$, déduite de la limite de haute fréquence ($f = 10^4 \text{ Hz}$).

À partir d'une analyse qualitative du diagramme de Nyquist (Figure 4.1c), il semble que, pour tous les jours d'immersion, la réponse d'impédance se compose d'une ou plusieurs contributions. La forme de ces données d'impédance est typique d'un système capacito-résistif ou pseudo-capacitif (associations de phénomènes capacitifs, accumulation de charges et phénomènes résistifs, transferts de charge ou résistance d'une couche). Cela signifie que le transfert de charge et, donc, les réactions sont très limitées ou que la couche passive d'oxyde est très protectrice [7, 8].

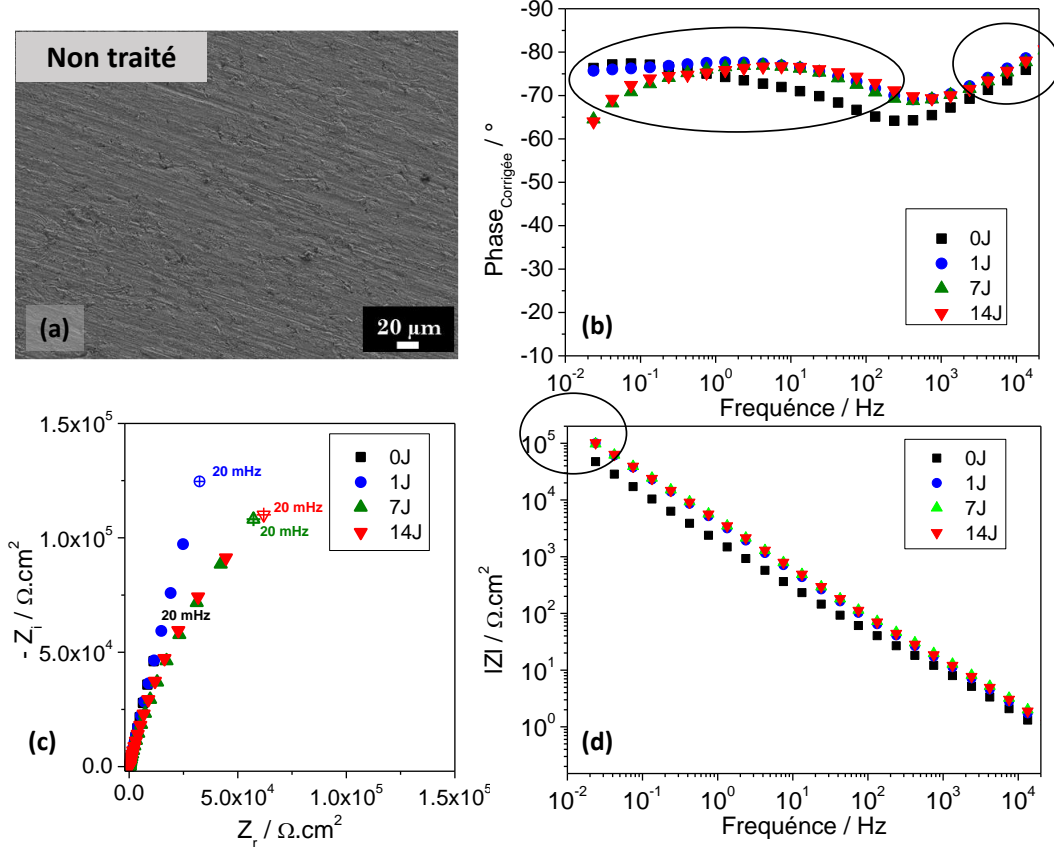


Figure 4.1 a) Micrographie MEB d'échantillons de TMZF non traités avant la période d'immersion ; résultats d'impédance pour les échantillons non-traités immergés dans SBF à 37 °C pendant différentes périodes (0, 1, 7, et 14 jours, indiqués comme 0J, 1J, 7J et 14J respectivement) ; Diagramme de Bode avec phase corrigée ; c) représentation de Nyquist et d) Diagramme de Bode avec module d'impédance, |Z|.

Sur la surface non traitée du TMZF, il est attendu la formation d'une couche passive poreuse comme il a été observé dans des alliages similaires en titane contenant zirconium et molybdène [9]. Cette couche passive poreuse serait composée par une couche poreuse externe et une barrière interne ; ainsi, il est prévu de retrouver deux processus de relaxation ou constantes de temps dans les résultats d'impédance.

Les représentations de Bode corrigées pour l'échantillon de TMZF non traité, sont montrées sur la Figure 4.1b et d. En utilisant le graphique de phase corrigée (Figure 4.1b), il est possible d'observer deux constantes de temps présentes pendant l'essai d'impédance. La première dans la gamme de 10⁻² Hz à 10² Hz et la seconde à haute fréquence environ 10⁴ Hz, ce qui confirme la théorie de la formation de la couche passive poreuse mentionnée ci-dessus. Ainsi, le circuit électrique équivalent (CEE, ou EEC en anglais, pour *Equivalent Electric Circuit*) le plus

approprié pour modéliser les résultats en impédance obtenus pour les échantillons non traités est celui montré sur la Figure 4.3.

Le principal désavantage du graphique de Bode de phase corrigée est le besoin d'une estimation précise de la résistance de l'électrolyte. Les estimations imprécises peuvent fournir l'idée équivoquée d'une constante de temps additionnelle à haute fréquence. De plus, les courbes corrigées sont très sensibles au bruit en haute fréquence [10]. Pour ces raisons, une courbe complémentaire des diagrammes de Bode est la représentation graphique en fonction de la fréquence de l'exposant CPE (en anglais, pour *Constant-Phase-Element*) α_{eff} , calculé selon [10] :

$$\alpha_{\text{eff}}(f) = \left| \frac{d \log |Z_i(f)|}{d \log f} \right| \quad (4.1)$$

Traditionnellement, dans la courbe de α_{eff} , les éléments CPE sont associés à des pics ou des plateaux. Dans ce sens, la Figure 4.2 montre deux constantes de temps pour tous les échantillons donc, attribuées à deux CPE, la première dans la gamme de 10^{-2} Hz à 10^2 Hz et la seconde de 10^4 Hz environ.

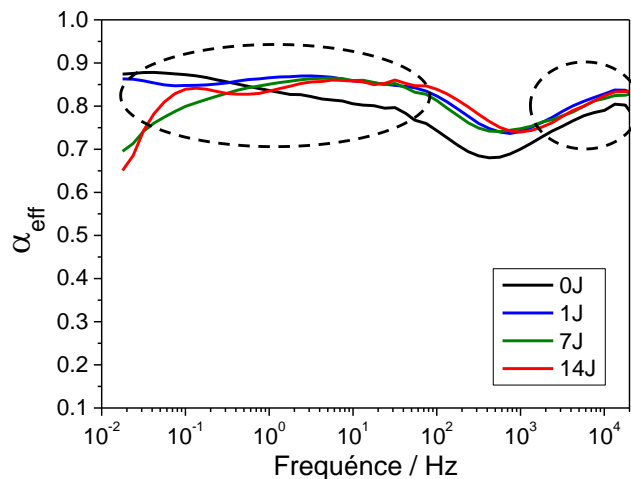


Figure 4.2 Évolution de α_{eff} versus fréquence, des échantillons de TMZF non traités pendant les différentes périodes d'immersion (0, 1, 7, et 14 jours, indiqués comme 0J, 1J, 7J et 14J respectivement) dans SBF à 37 °C.

Dans ce circuit électrique (Figure 4.3), R_e indique la résistance de la solution SBF, entre l'électrode de travail et l'électrode de référence. Le suffixe B et OP sont associés aux éléments qui représentent la couche de barrière interne et la couche d'oxyde poreuse externe, respectivement. L'usage d'un CPE, au lieu d'un condensateur pur, a été considéré en raison de l'hypothèse d'une distribution hétérogène de constante de temps sur la surface de l'échantillon [9, 11].

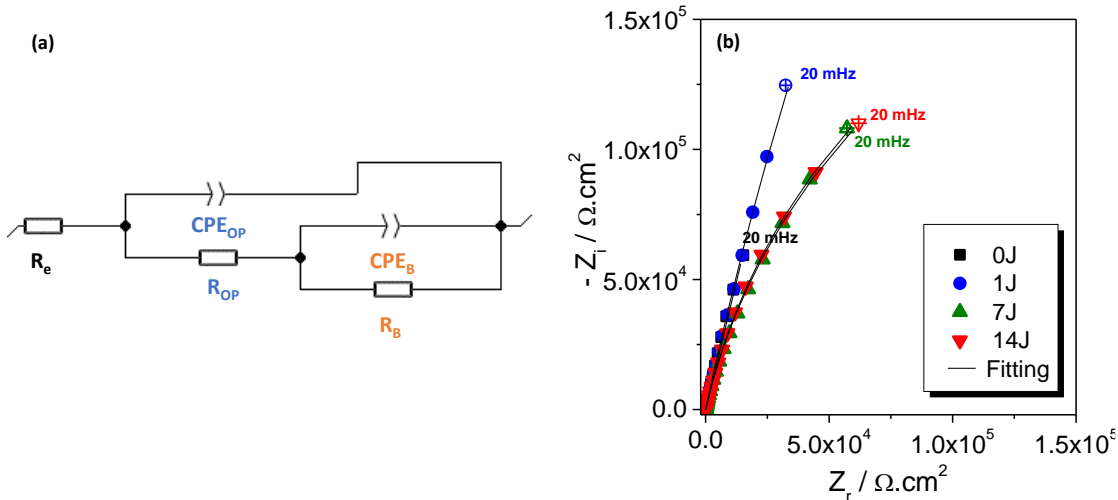


Figure 4.3 Circuit équivalent utilisé pour les échantillons non traités de l'alliage de TMZF et b) Représentation de Nyquist des résultats expérimentaux et des simulations obtenues via le logiciel « Simad », pour les différentes périodes d'immersion (0, 1, 7, et 14 jours, indiqués comme 0J, 1J, 7J et 14J respectivement) dans SBF à 37 °C. Le coefficient d'erreur est inférieur à 1% pour toutes les courbes.

Les valeurs de résistance, capacité et α des couches poreuses et barrières, obtenues par les ajustements des données expérimentales utilisant le CEE illustrées sur la Figure 4.3, sont présentées sur le Tableau 4.1. Les valeurs de α , d'environ 0,9, suggèrent que le comportement de cette couche passive se rapproche de celui d'un condensateur idéal, indépendamment du temps d'immersion [11].

Tableau 4.1 Paramètres électriques du circuit équivalent obtenus par ajustement des résultats expérimentaux d'impédance pour les échantillons non traités à 37 °C dans la solution SBF.

Jours	R_e ($\Omega \cdot \text{cm}^2$)	Q_{OP} ($\Omega s^{-\alpha} \cdot \text{cm}^2$)	α_{OP}	R_{OP} ($\Omega \cdot \text{cm}^2$)	Q_B ($\Omega s^{-\alpha} \cdot \text{cm}^2$)	α_B	R_B ($10^5 \Omega \cdot \text{cm}^2$)	d_{ox} (nm)	X (%)
0	23	1.74E-05	0.85	94	1.37E-05	0.83	2.83	7	0.45
1	20	8.35E-06	0.88	63	6.02E-06	0.84	2.90	18	0.23
7	21	4.80E-06	0.92	49	8.55E-06	0.81	4.64	16	0.22
14	20	1.04E-05	0.84	77	2.95E-06	0.88	4.60	27	0.77

Le film passif se compose de deux couches, la couche barrière interne, dont les valeurs de résistance, R_B , augmentent avec les jours d'immersion et sont considérablement plus grandes que les valeurs associées à la couche poreuse externe, R_{OP} , qui reste presque constante, comme il est montré sur le Tableau 4.1. Ces résultats indiquent que la protection fournie par la couche passive est due

principalement à la couche barrière interne, comme également observé sur d'autres alliages de titane [9, 12, 13].

La résistance Ohmique (R_e), estimée à partir du modèle proposé, varie entre 20-23 $\Omega \cdot \text{cm}^2$ pendant les jours d'immersion et elle se trouve en bonne concordance avec la résistance déduite de la limite de haute fréquence (20-30 $\Omega \cdot \text{cm}^2$) des diagrammes de Bode (Figure 4.1).

À partir des paramètres du CPE (Q et α), R_e , et R_{OP} , R_B et, en utilisant la relation de Brug (Relation 4.2), il est possible d'obtenir les valeurs de capacité effective de la couche passive (bi-couche).

$$C_{eff} = Q^{1/\alpha} (R_e^{-1} + R_{OP,B}^{-1})^{(\alpha-1)/\alpha} \quad (4.2)$$

Les capacités effectives calculées à partir des valeurs énumérées sur le Tableau 4.1 varient entre 18 et 9 $\mu\text{F} \cdot \text{cm}^{-2}$ pour la couche poreuse et entre 12 et 3 $\mu\text{F} \cdot \text{cm}^{-2}$ pour la couche compacte interne, pendant les différents jours d'immersion, du même ordre de grandeur qu'un acier inoxydable AISI 316L immergé dans des solutions physiologiques [14, 15]. La réduction de capacité avec le temps est associée à une augmentation de l'épaisseur de la couche passive [16, 17]. Des capacités réduites associées à des hautes résistances de la couche sont caractéristiques d'un comportement électrochimique plus noble [13, 16, 17].

$$d_{ox} = \frac{\epsilon_r \epsilon_0}{C_{ox}} \quad (4.3)$$

En ce sens, l'épaisseur de la couche compacte interne peut être calculée à partir de la Relation 4.3, qui est valable pour un modèle de condensateur à plaque parallèle d'une couche d'oxyde homogène, ce qui associe la capacité effective générale à la capacité de la couche protectrice d'oxyde :

Où ϵ_0 est la permittivité du vide ($8.85 \times 10^{-14} \text{ F} \cdot \text{cm}^{-1}$) et ϵ_r i est la constante diélectrique relative du matériau (prise en tant que $\epsilon_r = 100$, la constante diélectrique du TiO_2 [17]). Avec ses informations, il a été possible d'obtenir une approximation de l'épaisseur de la couche passive pour les différents jours d'immersion. La couche passive a grandi avec l'augmentation des jours d'immersion ; de 7 nm pour les échantillons non immersés, à 27 nm après 14 jours (Tableau 4.1).

4.2 Mesures SIE sur les échantillons de TMZF traités avec HCl et NaOH

L'effet du temps d'immersion pour les échantillons traités avec acide et alcalins est présenté sur la Figure 4.4. L'évolution de l'impédance sur les graphiques de Nyquist montre des demi-cercles aplatis à basses fréquences. Le rayon de ces arcs de cercle diminue avec l'augmentation du temps d'immersion (Figure 4.4 c).

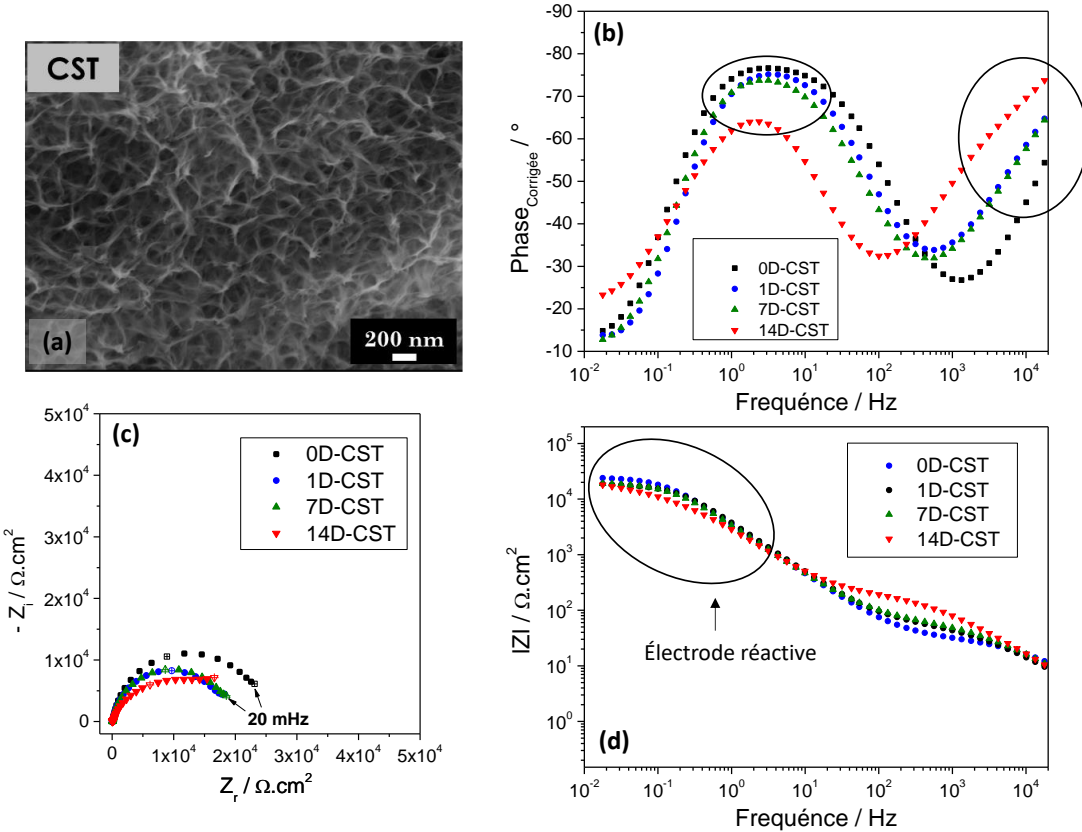


Figure 4.4 a) Microographies MEB des échantillons de CST avant les périodes d'immersion ; résultats d'impédance pour les échantillons de CST immergés dans SBF à 37 °C pendant différentes périodes (0, 1, 7, et 14 jours, indiqués comme 0J, 1J, 7J et 14J respectivement) : b) Diagramme de Bode avec phase corrigée ; c) représentation de Nyquist et d) Diagramme de Bode avec module d'impédance, $|Z|$.

Les représentations de Bode pour l'échantillon de CST sont montrées sur la Figure 4.4b et d. En utilisant le graphique de phase corrigée (Figure 4.4b), il est possible de déterminer deux processus de relaxation ou constantes de temps. Il est possible d'observer que les deux gammes de fréquence présentant des phases constantes pour les échantillons traités chimiquement sont plus resserées en comparaison avec des échantillons non traités. Cette distribution des constantes de temps sur des gammes de fréquence plus courtes indique une surface moins protectrice et homogène.

La courbe de l'exposant α_{eff} est utilisée pour une meilleure caractérisation des processus de relaxation qui se produisent sur la surface des échantillons traités chimiquement. La Figure 4.5 montre un comportement similaire en haute et moyenne fréquence sur le graphique de phase corrigée. Toutefois, ce graphique montre une constante additionnelle en basses fréquences (10^{-2} Hz to 10^{-1} Hz). Ce comportement intéressant a été associé à un processus de relaxation supplémentaire.

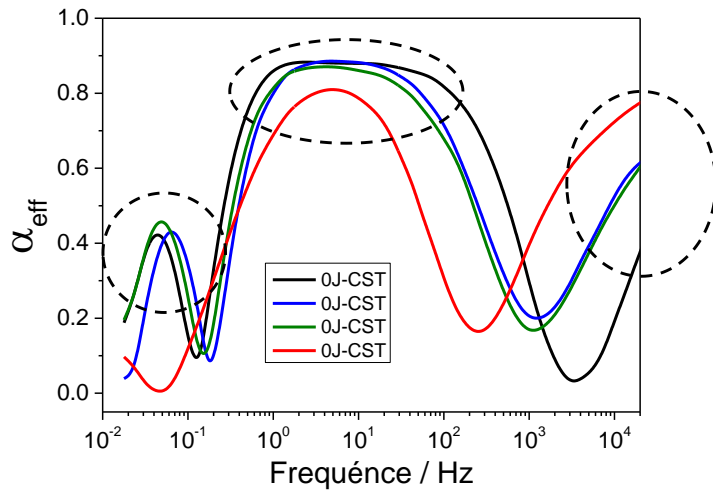


Figure 4.5 Évolution de α_{eff} versus fréquence des échantillons de TMZF de CST pour les différentes périodes d'immersion (0, 1, 7, et 14 jours, indiqués comme 0J, 1J, 7J et 14J respectivement) dans SBF à 37 °C.

Dans les échantillons traités avec CST, on s'attend à trouver trois processus de relaxation, un de plus que les deux trouvés dans les échantillons non traités, qui est associé à la couche externe de titanate de sodium créée pendant le traitement chimique avec HCl et NaOH.

Comme mentionné avant et confirmé par les informations obtenues des diagrammes de phase Bode et des courbes de α_{eff} , le CEE pour des échantillons CST doit être composé de trois processus de relaxation. Le circuit de la Figure 4.6 fournit une bonne représentation pour les systèmes avec une couche compacte interne, une couche intermédiaire d'oxyde poreux et une couche externe de gel de titanate de sodium.

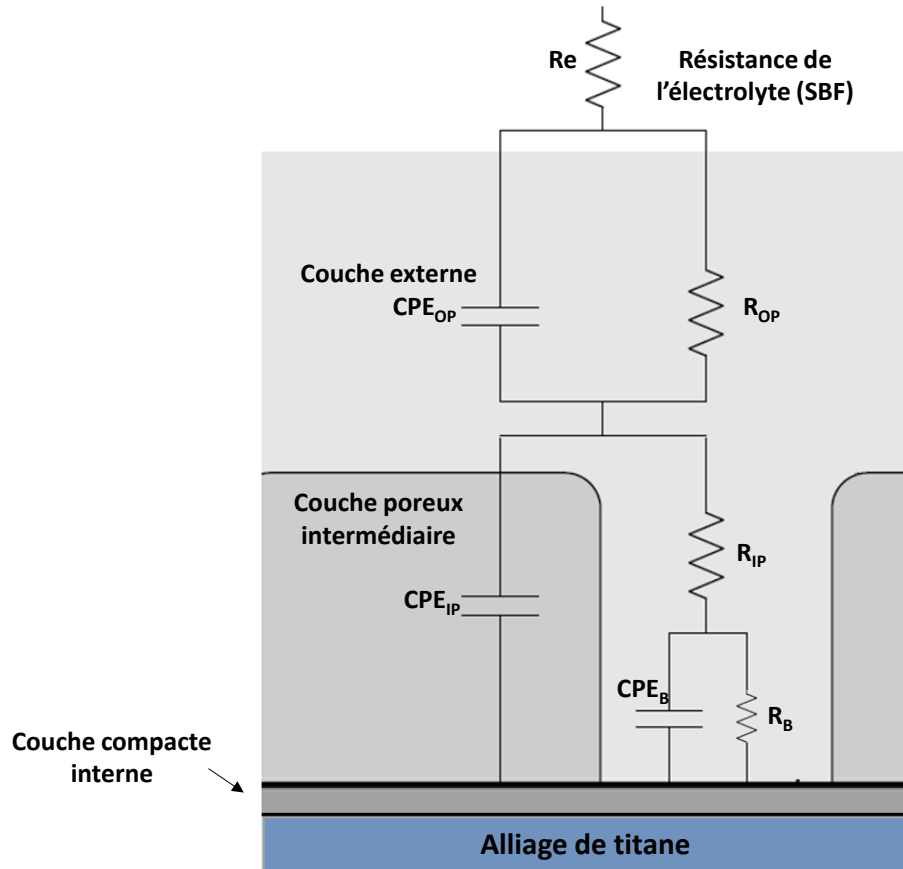


Figure 4.6 Circuit électrique équivalent (CEE) pour les échantillons de CST (Adapté de [11]).

Dans le circuit de la Figure 4.6, R_e représente la résistance de l'électrolyte (solution SBF), R_{OP} et CPE_{OP} représentent les résistances et les capacités de la couche poreuse externe, associées à la dissolution de la couche en titanate de sodium et à la croissance de Hap. R_{IP} et R_B sont les résistances de la couche d'oxyde poreux intermédiaire et des couches de barrières internes ; CPE_{IP} et CPE_B sont utilisés pour désigner les capacités de la couche poreuse externe et compacte interne, respectivement.

La représentation de Nyquist des données SIE modelées des échantillons de CST est montrée sur la Figure 4.7, avec les courbes simulées (modélisées par le CEE de la Figure 4.6). Les erreurs mesurées (X) pour les données expérimentales et simulées ont été inférieures à 1%, indépendamment de la période d'immersion, ce qui indique un niveau d'ajustement satisfaisant.

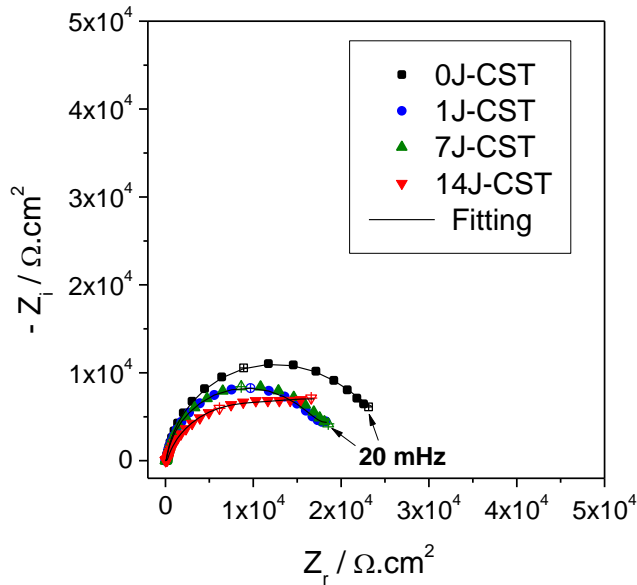


Figure 4.7 Représentation de Nyquist des résultats expérimentaux et simulés obtenus via le logiciel Simad, pour les échantillons de CST immergés dans SBF à 37 °C pour différentes durées (0, 1, 7, et 14 jours, indiqués comme 0J, 1J, 7J et 14J respectivement).

Les paramètres d'impédance électrochimique, comme résistances, capacités et valeurs de α des couches poreuses et barrières obtenues du circuit équivalent, sont détaillées dans le Tableau 4.2.

Tableau 4.2. Paramètres SIE des échantillons immergés dans SBF à 37 °C pour des durées de 0, 1, 4 et 14 jours.

Jours d'immersion	R_e ($\Omega \cdot \text{cm}^2$)	Q_{OP} ($\Omega s^{-\alpha} \cdot \text{cm}^2$)	α_{OP}	R_{OP} ($\Omega \cdot \text{cm}^2$)	Q_{IP} ($\Omega s^{-\alpha} \cdot \text{cm}^2$)	α_{IP}	R_{IP} ($\Omega \cdot \text{cm}^2$)	Q_B ($\Omega s^{-\alpha} \cdot \text{cm}^2$)	α_B	R_B ($\Omega \cdot \text{cm}^2$)	C_{effB} ($\mu\text{F}/\text{cm}^2$)	X (%)
0	25	8.61 E-04	0.57	35.05	3.31 E-06	0.71	819	1.69 E-05	0.91	48562	32	0.39
1	21	2.79 E-04	0.55	50.14	6.66 E-06	0.72	283	1.39 E-05	0.95	16366	29	0.26
7	24	3.30 E-04	0.53	112.33	9.28 E-06	0.60	283	2.46 E-05	0.84	11916	22	0.71
14	23	1.45 E-04	0.80	178.97	4.08 E-06	0.76	155	1.81 E-05	0.85	11513	18	0.82

Avec l'augmentation des jours d'immersion de 0 à 7, les valeurs de Q_{OP} ont baissé, ce qui montre un processus de dissolution de la couche en titanate de sodium. Cela peut être associé à l'interaction entre les ions présents dans la solution physiologique et les ions de la couche en titanate [6].

Entre 7 et 14 jours dans la solution de SBF, une couche de HAp apparaît en parallèle de la dissolution complète de la couche de titanate de sodium, qui agit

comme une barrière de diffusion, hypothèse renforcée par valeur élevée de α_{OP} à 14 jours. Ce comportement est confirmé sur le diagramme de Nyquist à 14 jours d'immersion (Figure 4.7), où il est possible de voir une contribution différente à basses fréquences [6].

La résistance R_B a diminué continuellement et, en même temps, la R_{OP} a augmenté avec les jours d'immersions et a atteint une valeur constante entre 7 et 14 jours. Ce comportement peut être associé aux processus continus de dissolution et formation de la couche barrière et de la couche HAp, respectivement [6].

À travers les résultats d'impédance, l'usage de la Relation 4.3 et les résultats des ajustements C_{effB} du Tableau 4.2, il est possible de calculer une valeur approximative de l'épaisseur de la couche interne d'oxyde de titane (d_{ox}), dont les valeurs sont résumées sur le Tableau 4.2. De façon similaire aux échantillons non traités, l'épaisseur de la couche passive des échantillons de CST a augmenté avec les jours d'immersion.

4.3 Mesures SIE des échantillons TMZF anodisés

Des résultats d'impédance électrochimique ont été analysés pour examiner les propriétés des deux systèmes anodisés différents (surfaces avec nanotubes et nanopores) après différentes périodes d'immersion dans la solution de SBF (0, 1, 7 et 14 jours).

L'image MEB de haute résolution sur la Figure 4.8 montre la condition de la surface des échantillons TMZF avec nanotubes avant les périodes d'immersion. D'abord, il a été analysé l'évolution électrochimique des échantillons recouverts de nanotubes au travers des diagrammes de Nyquist et Bode montrés sur la Figure 4.8 (b-d).

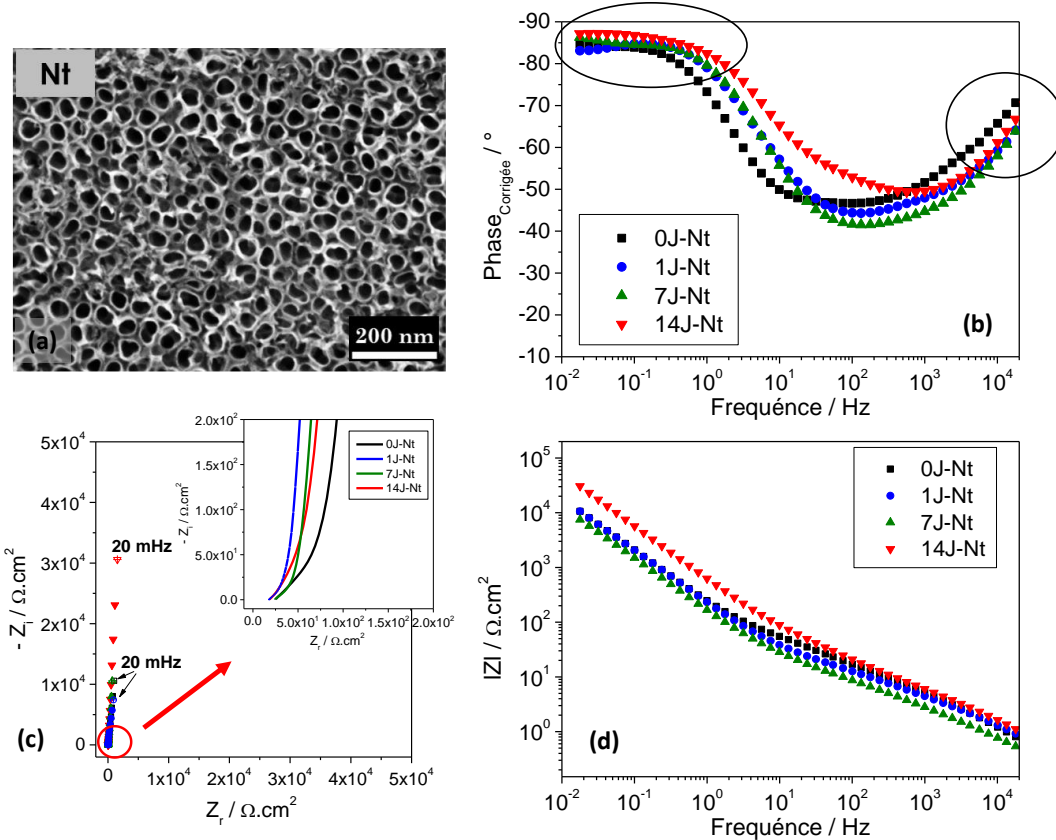


Figure 4.8 a) Microographies MEB de l'échantillon de TMZF avec nanotubes avant les périodes d'immersion ; Représentation schématique des résultats d'impédance pour des échantillons avec des nanotubes immergés dans SBF à 37 ° C pour les différentes périodes (0, 1, 7 et 14 indiqués comme 0J, 1J, 7J et 14J respectivement) : b) Diagramme de Bode avec phase corrigée ; c) représentation de Nyquist et d) Diagramme de Bode avec module d'impédance, |Z|.

L'observation des diagrammes de Nyquist révèle que, quel que soit le temps d'immersion étudié, la forme des spectres d'impédance du CST (arc) est typique d'un système réactif (section 4.2), alors que sur la Figure 4.8 (c), apparemment, les échantillons avec des nanotubes sont plutôt purement capacitifs (ligne droite) ou, au moins, pseudo-capacitifs (ligne droite inclinée). Cela signifie que les réactions électrochimiques sont très limitées.

Ces échantillons anodisés montrent un comportement particulier dans le diagramme de Nyquist : il est possible d'y observer une ligne droite inclinée ou un arc à haute fréquence (région agrandie Figure 4.8c) et une branche capacitive ou pseudo-capacitive à basse fréquence. Il s'agit d'une caractéristique typique d'une électrode poreuse, comme cela sera détaillé dans la section 4.3.1.

La Figure 4.9 montre l'évolution des courbes de Nyquist et des diagrammes de Bode avec le temps d'immersion dans la solution SBF, pour les échantillons de TMZF avec des nanopores. De plus, sur la Figure 4.9 (a), il est possible de voir l'état de la surface des échantillons nanoporeux de TMZF avant les périodes d'immersion.

De la même façon que les nanotubes, les échantillons nanoporeux présentent un comportement capacitif ou pseudo-capacitif, sur le diagramme de Nyquist indépendamment du temps d'immersion étudié (Figure 4.9 (c)). Ce type de courbes est généralement observé dans les systèmes poreux à faible réactivité.

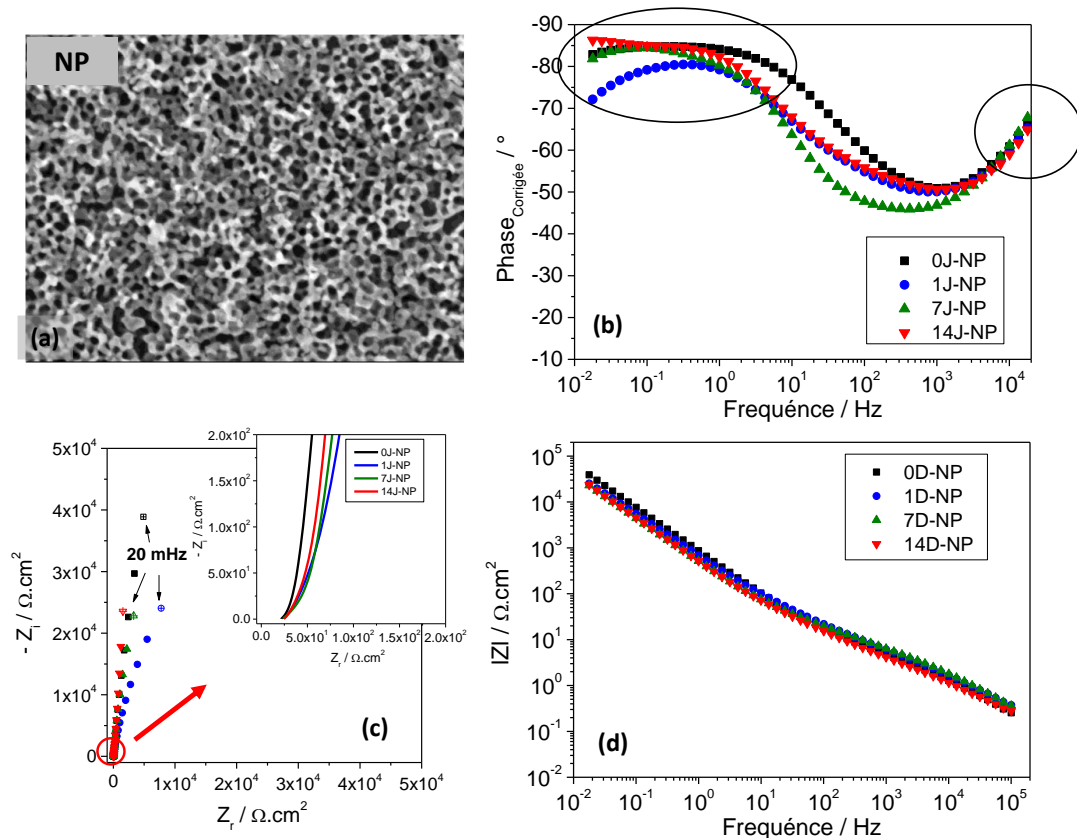


Figure 4.9 a) Microographies MEB de l'échantillon avec des nanopores de TMZF avant les périodes d'immersion ; Représentation schématique des résultats d'impédance pour des échantillons non traités immersés dans SBF à 37 °C pendant les différentes périodes (0, 1, 7 et 14 jours indiqués respectivement 0J, 1J, 7J et 14J); b) Diagramme de Bode avec phase corrigée ; c) représentation de Nyquist et d) Diagramme de Bode avec module d'impédance, $|Z|$.

Les représentations graphiques de α_{eff} (Figure 4.10) ont été tracées pour déterminer le nombre de constantes de temps présentes et nous aider à choisir le CEE le plus approprié pour modéliser les résultats des échantillons anodisés (NT et

NP). La Figure 4.10 montre les deux constantes temps pour les échantillons NT et NP, quel que soit le temps d'immersion.

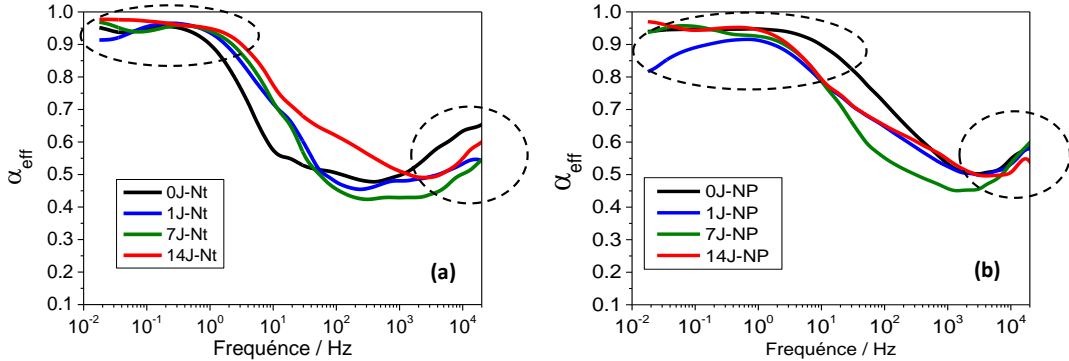


Figure 4.10 Évolution de α_{eff} avec la fréquence des échantillons de TMZF anodisés pour les différentes périodes d'immersion (0, 1, 7 et 14 jours indiqués respectivement 0J, 1J, 7J et 14J) dans SBF à 37 ° C : a) nanotubes et b) nanopores.

A l'aide des informations obtenues par le diagramme de Bode et les tracés de α_{eff} , le comportement des échantillons anodisés a été modélisé en considérant un circuit électrique similaire à celui utilisé pour les échantillons non traités (Figure 4.3 – bi-couche passive). Cependant, les résultats d'ajustement pour ces deux conditions n'ont pas été satisfaisants, comme déjà mentionné dans différents travaux [17, 19] ; les erreurs d'ajustement sont élevées et les valeurs des paramètres obtenues sont aberrantes.

Ainsi, un nouveau modèle basé sur la théorie de De Levie est utilisé pour modéliser la réponse d'impédance des échantillons de TMZF anodisés dans SBF. De Levie a observé un comportement similaire dans les électrodes poreuses [20]. Cet auteur a modélisé les résultats d'impédance d'une électrode poreuse à travers un modèle alternatif décrit comme le modèle de ligne de transmission (TL, ou LT en anglais, pour *Transmission Line*).

4.3.1 Utilisation du modèle de ligne de transmission dans le cas d'échantillons de TMZF anodisés dans SBF

La Figure 4.11 montre une représentation schématique du modèle TL proposé dans cette étude, il peut être utile pour modéliser différentes microstructures et géométries par rapport à des différents types d'hypothèses. En outre, il est nécessaire de remarquer que ce modèle implique les processus de volume distribués sur toute la surface de l'électrode. Le canal 1 est représenté comme une résistance distribuée, le transport dans le canal 2 est considéré comme anormal, c'est-à-dire que l'impédance X_2 est équivalente à une disposition parallèle d'un CPE (Q_2) et d'une résistance (R_2). L'impédance interfaciale ζ est considérée comme

pseudo-capacitive (Q_3) et dans les limites une impédance Z_B (Q_B) et une résistance Z_A (R_A).

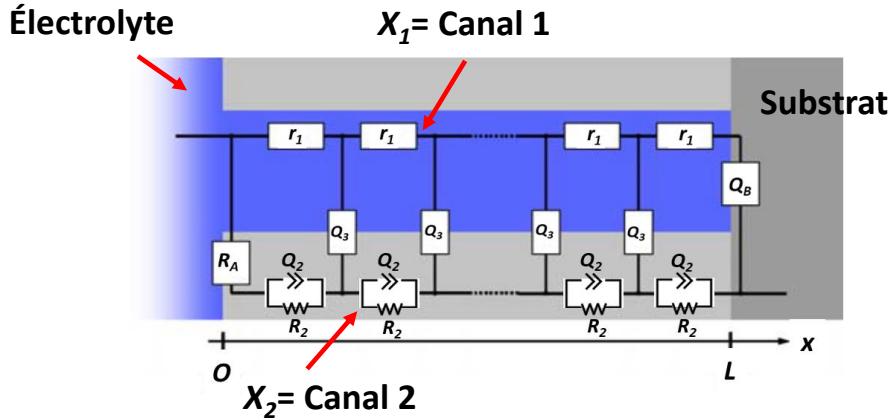


Figure 4.11 Le modèle de ligne de transmission proposé pour décrire la réponse d'impédance des échantillons de TMZF anodisés immergés dans SBF à 37 ° C pendant les différentes périodes évaluées.

Dans cette étude, un modèle de ligne de transmission a été proposé pour décrire la réponse en'impédance des échantillons de TMZF anodisés immergés dans SBF à 37 ° C pendant différentes périodes.

L'Équation 4.4 montre la solution de la TL utilisée dans ce travail pour modéliser les résultats d'impédance :

$$Z = \frac{1}{X_1 + X_2} \left[\lambda(X_1 + X_2)S_\lambda + (Z_A + Z_B)C_\lambda + \frac{1}{\lambda(X_1 + X_2)} Z_A Z_B \lambda \right]^{-1} \cdot \left(L\lambda X_1 X_2 (X_1 + X_2)S_\lambda + X_1 [\lambda X_1 S_\lambda + L X_2 C_\lambda] Z_A + X_2 [\lambda X_2 S_\lambda + L X_1 C_\lambda] Z_B + \frac{1}{X_1 + X_2} \left[2X_1 X_2 + (X_1^2 + X_2^2)C_\lambda + \frac{L}{\lambda} X_1 X_2 S_\lambda \right] Z_A Z_B \right) \quad (4.16)$$

Where $X_1 = r_1$; $X_2 = \frac{1}{1 + r_2 q_2 (iw)^\beta}$; $\zeta = \frac{1}{q_3} (iw)^{-\beta}$; $Z_A = R_A$; $Z_B = \frac{1}{Q_B} (iw)^{-\beta}$

$C_\lambda = \cosh(L/\lambda)$, $S_\lambda = \sinh(L/\lambda)$, and $\lambda = [\zeta/(X_1 + X_2)]^{1/2}$.

La Figure 4.12 montre les résultats de l'ajustement (indiqué par une ligne pleine) des mesures expérimentales d'échantillons anodisés avec des nanotubes et des nanopores en utilisant le modèle proposé dans l'Équation 4.4 et illustré sur la Figure 4.11. Le modèle TL est composé de 10 paramètres qui décrivent de manière satisfaisante le comportement de l'interface. L'erreur entre les points expérimentaux et la simulation, quelle que soit la morphologie anodisée, a été inférieure à 1,0%

indépendamment du temps d'immersion. Seul l'échantillon des nanotubes après 14 jours a montré une valeur plus élevée (1,7%), ce qui est tout à fait raisonnable.

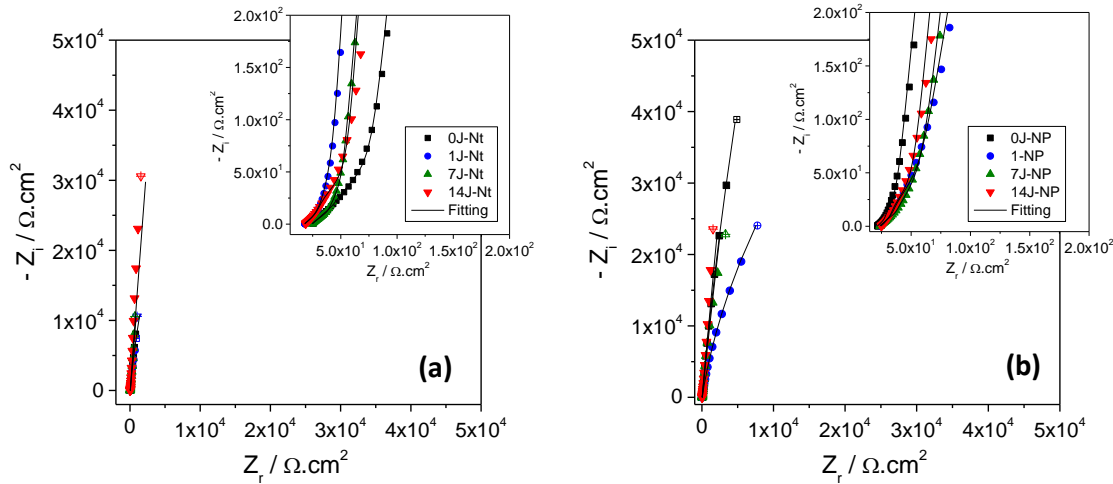


Figure 4.12 Diagrammes de Nyquist des résultats expérimentaux et simulés acquis à partir du logiciel *Simad* pour les échantillons anodisés immergés dans SBF à 37 °C pendant différentes périodes (0, 1, 7 et 14 jours, indiqués respectivement 0J, 1J, 7J et 14J) : a) Nanotubes et b) Nanopores.

Le Tableau 4.3 montre les paramètres d'impédance électrochimique obtenus en ajustant les résultats expérimentaux d'échantillons de nanotubes pour les différents jours d'immersion. De plus, les valeurs de la fréquence de coupure (ω_c) qui représentent le mécanisme de transport à travers le canal 2 (X_2) ont été calculées en utilisant la formule 4.17 et elles sont récapitulées dans le Tableau 4.3.

$$\omega_c = \frac{1}{r_2 q_2 (iw)^{1/\beta}} \quad (4.5)$$

Tableau 4.3 Paramètres d'impédance électrique obtenus en ajustant les résultats expérimentaux des échantillons avec nanotubes.

Jours	X1		X2		ζ		ZA		ZB		L (cm)	ω_c (Hz)	X (%)
	R ₁ ($\Omega \cdot \text{cm}$)	R ₂ ($\Omega \cdot \text{cm}^2$)	Q ₂ ($\Omega \text{s}^{-e} \cdot \text{cm}^2$)	e	Q ₃ ($\Omega \text{s}^{-b} \cdot \text{cm}$)	b	R _A ($\Omega \cdot \text{cm}^2$)	Q _B ($\Omega \text{s}^{-n} \cdot \text{cm}^2$)	n				
0	827	217	6.53 E-07	0.96	1.63 E-04	0.96	7.22 E+06	3.69 E-05	0.91	2.0 E-05	0.035	0.77	
1	956	222	4.55 E-07	0.76	2.96 E-04	0.96	2.99 E+05	1.69 E-05	0.84	2.0 E-05	0.023	0.48	
7	938	209	6.06 E-07	0.78	3.91 E-04	0.95	4.90 E+08	5.58 E-06	0.92	2.0 E-05	0.019	0.43	
14	860	145	2.81 E-06	0.72	9.96 E-05	0.96	5.25 E+09	7.80 E-06	0.89	2.0 E-05	0.003	1.70	

La Figure 4.13 a été représentée graphiquement pour comprendre le comportement des points d'extrémité de la ligne (Z_A et Z_B) pendant les jours d'immersion, représentés par la résistance et la capacité de R_A et Q_B , respectivement. Les valeurs de R_A et Q_B ont été obtenues à partir du Tableau 4.3.

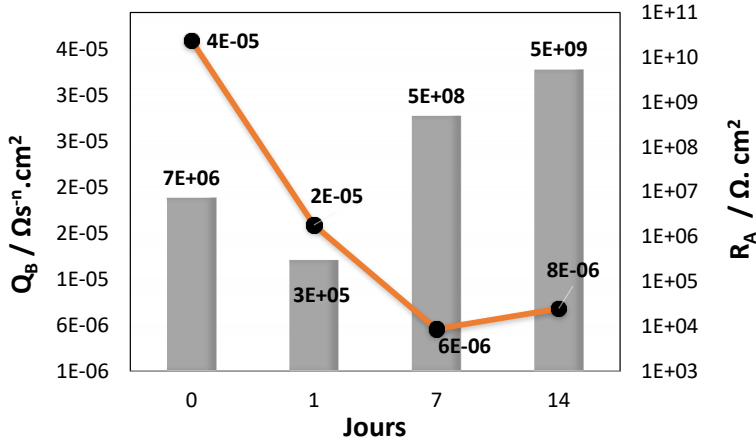


Figure 4.13 Paramètres R_A et Q_B , obtenus à partir du modèle de ligne de transmission pour les échantillons de nanotubes pour différentes durées d'immersion dans SBF.

La résistance R_A augmente progressivement et Q_B diminue avec le temps d'immersion dans SBF. Ce comportement pourrait être associé à la formation et à la croissance de noyaux de phosphate de calcium (étape initiale pour la formation d'apatite) sur la partie externe du nanotube et sur la partie inférieure du canal. Ce comportement est observé sur la Figure 4.14 (cercles rouges). De plus, la diminution de Q_B pourrait être associée à la croissance du film passif interne [6].

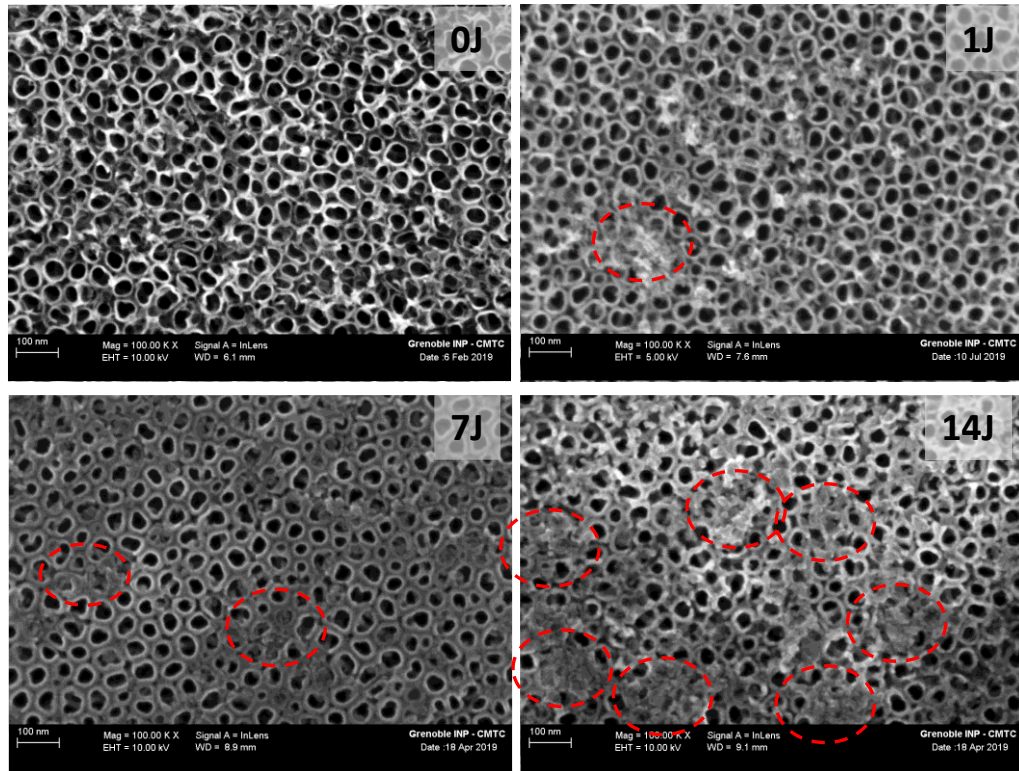


Figure 4.14 Formation d'apatite sur des échantillons de nanotubes après différentes périodes d'immersion dans SBF (0, 1, 7 et 14 jours, indiqués respectivement 0J, 1J, 7J et 14J).

Le Tableau 4.4 montre les paramètres d'impédance électrochimique obtenus en ajustant les résultats expérimentaux d'échantillons nanoporeux pour les différents jours d'immersion. Comme dans le cas de l'ajustement pour les échantillons de nanotubes, une valeur moyenne a été choisie de L (2×10^{-5} cm) pour les échantillons nanoporeux. Cette valeur a été utilisée dans le modèle d'ajustement.

Tableau 4.4 Paramètres d'impédance électrique obtenus en ajustant les résultats expérimentaux d'échantillons nanoporeux.

Jours	X1		X2		ζ	ZA	ZB		L (cm)	ω_C (Hz)	X (%)		
	R_1 ($\Omega \cdot \text{cm}$)	R_2 ($\Omega \cdot \text{cm}^2$)	Q_2 ($\Omega \text{s}^e \cdot \text{cm}^2$)	e			Q_3 ($\Omega \text{s}^b \cdot \text{cm}$)	b	R_A ($\Omega \cdot \text{cm}^2$)	Q_B ($\Omega \text{s}^{-n} \cdot \text{cm}^2$)			
0	559	203	8.52 E-07	0.60	7.73 E-05	0.96	1.40 E+06		5.32 E-06	0.90	2.0E-05	0.003	0.60
1	826	207	9.24 E-07	0.64	7.52 E-05	0.97	2.00 E+05		1.15.E-05	0.82	2.0E-05	0.004	0.97
7	787	209	6.06 E-07	0.96	8.68 E-05	0.97	8.83 E+07		9.18 E-06	0.92	2.0E-05	0.004	0.43
14	936	218	6.88 E-07	0.60	7.60 E-05	0.97	4.90 E+08		5.59 E-06	0.89	2.0E-05	0.003	1.00

La Figure 4.15 montre les paramètres des points d'extrémité représentés, respectivement, par la résistance et la capacité de R_A et Q_B . Ces valeurs ont été représentées graphiquement pour comprendre le comportement des points d'extrémité de la ligne de transmission (Z_A et Z_B) pendant les jours d'immersion. Les valeurs de R_A et Q_B ont été obtenues à partir du Tableau 4.4.

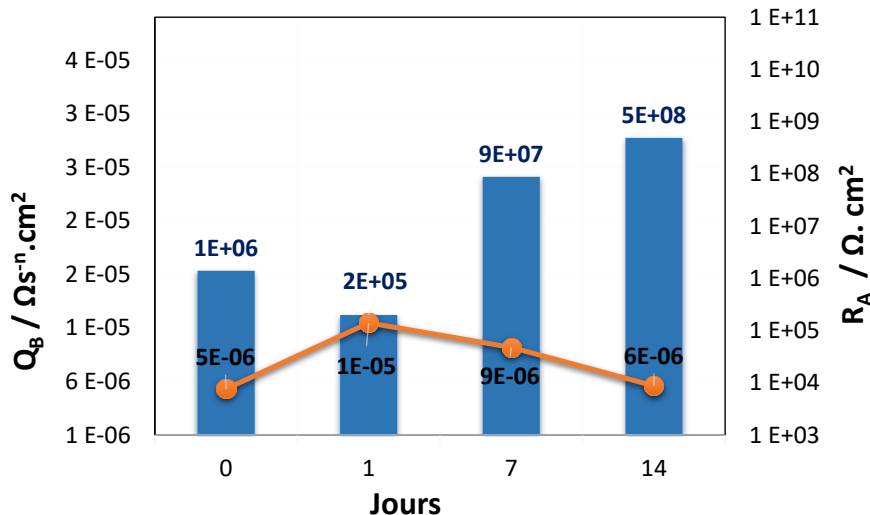


Figure 4.15 Paramètres R_A et Q_B , obtenus à partir du modèle de ligne de transmission utilisé dans les échantillons nanoporeux après différentes périodes d'immersion dans SBF.

La résistance R_A augmente progressivement avec le temps d'immersion. Ce comportement pourrait être associé à la nucléation et à la croissance possible de gel de silice hydraté et de phosphate de calcium amorphe sur les parties externes et internes des nanopores, deux prédecesseurs de la formation d'apatite [25]. Ce comportement peut être observé sur la Figure 4.16 (cercles rouges). De plus, les valeurs de Q_B ont été faibles et constantes, indiquant un comportement stable et protecteur du film passif intérieur pendant tout le temps analysé.

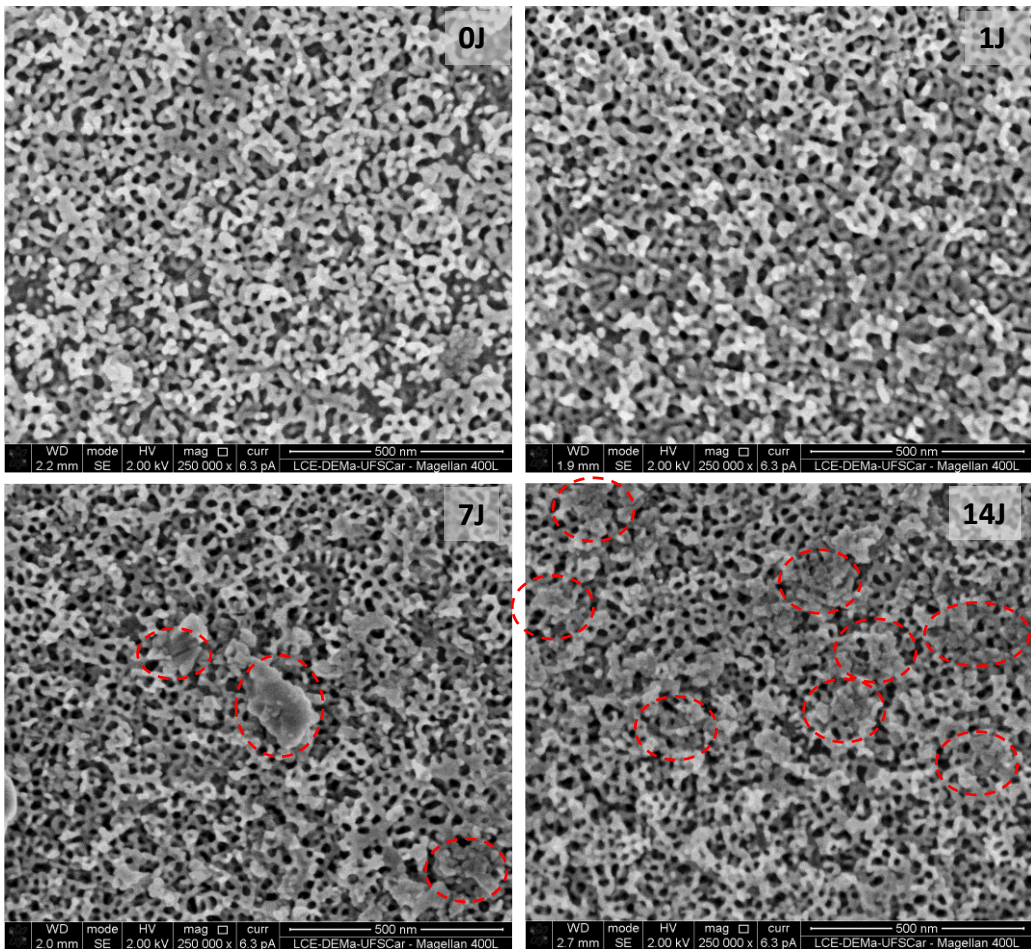


Figure 4.16 Formation d'apatite sur des échantillons nanoporeux après différentes périodes d'immersion dans SBF (0, 1, 7 et 14 jours, indiqués respectivement 0J, 1J, 7J et 14J).

Comme indiqué le processus de transport dans le canal 2 (X_2), est représenté par un modèle différent appelé « mode de transport anormal » (connexion parallèle d'un CPE, Q_2 , et d'une résistance, R_2), puisque le mécanisme de transport de charge dépend de la fréquence. Pour les deux conditions d'anodisation, ω_c était compris entre 0,003 et 0,035 Hz. Ces faibles valeurs indiquent un faible transfert de charge à travers le canal 2 dans le régime des fréquences étudiées dans ce travail (10^2 - 10^4 Hz).

La Figure 4.17 résume la réponse à la corrosion et la bioactivité, après 14 jours d'immersion dans SBF, des différentes conditions de surface étudiées dans ce travail ; les valeurs de résistance barrière (R_B ou R_A pour les échantillons anodisés) associées à la résistance à la corrosion ont été obtenues à partir les données d'impédance, le I_{pass} , obtenu à partir les courbes de polarisation et, la bioactivité, par le gain de masse.

Les échantillons non traités ont montré une assez bonne résistance à la corrosion indiquée par une valeur élevée de résistance et un I_{pass} acceptable, inférieur à $2 \mu\text{A.cm}^{-2}$; cependant, dans ce cas, aucune formation de HAp n'a pas été détectée.

Les échantillons traités avec HCl et NaOH, contrairement aux échantillons non traités, ont montré une excellente bioactivité avec la valeur de gain de masse la plus élevée, d'environ 1,8 mg après 14 jours d'immersion dans SBF. Pourtant, leur résistance à la corrosion est faible avec le plus bas R_B et les valeurs de I_{pass} les plus élevées.

Enfin, les échantillons anodisés ont montré la meilleure résistance à la corrosion avec les valeurs les plus élevées et les plus faibles de R_A et I_{pass} , respectivement. Néanmoins les échantillons avec des nanotubes et des nanopores ont présenté des valeurs faibles et modérées de formation de HAp après 14 jours dans SBF.

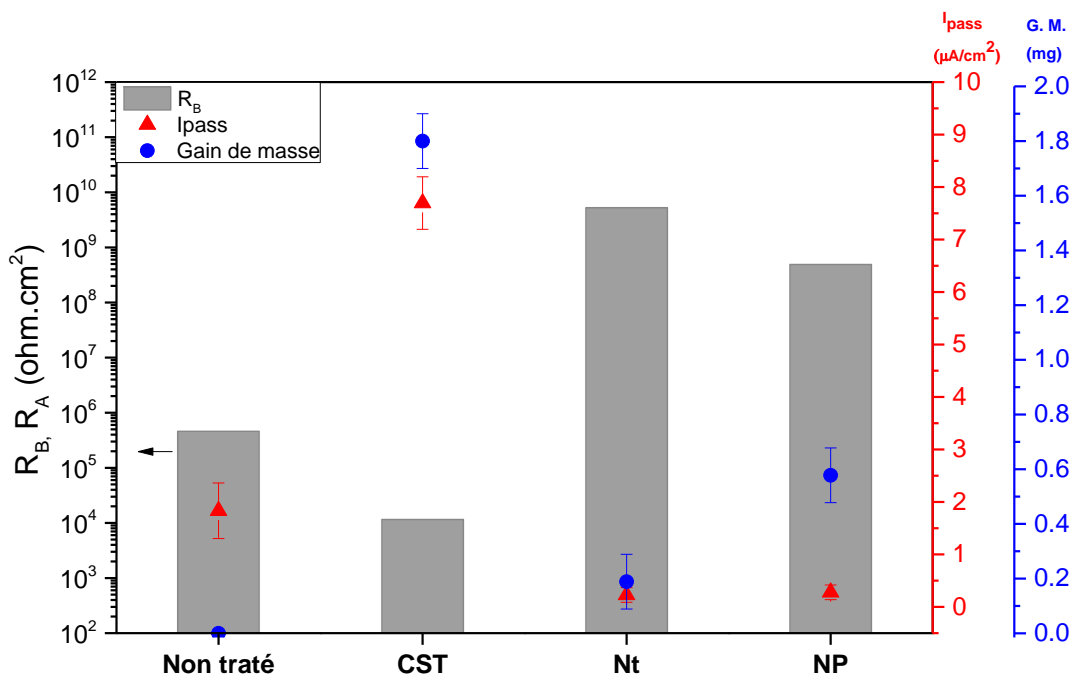


Figure 4.17 Réponse à la corrosion et bioactivité d'échantillons non traités, traités avec CST, avec des nanotubes et des nanopores après 14 jours d'immersion dans SBF à 37 °C. Résistance barrière (R_B ou R_A pour les échantillons anodisés) obtenue à partir les données d'impédance, le courant de passivation (I_{pass}), à partir les courbes de polarisation et, de la bioactivité, à travers le gain de masse.

5 Comportement en fatigue de TMZF avec différents états de surface

5.1 Résistance à la fatigue des échantillons de TMZF non traités et traités avec CST et nanopores

Pendant certaines étapes de ces processus de modification de surface, de l'hydrogène est produit. Il pourrait être absorbé dans l'alliage et causer des problèmes de fragilisation, en raison de l'affinité de la phase β du titane pour l'hydrogène et cela pourrait affecter directement le processus de propagation de fissures par fatigue.

Ainsi, la réponse à la fatigue des échantillons non traités (surface polie), traités avec HCl et NaOH (CST) et des échantillons anodisés (nanopores) a été évaluée. La résistance à la fatigue a été déterminée par le protocole de type Staircase (ou méthode de l'escalier) et puis les surfaces de rupture ont été analysées pour évaluer les preuves des mécanismes de fragilisation.

Les implants orthopédiques sont sujets aux charges cycliques en raison des sollicitations mécaniques du corps humain. Des essais de fatigue à grand nombre de cycles (HCF, en anglais, pour *High Cycle Fatigue* - $N = 5 \times 10^6$ cycles) ont été effectués avec le protocole Staircase afin d'évaluer la résistance à la fatigue des différentes surfaces étudiées dans ce travail.

Les échantillons non traités ont été moulés et polis, en vue d'atténuer l'influence des défauts de surface induits par l'usinage sur les propriétés de fatigue. La limite de fatigue en termes de la contrainte maximale et de l'écart-type, calculées à partir l'approche statistique Dixon-Mood, sont respectivement 730 et 13 MPa (voir le Tableau 5.1).

Tableau 5.1 Mesures topographiques des rugosités de R_a et R_z , réponse à la fatigue, teneur en hydrogène et observations fractographiques pour les différentes conditions de surface étudiées dans ce travail.

	Rugosités (μm)		Contrainte Max Fatigue (MPa)	H (ppm)	Observations fractographiques
	Ra	Rz			
Non traité	<0.100	<0.100	730 \pm 13	99 \pm 22	<ul style="list-style-type: none"> • Stries de fatigue et des motifs de rivière bien définis.
CST non polis	0.443	3.390	< 300	310 \pm 23	<ul style="list-style-type: none"> • Propagation circonférentielle des fissures associée au mécanisme HELP. • Rugosité élevée, possibilité d'effet d'entaille.
CST-polis	<0.100	<0.100	563 \pm 28	261 \pm 4	<ul style="list-style-type: none"> • Fissures secondaires aux joints de grains. • Preuve de formation d'hydrure. • Fracture intergranulaire dans des échantillons testés avec un niveau d'effort élevé et en corrélation avec le mécanisme de décohésion induite par l'hydrogène.
Nanopores	<0.100	0.313	< 300	127 \pm 23	<ul style="list-style-type: none"> • Propagation circonférentielle de fissures associée au mécanisme HELP.

La Figure 5.1 illustre la surface de rupture des échantillons non traités pour examiner et pour déterminer la caractéristique de la rupture après les essais de fatigue. La nucléation de fissures sur la surface (région 1) a été le principal site d'initiation pour les échantillons non traités. La zone de propagation stable des fissures, ou région 2, occupe environ 50% de la surface totale et elle se caractérise par des stries de fatigue et des motifs de rivière bien définis. La superficie restante comprend une zone transitoire de propagation instable de fissures.

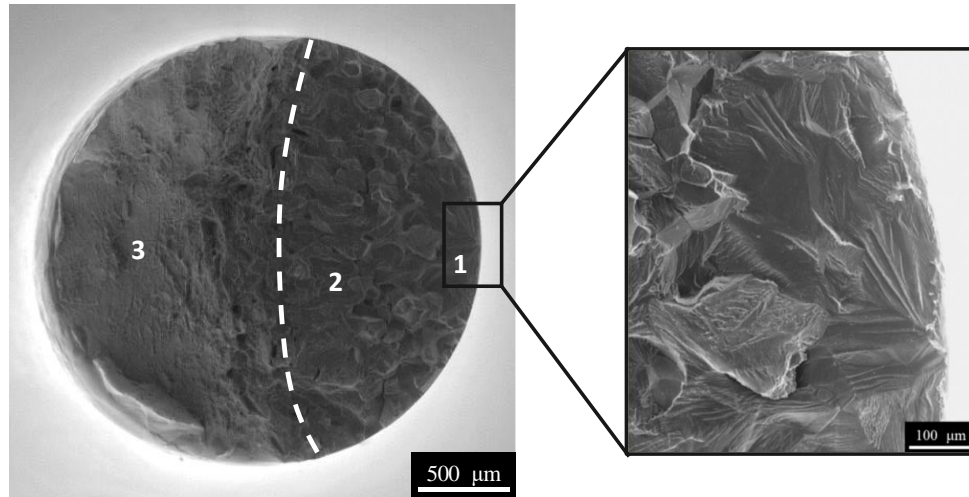


Figure 5.1 Fractographie de l'échantillon non traité, la ligne en tirets indique la transition approximative entre la zone stable et de la zone instable de propagation de fissures ; le carré indique la région agrandie du côté droit, signalant le site d'initiation de fissures.

À l'aide d'un microscope à balayage laser confocal, des caractéristiques topographiques ont été obtenues, comme la rugosité et la morphologie des différents traitements étudiés.

Le Tableau 5.1 indique les valeurs moyennes de rugosité (R_a) et la rugosité crête-vallée (R_z) pour chacun des traitements. Des échantillons non traités ont été polis afin d'obtenir une surface souple et homogène, comme illustré sur la Figure 5.2 (a). Le procédé de polissage élimine les risques liés au procédé d'usinage, ce qui est corroboré par les faibles valeurs de rugosité de R_a et R_z .

La Figure 5.2 (b) illustre la topographie d'un échantillon représentatif traité avec HCl et NaOH. Cette attaque produit une surface avec la formation généralisée de micro-alvéoles d'une taille à peu près de 3.40 μm . Elle est supérieure à celle observée dans les échantillons polis (<100 μm).

La dispersion de la rugosité (i.e., entailles) peut entraîner des différences considérables dans la réponse à la fatigue du composant. Par exemple, des rainures d'environ 3.50 μm dans l'alliage de Ti-6Al-4V pourraient réduire la résistance à la fatigue d'environ 12% [26].

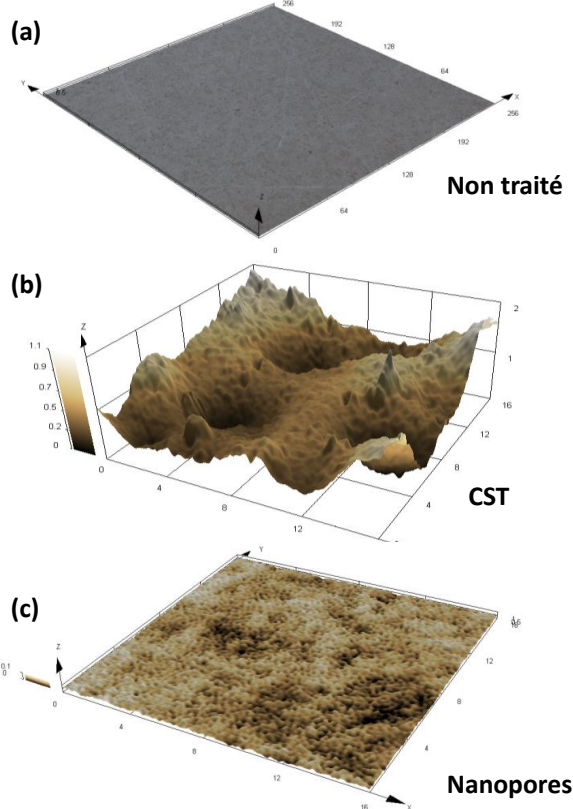


Figure 5.2. Images 3D réalisés en microscopie confocale à balayage laser d'échantillons : a) non traité, b) CST et nanopores.

Les résultats préliminaires de fatigue des échantillons CST ont montré une diminution drastique de la résistance à la fatigue jusqu'à une valeur inférieure à 370 MPa (contrainte de traction maximale pour la géométrie de la tige de la hanche [27]). Cette forte réduction de la résistance à la fatigue (~ 50% en comparaison avec les échantillons non traités) indique l'existence d'un phénomène supplémentaire à la sensibilité à l'entaille qui affecte la réponse à la fatigue du matériel.

Des études antérieures employant une attaque au HCl et un traitement au NaOH sur un alliage de titane $\alpha + \beta$ ont montré une augmentation significative de la teneur en hydrogène [28]. Même une légère augmentation de la teneur en hydrogène pourrait entraîner une fragilisation des alliages de titane, ce qui produirait une réduction de la ténacité à la rupture et de la résistance à la fatigue [29, 30].

En ce sens, la teneur en hydrogène des différentes conditions de surface a été calculée (Tableau 5.1), et montre une augmentation après les traitements de surface en comparaison avec les échantillons non traités. Les échantillons CST présentent les valeurs les plus élevées, de près de 310 ppm. Cette teneur élevée en hydrogène pourrait expliquer la diminution drastique de la résistance à la fatigue des échantillons CST.

Pour déterminer s'il y a une altération de la résistance à la fatigue par l'hydrogène absorbé après le traitement chimique, les échantillons de TMZF traités chimiquement ont été moulés et polis (en utilisant le même procédé employé dans les échantillons non traités) afin d'éliminer les micro-alvéoles formés et donc, d'éviter l'effet d'entaille. Puis, les échantillons ont été testés par le protocole de type Staircase.

La limite de fatigue, en termes de la contrainte maximale et de l'écart-type calculés sont respectivement 563 et 28 MPa pour les échantillons traités chimiquement et polis. La réduction de 25% de la résistance à la fatigue, en comparaison avec les échantillons non traités, pourrait être associée à l'augmentation significative de la teneur en hydrogène observée dans le matériel, même après le moulage et le polissage de la surface des spécimens.

La Figure 5.3 présente la surface de rupture des spécimens CST polis. Dans ce cas, la zone de propagation est caractérisée par des marches de clivage ou par des motifs de rivières. Les branches de ces motifs de rivières se rejoignent dans la direction de propagation des fissures ; elles peuvent servir à l'établissement de la direction de la fracture local et du point de nucléation de la fissure, indiqué par le carré noir.

La région agrandie dans la Figure 5.3 montre l'évidence de fissures secondaires, celles-ci formées à travers les limites du grain. Généralement, ce genre de fracture est associée au phénomène de fragilisation par l'hydrogène, comme la fragilisation des joints des grains ou même la formation et rupture multiple des phases fragiles de l'hydrure, près des joints de grain [31, 32].

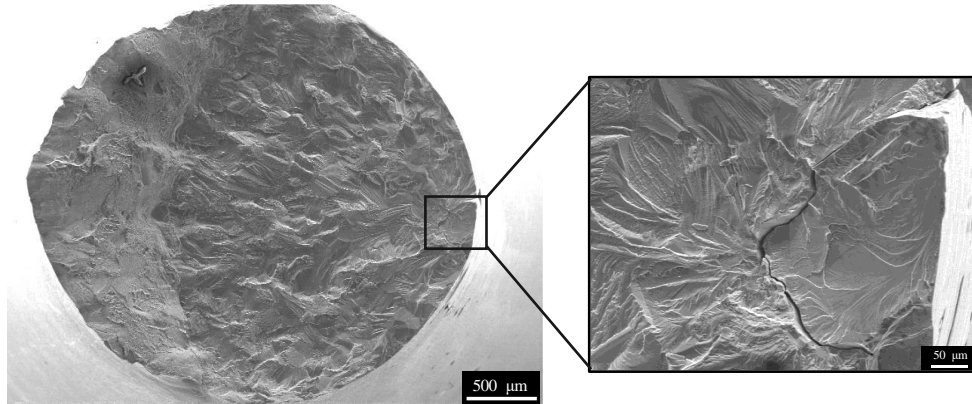


Figure 5.3 Fractographie de l'échantillon CST poli, le carré indique la région agrandie du côté droit, signalant le site d'initiation de fissures.

Comme référencé dans le Tableau 5.1, les échantillons anodisés avec nanopores ont présenté une légère augmentation de la teneur en hydrogène, près de 150 ppm. Cette valeur est inférieure à celle observée en échantillons traités avec CST. En outre, à partir des mesures confocales (Tableau 5.1), les échantillons

nanoporeux ont présenté une surface avec des valeurs faibles de rugosité ($R_z = 0.3 \mu\text{m}$), ce qui pourrait éviter un possible effet d'entaille. Ces deux conditions pourraient indiquer un comportement meilleur à la fatigue que celui des échantillons CST.

Contrairement au comportement attendu, tous les alliages avec des nanopores ont échoué - même un échantillon testé à 300 MPa, à des valeurs inférieures de contrainte de traction principale maximale pour une géométrie de la tige de la hanche (370 MPa) [27]. Seul l'échantillon testé à 200 MPa a survécu à l'usure. Cela révèle que, même en évitant la possibilité d'effet d'entaille, le procédé d'anodisation réduit la résistance à la fatigue et cet effet pourrait être associé à la teneur d'hydrogène dans les échantillons.

La surface de rupture par fatigue correspondant aux échantillons nanoporeux qui ont été testés à 500 MPa est illustrée sur la Figure 5.4(a). Comme on l'observe dans la région (b), les caractéristiques typiques du développement de fissure de fatigue cyclique, comme les marches de rivières et les marches de clivage apparaissent et deviennent le principal mécanisme de propagation dans cette région. Cette zone de propagation stable des fissures par fatigue est limitée à une petite région elliptique.

Les fractographies sur la Figure 5.4 (c-d) des échantillons CST et traités avec nanopores montrent plus de signes de rupture fragile. Ici, il y a la présence d'une forme de clivage distincte, appelée lignes de Wallner (indiquée par des flèches noires). Cette géométrie est observée dans les surfaces de rupture des matériaux fragiles, dans les inclusions ou dans les composés intermétalliques. Elle est composée de deux séries d'étapes de marches de clivage parallèles qui se croisent souvent pour produire un motif entrecroisé. Le résultat des lignes de Wallner est la propagation simultanée d'un front de fissure et d'une onde de choc élastique dans le matériel [33].

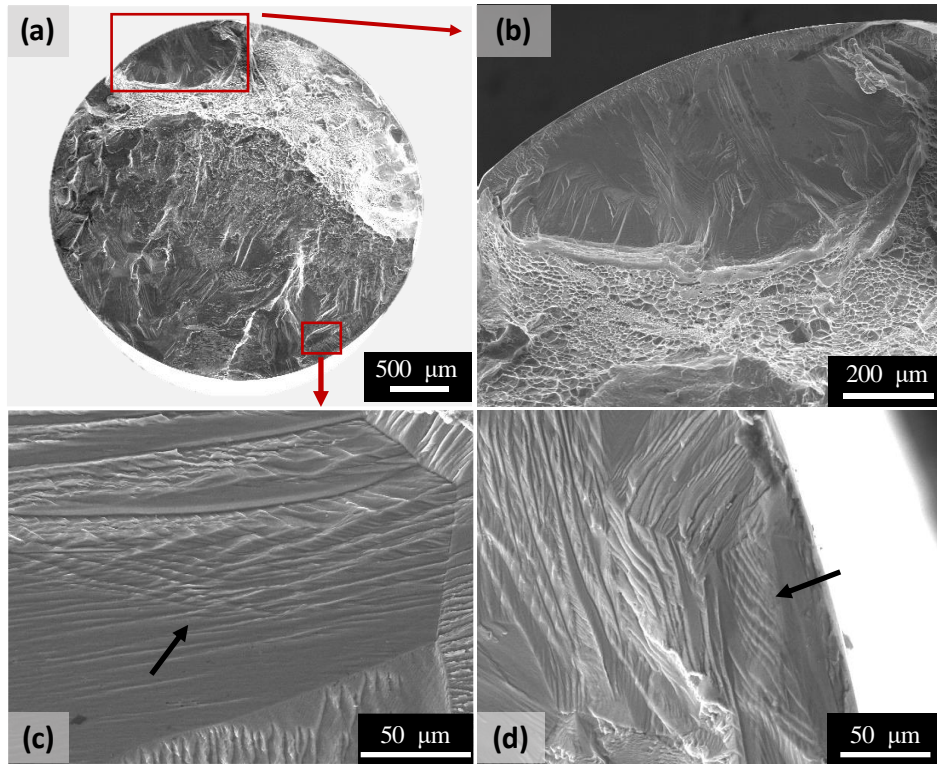


Figure 5.4 a) Fractographie de l'échantillon nanoporeux testé à 500 MPa, b) région agrandie indiquant une zone de propagation stable des fissures, c) région agrandie des échantillons nanoporeux indiquant des lignes de Wallner et d) région agrandie de l'échantillon CST poli, qui a été testé à la fatigue à 550 MPa indiquant la forme des lignes de Wallner.

5.2 La fragilisation par l'hydrogène

La fragilisation par l'hydrogène (HE en anglais, pour *Hydrogen embrittlement*) est un phénomène intéressant, mais nocif et il pourrait être présent dans une grande variété de métaux et d'alliages. Le HE comprend un groupe de mécanismes associés à la réduction des propriétés mécaniques attribuées à l'hydrogène en tant qu'élément principal [31].

Le mécanisme de rupture sous-jacent à cette fragilisation dans les alliages de titane n'est pas totalement compris. Cette difficulté est particulièrement vraie pour les alliages de titane β -métastable, où l'effet de l'hydrogène dans le comportement mécanique a été expliqué en termes de : (i) défaillance due à la formation d'hydrure induite par le stress [29, 34], (ii) décohésion induite par l'hydrogène [31, 35, 36] et (iii) plasticité localisée améliorée par l'hydrogène (HELP en anglais, pour *hydrogen-enhanced localized plasticity*) [37, 38]. Même dans les systèmes monophasés, comme dans le cas de l'alliage de TMZF, l'identification du mécanisme de fragilisation est complexe et plusieurs mécanismes de fracture liés à l'hydrogène

peuvent fonctionner simultanément [35, 36, 38]. Bien que de nombreux mécanismes aient été proposés pour expliquer la fragilisation par hydrogène, ceux mentionnés ci-dessus sont considérés comme les plus applicables à cette étude.

La Figure 5.5 montre l'analyse par cartographie d'orientation cristalline automatisée (ACOM-TEM) des échantillons CST et puis testés à la fatigue. En plus de la phase β de la matrice, il est possible d'observer, sur la cartographie de phase, la présence de particules très fines de TiH_2 ou des graines avec un réseau tétragonal. La présence de ces hydrures fragiles est une preuve de l'effet de l'hydrogène sur la réduction de la résistance à la fatigue du matériau.

Ces hydrures peuvent résulter de l'augmentation de la concentration locale d'hydrogène dans le champ de contrainte de traction de défauts étendus du réseau, tels que des dislocations. Alors, il semble que, comme l'hydrogène présente une solubilité considérable dans la phase β et, la déformation localisée pendant l'essai de fatigue a induit la ségrégation de l'hydrogène [39, 40]. Par conséquent, la précipitation de TiH_2 s'est produite aux joints de grains à haute énergie, comme illustré dans la Figure 5.5 b et 5.5 c.

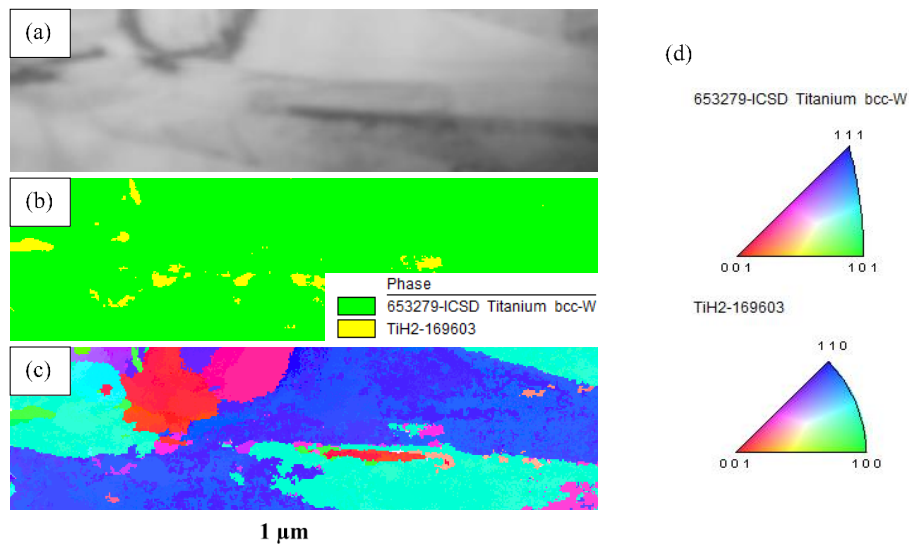


Figure 5.5 Images de l'échantillon CST poli et testé en fatigue, générées à l'aide du système ASTAR couplé à TEM : (a) image virtuelle en champ clair (VBF, en anglais, pour *virtual bright-field*), (b) cartographie de phase (PM, en anglais, pour *phase mapping*), (c) *orientation image mapping* (OIM, en anglais) et (d) figure de pôle inverse (IPF, en anglais, pour *inverse pole figure*), d'où les couleurs ont été utilisées pour indexer les orientations dans l'OIM.

Un autre mécanisme HE étudié dans ce travail est la HELP. Dans cette théorie, la nucléation et le mouvement des dislocations sont favorisés par la teneur en hydrogène [35, 41]. En ce sens, il est prévu une augmentation de la déformation et

de la plasticité au niveau de la zone à forte concentration d'hydrogène. Ainsi, des preuves justifiant le mécanisme HELP sont observées en fractographie avec propagation localisée de fissure ductile [37, 38].

De l'hydrogène est produit lors destraitements à l'interface métal / électrolyte. En même temps, une quantité de cet élément est absorbée et diffuse dans l'alliage de titane ; cependant, une grande quantité s'accumule à côté de la surface de l'échantillon. Cette condition a facilité l'observation du mécanisme HELP agissant sur les nanopores et les échantillons CST non polis lors de l'essai de fatigue.

La Figure 5.6 présente des signes du mécanisme HELP agissant sur les échantillons CST non polis pendant l'essai de fatigue à 300 MPa. Grâce aux images agrandies, il est possible d'observer une fissure circonférentielle se propageant dans le spécimen rond. La propagation de cette fissure ductile localisée est confinée dans une région d'environ $26 \pm 5 \mu\text{m}$ de la surface de l'échantillon (Figure 5.6 b-d), favorisée par une augmentation de la nucléation et de la mobilité de dislocation, en raison d'une plus grande concentration d'hydrogène dans cette région souterraine.

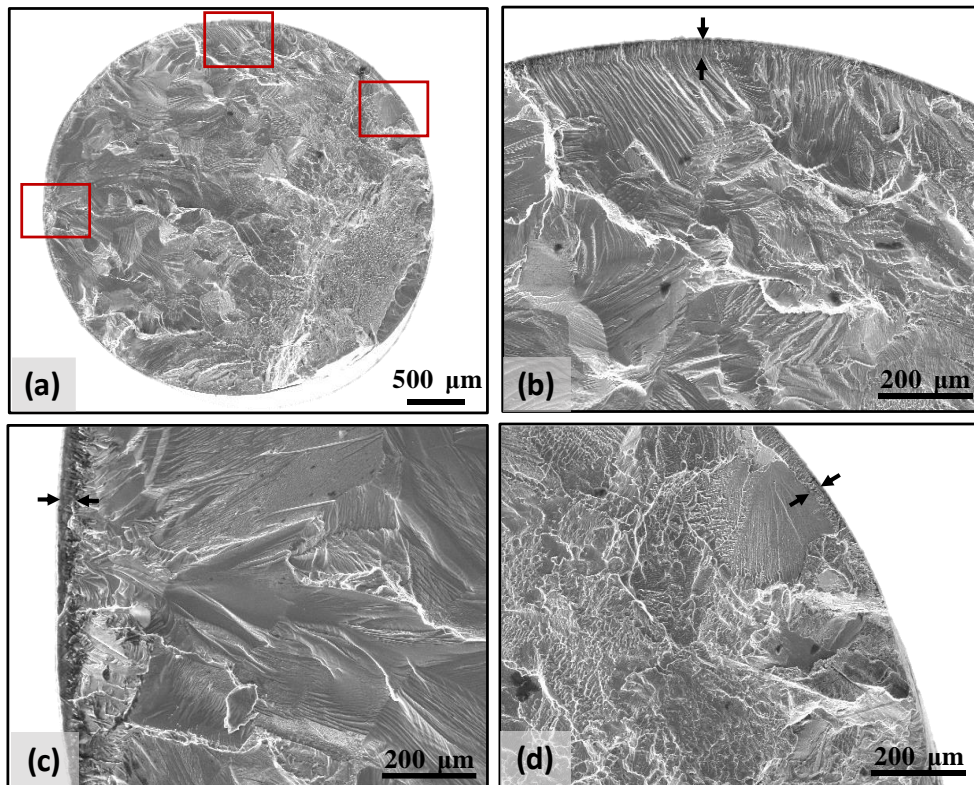


Figure 5.6 a) Fractographie de l'échantillon CST non poli, qui a été testé à la fatigue à 300 MPa, b), c) et d) région agrandie indiquant une zone de propagation stable de fissure dans la zone hydrogénée indiquée par des flèches noires.

Un comportement similaire a été observé dans les échantillons nanoporeux fracturés après les essais de fatigue. La Figure 5.7 montre la preuve d'une fissure circonférentielle se propageant autour de l'échantillon. Ici, la région confinée de la fissure circonférentielle est un peu plus diffuse que pour les échantillons CST. Cela suggère que les valeurs affichées dans le Tableau 5.1, pour les échantillons CST et nanopores, pourraient être plus élevées que celles indiquées, en raison de la difficulté expérimentale à obtenir la concentration d'hydrogène avec précision en surface.

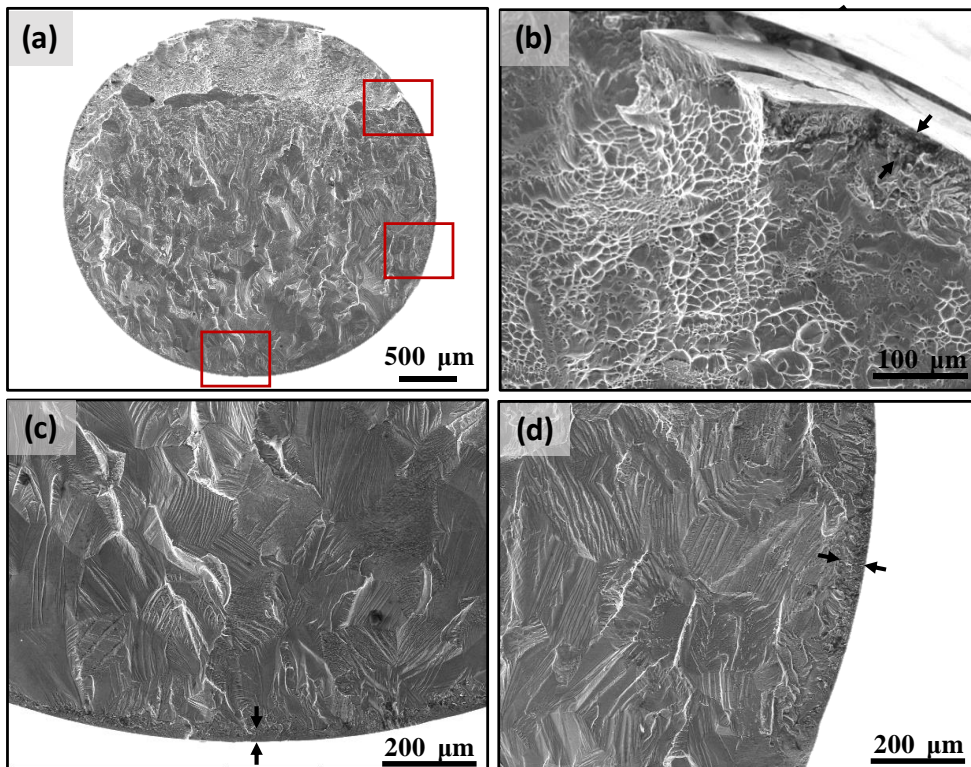


Figure 5.7 a) Fractographie d'un échantillon nanoporeux qui a été testé en fatigue à 300 MPa, b) zone agrandie de la rupture finale, c) et d) région indiquant une zone de propagation stable de fissure dans la zone hydrogénée, indiquée par des flèches noires.

La Figure 5.7 montre que la fissure de surface circonférentielle est générée et propagée au cours des cycles initiaux. À partir cela, de nouvelles fissures se nucléent, puis se propagent radialement dans l'échantillon sur un plan normal à la charge externe (Figure 5.7 c). Enfin, la rupture se produit sous une surcharge affichant des fossettes peu profondes. Comme observé sur la Figure 5.7, cette rupture finale se connecte directement à la fissure circonférentielle préexistante, ce qui corrobore la séquence de fracture mentionnée.

Conclusions Generales

Dans cette thèse, la biocompatibilité et la résistance à la corrosion des échantillons de Ti-12Mo-6Zr-2Fe avec des nanotubes, des nanopores et traités chimiquement, immergés pendant 0, 1, 7 et 14 jours dans du SBF,a été évaluée ainsi que la variation de résistance à la fatigue des échantillons non traités, traités avec CST et nanopores. Les conclusions de ces analyses sont résumées dans les paragraphes suivants :

- Les traitements de surface comme nanotubes, nanopores et traitement de surface chimique dans l'alliage β -TMZF ont été réalisés avec succès.
- Après 14 jours d'immersion dans le SBF, il n'a pas été possible d'observer la formation de HAp sur les échantillons non traités. Au cours de la même période, les échantillons de nanotubes et nanoporeux ont montré une formation de HAp modérée (respectivement) alors queles échantillons CST ont montré le meilleur comportement de bioactivité avec la formation de HAp la plus élevée de toutes les surfaces étudiées.
- Les valeurs de E_{corr} ont révélé un comportement plus noble des nanotubes et des nanopores que les échantillons CST et non traités, indiquant une surface plus protectrice. De plus, bien que ces surfaces anodisées aient montré des valeurs d' i_{pass} modérées aux premiers stades de l'immersion (0 et 1 jour), après 14 jours immergés dans SBF, elles ont montré les valeurs les plus faibles, proches de $0,2 \mu\text{A.cm}^{-2}$ placées dans la catégorie de résistance « Très stable ».
- Les diagrammes de Nyquist et de Bode pour les échantillons TMZF non traités ont montré un comportement pseudo-capacitif en raison de leur bi-couche passive très protectrice. L'augmentation continue du module d'impédance dans ces échantillons suggère que la résistance à la corrosion augmente avec le temps d'immersion en raison de la croissance de la barrière intérieure compacte.
- À travers les courbes de Nyquist et de Bode, les échantillons CST ont montré un comportement plus réactif par rapport aux échantillons non traités, indépendamment du temps d'immersion dans SBF. Dans ces échantillons, après 14 jours d'immersion, il a été possible d'observer une variation de la courbe d'impédance, associée à la formation de la couche de HAp sur la surface.
- Les courbes d'impédance des échantillons anodisés dans le SBF ont révélé un comportement capacitif ou au moins pseudo-capacitif, ce qui a corroboré la réponse protectrice de ces conditions de surface. De plus, il a été observé un comportement singulier qui ne pouvait pas être modélisé par les circuits équivalents traditionnels. Ainsi, un modèle de ligne de transmission à deux canaux a été proposé pour analyser les résultats d'impédance avec succès.

- Les échantillons de TMZF non traités ont montré une limite de fatigue élevée en termes de contrainte maximale de 730 MPa pour 5×10^6 cycles.
- Les résultats de fatigue des échantillons CST ont montré une diminution drastique de la résistance à la fatigue d'environ 50% par rapport aux échantillons non traités, en raison de l'effet d'entaille et de la forte teneur supplémentaire en hydrogène.
- Afin d'éviter l'effet d'entaille, les échantillons CST ont été polis et, ensuite, testés en fatigue. Cependant, ils ont montré une diminution de 25% de la résistance à la fatigue par rapport aux échantillons non traités, associé à l'hydrogène absorbé pendant le CST.
- Même avec une légère augmentation de l'hydrogène mesuré, les échantillons nanoporeux à faible rugosité de surface ont montré une réduction spectaculaire de la résistance à la fatigue, similaire aux échantillons CST non polis associé à une forte concentration d'hydrogène à la surface de l'échantillon.
- Dans cette étude, on a observé des preuves de trois mécanismes de fragilisation par l'hydrogène pouvant avoir agi sur les échantillons traités : formation d'hydrure induite par la contrainte, décohésion induite par l'hydrogène et plasticité localisée renforcée par l'hydrogène. Cependant, d'autres études sont nécessaires pour certifier ces mécanismes.
- Les résultats de fatigue et les mécanismes de fragilisation par l'hydrogène observés dans cette étude soulignent le risque des méthodes bien connues pour concevoir la surface de titane pour des améliorations d'ostéointégration, sans évaluation mécanique et électrochimique systématique.

REFERENCE

- [1] H. Takadama, H. M. Kim, T. Kokubo, and T. Nakamura, TEM-EDX study of mechanism of bonelike apatite formation on bioactive titanium metal in simulated body fluid, *J. Biomed. Mater. Res.*, vol. 57, no. 3, pp. 441–448, 2001.
- [2] R. J. Narayan, *ASM Handbook, Volume 23 Materials for Medical Devices*, 1 st., vol. 23. 2012.
- [3] A. K. Shukla, R. Balasubramaniam, and S. Bhargava, Properties of passive film formed on CP titanium, Ti-6Al-4V and Ti-13.4Al-29Nb alloys in simulated human body conditions, *Intermetallics*, vol. 13, no. 6, pp. 631–637, 2005.
- [4] F. Hilario, V. Roche, R. P. Nogueira, and A. M. J. Junior, Influence of morphology and crystalline structure of TiO_2 nanotubes on their electrochemical properties and apatite-forming ability, *Electrochim. Acta*, vol. 245, pp. 337–349, 2017.
- [5] E. Vasilescu, P. Drob, D. Raducanu, I. Cinca, D. Mareci, J. M. Calderon Moreno, M. Popa, C. Vasilescu, and J. C. Mirza Rosca, Effect of thermo-

- mechanical processing on the corrosion resistance of Ti6Al4V alloys in biofluids, *Corros. Sci.*, vol. 51, no. 12, pp. 2885–2896, 2009.
- [6] S. Tamilselvi, V. Raman, and N. Rajendran, Surface modification of titanium by chemical and thermal methods - Electrochemical impedance spectroscopic studies, *Corros. Eng. Sci. Technol.*, vol. 46, no. 4, pp. 585–591, 2011.
 - [7] F. Hilario, Synthèse et caractérisations de nanotubes de TiO₂ pour applications biomédicales : propriétés électrochimiques et bioactivité, Université Grenoble Alpes, 2018.
 - [8] V. Augustyn, P. Simon, and B. Dunn, Pseudocapacitive oxide materials for high-rate electrochemical energy storage, *Energy Environ. Sci.*, vol. 7, no. 5, pp. 1597–1614, 2014.
 - [9] H. Liu, J. Yang, X. Zhao, Y. Sheng, W. Li, C. L. Chang, Q. Zhang, Z. Yu, and X. Wang, Microstructure, mechanical properties and corrosion behaviors of biomedical Ti-Zr-Mo-xMn alloys for dental application, *Corros. Sci.*, vol. 161, no. May, pp. 2–15, 2019.
 - [10] P. Córdoba-Torres, N. T. C. Oliveira, C. Bolfarini, V. Roche, and R. P. Nogueira, Electrochemical impedance analysis of TiO₂ nanotube porous layers based on an alternative representation of impedance data, *J. Electroanal. Chem.*, vol. 737, pp. 54–64, 2015.
 - [11] Mark E. Orazem and B. Tribollet, Electrochemical Impedance Spectroscopy, in *Agricultural and Food Electroanalysis*, Second edi., 2015, pp. 381–419.
 - [12] S. L. De Assis, S. Wolynec, and I. Costa, Corrosion characterization of titanium alloys by electrochemical techniques, *Electrochim. Acta*, vol. 51, no. 8–9, pp. 1815–1819, 2006.
 - [13] D. Q. Martins, W. R. Osório, M. E. P. Souza, R. Caram, and A. Garcia, Effects of Zr content on microstructure and corrosion resistance of Ti-30Nb-Zr casting alloys for biomedical applications, *Electrochim. Acta*, vol. 53, no. 6, pp. 2809–2817, 2008.
 - [14] A. Kocijan, D. K. Merl, and M. Jenko, The corrosion behaviour of austenitic and duplex stainless steels in artificial saliva with the addition of fluoride, *Corros. Sci.*, vol. 53, no. 2, pp. 776–783, 2011.
 - [15] K. B. Devi, K. Singh, and N. Rajendran, Synthesis and characterization of nanoporous sodium-substituted hydrophilic titania ceramics coated on 316L SS for biomedical applications, *J. Coatings Technol. Res.*, vol. 8, no. 5, pp. 595–604, 2011.
 - [16] S. Gudi, J. Radoševi, and M. Kliški, Study of passivation of Al and Al-Sn alloys in borate buffer solutions using electrochemical impedance spectroscopy, *Electrochim. Acta*, vol. 47, no. 18, pp. 3009–3016, 2002.
 - [17] F. Hilario, V. Roche, A. M. Jorge, and R. P. Nogueira, Application of the transmission line model for porous electrodes to analyse the impedance response of TiO₂ nanotubes in physiological environment, *Electrochim. Acta*,

- vol. 253, pp. 599–608, 2017.
- [18] L. Jonášová, F. a. Müller, A. Helebrant, J. Strnad, and P. Greil, Biomimetic apatite formation on chemically treated titanium, *Biomaterials*, vol. 25, pp. 1187–1194, 2004.
 - [19] Diego Alfonso Godoy Pérez, *Influence Of Surface Treatments on Corrosion Resistance Properties Of Ultrafine Grained Titanium Alloys For Biomedical applications*, Universite Grenoble Alpes And Universidade Federal De São Carlos, 2019.
 - [20] R. de Levie, On porous electrodes in electrolyte solutions*, *Electrochim. Acta*, vol. 9, no. 9, pp. 1231–1245, 1964.
 - [21] P. Roy, S. Berger, and P. Schmuki, TiO₂ nanotubes: Synthesis and applications, *Angew. Chemie - Int. Ed.*, vol. 50, no. 13, pp. 2904–2939, 2011.
 - [22] G. Garcia-Belmonte, J. Bisquert, E. C. Pereira, and F. Fabregat-Santiago, Switching behaviour in lightly doped polymeric porous film electrodes. Improving distributed impedance models for mixed conduction conditions, *J. Electroanal. Chem.*, vol. 508, no. 1–2, pp. 48–58, 2001.
 - [23] G. Láng and K. E. Heusler, Remarks on the energetics of interfaces exhibiting constant phase element behaviour, *J. Electroanal. Chem.*, vol. 457, no. 1–2, pp. 257–260, 1998.
 - [24] T. Pajkossy, Impedance of rough capacitive electrodes, *J. Electroanal. Chem.*, vol. 364, no. 1–2, pp. 111–125, 1994.
 - [25] C. Shuai, H. Sun, P. Wu, C. Gao, Y. Yang, W. Guo, D. Yang, F. Xu, P. Feng, and S. Peng, Biosilicate scaffolds for bone regeneration: Influence of introducing SrO, *RSC Adv.*, vol. 7, no. 35, pp. 21749–21757, 2017.
 - [26] P. S. C. P. da Silva, L. C. Campanelli, C. A. Escobar Claros, T. Ferreira, D. P. Oliveira, and C. Bolfarini, Prediction of the surface finishing roughness effect on the fatigue resistance of Ti-6Al-4V ELI for implants applications, *Int. J. Fatigue*, vol. 103, pp. 258–263, 2017.
 - [27] B. J. S. de Oliveira, L. C. Campanelli, D. P. Oliveira, A. P. de Bribean Guerra, and C. Bolfarini, Surface characterization and fatigue performance of a chemical-etched Ti-6Al-4V femoral stem for cementless hip arthroplasty, *Surf. Coatings Technol.*, vol. 309, pp. 1126–1134, 2017.
 - [28] C. A. Escobar Claros, *Estudo da resistência à fadiga da liga Ti-6Al-4V com superfície modificada por tratamento químico*, Universidad de Sao carlos, 2016.
 - [29] V. Madina and I. Azkarate, Compatibility of materials with hydrogen. Particular case: Hydrogen embrittlement of titanium alloys, *Int. J. Hydrogen Energy*, vol. 34, no. 14, pp. 5976–5980, 2009.
 - [30] L. C. Campanelli, P. S. C. P. da Silva, A. M. Jorge, and C. Bolfarini, Effect of hydrogen on the fatigue behavior of the near-β Ti-5Al-5Mo-5V-3Cr alloy, *Scr. Mater.*, vol. 132, pp. 39–43, 2017.

- [31] P. P. Milella, *Fatigue and Corrosion in Metals*. 2013.
- [32] ASM International. *Handbook, ASM Handbook: Volume 12: Fractography, Met. Handb.*, vol. 2, p. 857, 1998.
- [33] ASM, *ASM Handbook Volume 12: Fractography*, vol. 2. 1987.
- [34] P. D. Nezhadfar, A. S. Johnson, and N. Shamsaei, Fatigue Behavior and Microstructural Evolution of Additively Manufactured Inconel 718 under Cyclic Loading at Elevated Temperature, *Int. J. Fatigue*, p. 105598, 2020.
- [35] D. F. Teter, I. M. Robertson, and H. K. Birnbaum, The effects of hydrogen on the deformation and fracture of β -titanium, *Acta Mater.*, vol. 49, no. 20, pp. 4313–4323, 2001.
- [36] A. M. Alvarez, I. M. Robertson, and H. K. Birnbaum, Hydrogen embrittlement of a metastable β -titanium alloy, *Acta Mater.*, vol. 52, no. 14, pp. 4161–4175, 2004.
- [37] W. Barrows, R. Dingreville, and D. Spearot, Traction-separation relationships for hydrogen induced grain boundary embrittlement in nickel via molecular dynamics simulations, *Mater. Sci. Eng. A*, vol. 650, pp. 354–364, 2016.
- [38] Y. Murakami, J. Yamabe, and H. Matsunaga, Microscopic mechanism of hydrogen embrittlement in fatigue and fracture, *Key Eng. Mater.*, vol. 592–593, pp. 3–13, 2014.
- [39] P. J. Ferreira, I. M. Robertson, and H. K. Birnbaum, Hydrogen effects on the character of dislocations in high-purity aluminum, *Acta Mater.*, vol. 47, no. 10, pp. 2991–2998, 1999.
- [40] J. Von Pezold, L. Lymerakis, and J. Neugebeauer, Hydrogen-enhanced local plasticity at dilute bulk H concentrations: The role of H-H interactions and the formation of local hydrides, *Acta Mater.*, vol. 59, no. 8, pp. 2969–2980, 2011.
- [41] Y. Murakami, T. Kanezaki, Y. Mine, and S. Matsuoka, Hydrogen embrittlement mechanism in fatigue of austenitic stainless steels, *Metall. Mater. Trans. A Phys. Metall. Mater. Sci.*, vol. 39 A, no. 6, pp. 1327–1339, 2008.

Resumo Detalhado em Português

ESTUDO DE BIOATIVIDADE, RESISTÊNCIA À CORROSÃO E COMPORTAMENTO EM FADIGA DA LIGA Ti-12Mo-6Zr-2Fe APÓS DIFERENTES TRATAMENTOS DE SUPERFÍCIE

1 Introdução

As ligas metálicas para implantes ortopédicos devem apresentar quatro características essenciais: a) baixo efeito de “stress-shielding”, que ocorre devido à incompatibilidade do módulo de elasticidade entre osso e implante; b) biocompatibilidade, evitando elementos tóxicos; c) excelente desempenho à fadiga para implantes sujeitos a esforço cíclico e d) alta resistência à corrosão [1].

Devido à presença de elementos como Al e V, considerados citotóxicos, e ao alto módulo de elasticidade do Ti–6Al–4V–ELI (ELI do inglês Extra Low Interstitial content) de aproximadamente 110 GPa, novas ligas de titânio sem elementos tóxicos e módulo de elasticidade inferior foram desenvolvidas. As ligas β -titânio metaestáveis, como a liga Ti-12Mo-6Zr-2Fe (TMZF), apresentam alta resistência mecânica e menor módulo de elasticidade do que a Ti–6Al–4V–ELI [2].

Materiais metálicos como titânio e suas ligas, aço inoxidável e ligas de cobalto-cromo são utilizados em condições de carga. No entanto, o contato direto metal-oso não implica a formação de uma forte ligação entre eles. Assim, é necessário desenvolver superfícies mais bioativas sobre esses metais [3].

Alguns tratamentos de superfície são aplicados a ligas de titânio para melhorar seu processo de osseointegração. Estudos anteriores demonstraram que o tratamento com HCl e depois com NaOH (CST) podem ser uma maneira eficaz de desenvolver características nanométricas na superfície de amostras de Ti–6Al–4V–ELI, sem alterar suas propriedades mecânicas estáticas e cíclicas [4].

Uma alternativa ao CST é o processo de anodização; esse procedimento é amplamente utilizado em titânio puro, criando nanotubos de TiO_2 na superfície, maximizando a área superficial específica do material e obtendo melhor biocompatibilidade [5].

Um indicador da capacidade de formação óssea em implantes metálicos é a nucleação e crescimento da camada de hidroxiapatita (HAp). Essa capacidade pode ser medida através da imersão da amostra em um fluido corporal simulado (SBF), cujas concentrações de íons são quase iguais às do plasma sanguíneo humano [3, 6].

Assim, o principal objetivo deste projeto é estudar o desempenho de biocompatibilidade e corrosão de amostras de Ti-12Mo-6Zr-2Fe com nanotubos,

nanoporos e tratamento químico de superfície (CST) imersos durante vários períodos no SBF, bem como a variação da resistência à fadiga destas diferentes condições de superfície.

2 Materiais e Metodos

Quatro condições diferentes de superfície foram investigadas em amostras de TMZF: superfície não tratada, superfície tratada com HCl e solução alcalina de NaOH (CST) e duas condições anodizadas - Nt e nanoporos NP.

A modificação com CST das amostras foi realizada em duas etapas: inicialmente com HCl e posteriormente com NaOH. Para o ataque ácido, foi utilizada uma placa aquecida a 60 °C por 30 min. Os tratamentos alcalinos foram realizados utilizando um recipiente de polietileno com 45 ml de NaOH 10 mol·L⁻¹ em uma temperatura de 60 °C por 24 h.

As nanoestruturas de TiO₂ foram obtidas por anodização das amostras polidas em uma célula eletroquímica com um arranjo convencional de dois eletrodos. Os experimentos de anodização foram realizados a 25 °C, num eletrólito orgânico constituído por glicerol, contendo 25% em volume de água e 0,25M de NH₄F. O potencial constante aplicado foi de 10V durante 2h para a formação de nanotubos e 20V durante 1h para os nanoporos. Finalmente, as amostras foram recozidas ao ar a 550 °C por 2h para cristalizar a superfície anodizada de TiO₂ em uma mistura de fases anatase e rutilo.

Para os estudos de corrosão, foram empregadas três técnicas eletroquímicas, utilizando uma solução eletrolítica de SBF a 37 °C e pH 7,4 em ambiente escuro, reproduzindo as condições corporais. Uma célula convencional de três eletrodos foi usada, onde as amostras de TMZF eram o eletrodo de trabalho com uma área exposta de 0,283 cm², uma grade de platina como contra eletrodo e um eletrodo de referência de SCE (do inglês Saturated Calomel Electrode). A distância entre o eletrodo de trabalho e o contra eletrodo foi de ~ 3 cm. Inicialmente, o potencial de circuito aberto (OCP) foi registrado durante 1h de imersão no eletrólito. Posteriormente, as medições de espectroscopia de impedância eletroquímica (EIS) foram registradas em estado estacionário com uma faixa de frequência de 100 MHz a 20 mHz e, finalmente, curvas de polarização potenciodinâmicas em uma faixa de potencial de 0,03 V / SCE a +1,2 V / SCE em relação ao OCP, e uma taxa de varredura de 0,3 mVs⁻¹. Esses testes de corrosão foram realizados em amostras não tratadas e com Nt, NP, CST; e em quatro diferentes tempos de imersão, 0, 1, 7 e 14 dias, dentro da solução SBF. Foram avaliadas três amostras por condição e tempo.

Após realizar as caracterizações eletroquímicas e de bioatividade, foram avaliadas as condições da superfície que apresentaram melhores resultados para

determinar se essas modificações afetam o comportamento em fadiga, por meio do teste de fadiga de alto ciclo denominado staircase.

3 Bioatividade e comportamento eletroquímico de amostras de TMZF não tratadas e tratadas com CST, nanoporos e nanotubos

A resposta biológica e eletroquímica do titânio comercialmente puro e da liga Ti-6Al-4V ELI tratada com processos químicos e eletroquímicos tem sido extensivamente estudada. No entanto, a necessidade do uso de ligas de titânio β com baixo módulo de elasticidade torna interessante o estudo desses tratamentos em ligas comerciais de β -Ti, como Ti-12Mo-6Zr-2Fe (TMZF).

No presente capítulo, o teste de ganho de massa de hidroxiapatita (HAp) foi realizado como um indicador do comportamento de osseointegração dos diferentes tratamentos de superfície obtidos sobre as amostras de TMZF. Além disso, o crescimento da HAp resultante das amostras imersas em solução SBF foi confirmado pelas técnicas de microscopia eletrônica de varredura (MEV), difração de raios X (DRX) e mapeamento Raman.

As imagens na Figura 3.1 referem-se à amostra tratada com ácido clorídrico (HCl) e hidróxido de sódio (NaOH); é possível observar o efeito do ataque em toda a superfície polida, alterando a morfologia inicial suave para uma superfície com microporos uniformemente distribuídos, revelando também os contornos dos grãos. Uma maior ampliação (Figura 3.1 b) foi usada para avaliar a presença de características nanométricas na superfície da amostra, confirmando o efeito do NaOH. Aqui é possível observar estruturas do tipo coral nas escaras submicrométrica e nanométrica formadas durante o tratamento alcalino.

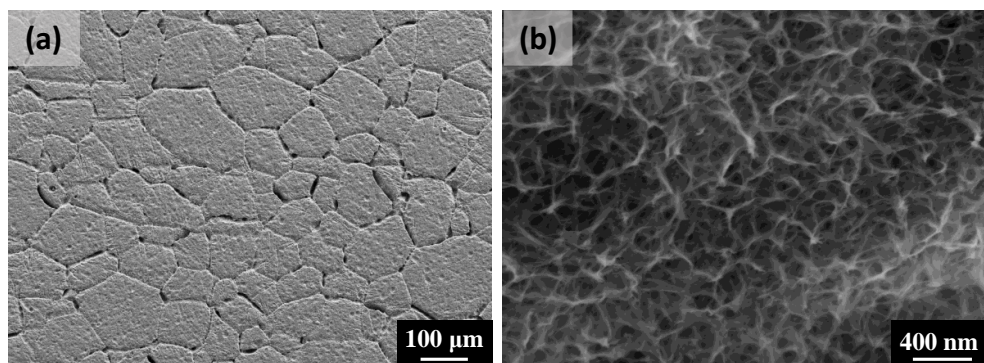


Figura 3.1 Imagens MEV da liga TMZF, tratadas quimicamente com HCl a 37% a 60 °C e NaOH 10 mol·L⁻¹ a 60 °C por 24h.

A imagem de MEV de alta resolução na Figura 3.2 mostra a condição final da superfície dos dois diferentes sistemas anodizados estudados neste trabalho. A Figura 3.2 (a) mostra a formação de uma rede de tubos auto-organizados verticalmente e distribuídos uniformemente por toda a superfície, enquanto a Figura

3.2 (b) mostra uma estrutura nanométrica desordenada; essa última superfície de mesoporos foi denominada nanoporos.

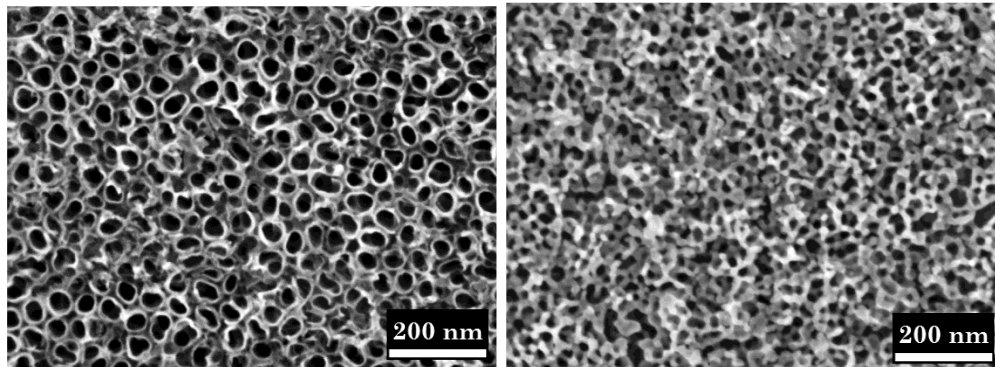


Figura 3.2 Imagem MEV de alta resolução de amostras anodizadas: a) Nanotubos e b) Nanoporos.

3.1 Teste de formação de hidroxiapatita

A Figura 3.3 resume o valor médio do ganho de massa para três amostras de cada condição de superfície durante os diferentes períodos. É possível ver que não há depósito de apatita na liga TMZF não tratada e nem na tratada com nanotubos. Em contraste, as amostras com nanoporos mostraram uma formação moderada de HAp após 14 dias de imersão (ganho de massa superior a 0,5 mg).

Por outro lado, as amostras de CST mostraram uma melhor capacidade de ligação óssea em comparação com as amostras anodizadas e não tratadas. Após 7 dias de imersão, essa superfície evidenciou uma formação significativa de apatita com ganho de massa superior a 0,8 mg; esse processo de nucleação e crescimento é mantido, mostrando o maior valor de ganho de massa em torno de 1,8 mg após 14 dias.

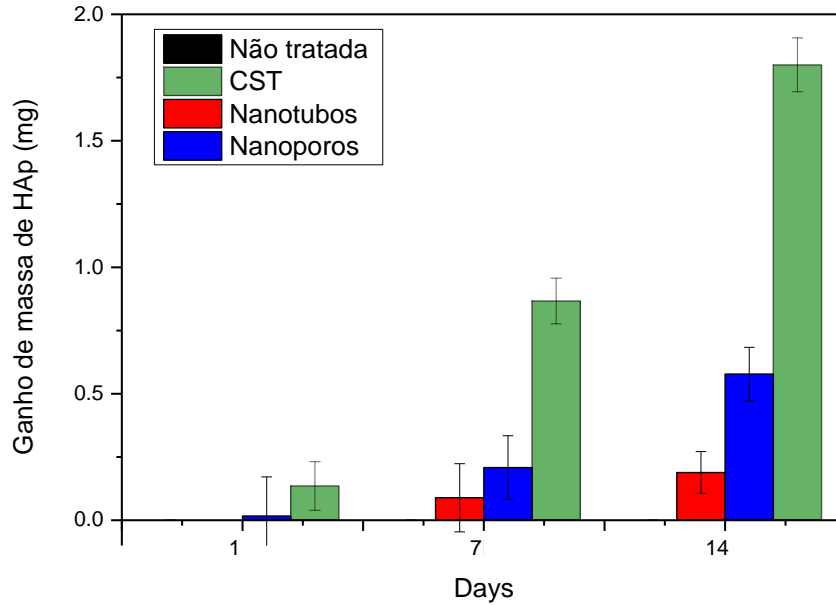


Figura 3.3 Avaliação quantitativa por ganho de massa de HAp nas amostras não tratadas, CST, nanotubos e nanoporos após diferentes tempos de imersão em SBF.

As imagens de MEV na Figura 3.4 revelam que, mesmo após 14 dias de imersão na solução fisiológica, nenhum ou um ligeiro traço de HAp é detectado em superfícies não tratadas, nanotubos e nanoporos. No entanto, foi possível observar esferas de HAp na amostra de CST após os mesmos 14 dias no SBF (Figura 3.4 d). Esta informação visual corrobora os valores de ganho de massa obtidos para os diferentes tratamentos de superfície após o tempo de imersão.

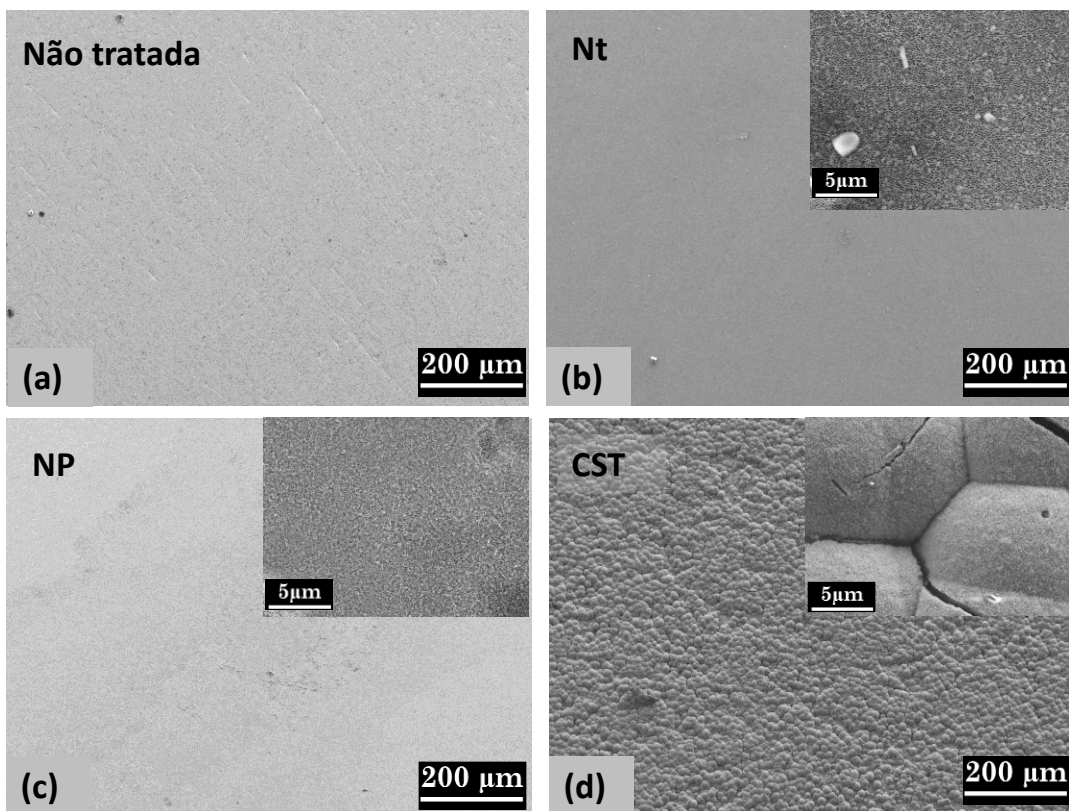


Figura 3.4 Imagens MEV para as amostras da liga TMZF submetidas aos testes de bioatividade após 14 dias imersos em SBF. a) Não tratada; b) Nanotubos; c) Nanoporos e d) amostras de CST.

A Tabela 3.1 mostra os resultados das análises de EDS realizadas em amostras não tratadas, tratadas com CST, nanotubos e nanoporos após 14 dias de imersão. Somente nas superfícies de CST e nanoporos foi detectada a presença de cálcio, fósforo e oxigênio, característicos da hidroxiapatita presente no corpo humano [1]. Este resultado é corroborado pelos padrões de DRX na Figura 3.5, onde é possível ver os picos de difração da fase HAp cristalina apenas nas amostras com CST após 14 dias de imersão.

Tabela 3.1 Análise química quantitativa de EDS das amostras não tratadas, nanotubos, nanoporos e CST. Após 14 dias de imersão em solução SBF.

Condição	Elemento químico (% at.)						
	Ti	Mo	Zr	Fe	O	Ca	P
Não tratada	67.32	3.79	2.15	1.94	22.75	-	-
Nanotubos	57.65	3.64	1.97	-	35.36	-	-
Nanoporos	46.28	3.10	1.60	-	48.89	0.60	0.40
CST	11.88	0.54	0.24	-	59.06	16.97	9.34

Outro teste complementar para saber se ocorre a forma cristalina do fosfato de cálcio (Hap) depositada nas superfícies tratadas é o mapeamento espectral Raman. Para este teste foi empregado o número de onda característico da HAp, 961cm^{-1} . Neste resultado qualitativo, a formação de HAp é determinada pela intensidade da cor vermelha; zonas de maior intensidade significam maior precipitação deste composto.

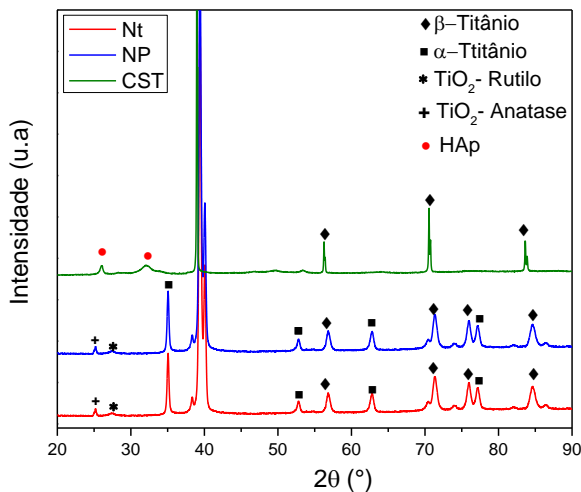


Figura 3.5 Padrões XRD de amostras não tratadas, CST, nanotubos e nanoporos após 14 dias de imersão em SBF.

A Figura 3.6 mostra a diferença entre as amostras tratadas após 7 e 14 dias de imersão em SBF. Independentemente do tempo de imersão, as amostras de nanotubos apresentaram mapas com baixa intensidade Raman, indicando baixa formação de HAp mesmo após 14 dias de imersão. No caso de amostras de nanoporos, os resultados são um pouco melhores, mostrando diferentes zonas com precipitados de HAp após 14 dias de imersão em SBF. As amostras de CST mostraram o melhor comportamento de bioatividade com uma quantidade maior de fosfato de cálcio cristalino precipitado ao longo de toda a superfície do material.

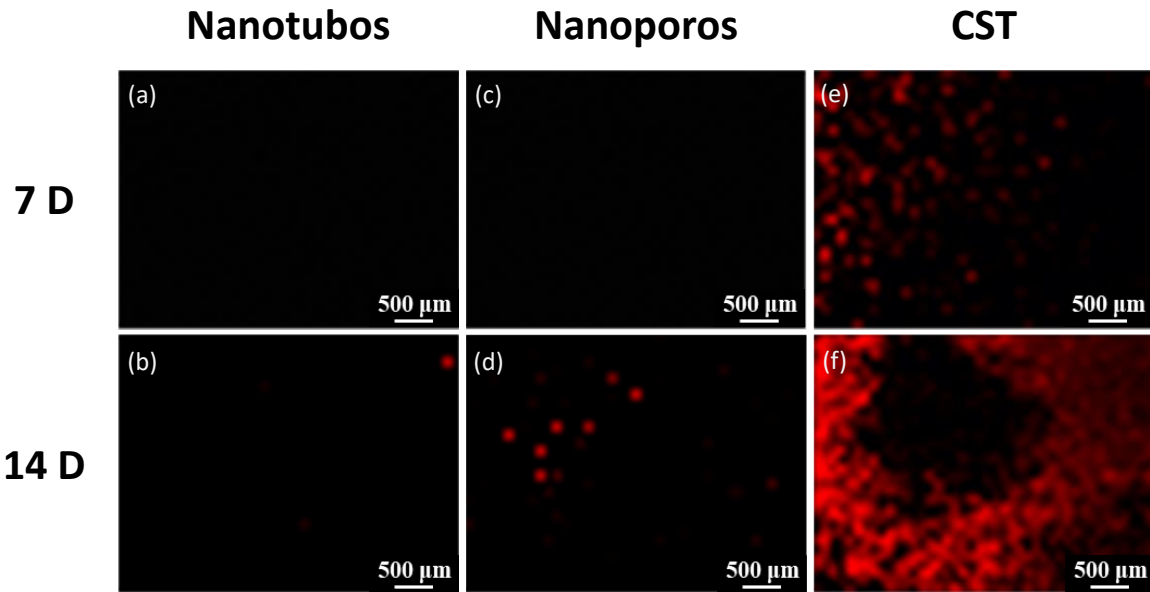


Figura 3.6 Mapeamento espectral Raman de amostras de nanotubos, nanoporos e CST embebidos durante 7 e 14 dias em SBF.

3.2 Caracterização eletroquímica

A Figura 3.7 compara curvas de polarização potenciodinâmica de uma amostra representativa para cada condição de superfície e tempo de imersão. A partir dessas curvas, foi calculado o potencial de corrosão (E_{corr}) correspondente à posição em que a corrente total é zero e é indicado como o "pico" direcionado para baixo nas curvas de polarização.

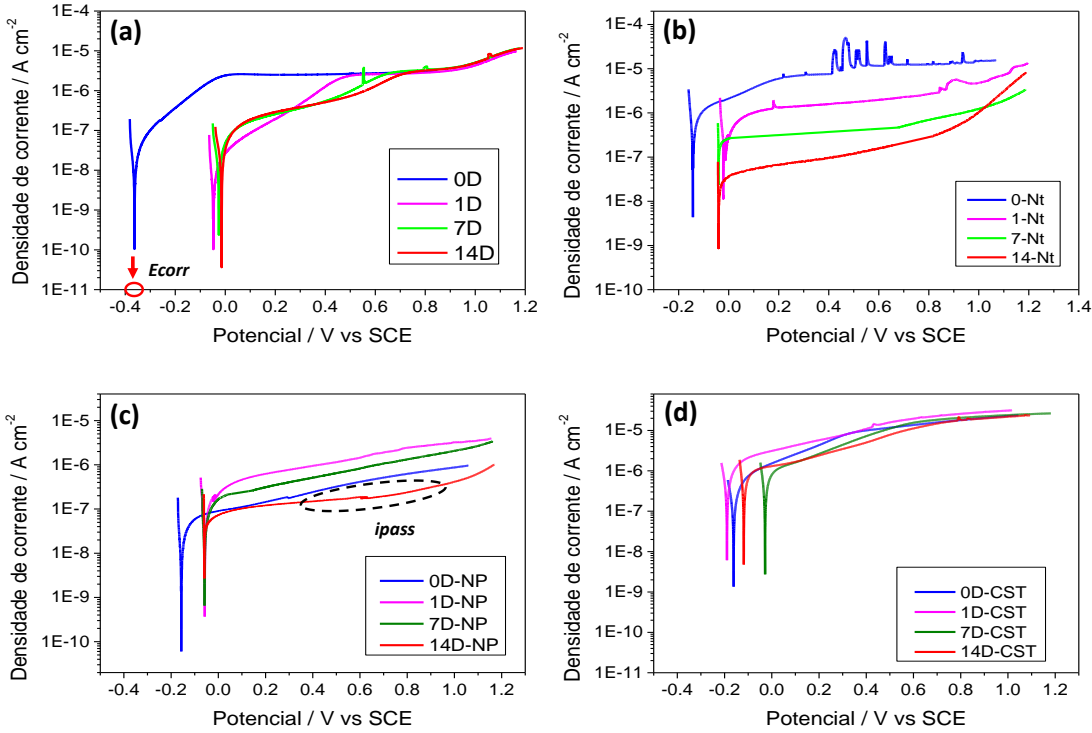


Figura 3.7 Curvas de polarização anódica, em eletrólito SBF a 37 °C para a liga TMZF: a) Não tratada; b) nanotubos; c) nanoporos e d) CST.

A natureza das curvas de polarização indicou um comportamento passivo estável para todas as condições de superfície e períodos de imersão. No entanto, na amostra de nanotubos em 0 dias, são observadas flutuações no domínio da passividade devido à criação de um ambiente agressivo localizado que quebra a camada de passivação [2]. Esses tipos de oscilações podem ser atribuídos à competição entre a formação e a dissolução do filme; íons fluoretos remanescentes presos nos tubos depois do processo de anodização favorecem esse fenômeno. Este fenômeno foi facilitado por um processo de limpeza insuficiente dessas amostras [3].

Os valores de E_{corr} para os quatro diferentes tratamentos de superfície estão resumidos na Figura 3.8. Esses valores são comparáveis ao potencial obtido para cada condição após 1h de OCP. Amostras não tratadas mostram, inicialmente, um baixo potencial de corrosão próximo a -0,370 mV vs SCE, mas esse valor aumenta consideravelmente após 1 dia de imersão e permanece quase constante em -0,050 V vs SCE até 14 dias de imersão.

Além disso, as amostras de nanotubos, nanoporos e CST mostraram um comportamento mais nobre (-0,072, -0,115 e -0,190 mV vs SCE, respectivamente) em comparação com amostras não tratadas no dia 0. Após 1 dia de imersão em solução de SBF, todos exibiram uma tendência a valores potenciais mais altos

próximos a -0,050 V vs SCE; esse comportamento foi menos pronunciado para as amostras tratadas com HCl mais NaOH, indicando uma menor proteção contra corrosão do que as amostras anodizadas (Figura 3.8).

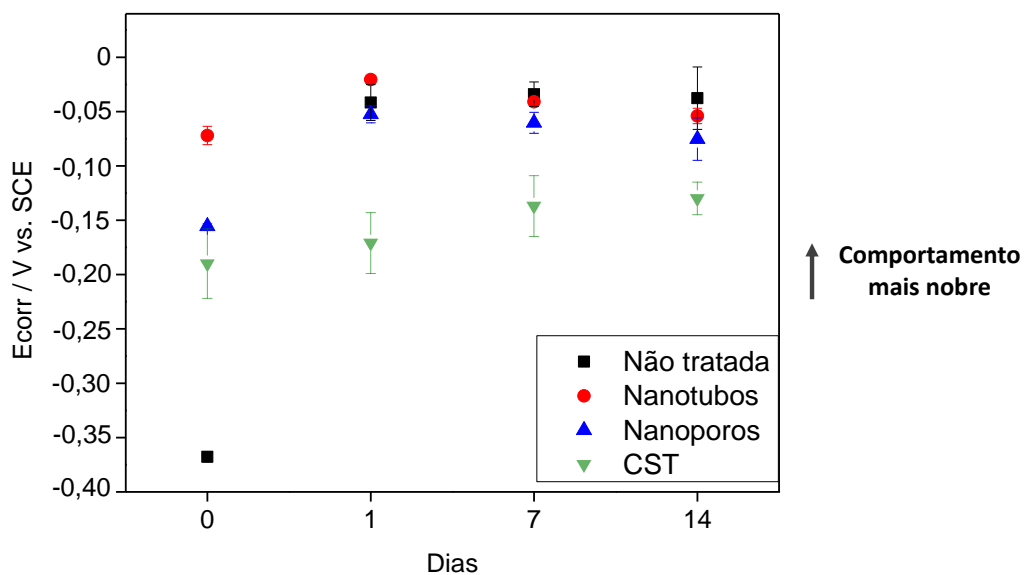


Figura 3.8 Medidas eletroquímicas do potencial de corrosão (E_{corr}) da liga TMZF não tratada e tratada com nanotubos, nanoporos e CST para diferentes tempos de imersão em SBF a 37 °C.

Como parte deste estudo, a densidade da corrente de corrosão (i_{corr}) foi considerada equivalente à densidade da corrente do platô passivo (i_{pass}). Na prática, as formas dos ramos anódicos não são idênticas para todas as amostras, e a determinação do i_{pass} pode não ser trivial (Figura 3.7). Por esses motivos, o método para a determinação do i_{pass} neste projeto consistiu no cálculo do valor médio das densidades de correntes medidas na faixa de potenciais entre +0,4 V / SCE e +1 V / SCE em relação ao OCP, para cada amostra [4].

Os implantes metálicos são considerados resistentes à corrosão e a taxa de transferência de íons estabelece a eficácia de sua camada passiva através do filme. Assim, os valores de i_{pass} são usados para determinar a resistência à corrosão [2]. Dessa forma, as ligas TMZF em um ambiente fisiológico com i_{pass} menor que 12,5 $\mu\text{A} \cdot \text{cm}^{-2}$ ou uma taxa de corrosão menor que 10⁻¹ mm/ano são consideradas pertencentes à categoria de resistência à corrosão "Estável" e menor que 1,25 $\mu\text{A} \cdot \text{cm}^{-2}$ ou 10⁻² mm / ano são colocados no grupo de resistência "Muito estável" [5] (Figura 3.9).

As amostras não tratadas apresentaram resultados moderados-baixos e estáveis, com i_{pass} próximo a 2,0 $\mu\text{A} \cdot \text{cm}^{-2}$, durante os diferentes períodos analisados, devido à presença de uma camada passiva homogênea e fina na superfície da liga.

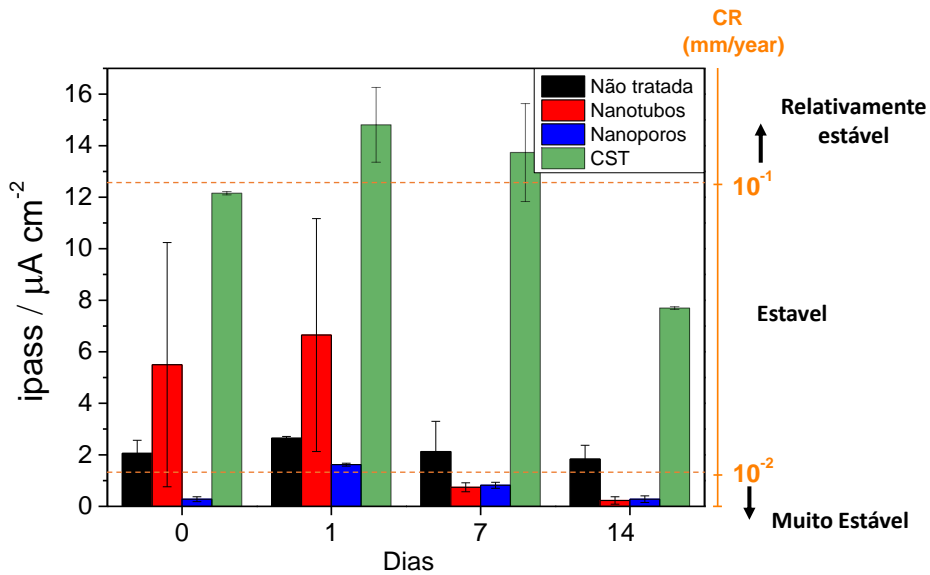


Figura 3.9 Medições eletroquímicas da densidade da corrente de passivação (i_{pass}) e da taxa de corrosão ou *corrosion rate* (CR) da liga TMZF não tratada e tratada com nanotubos, nanoporos e CST em diferentes tempos de imersão no SBF a 37 °C.

Inicialmente, para 0 e 1 dia de imersão, as amostras de nanotubos apresentaram altos valores de i_{pass} , em torno de $5,0 \mu\text{A.cm}^{-2}$. Esse comportamento pode ser atribuído a heterogeneidades de superfície criadas durante o processo de anodização. No entanto, após 7 e 14 dias, os valores de i_{pass} foram inferiores a $0,8 \mu\text{A.cm}^{-2}$. Inicialmente, os nanotubos ordenados ofereciam um caminho livre para a troca de carga entre o eletrólito e o eletrodo. Após alguns dias de imersão, esses canais começaram a fechar pela deposição de fosfato de cálcio na parte externa do nanotubo e na parte inferior do canal, com um crescimento adicional do filme passivo interno [6], o que dificulta a transferência de íons. Esta discussão será retomada na seção 4.3.3.

As amostras de nanoporos apresentaram bom comportamento eletroquímico com valores baixos e estáveis de i_{pass} durante todos os períodos de imersão, com valores de i_{pass} inferiores a $0,3 \mu\text{A.cm}^{-2}$ após 14 dias embebidos em SBF. Esse desempenho é devido à sua camada passiva homogênea na superfície do TMZF, que é mais espessa do que a camada passiva para as amostras não tratadas e mais compacta do que a camada para as amostras de nanotubos.

Do ponto de vista eletroquímico, as amostras com CST mostraram a menor resistência à corrosão entre os quatro sistemas estudados para os diferentes tempos de imersão, apresentando valores de i_{pass} superiores a $12 \mu\text{A.cm}^{-2}$ para 0, 1 e 7 dias de imersão no SBF. No entanto, após 14 dias, foi possível observar uma redução em seu valor de i_{pass} ($\sim 8,0 \mu\text{A.cm}^{-2}$) posicionando-o na categoria de resistência "Estável".

4 Análise e modelagem dos espectros de impedância para as diferentes condições de superfície obtidas

4.1 Medição de EIS sobre amostras TMZF não tratadas

Para concluir a caracterização eletroquímica das superfícies selecionadas para este estudo, foram obtidas informações adicionais das medições de EIS e da interpretação de seus dados. A Figura 4.1 mostra a evolução das curvas de Nyquist e dos diagramas de Bode com o tempo de imersão na solução de SBF, das amostras de TMZF não tratadas; as amostras replicadas mostram resultados semelhantes, mas não são plotadas para melhor visualização dos diagramas (a reprodutibilidade foi verificada).

As representações de Nyquist e Bode das medições de impedância de amostras sem tratamento de superfície são mostradas na Figura 4.1 (b-d). Todos os dados plotados neste trabalho foram corrigidos pela área geométrica ($0,283\text{ cm}^2$) exposta ao eletrólito. Os gráficos das Figuras 4.1b e 4.1.d foram corrigidos para a resistência ôhmica ou resistência a eletrólitos (Re), estimada entre $20\text{--}30\text{ }\Omega\cdot\text{cm}^2$, que foi deduzida do limite de alta frequência ($f = 10^4\text{ Hz}$).

A partir de uma análise qualitativa do diagrama de Nyquist apresentado na Figura 4.1c, parece que, para todos os dias de imersão, a resposta de impedância consiste em um braço curvo. A forma desses dados de impedância é típica de um sistema capacitivo-resistivo ou pseudocapacitivo. Isso significa que a transferência de carga e, portanto, as reações são muito limitadas ou que a camada passiva de óxido é muito protetora [7, 8].

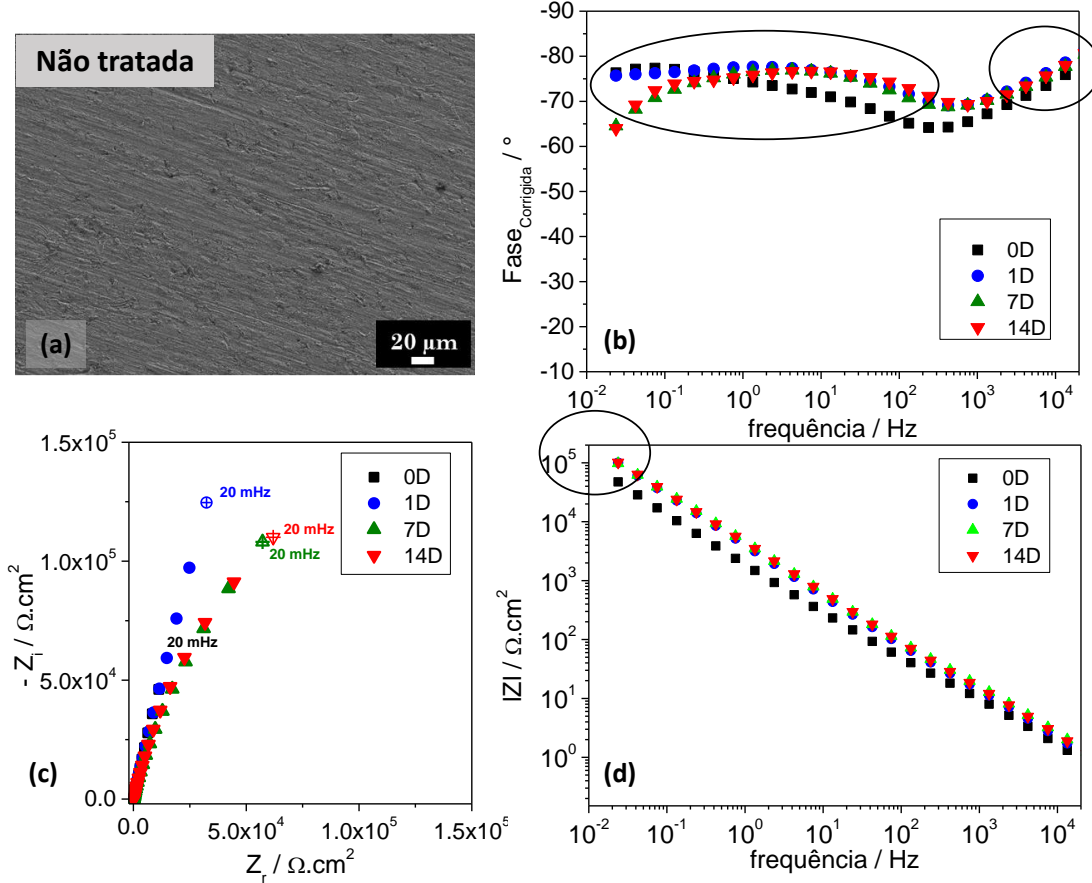


Figura 4.1 a) Micrografia MEV das amostras de TMZF não tratadas antes dos períodos de imersão; Resultados de impedância para amostras não tratadas imersas em SBF a 37 °C: b) ângulo de fase corrigida; c) Gráfico de Nyquist e d) Magnitude da impedância para os diferentes tempos de imersão (0, 1, 7 e 14 dias indicados como 0D, 1D, 7D e 14D, respectivamente).

Sobre a superfície não tratada da TMZF, espera-se a formação de uma camada passiva porosa como foi observada em ligas de titânio semelhantes contendo zircônio e molibdênio [9]. Essa camada passiva porosa estaria composta por uma camada porosa externa e uma barreira interna; assim, espera-se encontrar dois processos de relaxamento ou constantes de tempo nos resultados de impedância.

As representações de Bode corrigidas para a amostra de TMZF não tratada são mostradas na Figura 4.1b e d. Usando o gráfico de fase corrigida (Figura 4.1b), é possível observar duas constantes de tempo presentes durante o teste de impedância. Uma delas está na faixa de 10⁻² Hz a 10² Hz e a segunda em alta frequência em torno de 10⁴ Hz, confirmando a teoria da formação da camada passiva porosa indicada acima. Assim, o Circuito elétrico equivalente (EEC) mais

apropriado para modelar os resultados de impedância obtidos para as amostras sem tratamento é o modelo mostrado na Figura 4.3.

A principal desvantagem do gráfico de Bode de fase corrigida é a necessidade de uma estimativa precisa da resistência do eletrólito. Estimativas imprecisas podem fornecer a ideia errada de uma constante de tempo adicional em altas frequências. Além disso, as curvas corrigidas são muito sensíveis ao ruído de dados em altas frequências [10]. Por essas razões, uma curva complementar para os diagramas de Bode é a representação gráfica do expoente do CPE efetivo (α_{eff}), extraído da parte imaginária da impedância (Z) de acordo com [10]:

$$\alpha_{\text{eff}}(f) = \left| \frac{d \log |Z_i(f)|}{d \log f} \right| \quad (4.1)$$

Tradicionalmente, na curva de α_{eff} , os elementos CPE são associados a platôs estendidos durante vários níveis de frequências. No entanto, essas regiões podem diminuir para formar saliências ou picos suaves devido à interação de eventos com processos de relaxamento próximos [10]. Nesse sentido, a Figura 4.2 mostra claramente duas constantes de tempo para todas as amostras e, portanto, modeladas por dois CPE, um deles na faixa de 10^{-2} Hz a 10^2 Hz e o segundo em alta frequência em torno de 10^4 Hz.

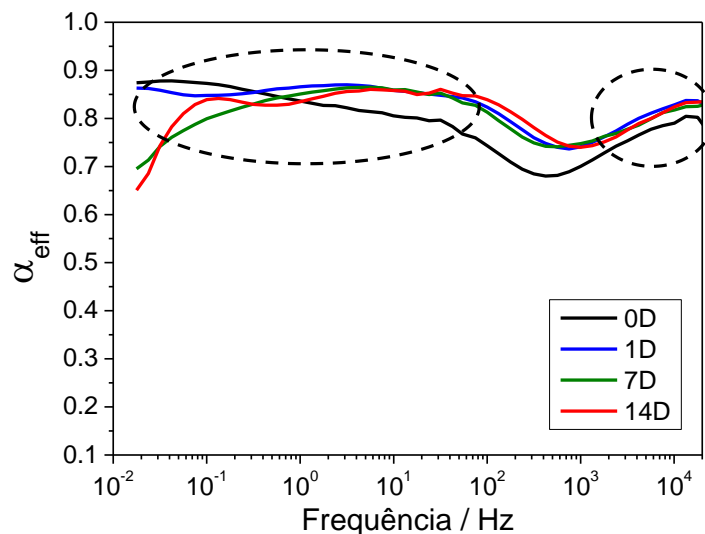


Figura 4.2 Evolução do α_{eff} versus frequência, das amostras não tratadas de TMZF para os diferentes períodos de imersão (0, 1, 7 e 14 dias denotados como 0D, 1D, 7D e 14D respectivamente). Em SBF a 37 °C.

Neste circuito elétrico (Figura 4.3), R_e denota a resistência da solução SBF entre o eletrodo de trabalho e o eletrodo de referência. O sufixo B e OP estão associados aos elementos que representam a camada de barreira interna e a

camada de óxido poroso externo, respectivamente. O uso de um CPE, em vez de um capacitor puro, foi considerado devido à suposição de uma distribuição heterogênea de carga na superfície da amostra [9, 11].

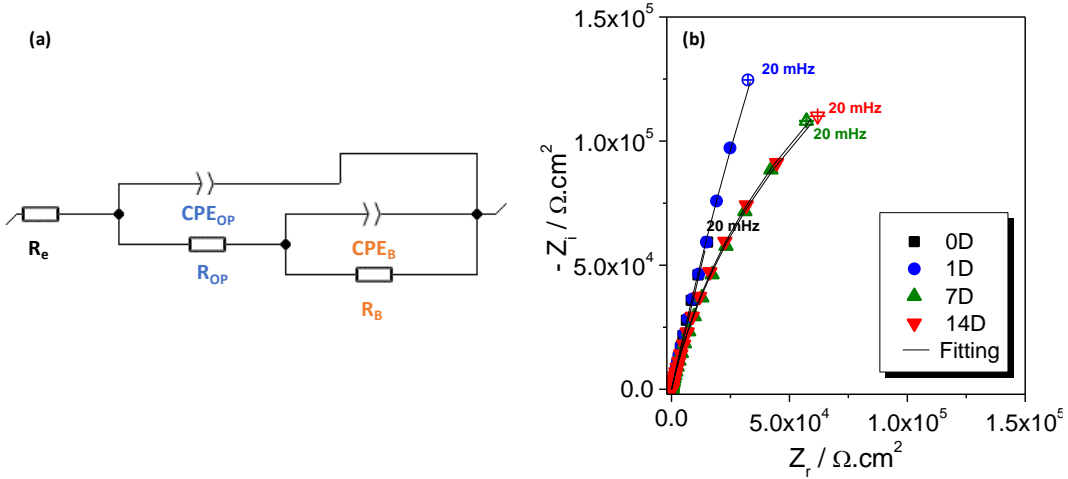


Figura 4.3 Circuito equivalente para amostras não tratadas da liga TMZF e b) Gráficos de Nyquist de resultados experimentais e simulados obtidos pelo software Simad, para os diferentes períodos de imersão (0, 1, 7 e 14 dias indicados como 0D, 1D, 7D e 14D respectivamente) em SBF a 37 °C. O coeficiente de erro foi inferior a 1% para todas as curvas.

Os valores de resistência, capacitância e α das camadas porosa e barreira, obtidos pelo ajuste dos dados experimentais usando o EEC ilustrado na Figura 4.3, são apresentados na Tabela 4.1. Os valores de α cerca de 0,9 sugerem que o comportamento dessa camada passiva se aproximava ao comportamento de um capacitor ideal, independentemente do tempo de imersão [11].

Tabela 4.1 Parâmetros elétricos do circuito equivalente obtidos por ajuste dos resultados experimentais de impedância para amostras não tratadas a 37 °C em solução SBF.

Dias de imersão	R_e ($\Omega \cdot \text{cm}^2$)	Q_{OP} ($\Omega s^{-\alpha} \cdot \text{cm}^2$)	α_{OP}	R_{OP} ($\Omega \cdot \text{cm}^2$)	Q_B ($\Omega s^{-\alpha} \cdot \text{cm}^2$)	α_B	R_B ($10^5 \Omega \cdot \text{cm}^2$)	d_{ox} (nm)	X (%)
0	23	1.74E-05	0.85	94	1.37E-05	0.83	2.83	7	0.45
1	20	8.35E-06	0.88	63	6.02E-06	0.84	2.90	18	0.23
7	21	4.80E-06	0.92	49	8.55E-06	0.81	4.64	16	0.22
14	20	1.04E-05	0.84	77	2.95E-06	0.88	4.60	27	0.77

O filme passivo consiste em duas camadas, a camada de barreira interna, cujos valores de resistência, R_B , aumentam com os dias de imersão e são

significativamente maiores que os valores associados à camada porosa externa, R_{OP} , que permanece quase constante, como mostra a Tabela 4.1. Esses resultados indicam que a proteção fornecida pela camada passiva deve-se principalmente à camada barreira interna, como também foi observado em outras ligas de titânio [9, 12, 13].

A resistência ôhmica (R_e), estimada a partir do modelo proposto, varia entre 20-23 $\Omega \cdot \text{cm}^2$ durante os dias de imersão e está em boa concordância com a resistência deduzida no limite de alta frequência (20-30 $\Omega \cdot \text{cm}^2$) nos diagramas de Bode (Figura 4.1).

A partir dos valores de CPE (Q e α), R_e e R_{OP} , R_B e utilizando a equação de Brug (Equação 4.2), é possível obter os valores da capacitância efetiva da camada passiva, considerando a superfície de titânio composta por uma camada porosa externa e uma camada compacta interna.

$$C_{eff} = Q^{1/\alpha} (R_e^{-1} + R_{OP,B}^{-1})^{(\alpha-1)/\alpha} \quad (4.2)$$

As capacitâncias efetivas calculadas a partir dos valores listados na Tabela 4.1 variam de 18 a 9 $\mu\text{F} \cdot \text{cm}^{-2}$ para a camada porosa e de 12 a 3 $\mu\text{F} \cdot \text{cm}^{-2}$ para a camada compacta interna, durante os diferentes dias de imersão, na mesma ordem de magnitude do aço inoxidável AISI 316L imerso em soluções fisiológicas [14, 15]. Essa redução de capacitância está associada a um aumento na espessura da camada passiva [16, 17]. Baixas capacitâncias associadas a altas resistências da camada são características de um comportamento eletroquímico mais nobre [13, 16, 17].

Nesse sentido, a espessura do filme passivo da camada compacta interna pode ser calculada a partir da Equação 4.3, que é válida para um modelo de capacitor de placa paralela de uma camada de óxido homogênea, associando a capacitância efetiva geral à capacitância da camada de óxido de proteção:

$$d_{ox} = \frac{\varepsilon_r \varepsilon_0}{C_{eff}} \quad (4.3)$$

Onde ε_0 é a permissividade no vácuo ($8.85 \times 10^{-14} \text{ F} \cdot \text{cm}^{-1}$) e ε_r é a constante dielétrica relativa do material (tomada como $\varepsilon_r = 100$, constante dielétrica do TiO_2 [17]). Com essas informações, foi possível obter uma aproximação da espessura da camada passiva para os diferentes dias de imersão. A camada passiva cresceu com o aumento dos dias de imersão, inicialmente com 7 nm para amostras não imersas para 27 nm após 14 dias (Tabela 4.1).

4.2 Medições de EIS sobre amostras de TMZF tratadas com HCl e NaOH

O efeito dos períodos de imersão através de curvas de impedância para as amostras tratadas com ácido e álcalis é apresentado na Figura 4.4. A evolução da impedância geral nos gráficos de Nyquist exibe semicírculos achatados em baixas

frequências. O raio desses arcos diminui com o aumento do tempo de imersão (Figura 4.4 c).

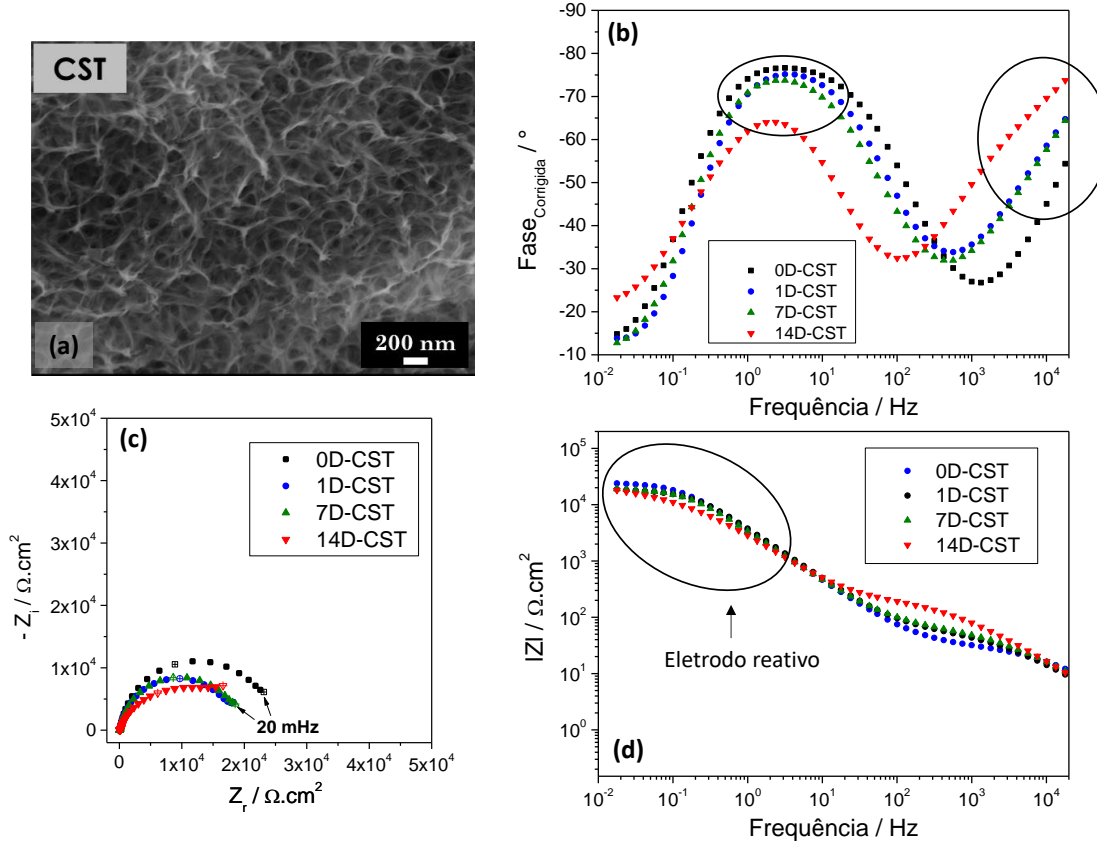


Figura 4.4 a) Micrografias MEV das amostras de CST antes dos períodos de imersão; resultados de impedância para amostras de CST imersas no SBF a 37 °C durante os diferentes períodos (0, 1, 7 e 14 dias, denotados como 0D, 1D, 7D e 14D, respectivamente): b) ângulo de fase corrigida; c) Gráfico de Nyquist e d) Magnitude da impedância.

As representações de Bode para a amostra de CST são mostradas na Figura 4.4b e 4.4d. Usando o gráfico de fase corrigida (Figura 4.4b), é possível determinar dois processos de relaxamento ou constantes de tempo presentes durante o teste de impedância. Pode-se observar que as duas regiões de ângulo de fase constante para as amostras tratadas quimicamente são menores em comparação com a região constante das amostras não tratada. Essa distribuição curta das constantes de tempo indica uma superfície menos protetora e homogênea.

A curva do expoente efetivo do CPE (α_{eff}) é usada para uma melhor caracterização do processo de relaxamento que ocorre sobre a superfície das amostras tratadas quimicamente. A Figura 4.5 mostra um comportamento semelhante em frequências altas e intermediárias no gráfico de fase corrigida. No entanto, este gráfico mostra um aumento adicional em baixas frequências (10⁻² Hz

to 10^{-1} Hz). Esse comportamento interessante foi associado a um processo de relaxamento extra.

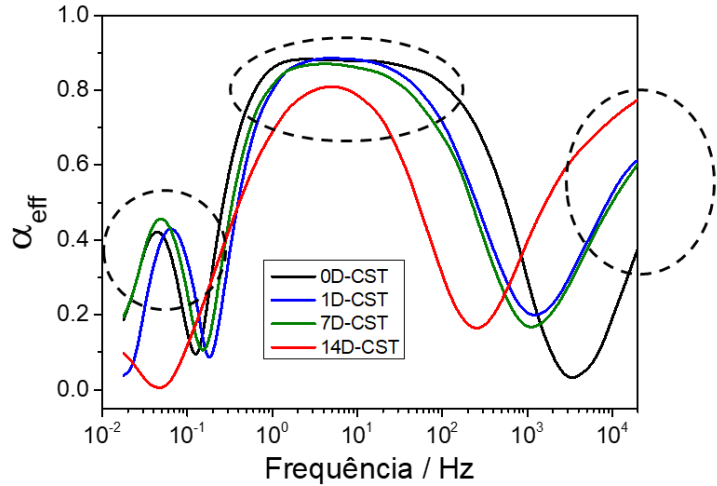


Figura 4.5 Evolução do α_{eff} versus frequência, das amostras de CST para os diferentes períodos de imersão (0, 1, 7 e 14 dias denotados como 0D, 1D, 7D e 14D respectivamente) na solução de SBF a 37 °C.

Nas amostras tratadas com CST, espera-se encontrar três processos de relaxamento que atuam durante o teste de impedância, um a mais que os dois encontrados nas amostras não tratadas, que está associado à camada externa de titanato de sódio criada durante o tratamento químico com HCl e NaOH.

Conforme mencionado acima e confirmado pelas informações obtidas dos diagramas de fase Bode e das curvas de α_{eff} , o EEC para as amostras CST deve ser composto de três processos de relaxação. O circuito é mostrado na Figura 4.6 e fornece uma boa representação para sistemas com uma camada compacta interna, uma camada intermediária de óxido poroso e uma camada externa de titanato de sódio em gel.

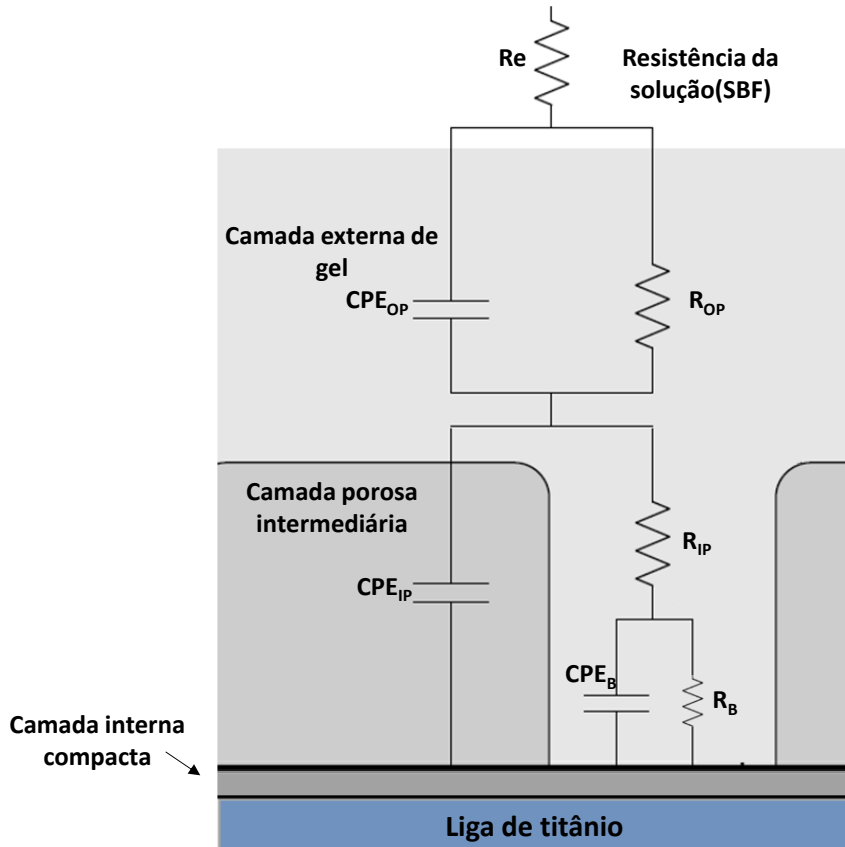


Figura 4.6 Circuito equivalente para amostras de CST (Adaptada de [11]).

No circuito elétrico da Figura 4.6, Re representa a resistência do eletrólito (solução SBF), R_{OP} e CPE_{OP} representam as resistências e as capacitâncias da camada porosa externa, associadas à dissolução da camada de titanato de sódio e ao crescimento da HAp. R_{IP} e R_B são as resistências da camada de óxido poroso intermediário e das camadas de barreira interna, e o CPE_{IP} e o CPE_B são usados para designar as capacitâncias da camada porosa externa e da camada compacta interna, respectivamente.

A representação de Nyquist dos dados EIS modelados das amostras de CST é mostrada na Figura 4.7. As curvas simuladas foram modeladas através do EEC apresentado na Figura 4.6. Os erros medidos (X) para os dados experimentais e simulados foram inferiores a 1%, independentemente do período de imersão, indicando um nível de ajuste satisfatório.

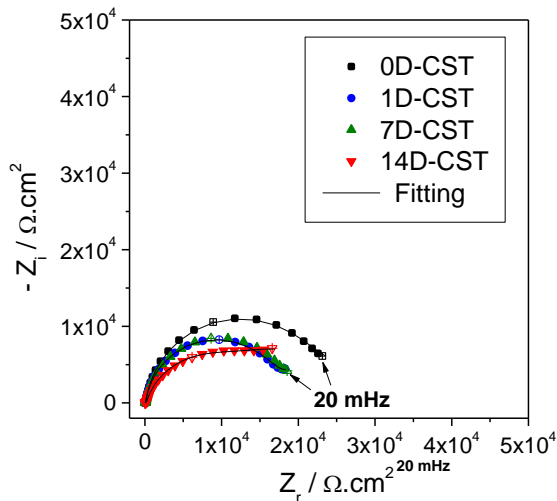


Figura 4.7 Gráficos de Nyquist dos resultados experimentais e simulados obtidos através do software Simad, para as amostras de CST imersas em SBF a 37 °C durante os diferentes períodos (0, 1, 7 e 14 dias, respectivamente, 0D, 1D, 7D e 14D, respectivamente).

Os parâmetros de impedância eletroquímica, como resistência, capacidade e valores de α das camadas porosa e barreira obtidos do circuito equivalente, são mostrados na Tabela 4.2.

Tabela 4.2 Parâmetros de impedância elétrica pelo ajuste dos resultados experimentais das amostras de CST imersas em SBF a 37 °C nos diferentes períodos de 0, 1, 7 e 14 dias.

Dias de imersão	R_e ($\Omega \cdot \text{cm}^2$)	Q_{OP} ($\Omega s^{-\alpha} \cdot \text{cm}^2$)	α_{OP}	R_{OP} ($\Omega \cdot \text{cm}^2$)	Q_{IP} ($\Omega s^{-\alpha} \cdot \text{cm}^2$)	α_{IP}	R_{IP} ($\Omega \cdot \text{cm}^2$)	Q_B ($\Omega s^{-\alpha} \cdot \text{cm}^2$)	α_B	R_B ($\Omega \cdot \text{cm}^2$)	C_{effB} ($\mu\text{F}/\text{cm}^2$)	X (%)
0	25	8.61 E-04	0.57	35.05	3.31 E-06	0.71	819	1.69 E-05	0.91	48562	32	0.39
1	21	2.79 E-04	0.55	50.14	6.66 E-06	0.72	283	1.39 E-05	0.95	16366	29	0.26
7	24	3.30 E-04	0.53	112.33	9.28 E-06	0.60	283	2.46 E-05	0.84	11916	22	0.71
14	23	1.45 E-04	0.80	178.97	4.08 E-06	0.76	155	1.81 E-05	0.85	11513	18	0.82

Com o aumento dos dias de imersão de 0 a 7 dias, os valores de Q_{OP} diminuíram, mostrando um processo de dissolução da camada de titanato de sódio. Isso pode estar associado à interação entre os íons presentes na solução fisiológica e os íons na camada de titanato [6].

Entre 7 e 14 dias na solução SBF, uma camada de HAp surge da dissolução completa da camada de titanato de sódio, atuando como uma barreira de difusão, corroborado pelo maior valor de α_{OP} em 14 dias. Esse comportamento é confirmado

no diagrama de Nyquist aos 14 dias de imersão (Figura 4.7), onde é possível ver um semicírculo suavizado em baixas frequências [6].

A resistência R_B diminuiu continuamente e, ao mesmo tempo, a R_{OP} aumentou com os dias de imersão, atingindo um valor constante entre 7 e 14 dias. Esse comportamento pode ser associado aos processos contínuos de dissolução e formação da camada barreira e da camada HAp, respectivamente [6].

Através dos resultados da impedância e do uso da Equação 4.3 e os resultados do ajuste CeffB da Tabela 4.2, é possível calcular um valor aproximado da espessura da camada interna do óxido de titânio (dox), cujos valores estão resumidos na Tabela 4.2. Semelhante às amostras não tratadas, a camada passiva nas amostras de CST cresceu com o aumento dos dias de imersão.

4.3 Medições EIS das amostras TMZF anodizadas

Resultados de impedância eletroquímica foram empregados para investigar as alterações em dois sistemas anodizados diferentes (superfícies com nanotubos e nanoporos) após diferentes períodos de imersão na solução de SBF (0, 1, 7 e 14 dias).

A imagem MEV de alta resolução na Figura 4.8 mostra a condição da superfície das amostras de TMZF com nanotubos antes dos períodos de imersão. Inicialmente foi analisada a evolução eletroquímica das amostras de nanotubos através das plotagens de Nyquist e os diagramas de Bode mostrados na Figura 4.8 (b-d).

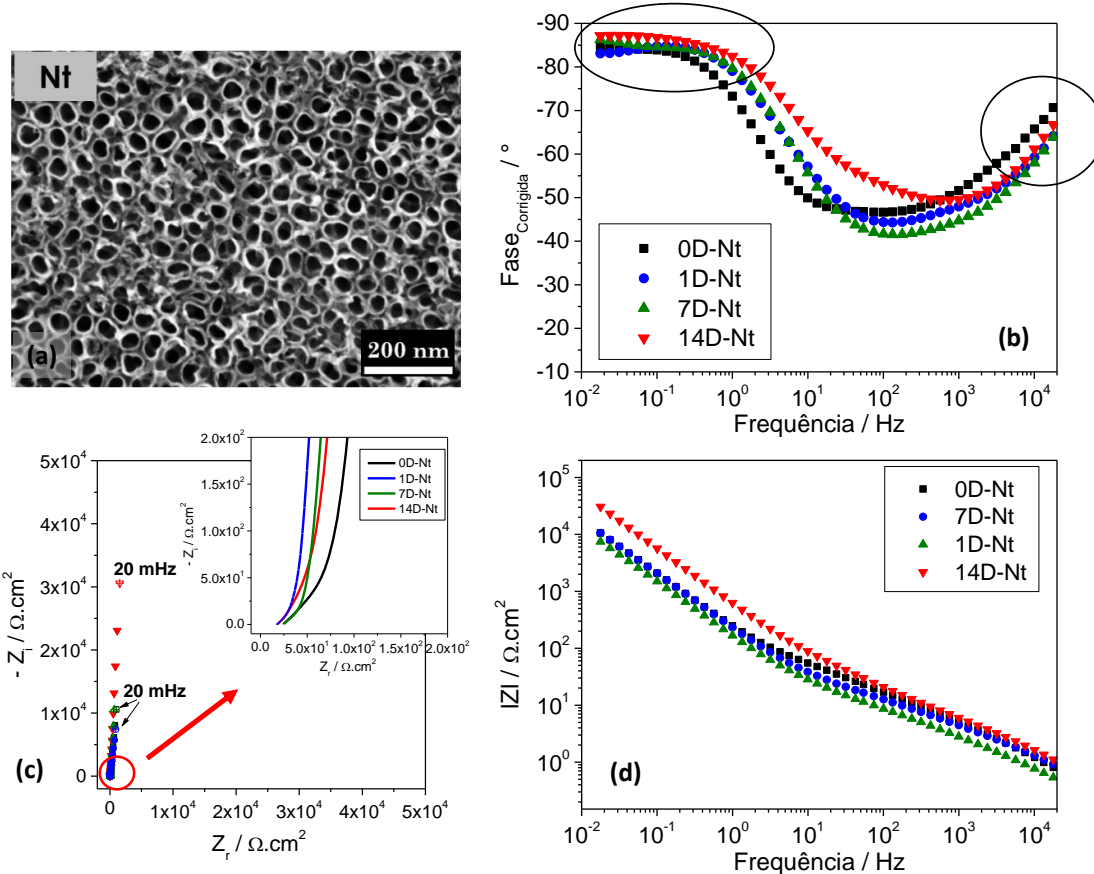


Figura 4.8 a) Micrografias MEV da amostra de TMZF com nanotubos antes da imersão; resultados da impedância para amostras de nanotubos imersos no SBF a 37 °C nos diferentes períodos (0, 1, 7 e 14 dias, denotados como 0D, 1D, 7D e 14D, respectivamente); b) ângulo de fase corrigida; c) Gráfico de Nyquist e d) Magnitude da impedância.

Observação dos diagramas de Nyquist revela que, independentemente do tempo de imersão estudado, a forma dos espectros de impedância do CST (arco) é típica de um sistema reativo (seção 4.2), enquanto na Figura 4.8 (c) as amostras com nanotubos são aparentemente puramente capacitivas (linha reta) ou pelo menos pseudocapacitivas (linha reta inclinada). Isso significa que a troca de elétrons e, portanto, as reações eletroquímicas, são muito limitadas.

Essas amostras anodizadas mostraram um comportamento particular no diagrama de Nyquist, mostrando uma linha reta inclinada ou um arco em altas frequências (região ampliada Figura 4.8c) e um ramo capacitivo ou pseudocapacitivo em baixas frequências. Essa é uma característica típica de um eletrodo poroso, como será demonstrado na seção 4.3.1.

A Figura 4.9 mostra a evolução das curvas de Nyquist e dos diagramas de Bode com o tempo de imersão na solução SBF, para as amostras de TMZF com

nanoporos. Além disso, na Figura 4.9 (a) é possível ver a condição da superfície das amostras nanoporos TMZF antes dos períodos de imersão.

Similar aos nanotubos, as amostras com nanoporos mostram um comportamento capacitivo ou pseudo-capacitivo, o que foi observado no diagrama de Nyquist independentemente do tempo de imersão estudado (Figura 4.9 (c)). Essas curvas são normalmente observadas em sistemas porosos de baixa reatividade.

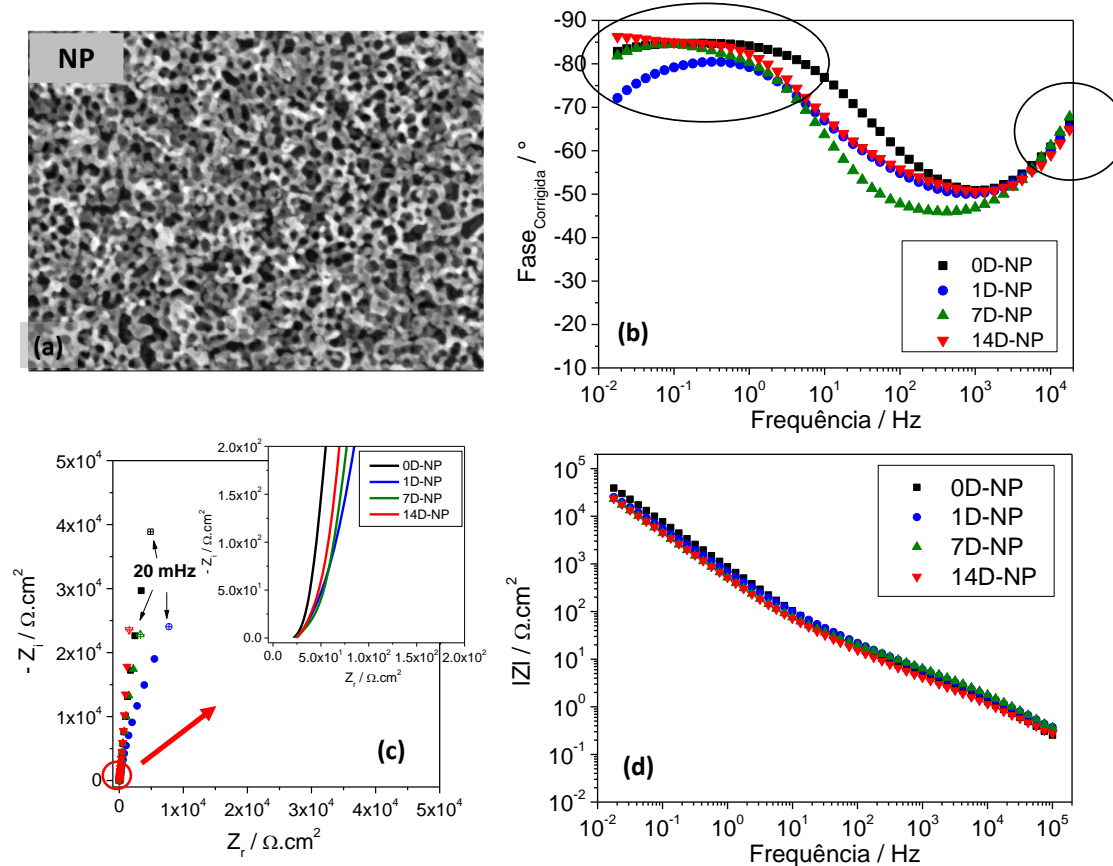


Figura 4.9 a) Micrografias MEV da amostra com nanoporos antes dos períodos de imersão; resultados da impedância para amostras não tratadas imersas no SBF a 37 °C durante os diferentes períodos (0, 1, 7 e 14 dias denotados como 0D, 1D, 7D e 14D, respectivamente): b) ângulo de fase corrigida; c) Gráfico de Nyquist ed) Magnitude da impedância.

Gráficos do α_{eff} (Figura 4.10) foram construídos para determinar o número de constantes de tempo presentes durante os testes de impedância para nos ajudar a escolher o sistema EEC mais apropriado para modelar os resultados das amostras anodizadas (Nt e NP). A Figura 4.10 mostra duas constantes de tempo para as amostras Nt e NP, independentemente do tempo de imersão.

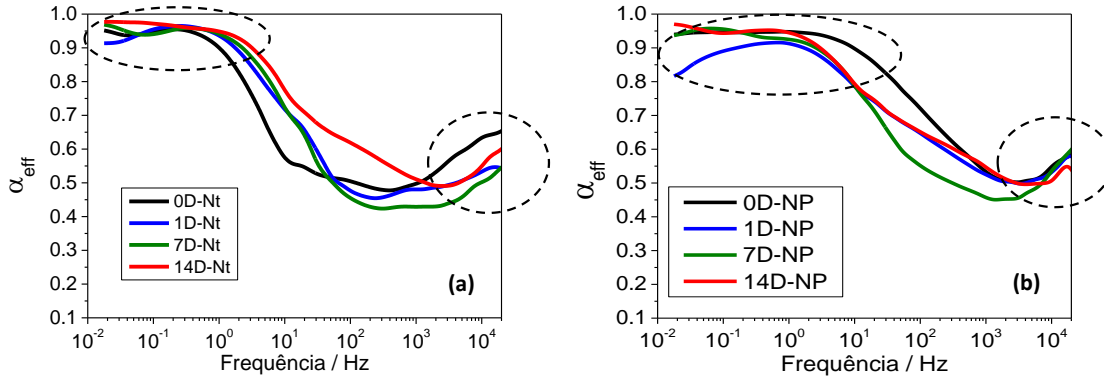


Figura 4.10 Evolução do α_{eff} com a frequência, das amostras anodizadas para os diferentes períodos de imersão (0, 1, 7 e 14 dias denotados como 0D, 1D, 7D e 14D respectivamente) no SBF a 37 °C: a) nanotubos e b) nanoporos.

De acordo com as informações obtidas através do diagrama de fase Bode e das curvas de α_{eff} , inicialmente as amostras anodizadas foram ajustadas considerando um circuito elétrico semelhante ao utilizado para amostras com superfícies não tratadas (Figura 4.3), que se refere ao filme passivo com microestrutura de duas camadas. No entanto, os resultados do ajuste para ambas as condições anodizadas foram insatisfatórios, como já mencionado em diferentes trabalhos [17, 19]; os erros de ajuste são grandes e os valores dos parâmetros obtidos são discrepantes.

Assim, um novo modelo baseado em uma teoria não clássica é empregado para modelar a resposta de impedância das amostras anodizadas e imersas em SBF. De Levie observou um comportamento semelhante em eletrodos porosos e analisou os resultados de impedância por meio de um modelo alternativo descrito como modelo de linha de transmissão (LT) [20].

4.3.1 Emprego do modelo de linha de transmissão no caso de amostras de TMZF anodizadas e imersas em SBF

A Figura 4.11 mostra uma representação esquemática do modelo LT proposto neste estudo, podendo ser útil para analisar diferentes microestruturas e geometrias em relação a diferentes tipos de hipóteses. Além disso, é necessário observar que esse modelo envolve os processos de volume distribuídos por toda a superfície do eletrodo. O canal 1 é representado como uma resistência distribuída, o transporte no canal 2 é considerado anômalo, ou seja, a impedância X_2 é equivalente a um arranjo paralelo de um CPE (Q_2) e uma resistência (R_2). A impedância interfacial ζ é considerada pseudo-capacitiva (Q_3) e nos limites dos canais uma impedância Z_B (Q_B) e uma resistência Z_A (R_A).

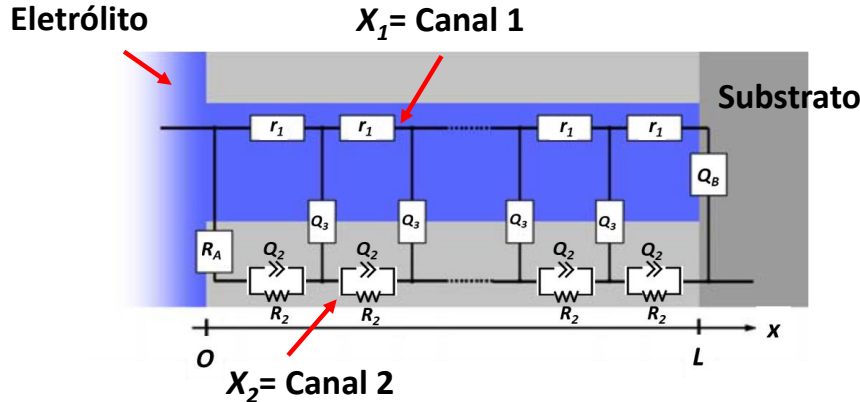


Figura 4.11 O modelo da linha de transmissão proposto para descrever a resposta de impedância das amostras de TMZF anodizadas e imersas em SBF a 37 °C durante os diferentes períodos avaliados.

Neste estudo foi proposto um modelo de linha de transmissão para descrever a resposta de impedância das amostras anodizadas de TMZF imersas no SBF a 37 °C durante diferentes períodos.

A equação 4.4 mostra o modelo de LT empregado neste trabalho para modelar os resultados da impedância:

$$\begin{aligned}
 Z = & \frac{1}{X_1 + X_2} \left[\lambda(X_1 + X_2)S_\lambda + (Z_A + Z_B)C_\lambda + \frac{1}{\lambda(X_1 + X_2)} Z_A Z_B \lambda \right]^{-1} \cdot \left(L\lambda X_1 X_2 (X_1 + \right. \\
 & X_2) S_\lambda + X_1 [\lambda X_1 S_\lambda + L X_2 C_\lambda] Z_A + X_2 [\lambda X_2 S_\lambda + L X_1 C_\lambda] Z_B + \frac{1}{X_1 + X_2} \left[2 X_1 X_2 + \right. \\
 & \left. \left(X_1^2 + X_2^2 \right) C_\lambda + \frac{L}{\lambda} X_1 X_2 S_\lambda \right] Z_A Z_B \right) \quad (4.16)
 \end{aligned}$$

Where $X_1 = r_1$; $X_2 = \frac{1}{1 + r_2 q_2 (iw)^\beta}$; $\zeta = \frac{1}{q_3} (iw)^{-\beta}$; $Z_A = R_A$; $Z_B = \frac{1}{Q_B} (iw)^{-\beta}$

$C_\lambda = \cosh(L/\lambda)$, $S_\lambda = \sinh(L/\lambda)$, and $\lambda = [\zeta/(X_1 + X_2)]^{1/2}$.

A Figura 4.12 mostra os resultados do ajuste (indicado por uma linha sólida) das medições experimentais das amostras anodizadas com nanotubos e nanoporos usando o modelo proposto na Equação 4.4 e ilustrado na Figura 4.11. O modelo LT é composto por 10 parâmetros que descrevem satisfatoriamente o comportamento da interface. O erro entre os pontos experimentais e a simulação, independentemente da morfologia anodizada e do tempo de imersão, foi inferior a 1,0%. Somente a condição com nanotubos após 14 dias apresentou um valor mais alto (1,7%), o que é bastante razoável.

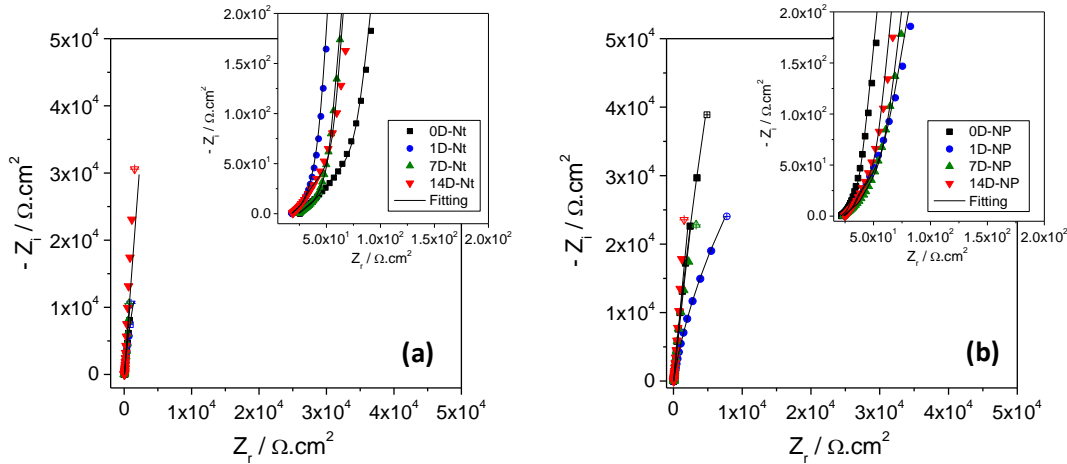


Figura 4.12 Gráficos de Nyquist dos resultados experimentais e simulados adquiridos do software Simad para as amostras anodizadas imersas no SBF a 37 °C durante diferentes períodos (0, 1, 7 e 14 dias denotados como 0D, 1D, 7D e 14D, respectivamente): a) Nanotubos e b) Nanoporos.

A Tabela 4.3 mostra os parâmetros de impedância obtidos pelo ajuste dos resultados experimentais das amostras de nanotubos para os diferentes dias de imersão. Além disso, os valores da frequência de corte (ω_c) que representam o mecanismo de transporte através do canal 2 (X_2) foram calculados usando 4.17 e mostrados na Tabela 4.3.

$$\omega_c = \frac{1}{r_2 q_2 (iw)^{1/\beta}} \quad (4.5)$$

Tabela 4.3 Parâmetros de impedância elétrica obtidos pelo ajuste dos resultados experimentais das amostras com nanotubos.

Dias de imersão	X1		X2		ζ		ZA		ZB		L (cm)	ω_c (Hz)	X (%)
	R ₁ (Ω.cm)	R ₂ (Ω.cm ²)	Q ₂ (Ωs ^{-e} .cm ²)	e	Q ₃ (Ωs ^{-b} .cm)	b	R _A (Ω.cm ²)	Q _B (Ωs ⁻ⁿ .cm ²)	n				
0	827	217	6.53 E-07	0.96	1.63 E-04	0.96	7.22 E+06	3.69 E-05	0.91	2.0 E-05	0.035	0.77	
1	956	222	4.55 E-07	0.76	2.96 E-04	0.96	2.99 E+05	1.69 E-05	0.84	2.0 E-05	0.023	0.48	
7	938	209	6.06 E-07	0.78	3.91 E-04	0.95	4.90 E+08	5.58 E-06	0.92	2.0 E-05	0.019	0.43	
14	860	145	2.81 E-06	0.72	9.96 E-05	0.96	5.25 E+09	7.80 E-06	0.89	2.0 E-05	0.003	1.70	

A Figura 4.13 foi representada graficamente para entender o comportamento dos pontos finais da linha (Z_A e Z_B) durante os dias de imersão, representados por resistência e capacitância de R_A e Q_B , respectivamente. Os valores de R_A e Q_B foram obtidos da Tabela 4.3.

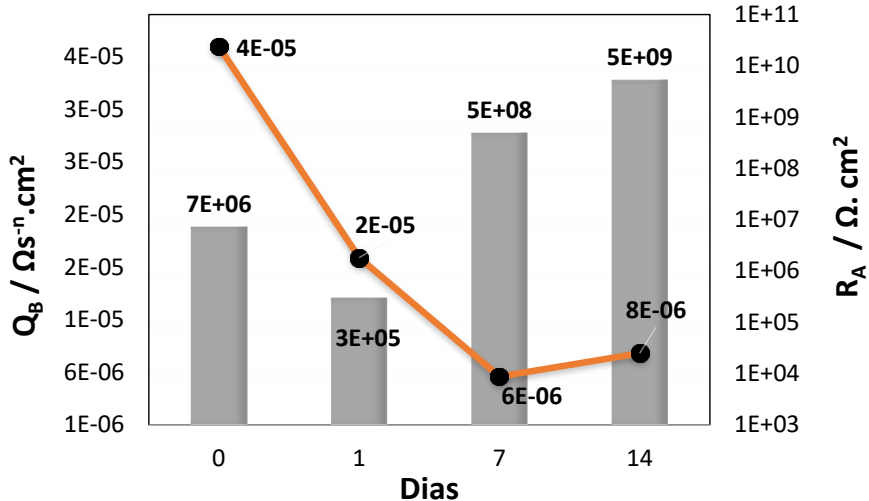


Figura 4.13 Parâmetros dos pontos finais, R_A e Q_B , obtidos a partir do modelo de linha de transmissão usado em amostras de nanotubos após diferentes períodos de imersão no SBF.

Durante o tempo de imersão em SBF, a resistência R_A aumenta gradualmente e o Q_B diminui. Esse comportamento pode estar associado à formação e crescimento de núcleos de fosfato de cálcio (etapa inicial para a formação de apatita) na parte externa do nanotubo e na parte inferior do canal. Esse comportamento é observado na Figura 4.14 (círculos vermelhos). Além disso, a diminuição do Q_B pode estar associada ao crescimento do filme passivo interno [6].

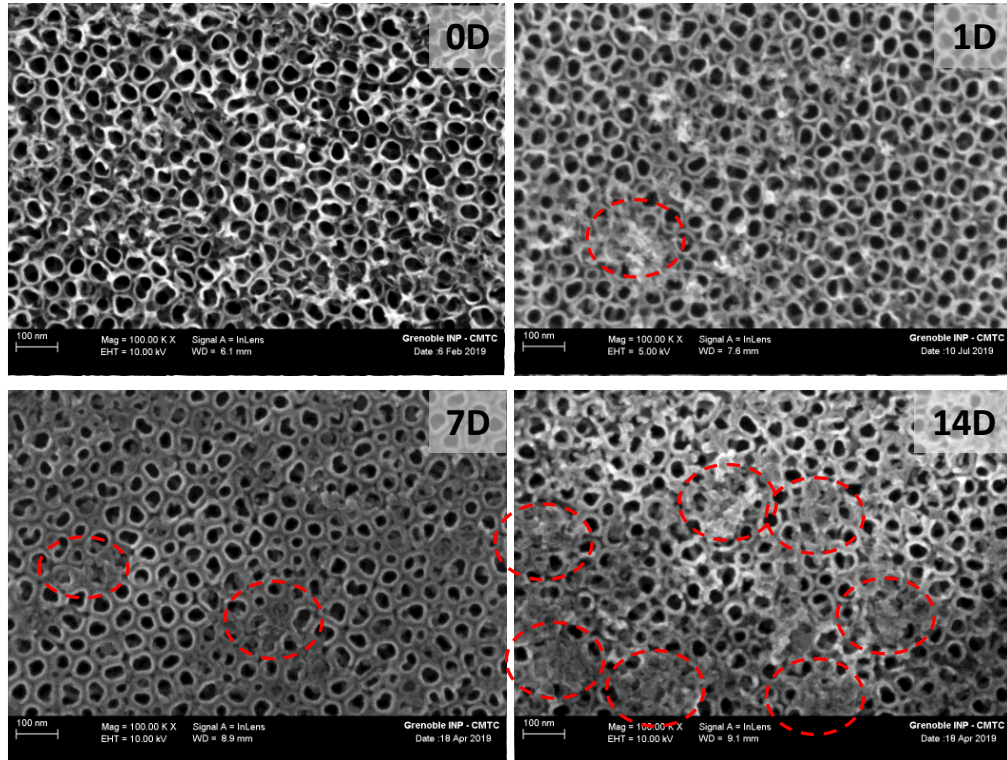


Figura 4.14 Formação de apatita sobre amostras de nanotubos após diferentes períodos de imersão em SBF (0, 1, 7 e 14 dias).

A Tabela 4.4 mostra os parâmetros de impedância eletroquímica obtidos pelo ajuste dos resultados experimentais de amostras de nanoporos para os diferentes dias de imersão. Semelhante ao ajuste para as amostras de nanotubos, foi escolhido um valor médio de L (2×10^{-5} cm) para as amostras de nanoporos. Este valor foi usado no modelo de ajuste.

Tabela 4.4 Parâmetros de impedância obtidos pelo ajuste dos resultados experimentais das amostras de nanoporos.

Days	X1		X2		ζ	ZA	ZB		L (cm)	ω_c (Hz)	X (%)
	R ₁ ($\Omega \cdot \text{cm}$)	R ₂ ($\Omega \cdot \text{cm}^2$)	Q ₂ ($\Omega \text{s}^{-e} \cdot \text{cm}^2$)	e	Q ₃ ($\Omega \text{s}^{-b} \cdot \text{cm}$)	b	R _A ($\Omega \cdot \text{cm}^2$)	Q _B ($\Omega \text{s}^{-n} \cdot \text{cm}^2$)			
0	559	203	8.52 E-07	0.60	7.73 E-05	0.96	1.40 E+06	5.32 E-06	0.90	2.0E-05	0.003
1	826	207	9.24 E-07	0.64	7.52 E-05	0.97	2.00 E+05	1.15.E-05	0.82	2.0E-05	0.004
7	787	209	6.06 E-07	0.96	8.68 E-05	0.97	8.83 E+07	9.18 E-06	0.92	2.0E-05	0.004
14	936	218	6.88 E-07	0.60	7.60 E-05	0.97	4.90 E+08	5.59 E-06	0.89	2.0E-05	0.003

A Figura 4.15 mostra os parâmetros dos pontos finais representados pela resistência e capacidade R_A e Q_B , respectivamente. Esses valores foram representados graficamente para entender o comportamento dos pontos finais da linha de transmissão (Z_A e Z_B) durante os diferentes dias de imersão. Os valores de R_A e Q_B foram obtidos da Tabela 4.4.

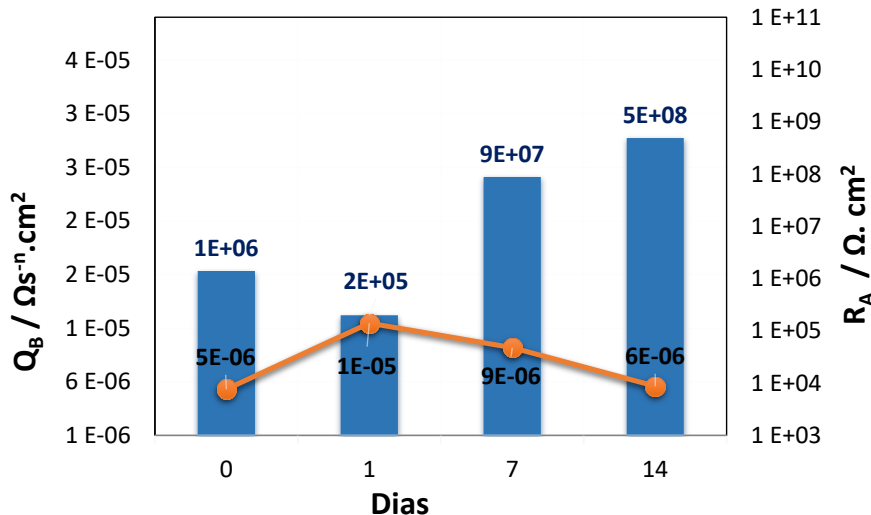


Figura 4.15 Parâmetros de dos pontos finais, R_A e Q_B , obtidos a partir do modelo de linha de transmissão usado em amostras de nanoporos após diferentes períodos de imersão em SBF.

Durante o tempo de imersão em SBF, a resistência R_A aumenta gradualmente. Esse comportamento pode estar associado à possível nucleação e crescimento de sílica gel hidratada e fosfato de cálcio amorfo nas partes externa e interna dos nanoporos, ambos antecessores da formação de apatita [25]. Esse comportamento pode ser observado na Figura 4.16 (círculos vermelhos). Além disso, os valores de Q_B foram baixos e constantes, indicando um comportamento estável e protetor do filme passivo interno durante todo o tempo analisado.

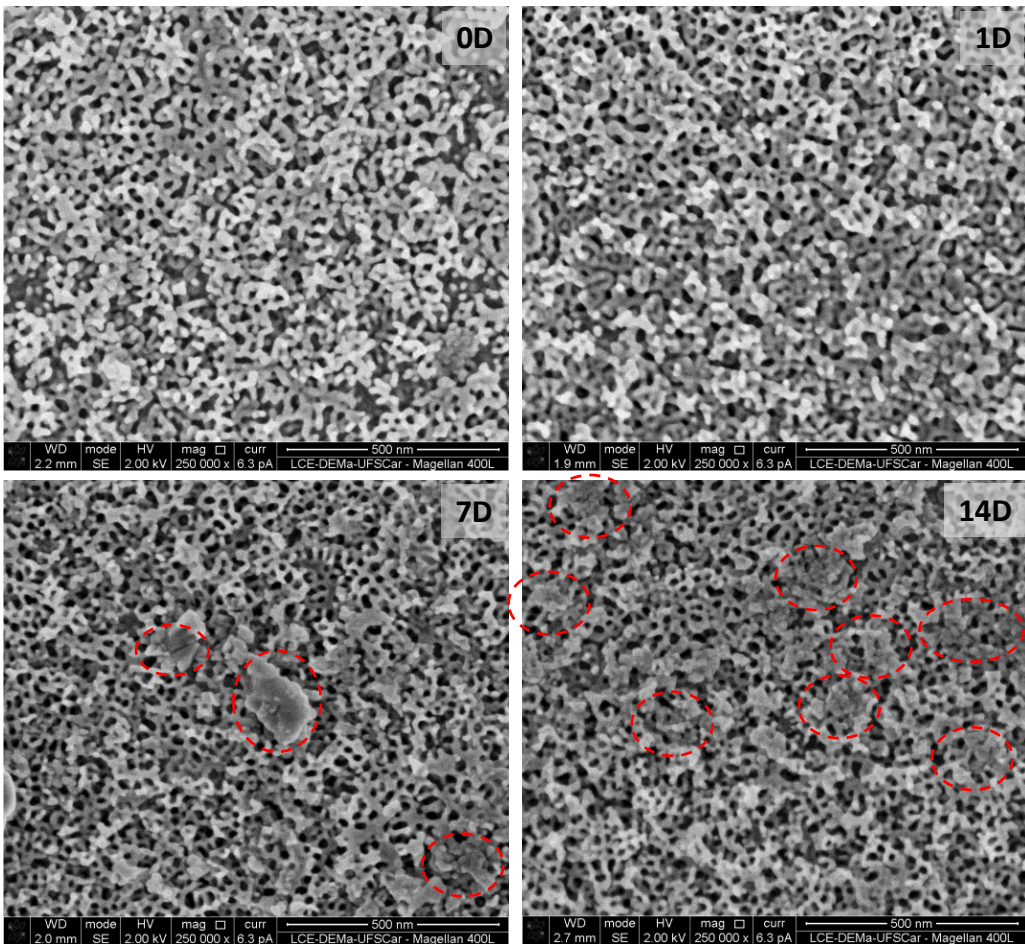


Figura 4.16 Formação de apatita sobre amostras de nanoporos após diferentes períodos de imersão no SBF (0, 1, 7 e 14 dias).

O processo de transporte no canal 2 (X_2), é representado por um modelo diferente denominado "modelo de transporte anômaloo" (conexão paralela de um CPE, Q_2 e uma resistência, R_2), onde mecanismo de transporte de carga depende da frequência. Para ambas as condições de anodização, ω_c estava entre 0,003 e 0,035 Hz. Esses baixos valores indicaram baixa transferência de carga através do canal 2 no regime de frequências estudado neste trabalho (10^{-2} - 10^4 Hz).

A Figura 4.17 resume a resposta à corrosão e a bioatividade após 14 dias de imersão em SBF das diferentes condições de superfície estudadas neste trabalho; os valores de resistência à barreira (R_B ou R_A para as amostras anodizadas) associados à resistência à corrosão foram obtidos a partir dos dados de impedância, o I_{pass} obtido a partir das curvas de polarização e a bioatividade através do ganho de massa.

Amostras não tratadas mostraram uma boa resposta à corrosão, indicada por um alto valor de resistência e I_{pass} aceitável, inferior a $2 \mu\text{A.cm}^{-2}$; no entanto, nesta condição de superfície não foi detectada formação de HAp.

As amostras tratadas com HCl e NaOH, ao contrário das amostras não tratadas, apresentaram excelente bioatividade com o maior valor de ganho de massa, em torno de 1,8 mg após 14 dias de imersão em SBF. Ainda assim, sua resistência à corrosão foi deficiente, comprovada pelos menores valores de R_B e I_{pass} .

Finalmente, as amostras anodizadas apresentaram a melhor resistência à corrosão corroborada pelos valores mais alto e mais baixo de R_A e I_{pass} , respectivamente. Por outro lado, amostras com nanotubos e nanoporos exibiram valores baixos e moderados da formação de HAp após 14 dias no SBF.

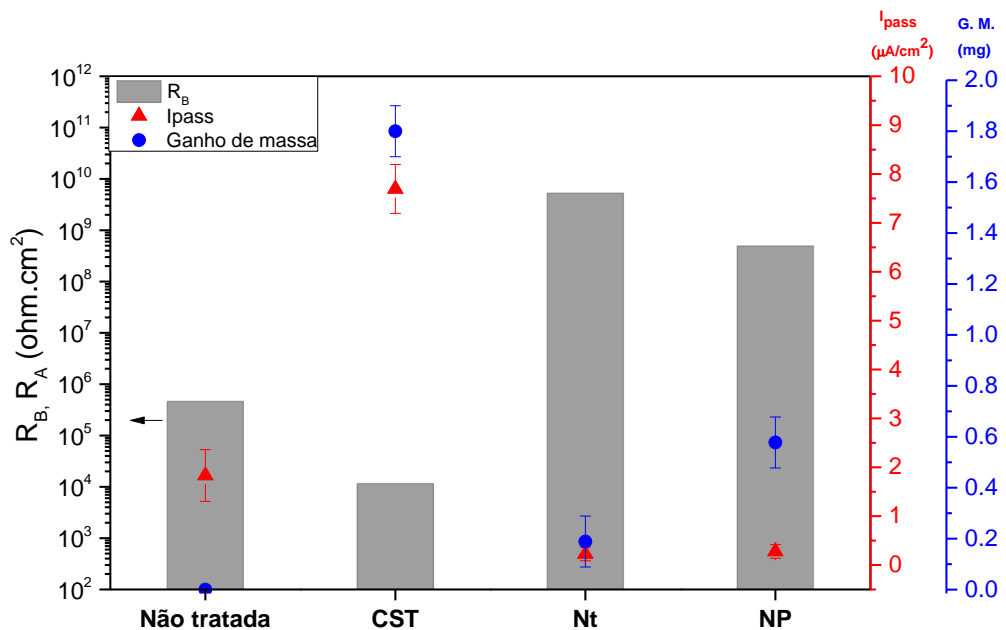


Figura 4.17 Resposta à corrosão e bioatividade de amostras não tratadas, e tratadas com CST, nanotubos e nanoporos após 14 dias de imersão em SBF a 37 °C. Resistência barreira (R_B ou R_A para as amostras anodizadas) obtida a partir dos dados de impedância, corrente de passivação (I_{pass}) das curvas de polarização e bioatividade através do ganho de massa.

5 Comportamento à fadiga dos diferentes tratamentos de superfície

5.1 Resistência à fadiga de amostras de TMZF não tratadas e tratadas com CST e nanoporos

Durante algumas etapas desses processos de modificação, o gás hidrogênio é produzido e, devido à afinidade da fase β de titânio pelo hidrogênio, ele pode ser absorvido em quantidade suficiente, causando problemas de fragilização do material, o que poderia afetar diretamente o processo de nucleação e propagação de trincas por fadiga.

Dessa forma, foi avaliada a resposta à fadiga de amostras não tratadas (superfície polida), tratadas com HCl e NaOH (CST) e amostras anodizadas (nanoporos). A resistência à fadiga foi determinada através dos testes de *staircase* ou escada e, em seguida, as superfícies das fraturas foram analisadas para avaliar a evidência de mecanismos de fragilização.

Os implantes ortopédicos são submetidos a cargas cíclicas devido às demandas mecânicas do corpo humano, submetendo esses componentes a condições de fadiga de alto ciclo (HCF). Testes de fadiga de alto ciclo ($N = 5 \times 10^6$ ciclos) foram realizados usando o método da escada para avaliar o desempenho de fadiga das diferentes superfícies estudadas neste trabalho.

As amostras não tratadas foram lixadas e polidas com o objetivo de minimizar a influência dos defeitos superficiais induzidos pela usinagem nas propriedades de fadiga. O limite de fadiga em termos de tensão máxima e o desvio padrão calculado pela abordagem estatística de Dixon-Mood são 730 e 13 MPa, respectivamente (Tabela 5.1).

Tabela 5.1 Lista das medidas topográficas da rugosidade R_a e R_z , resistência à fadiga, teor de hidrogênio e observações fractográficas para as diferentes condições de superfície estudadas.

	Rugosidade (μm)		Tensão Max Fadiga (MPa)	H (ppm)	Observações Fractográficas
	Ra	Rz			
Não tratadas	<0.100	<0.100	730 ± 13	99 ± 22	<ul style="list-style-type: none"> • Estrias de fadiga bem definidas e padrões de rio. • Propagação circumferencial da trinca associada ao mecanismo HELP. • Alta rugosidade, possibilidade do efeito de entalhe.
CST não polido	0.443	3.390	< 300	310 ± 23	<ul style="list-style-type: none"> • Trincas secundárias nos limites dos grãos. • Evidência de formação de hidretos.
CST-polido	<0.100	<0.100	563 ± 28	261 ± 4	<ul style="list-style-type: none"> • Fratura intergranular em amostras testadas com alto nível de esforço e correlacionadas com o mecanismo de decoesão induzido por hidrogênio. • Propagação circumferencial da trinca associada ao mecanismo HELP.
Nanoporos	<0.100	0.313	< 300	127 ± 23	<ul style="list-style-type: none"> • Nucleação

Figura 5.1 mostra a superfície de fratura das amostras não tratadas para examinar e determinar suas características após os testes de fadiga. A nucleação

de trincas na superfície (região 1) foi o principal local de iniciação para amostras não tratadas. A zona de propagação estável ou região 2 ocupa cerca de 50% de toda a superfície e é caracterizada por estrias de fadiga bem definidas e padrões de rios. A área restante compreende uma zona de transição de propagação instável da trinca.

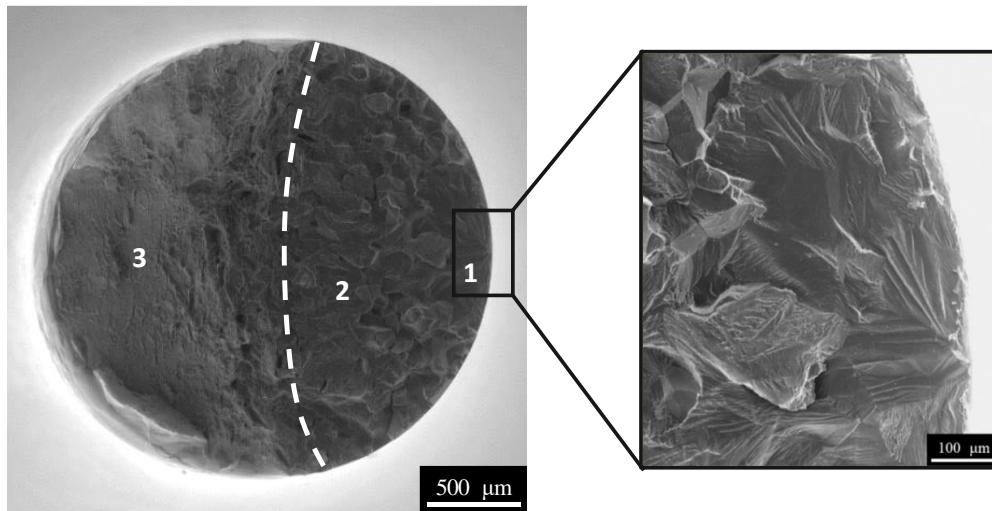


Figura 5.1 Fractografia da amostra não tratada, a linha tracejada designa a transição aproximada entre as regiões de propagação de trinca estável e instável e o quadrado indica a região ampliada no lado direito, apontando o local de iniciação da trinca.

Com o auxílio de um microscópio confocal de varredura a laser, foram obtidas características topográficas, como rugosidade e morfologia dos diferentes tratamentos estudados.

A Tabela 5.1 mostra os valores médios da rugosidade (R_a) e a rugosidade do pico ao vale (R_z) para cada um dos tratamentos. Amostras não tratadas foram polidas para obter uma superfície homogênea e lisa, como pode ser visto na Figura 5.2 (a). O processo de polimento elimina os riscos decorrentes do processo de usinagem, o que é corroborado pelos baixos valores de rugosidade R_a e R_z .

A Figura 5.2 (b) mostra a topografia de uma amostra representativa tratada com HCl e NaOH. Esse ataque combinado produz uma superfície com formação de microporos de tamanho aproximado de $3,40 \mu\text{m}$, superior ao valor observado nas amostras polidas ($<0,100 \mu\text{m}$).

A dispersão da rugosidade (por exemplo, entalhes) pode levar a diferenças consideráveis na resposta à fadiga do componente. Por exemplo, trincas de aproximadamente $3,50 \mu\text{m}$ na liga Ti-6Al-4V, podem reduzir a resistência à fadiga em cerca de 12% [26].

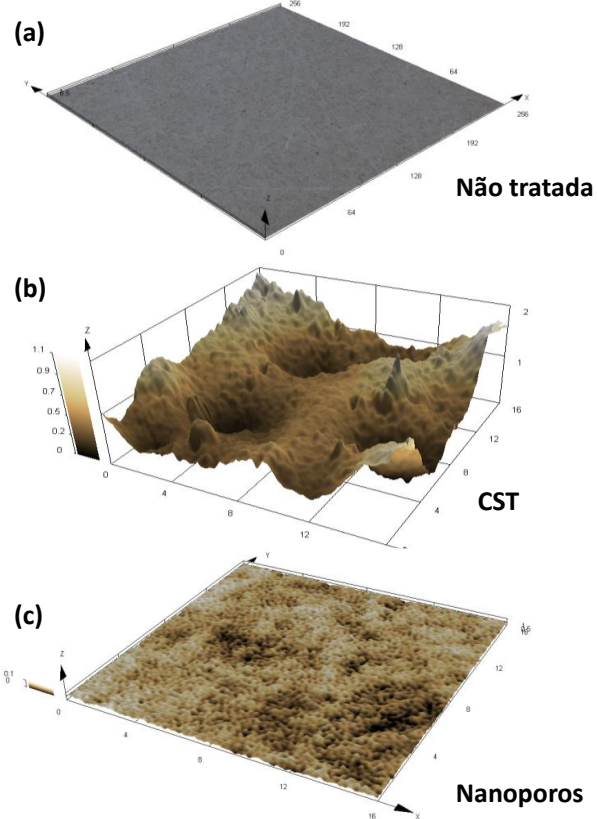


Figura 5.2. Imagens 3D determinadas por microscopia confocal de varredura a laser de: a) amostras não tratadas, b) CST e c) nanoporos.

Resultados preliminares de fadiga das amostras de CST mostraram uma diminuição drástica da resistência para um valor menor a 370 MPa (tensão de tração principal máxima para uma geometria da haste do quadril [27]). Essa alta redução da resistência (~ 50% em comparação com as amostras não tratadas) indica a existência de um fenômeno adicional à sensibilidade ao entalhe que está afetando a resposta à fadiga do material.

Estudos anteriores empregando o tratamento com HCl e NaOH sobre uma liga de titânio $\alpha+\beta$ mostraram um aumento significativo no teor de hidrogênio [28]. Mesmo um ligeiro aumento no teor de hidrogênio pode causar fragilização nas ligas de titânio, produzindo uma redução na tenacidade à fratura e na resistência à fadiga [29, 30].

Dessa forma, foi calculado o teor de hidrogênio das diferentes condições de superfície (Tabela 5.1), mostrando um aumento após os tratamentos de superfície em comparação com as amostras não tratadas. As amostras de CST mostram os valores mais altos, próximos a 310 ppm. Esse alto teor de hidrogênio poderia explicar a drástica diminuição da resistência à fadiga das amostras de CST.

Para determinar se há uma alteração no desempenho à fadiga pelo hidrogênio absorvido após o tratamento químico, as amostras de TMZF tratadas quimicamente foram lixadas e polidas (usando o mesmo protocolo empregado em amostras não tratadas) para eliminar os microporos formados e, assim, evitar o efeito de entalhe. Em seguida, os espécimes foram testados em fadiga pelo método escada.

O limite de fadiga em termos de tensão máxima e o desvio padrão calculado são respectivamente 563 e 28 MPa para as amostras CST-polidas. A redução de 25% da resistência à fadiga em comparação com as amostras não tratadas pode estar associada ao aumento significativo no conteúdo de hidrogênio detectado no material, mesmo após ao lixamento e polimento da superfície das amostras.

A Figura 5.3 mostra a superfície de fratura das amostras CST-polidas. Aqui a região de propagação é caracterizada por degraus de clivagem ou padrões de rios. Os ramos desses padrões de rio se unem na direção da propagação da fissura e podem ser usados para estabelecer a direção da fratura local e o ponto de nucleação da trinca, indicado pelo quadrado preto.

A região ampliada na Figura 5.3 mostra evidências de trincas secundárias formadas através dos limites dos grãos. Geralmente, esse tipo de fratura está associado a fenômenos de fragilização por hidrogênio, como fragilização nos contornos de grãos ou mesmo a formação e ruptura repetidas de fases de hidreto frágeis próximas aos contornos de grãos [31, 32].

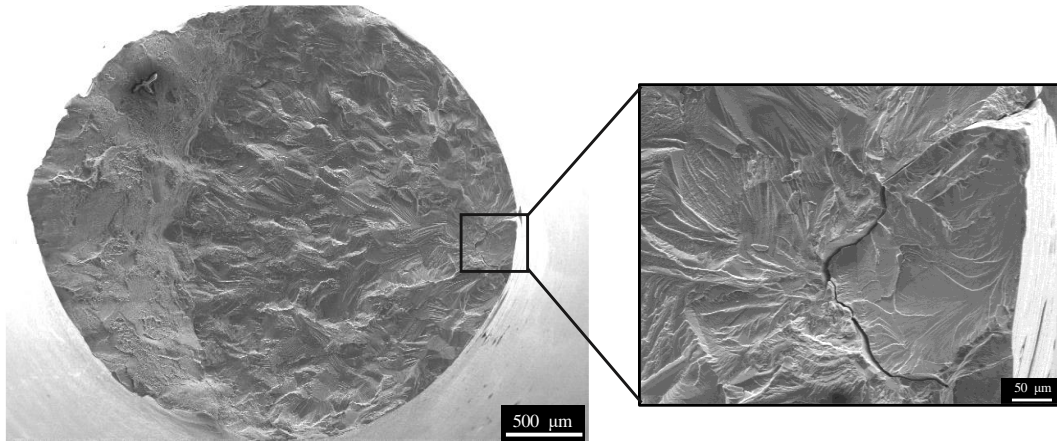


Figura 5.3 Fractografia da amostra CST-polida, o quadrado preto indica a região ampliada no lado direito, apontando o local de iniciação da fissura.

Conforme observado na Tabela 5.1, as amostras anodizadas com nanoporos apresentaram um ligeiro aumento no teor de hidrogênio, próximo a 150 ppm. Este valor é inferior ao observado em amostras tratadas com CST. Além disso, a partir de medições de rugosidade (Tabela 5.1), as amostras com nanoporos exibiram uma superfície mais lisa com valores de rugosidade baixos ($R_z = 0,3 \mu\text{m}$), evitando um

possível efeito de entalhe. Essas duas condições podem indicar um melhor comportamento à fadiga do que as amostras de CST.

Ao contrário do comportamento esperado, todas as amostras com nanoporos falharam, em valores de tensão inferiores ao valor de tensão principal máxima para uma geometria da haste do quadril (370 MPa) [27], até mesmo a amostra testada a 300 MPa. Apenas a amostra testada a 200 MPa sobreviveu ao ensaio, indicando que, mesmo evitando a possibilidade de efeito de entalhe, o processo de anodização reduz a resistência à fadiga e pode estar associado ao teor de hidrogênio na superfície das amostras.

A superfície de fratura por fadiga correspondente à amostra de nanoporos testada a 500 MPa é ilustrada na Figura 5.4. Como é observado na região (b), características típicas do crescimento cíclico de trincas por fadiga, como padrões de rios e clivagem, aparecem e se tornam o principal mecanismo de propagação nessa região. Esta zona de propagação estável da trinca por fadiga é restrita a uma pequena região elíptica.

As fractografias da Figura 5.4 (c-d) das amostras tratadas com nanoporos e CST mostraram mais evidências de fratura frágil. Aqui é observado um padrão de clivagem interessante e distinto chamado linhas de Wallner (indicado por setas pretas). Esse arranjo é observado em superfícies de fratura de materiais frágeis, inclusões ou compostos intermetálicos. Consiste em dois conjuntos de etapas de clivagem paralelas que frequentemente se intersectam para produzir um padrão cruzado. As linhas de Wallner resultam da propagação simultânea de uma frente de trinca e de uma onda de choque elástica no material [33].

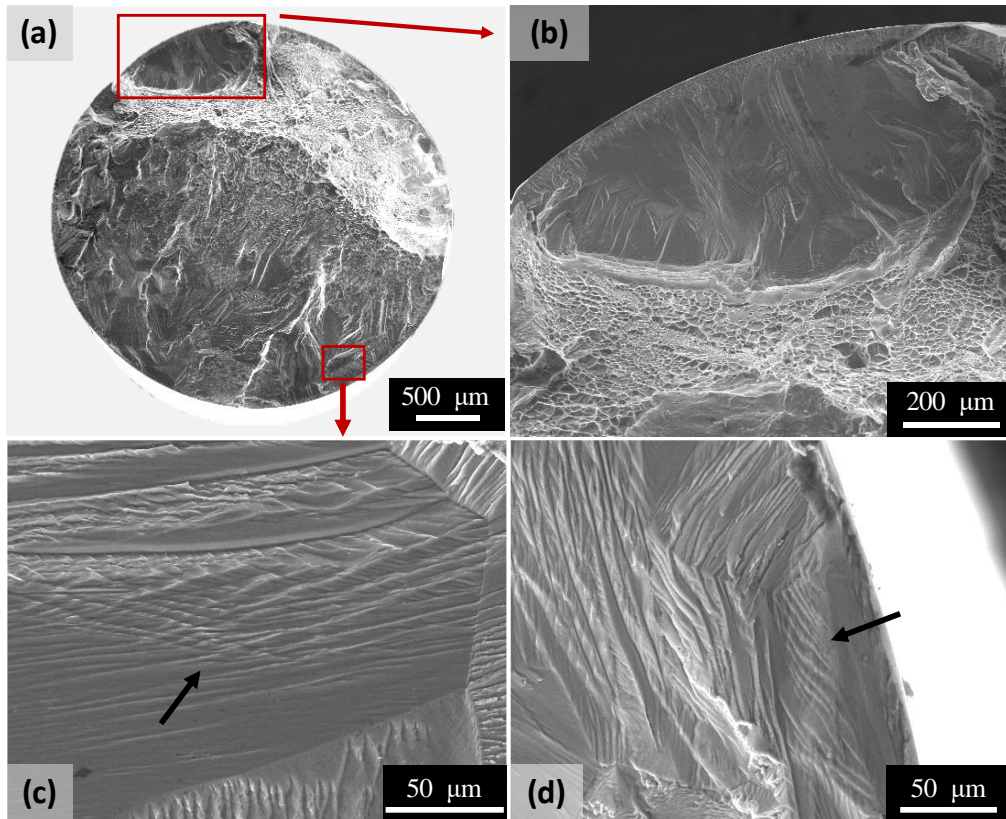


Figura 5.4 a) Fractografia da amostra de nanoporos que foi testada a 500 MPa, b) zona ampliada indicando uma região de propagação de trincas estável, c) região ampliada da amostra de nanoporos indicando linhas de Wallner e d) região ampliada da amostra CST-polida testada em fadiga a 550 MPa indicando o padrão de linhas de Wallner.

5.2 Fragilização por hidrogênio

A fragilização por hidrogênio (FH) é um fenômeno interessante, mas prejudicial, e pode ocorrer em uma ampla variedade de metais e ligas. A FH envolve um grupo de mecanismos associados à redução das propriedades mecânicas atribuídas ao hidrogênio como ator principal [31].

O mecanismo de fratura por trás dessa fragilização nas ligas de titânio não é totalmente conhecido. Essa dificuldade é especialmente verdadeira para ligas de titânio β metaestáveis, nas quais o efeito do hidrogênio no comportamento mecânico foi explicado em termos de: (i) falha devido à formação de hidreto induzidos por tensão [29, 34], (ii) descoesão induzida por hidrogênio [31, 35, 36] e (iii) plasticidade localizada assistida por hidrogênio (HELP do inglês) [37, 38]. Mesmo em sistemas monofásicos, como é o caso da liga TMZF, a identificação do mecanismo de fragilização é complexa e vários mecanismos de fratura relacionados ao hidrogênio podem operar simultaneamente [35, 36, 38]. Embora vários

mecanismos tenham sido propostos para explicar a fragilização por hidrogênio, os mencionados acima são considerados os mais aplicáveis a este estudo.

A Figura 5.5 mostra a análise pelo mapeamento automatizado de orientação de cristais (ACOM-TEM) das amostras tratadas com CST e testadas em fadiga. Além da fase β da matriz, é observada no mapa de fases a presença de partículas muito finas de TiH_2 com uma estrutura tetragonal. A presença desses hidretos frágeis é uma forte evidência do efeito do hidrogênio na redução da resistência à fadiga do material.

Esses hidretos podem resultar do aumento da concentração local de hidrogênio no campo de deformação de tensão dos defeitos estendidos da rede, como discordâncias e contornos de grãos. Portanto, sugere-se que, como o hidrogênio tem uma considerável solubilidade na fase β e, de acordo com o fenômeno conhecido como hidreto induzido por tensão, a deformação localizada durante o teste de fadiga induza a difusão do hidrogênio para estes defeitos [39, 40]. Consequentemente, o TiH_2 precipita nos contornos de grãos de alta energia, conforme observado nas Figuras 5.5 b e 5.5 c.

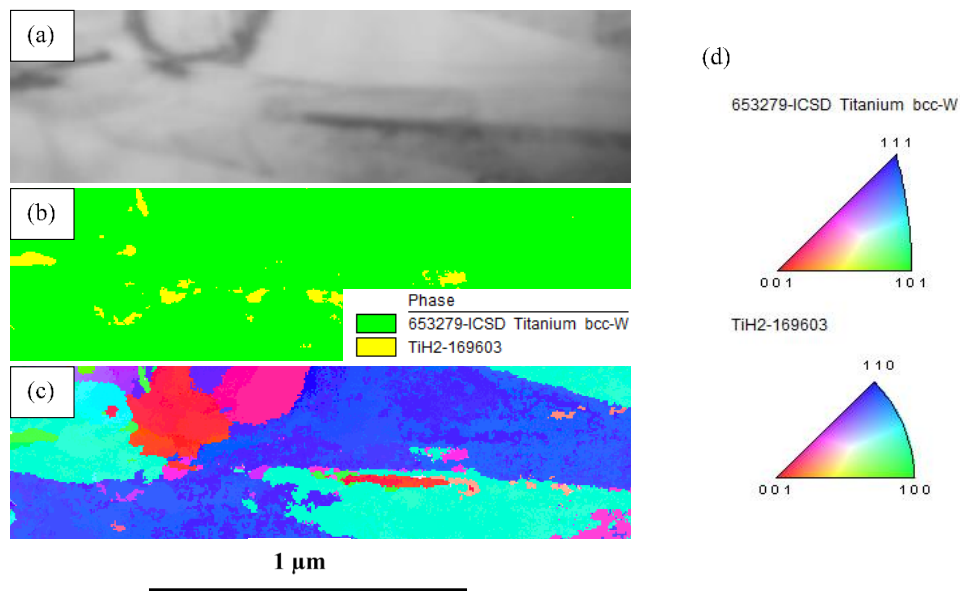


Figura 5.5 Imagens da amostra CST-polida e testadas por fadiga, geradas usando o sistema ASTAR acoplado ao TEM: (a) imagem de campo claro virtual (VBF), (b) mapeamento de fase (PM), (c) mapeamento de imagem de orientação (OIM) e (d) figura de pólo inverso (IPF) de onde as cores foram usadas para indexar orientações no OIM.

Outro mecanismo de FH estudado neste trabalho é a plasticidade localizada assistida por hidrogênio ou HELP. Nesta teoria, a nucleação e o movimento das

discordâncias são favorecidos pela concentração do hidrogênio [35, 41]. Nesse sentido, espera-se um aumento de deformação e plasticidade na zona com alta concentração de hidrogênio. Assim, evidências que justificam o mecanismo HELP são observadas na fractografia com propagação localizada de trincas dúcteis [37, 38].

Hidrogênio é produzido durante os dois tratamentos, CST e anodizado, na interface metal / eletrólito. Simultaneamente, uma quantidade desse elemento é absorvida e difundida dentro da liga de titânio; no entanto, uma quantidade alta é acumulada adjacente à superfície da amostra. Essa condição facilitou a observação do mecanismo HELP atuando durante o teste de fadiga na superfície dos corpos de prova com nanoporos e nas amostras CST não polidas.

A Figura 5.6 mostra evidências do mecanismo HELP atuando nas amostras CST não polidas durante o teste de fadiga a 300 MPa. Através das imagens ampliadas é possível observar uma trinca circumferencial propagando-se na amostra circular. A propagação dessa trinca dúctil localizada é confinada em uma região de aproximadamente $26 \pm 5 \mu\text{m}$ da superfície da amostra (Figura 5.6 b-d), favorecida por um aumento na nucleação e mobilidade das discordâncias, devido à maior concentração de hidrogênio nessa região da subsuperfície.

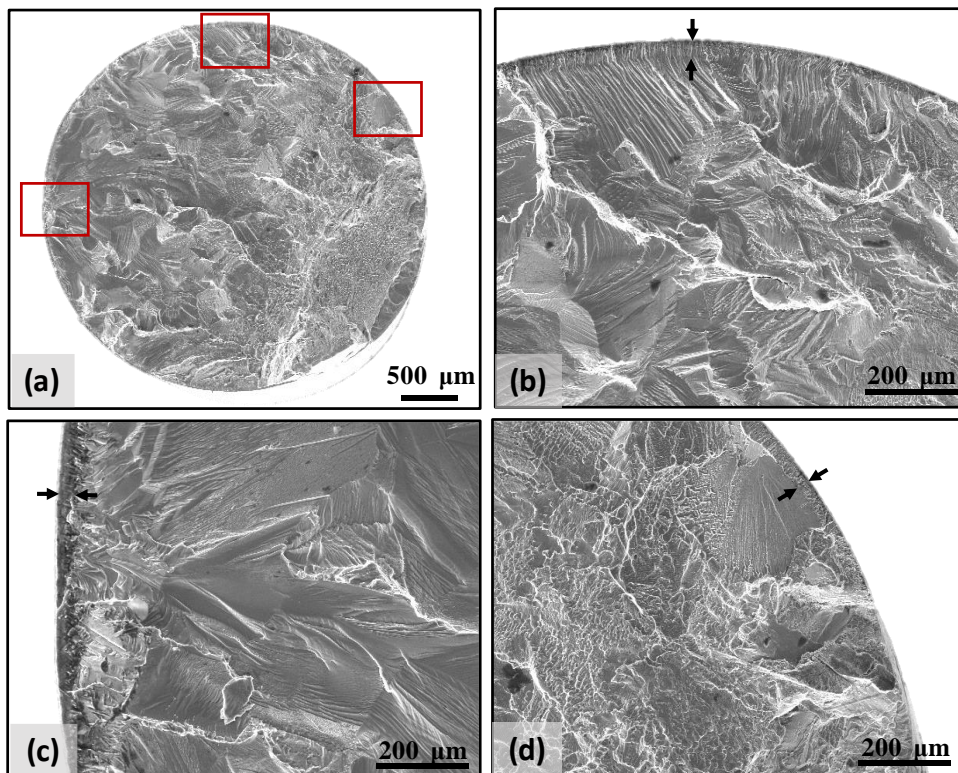


Figura 5.6 a) Fractografia da amostra CST não polida que foi testada em fadiga a 300 MPa, b), c) e d) zona ampliada, indicando uma região de propagação de trinca estável na zona hidrogenada, indicada por setas pretas.

Um comportamento semelhante foi observado nas amostras de nanoporos fraturados após os testes de fadiga. A Figura 5.7 mostra a evidência de uma trinca circunferencial propagando-se ao redor da amostra. Estas observações sugerem que os valores exibidos na Tabela 5.1 para as amostras com nanoporos e CST poderiam ser maiores do que o indicado, devido à alta concentração do hidrogênio na superfície e à dificuldade experimental de obter com precisão a concentração nesta região.

A Figura 5.7 mostra que a trinca circunferencial da superfície é gerada e propagada durante os ciclos iniciais. A partir disso, novas trincas nucleiam e depois se propagam radialmente na amostra em um plano normal à carga externa (Figura 5.7 c). Finalmente, a falha ocorre por sobrecarga, exibindo alvéolos rasos. Como observado na Figura 5.7, essa falha final se conecta diretamente à trinca circunferencial preexistente, o que corrobora a sequência de fratura mencionada.

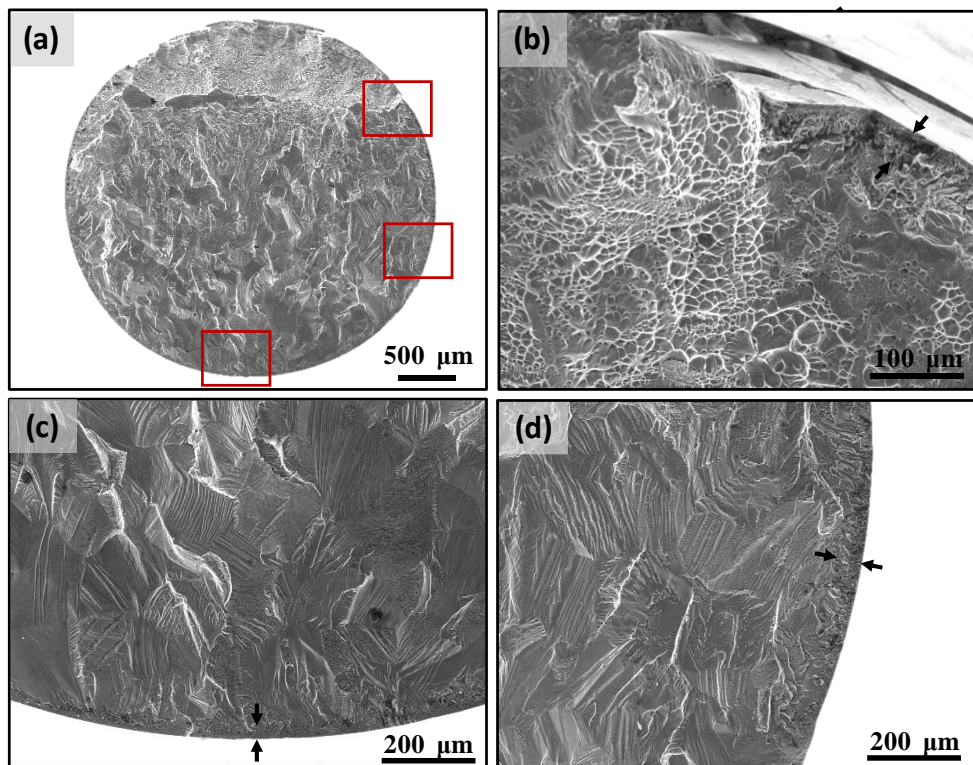


Figura 5.7 a) Fractografia da amostra com nanoporos, que foi testada em fadiga a 300 MPa, b) zona ampliada da falha final, c) e d) zona indicando uma região de propagação de trincas estável na área hidrogenada, indicada por setas pretas.

Conclusões Gerais

Nesta tese foram estudados os desempenhos de biocompatibilidade e corrosão de amostras de Ti-12Mo-6Zr-2Fe com nanotubos, nanoporos e CST imersos durante 0, 1, 7 e 14 dias no SBF, bem como a variação da resistência à fadiga de amostras não tratadas, tratadas com CST e nanoporos. As conclusões dessas análises estão resumidas nos seguintes parágrafos:

- Tratamentos de superfície como nanotubos, nanoporos e CST na liga β-TMZF foram obtidos satisfatoriamente.
- Após 14 dias de imersão no SBF, não foi possível observar a formação de HAp nas amostras não tratadas. Durante o mesmo período, as amostras de nanotubos e nanoporos apresentaram uma formação de HAp menor e moderada (respectivamente). Enquanto isso, as amostras de CST apresentaram o melhor comportamento de bioatividade com a maior formação de HAp dentre todas as superfícies estudadas.
- Os valores de E_{corr} revelaram que os nanotubos e nanoporos apresentaram um comportamento mais nobre do que as amostras não tratadas e as CST, indicando uma superfície mais protetora. Além disso, embora essas superfícies anodizadas apresentassem valores moderados de i_{pass} nos estágios iniciais de imersão (0 e 1 dia), após 14 dias imersos em SBF apresentaram os valores mais baixos, próximos a $0,2 \mu\text{A.cm}^{-2}$, colocando-os na classe de resistência “Muito estável”.
- As curvas de Nyquist e Bode para amostras de TMZF não tratadas mostraram um comportamento pseudocapacitivo devido à sua camada passiva muito protetora. O aumento contínuo do módulo de impedância nessas amostras sugeriu que a resistência à corrosão aumenta com o tempo de imersão.
- Através das curvas Nyquist e Bode, as amostras de CST mostraram um comportamento mais reativo em comparação com as amostras não tratadas, independentemente do tempo de imersão em SBF. Nestas amostras, após 14 dias de imersão, foi possível observar uma variação na curva de impedância, a qual foi associada à formação da camada de HAp sobre a superfície.
- As curvas de impedância das amostras anodizadas e imersas em SBF revelaram um comportamento capacitivo ou pelo menos pseudocapacitivo, corroborando a resposta protetora dessas condições de superfície. Além disso, foi observado um comportamento singular que não pôde ser modelado pelos circuitos equivalentes tradicionais. Assim, foi proposto um modelo de linha de transmissão de dois canais para analisar os resultados de impedância com sucesso.
- Amostras de TMZF não tratadas mostraram um alto limite de fadiga em termos de tensão máxima de 730 Mpa para 5×10^6 ciclos.

- Os resultados de fadiga das amostras de CST mostraram uma diminuição drástica da resistência à fadiga, em torno de 50%, em comparação com as amostras não tratadas, devido ao efeito de entalhe e ao alto conteúdo adicional de hidrogênio.
- Para evitar o efeito do entalhe, novas amostras de CST foram polidas e depois testadas em fadiga. No entanto, elas mostraram uma diminuição de 25% da resistência à fadiga em comparação com as amostras não tratadas, o que foi associado ao hidrogênio absorvido durante o CST.
- Amostras com nanoporos com baixa rugosidade na superfície e mesmo com um ligeiro aumento do hidrogênio medido mostraram uma redução drástica na resistência à fadiga, semelhante às amostras CST não polidas. Esse comportamento foi associado à possibilidade de uma alta concentração de hidrogênio na superfície da amostra.
- Neste estudo, foram observadas evidências de três mecanismos de fragilização por hidrogênio possivelmente atuando sobre as amostras tratadas: formação de hidreto induzido por tensão, decoesão induzida por hidrogênio e plasticidade localizada assistida por hidrogênio. No entanto, são necessários mais estudos para certificar esses mecanismos.
- Os resultados de fadiga e os mecanismos de fragilização por hidrogênio observados neste estudo apontam o risco de uso destes métodos conhecidos para projetar superfícies de titânio que melhoram a osseointegração, sem uma avaliação mecânica e eletroquímica sistemática.

REFERENCE

- [1] H. Takadama, H. M. Kim, T. Kokubo, and T. Nakamura, TEM-EDX study of mechanism of bonelike apatite formation on bioactive titanium metal in simulated body fluid, *J. Biomed. Mater. Res.*, vol. 57, no. 3, pp. 441–448, 2001.
- [2] R. J. Narayan, ASM Handbook, Volume 23 Materials for Medical Devices, 1 st., vol. 23. 2012.
- [3] A. K. Shukla, R. Balasubramaniam, and S. Bhargava, Properties of passive film formed on CP titanium, Ti-6Al-4V and Ti-13.4Al-29Nb alloys in simulated human body conditions, *Intermetallics*, vol. 13, no. 6, pp. 631–637, 2005.
- [4] F. Hilario, V. Roche, R. P. Nogueira, and A. M. J. Junior, Influence of morphology and crystalline structure of TiO_2 nanotubes on their electrochemical properties and apatite-forming ability, *Electrochim. Acta*, vol. 245, pp. 337–349, 2017.
- [5] E. Vasilescu, P. Drob, D. Raducanu, I. Cinca, D. Mareci, J. M. Calderon Moreno, M. Popa, C. Vasilescu, and J. C. Mirza Rosca, Effect of thermo-mechanical processing on the corrosion resistance of Ti6Al4V alloys in

- biofluids, *Corros. Sci.*, vol. 51, no. 12, pp. 2885–2896, 2009.
- [6] S. Tamilselvi, V. Raman, and N. Rajendran, Surface modification of titanium by chemical and thermal methods - Electrochemical impedance spectroscopic studies, *Corros. Eng. Sci. Technol.*, vol. 46, no. 4, pp. 585–591, 2011.
 - [7] F. Hilario, Synthèse et caractérisations de nanotubes de TiO₂ pour applications biomédicales : propriétés électrochimiques et bioactivité, Université Grenoble Alpes, 2018.
 - [8] V. Augustyn, P. Simon, and B. Dunn, Pseudocapacitive oxide materials for high-rate electrochemical energy storage, *Energy Environ. Sci.*, vol. 7, no. 5, pp. 1597–1614, 2014.
 - [9] H. Liu, J. Yang, X. Zhao, Y. Sheng, W. Li, C. L. Chang, Q. Zhang, Z. Yu, and X. Wang, Microstructure, mechanical properties and corrosion behaviors of biomedical Ti-Zr-Mo-xMn alloys for dental application, *Corros. Sci.*, vol. 161, no. May, pp. 2–15, 2019.
 - [10] P. Córdoba-Torres, N. T. C. Oliveira, C. Bolfarini, V. Roche, and R. P. Nogueira, Electrochemical impedance analysis of TiO₂ nanotube porous layers based on an alternative representation of impedance data, *J. Electroanal. Chem.*, vol. 737, pp. 54–64, 2015.
 - [11] Mark E. Orazem and B. Tribollett, Electrochemical Impedance Spectroscopy, in *Agricultural and Food Electroanalysis*, Second edi., 2015, pp. 381–419.
 - [12] S. L. De Assis, S. Wolynec, and I. Costa, Corrosion characterization of titanium alloys by electrochemical techniques, *Electrochim. Acta*, vol. 51, no. 8–9, pp. 1815–1819, 2006.
 - [13] D. Q. Martins, W. R. Osório, M. E. P. Souza, R. Caram, and A. Garcia, Effects of Zr content on microstructure and corrosion resistance of Ti-30Nb-Zr casting alloys for biomedical applications, *Electrochim. Acta*, vol. 53, no. 6, pp. 2809–2817, 2008.
 - [14] A. Kocijan, D. K. Merl, and M. Jenko, The corrosion behaviour of austenitic and duplex stainless steels in artificial saliva with the addition of fluoride, *Corros. Sci.*, vol. 53, no. 2, pp. 776–783, 2011.
 - [15] K. B. Devi, K. Singh, and N. Rajendran, Synthesis and characterization of nanoporous sodium-substituted hydrophilic titania ceramics coated on 316L SS for biomedical applications, *J. Coatings Technol. Res.*, vol. 8, no. 5, pp. 595–604, 2011.
 - [16] S. Gudi, J. Radoševi, and M. Kliški, Study of passivation of Al and Al-Sn alloys in borate buffer solutions using electrochemical impedance spectroscopy, *Electrochim. Acta*, vol. 47, no. 18, pp. 3009–3016, 2002.
 - [17] F. Hilario, V. Roche, A. M. Jorge, and R. P. Nogueira, Application of the transmission line model for porous electrodes to analyse the impedance response of TiO₂ nanotubes in physiological environment, *Electrochim. Acta*, vol. 253, pp. 599–608, 2017.

- [18] L. Jonášová, F. a. Müller, A. Helebrant, J. Strnad, and P. Greil, Biomimetic apatite formation on chemically treated titanium, *Biomaterials*, vol. 25, pp. 1187–1194, 2004.
- [19] Diego Alfonso Godoy Pérez, Influence Of Surface Treatments on Corrosion Resistance Properties Of Ultrafine Grained Titanium Alloys For Biomedical applications, Universite Grenoble Alpes And Universidade Federal De São Carlos, 2019.
- [20] R. de Levie, On porous electrodes in electrolyte solutions*, *Electrochim. Acta*, vol. 9, no. 9, pp. 1231–1245, 1964.
- [21] P. Roy, S. Berger, and P. Schmuki, TiO₂ nanotubes: Synthesis and applications, *Angew. Chemie - Int. Ed.*, vol. 50, no. 13, pp. 2904–2939, 2011.
- [22] G. Garcia-Belmonte, J. Bisquert, E. C. Pereira, and F. Fabregat-Santiago, Switching behaviour in lightly doped polymeric porous film electrodes. Improving distributed impedance models for mixed conduction conditions, *J. Electroanal. Chem.*, vol. 508, no. 1–2, pp. 48–58, 2001.
- [23] G. Láng and K. E. Heusler, Remarks on the energetics of interfaces exhibiting constant phase element behaviour, *J. Electroanal. Chem.*, vol. 457, no. 1–2, pp. 257–260, 1998.
- [24] T. Pajkossy, Impedance of rough capacitive electrodes, *J. Electroanal. Chem.*, vol. 364, no. 1–2, pp. 111–125, 1994.
- [25] C. Shuai, H. Sun, P. Wu, C. Gao, Y. Yang, W. Guo, D. Yang, F. Xu, P. Feng, and S. Peng, Biosilicate scaffolds for bone regeneration: Influence of introducing SrO, *RSC Adv.*, vol. 7, no. 35, pp. 21749–21757, 2017.
- [26] P. S. C. P. da Silva, L. C. Campanelli, C. A. Escobar Claros, T. Ferreira, D. P. Oliveira, and C. Bolfarini, Prediction of the surface finishing roughness effect on the fatigue resistance of Ti-6Al-4V ELI for implants applications, *Int. J. Fatigue*, vol. 103, pp. 258–263, 2017.
- [27] B. J. S. de Oliveira, L. C. Campanelli, D. P. Oliveira, A. P. de Bribean Guerra, and C. Bolfarini, Surface characterization and fatigue performance of a chemical-etched Ti-6Al-4V femoral stem for cementless hip arthroplasty, *Surf. Coatings Technol.*, vol. 309, pp. 1126–1134, 2017.
- [28] C. A. Escobar Claros, Estudo da resistência à fadiga da liga Ti-6Al-4V com superfície modificada por tratamento químico, Universidad de Sao carlos, 2016.
- [29] V. Madina and I. Azkarate, Compatibility of materials with hydrogen. Particular case: Hydrogen embrittlement of titanium alloys, *Int. J. Hydrogen Energy*, vol. 34, no. 14, pp. 5976–5980, 2009.
- [30] L. C. Campanelli, P. S. C. P. da Silva, A. M. Jorge, and C. Bolfarini, Effect of hydrogen on the fatigue behavior of the near-β Ti-5Al-5Mo-5V-3Cr alloy, *Scr. Mater.*, vol. 132, pp. 39–43, 2017.
- [31] P. P. Milella, *Fatigue and Corrosion in Metals*. 2013.

- [32] ASM International. Handbook, ASM Handbook: Volume 12: Fractography, Met. Handb., vol. 2, p. 857, 1998.
- [33] ASM, ASM Handbook Volume 12: Fractography, vol. 2. 1987.
- [34] P. D. Nezhadfar, A. S. Johnson, and N. Shamsaei, Fatigue Behavior and Microstructural Evolution of Additively Manufactured Inconel 718 under Cyclic Loading at Elevated Temperature, *Int. J. Fatigue*, p. 105598, 2020.
- [35] D. F. Teter, I. M. Robertson, and H. K. Birnbaum, The effects of hydrogen on the deformation and fracture of β -titanium, *Acta Mater.*, vol. 49, no. 20, pp. 4313–4323, 2001.
- [36] A. M. Alvarez, I. M. Robertson, and H. K. Birnbaum, Hydrogen embrittlement of a metastable β -titanium alloy, *Acta Mater.*, vol. 52, no. 14, pp. 4161–4175, 2004.
- [37] W. Barrows, R. Dingreville, and D. Spearot, Traction-separation relationships for hydrogen induced grain boundary embrittlement in nickel via molecular dynamics simulations, *Mater. Sci. Eng. A*, vol. 650, pp. 354–364, 2016.
- [38] Y. Murakami, J. Yamabe, and H. Matsunaga, Microscopic mechanism of hydrogen embrittlement in fatigue and fracture, *Key Eng. Mater.*, vol. 592–593, pp. 3–13, 2014.
- [39] P. J. Ferreira, I. M. Robertson, and H. K. Birnbaum, Hydrogen effects on the character of dislocations in high-purity aluminum, *Acta Mater.*, vol. 47, no. 10, pp. 2991–2998, 1999.
- [40] J. Von Pezold, L. Lymerakis, and J. Neugebeauer, Hydrogen-enhanced local plasticity at dilute bulk H concentrations: The role of H-H interactions and the formation of local hydrides, *Acta Mater.*, vol. 59, no. 8, pp. 2969–2980, 2011.
- [41] Y. Murakami, T. Kanezaki, Y. Mine, and S. Matsuoka, Hydrogen embrittlement mechanism in fatigue of austenitic stainless steels, *Metall. Mater. Trans. A Phys. Metall. Mater. Sci.*, vol. 39 A, no. 6, pp. 1327–1339, 2008.